

5-2017

Imaging Polarimetry with Polarization-Sensitive Focal Plane Arrays

Dmitry V. Vorobiev
dxv2686@rit.edu

Follow this and additional works at: <http://scholarworks.rit.edu/theses>

Recommended Citation

Vorobiev, Dmitry V., "Imaging Polarimetry with Polarization-Sensitive Focal Plane Arrays" (2017). Thesis. Rochester Institute of Technology. Accessed from

This Dissertation is brought to you for free and open access by the Thesis/Dissertation Collections at RIT Scholar Works. It has been accepted for inclusion in Theses by an authorized administrator of RIT Scholar Works. For more information, please contact ritscholarworks@rit.edu.

IMAGING POLARIMETRY WITH POLARIZATION-SENSITIVE FOCAL PLANE ARRAYS

By

Dmitry V. Vorobiev

A dissertation submitted
in partial fulfillment of the requirements for
the degree of Ph.D. in Astrophysical Sciences and Technology,
in the School of Physics and Astronomy,
College of Science,
Rochester Institute of Technology

May 2017

Approved by _____

Prof. Andrew Robinson

Date

Director, Astrophysical Sciences and Technology

ASTROPHYSICAL SCIENCES AND TECHNOLOGY
COLLEGE OF SCIENCE
ROCHESTER INSTITUTE OF TECHNOLOGY
ROCHESTER, NEW YORK

CERTIFICATE OF APPROVAL

Ph.D. DEGREE DISSERTATION

The Ph.D. Degree Dissertation of Dmitry V. Vorobiev
has been examined and approved by the dissertation committee
as satisfactory for the dissertation requirement for the Ph. D. degree
in Astrophysical Sciences and Technology.

Dr. Zoran Ninkov, Dissertation Advisor Date

Dr. Grover Swartzlander, Jr., Committee Chair Date

Dr. Michael G. Gartley Date

Dr. Dean C. Hines Date

Dr. David W. Messinger Date

Dr. Andrew Robinson Date

“I have decided to remain a modest engineer of bridges and roads, and even to abandon physics, if circumstances require it. I would resolve to do so more easily, that I now see it’s a stupid plan troubling oneself to acquire a small bit of glory, that they’ll always quarrel with you about it... Fie on contested glory!”

Augustin-Jean Fresnel

September 25, 1816

Two years later, Fresnel published the theory for near-field diffraction.

Abstract

Astrophysical Sciences and Technology

Doctor of Philosophy

Imaging polarimetry with polarization-sensitive focal plane arrays

by Dmitry VOROBIEV

Polarization is an intrinsic property of light, like frequency or coherence. Humans have long benefited from our ability to distinguish light of different frequency based on its color. However, our eyes are not sensitive to the polarization of light. Devices to measure polarization are relatively rare and expertise in polarimetry even more so. Polarization sensors based on micropolarizer arrays appear to be the first devices capable of bringing polarimetric capability to a wide range of applications. Whereas previous polarimeters were built to perform very specific measurements, the same micropolarizer-based camera can be used on a telescope, a microscope, or with a conventional camera lens.

In this work, I investigate the operating principles of micropolarizer arrays using high resolution 3D simulations and describe several strategies to fabricate and characterize micropolarizer-based imaging polarimeters. Furthermore, I show how to incorporate the device characterization into a calibrated demodulation procedure to extract polarimetric quantities from the raw pixel intensities. As part of this effort, I show how the measured sensor properties, like pixel throughput and contrast ratio, can be used to construct a software model to produce synthetic observations of various scenes. These synthetic data are a powerful tool to study the many effects which can give rise to systematic and/or random errors during the data analysis process. Finally, I present the polarimetry performed on several astronomical sources using the RIT Polarization Imaging Camera and compare my results to previous measurements made with conventional polarimeters. Using the current calibration of the RIT Polarization Imaging Camera, I was able to achieve a polarimetric accuracy of $\sim 0.3\%$ in images of extended objects and unresolved sources.

Acknowledgements

This work would not have been possible without the support and guidance of my advisor, Zoran Ninkov. I am deeply grateful to him for the advice and encouragement that I've received over the last five years. I also thank Mike Gartley, Dean Hines, Dave Messinger, Andy Robinson, and Grover Swartzlander for serving on my dissertation committee. Their input dramatically improved this dissertation.

I owe a special thanks to Ray West and Roger Ketcheson of Moxtek, Inc., who funded much of this research and were champions of this work within their company. I am also grateful to Neal Brock of 4D Technology for his insights and continued support of my research. The data used in this dissertation were acquired using cameras built by Finger Lakes Instrumentation and I would like to thank Gary McAnally for his help with my (sometimes) unusual and (always) very last minute requests.

During the six years I spent at RIT, I benefited enormously from the efforts of numerous faculty, staff, and students. Jan Maneti and Rob Kraynik from the College of Engineering machined many parts for me and helped me avoid more than one fabrication-related crisis. Bruce Smith allowed me to occupy a part of his clean room for over two years, where the first RITPIC prototypes were built. Peter Bajorski helped me develop a deeper understanding and appreciation of statistics, through his course, book, and very engaging discussions. Al Raisanen has been a constant source of intriguing ideas and fabricated several key components for me, often on the weekend.

The simulations presented in this dissertation were performed on the RIT Research Computing cluster Ion. The architecture of Ion is uniquely suited for large computations that are not embarrassingly parallel. Ion is a wonderful tool in the kit of RIT's researchers. Ion's genesis is due to the efforts and vision of Gurcharan Khanna and its continued existence is largely thanks to the work of Paul Mezzanini and his small, but dedicated, crew.

While studying at RIT, I was fortunate to meet Judy Pipher, Dan Watson, Craig McMurtry, and Bill Forrest, from the astronomy department at the University of Rochester. Their knowledge and support were instrumental in the development of my own ideas.

Much of the metrology in this work was done with the help of Brian McIntyre at the Institute of Optics, who is a wizard and a dedicated mentor.

The on-sky evaluation of our instrument was done on the 0.9 m telescope operated by Todd Henry and the SMARTS consortium at the Cerro Tololo Inter-American Observatory. Todd and the staff at CTIO worked hard to ensure the success of my observing run; I am especially grateful to Hernan Tirado and Humberto Orrego.

For the last seven years, I had the pleasure and privilege of studying astronomy. I was given this opportunity when John McGraw invited me to join his research group at the University of New Mexico, despite my questionable academic transcript. I learned what good work looks like from John and Pete Zimmer. Their passion, creativity, work ethic, and good humor are a constant inspiration. I am forever grateful to them for their mentorship and the chance to “do good work.”

Contents

Certificate of Approval	i
Abstract	iii
Acknowledgements	iv
Contents	vi
List of Figures	x
List of Tables	xxix
Abbreviations	xxx
1 Introduction	1
2 Polarization of Light	5
2.1 A Mathematical Description	7
3 Production of Polarized Light	12
3.1 Polarization Upon Reflection	13
3.1.1 Reflection from Dielectric Surfaces	14
3.1.2 Reflection from Metal Surfaces	16
3.2 Polarization from Scattering	19
3.2.1 Rayleigh Scattering	19
3.2.2 Mie Scattering	22
3.3 Polarization from Anisotropic Materials	26
3.3.1 Diattenuation due to Aligned Asymmetric Particles	26
3.4 Intrinsically Polarized Sources	28
3.4.1 Synchrotron Radiation	28
3.4.2 Lasers	32
3.5 Polarizers	33
3.5.1 Polarizing Prisms	33

3.5.2	Polarizers Based On Diattenuation	33
3.5.2.1	Absorptive Polarizers	34
4	The Wire Grid Polarizer	35
4.1	Simulations of Wire Grid Polarizer Performance	38
4.1.1	Simulation Methods	39
4.1.2	2D Simulations - Setup and Convergence Testing	40
4.1.2.1	Testing Numerical Convergence in 2D	40
	Summary	43
4.1.3	2D Simulations - Effects of Wire Shape and Spacing	45
4.1.3.1	Effects of Wire Width	45
4.1.3.2	Effects of Wire Spacing	48
4.1.3.3	Effects of Wire Height	51
4.1.4	3D Simulations - Effects of Wire Shape and Spacing	54
4.1.4.1	Testing Numerical Convergence in 3D	54
4.1.4.2	Effects of Wire Width	55
4.1.4.3	Effects of Wire Spacing	57
4.1.4.4	Effects of Wire Height	59
4.1.5	A Comparison of 2D and 3D Simulations	60
4.1.6	Comparing Simulations to Experimental Results	61
4.1.6.1	Common Sources of Disagreement	63
4.1.7	Summary of Wire Grid Polarizer Simulations	65
5	Micropolarizer Arrays	66
5.1	Simulations of Pixelated Wire Grid Polarizers	67
5.1.1	Simulation Setup	68
5.1.2	Convergence of Non-rectilinear Structures	69
5.1.3	Performance of Pixelated Polarizers	70
5.2	Performance of Micropolarizer Superpixels	73
5.2.1	Simulation Results	74
5.2.2	Analysis Of Diffraction-induced Cross-talk	76
5.2.3	Summary of Pixelated Polarizer Simulations	79
6	Measurement of Polarization	80
6.1	Polarimetry With a Single Polarizer	80
6.2	Snapshot Polarimeters	82
6.2.1	Division of Focal Plane Polarimetry	83
6.3	The Dual-Beam Technique	84
6.4	Polarization-Sensitive Detectors	85
6.5	Polarimetry With Non-ideal Polarizers	87
6.5.1	Using Linear Least Squares	89
6.5.2	Distribution of the Stokes Parameters	91
6.5.3	Bias of Polarization Estimators	93
6.5.4	Estimation of Uncertainty	97

7	Fabrication of Micropolarizer Array-based Polarimeters	99
7.1	Fabrication of Polarization-Sensitive Sensors	99
7.1.1	Fabrication at RIT - Passive Alignment	101
7.1.2	Fabrication at RIT - Active Alignment	108
7.1.3	Alignment Using A Carrier	110
7.2	Fabrication at 4D Technologies	111
8	Performance and Calibration	112
8.1	Characterization of Device Properties	113
8.1.1	Modeling the System Response	114
8.1.2	Pixel Throughput	116
8.1.3	Relative Transmission - t_k	118
8.1.4	Polarizer Efficiency - ϵ_k	121
8.1.5	Pixel Orientation - ϕ_k	123
8.2	Simulating the Polarimetric Performance	125
8.2.1	Simulated Observations of Point Sources	125
8.2.1.1	Step 1. Generation of the Point Spread Function	125
8.2.1.2	Step 2. Modulating the PSF	127
8.2.2	Effects of Sampling	128
8.2.2.1	Case 1. Constant Photometric SNR	129
8.2.2.2	Case 2. Constant Peak Intensity	131
8.2.2.3	Case 3. Constant Sampling, Varying Flux	133
8.2.3	Correcting the Systematic Drift	134
8.2.4	Summary	139
8.2.5	Effects of Sub-Pixel Displacement	139
8.2.6	Simulated Observations of Extended Objects	143
9	Data Analysis Techniques	145
9.1	Polarimetric Errors in Various Polarimeters	146
9.2	Polarimetry of Unresolved Sources	147
9.2.1	Photometric Calibration	147
9.2.2	Demodulation Using Aperture Photometry	148
9.2.2.1	Pixel Non-Uniformity Correction With Flat Fields	148
9.2.2.2	Measure the Flux	150
9.2.2.3	Non-uniformity Correction Using the Full Characterization	152
9.2.3	Polarimetry of Spatially Resolved Sources	154
9.2.3.1	Demodulation Using a Per-Pixel Calibration	154
10	Initial On-Sky Evaluation	158
10.1	Evaluation of the Gen 1 Prototype	158
10.1.1	Data Processing	159
10.1.2	Polarimetric Analysis	160
10.2	Evaluation of the Gen 4 Prototype	162
10.2.1	Polarimetry of Point Sources	163
10.2.1.1	HD 90156	163

10.2.1.2	HD 78344	167
10.2.2	Polarimetry of Planets	169
10.2.2.1	Jupiter	169
10.2.2.2	Saturn	179
10.2.2.3	Venus	181
10.2.3	Observations of Nebulae	184
10.2.3.1	Hen 401	185
10.2.3.2	Hen 404	187
10.2.3.3	Frosty Leo	190
11	Conclusion	192
11.1	Design and Performance of MPA-based Sensors	192
11.2	Polarimetry with MPA-based Sensors	194
11.2.1	Device Nonuniformity and Characterization	194
11.2.1.1	Performing the Characterization	195
11.2.1.2	Determining the Quality of Device Characterization	196
11.2.2	Developing an Observing Strategy	197
11.2.3	Notes on Data Analysis	198
11.3	Performance of RITPIC and Future Outlook	198
11.3.1	Expected Performance of Similar Devices	199
11.4	Promising Science Cases	199
11.5	A General Purpose Polarimeter	201
A	Dissemination of Results	202
	Bibliography	205

List of Figures

1.1	Left: A sketch by Lomonosov of a “fiery arc” surrounding Venus, caused by light refraction in the Venusian atmosphere. Right: a photo of the same phenomenon during the 2004 transit ©Lorenzo Comolli. Used with permission.	2
2.1	Left: Electromagnetic waves oscillate in a plane orthogonal to the direction of propagation. The frequency of oscillation is related to the energy of the photon and is often expressed in terms of the associated wavelength, λ . Right: The direction of oscillation in the plane of oscillation describes the polarization of a single photon. In this case, the photon is linearly polarized at 45° with respect to the x-axis.	6
2.2	The polarization of a single photon, or the average polarization of a collection of photons, can be described by the path that is traced by the electric field vector in the $(\hat{x} - \hat{y})$ plane perpendicular to the direction of motion of the photon(s). The polarization can be purely linear, circular (a combination of two orthogonal linear states out of phase by $\frac{\pi}{2}$) or elliptical.	6
2.3	The Poincaré sphere can be used to specify the polarization state as a set of coordinates on its surface. Furthermore, it is a useful way to demonstrate the relationship between the Stokes parameters and the polarization state. Notice that polarization states that are purely linear or purely circular reside along the equator and at the poles, respectively. The rest of the surface corresponds to more general, elliptical states.	10
3.1	Randomly polarized light can become strongly polarized when reflected off a surface, with the angle of polarization parallel to the surface of reflection (and perpendicular to the plane of incidence).	13
3.2	The reflection of light is highly dependent on the polarization of the incident radiation and the geometry of the reflection. The reflection coefficients for the amplitude of the electric field (given by Equations 3.1 & 3.2, $n_i = 1, n_t = 1.50$) depend highly on the angle of incidence. At Brewster’s angle, θ_B (dashed line), the amplitude coefficients and the reflection coefficients for electric field components parallel to the plane of incidence (perpendicular to the reflecting surface) reach zero and the reflected light is polarized parallel to the reflecting surface.	15

- 3.3 Left: The Stokes parameters I and Q describe how randomly polarized light can become highly polarized through a reflection from a dielectric material. At normal incidence, $Q = 0$ (the \hat{x} and \hat{y} components are reflected equally) and it increases with angle of incidence until $Q = I$ at Brewster's angle. In other words, at this point the intensity of light polarized parallel to the surface is equal to the total intensity and the $DOLP = 1$ (Right). 16
- 3.4 Left: Reflection coefficients for the electric field components perpendicular and parallel to the plane on incidence, for 550 nm light reflecting off an aluminum mirror. The parallel component is suppressed at large angles of incidence, but never reaches 0, like for dielectrics. The reflection is minimal at the angle of principal incidence, indicated by the vertical dashed line. Right: The Stokes parameters show the changes in the reflection coefficients by a decrease in the total intensity, I , and an increase in Q . . 17
- 3.5 Left: The degree of polarization imparted to a randomly polarized beam during a reflection from a metal. Right: Telescopes with fold mirrors exhibit large instrumental polarization. 18
- 3.6 Left: When randomly polarized light interacts with an atom or molecule (orange circle in figure), the scattered photons will display a range of polarization states. The photons which are scattered in the plane orthogonal to the direction of propagation of the incident light will be completely linearly polarized. Right: Photons that are scattered at any other scattering angle will have a range of polarizations. Generally, the degree of polarization decreases as the scattering angle approaches $\alpha = 0^\circ$ or $\alpha = 180^\circ$ 20
- 3.7 Because the Sun's rays are nearly parallel when they enter the Earth's atmosphere, there exist regions in the sky where many photons are scattered at an angle $\alpha \approx 90^\circ$, which creates very strong linear polarization along the line of sight toward those regions. This region of maximum polarization depends on the position of the Sun and it changes throughout the day and year. For example, at sunset and sunrise the sky near zenith is highly polarized. 21
- 3.8 Rayleigh scattering produces primarily linearly polarized light, with the DOLP as a strong function of the scattering angle (Left). The DOLP is maximal for scattering angles near $\alpha = 90^\circ$, and minimal in the solar and anti-solar directions. In practice, multiple scattering in the atmosphere decreases the maximum observed DOLP to ~ 0.8 . The angle of linear polarization follows a circular pattern, centered on the Sun (Right). . . . 22
- 3.9 The radiation patterns for two orthogonal components of the electric field, for a wave scattered by a dielectric sphere with diameter of $1 \mu\text{m}$ can be very different. Here, the wave is incident from the left (180°) and the amplitude is shown on a logarithmic scale to emphasize the difference between the two components. The patterns also strongly depend on the wavelength of light. These patterns were calculated using Scott Prahl's convenient web-based Mie scattering calculator (http://omlc.org/calc/mie_calc.html). . . 25
- 3.10 The polarization dependence on the scattering angle can be very complex for the case of a single scattering event and the exact pattern has a strong dependence on the wavelength of light, as well as the particle diameter. . 25

-
- 3.11 *Left:* Elongated dust grains preferentially absorb the electric field component parallel to their “long” axis. If there is a mechanism that aligns the dust grains, they can polarize the light from background objects. *Right:* Dust samples brought back to Earth from interplanetary space show strong evidence that these elongated dust grains exist throughout the Galaxy. 26
- 3.12 Relativistic charged particles that are accelerated into circular orbits by magnetic fields emit synchrotron radiation. The polarization of this light depends strongly on the direction of radiation; for example, light emitted in the plane of the orbit is linearly polarized in that plane. 29
- 3.13 Relativistic charged particles that are accelerated into helical orbits by magnetic fields emit synchrotron radiation. The polarization of this light depends strongly on the direction of radiation; for example, light emitted in the plane of the instantaneous circular orbit is linearly polarized in that plane. 30
- 3.14 *Left:* The Crab Nebula is a large remnant of a supernova that was observed in 1054 CE. This is a map of the flux in the visible V band. *Right:* The Crab Nebula shows a strong and complex polarization pattern (white corresponds to large polarization), with peak fractional polarization of $\sim 30\%$. Observations of D. Vorobiev, made using the SMARTS 0.9 m telescope at Cerro Tololo Inter-American Observatory. 31
- 3.15 Some lasers use Brewster windows, due to their extremely low reflectivity for the parallel polarization states. Only these states remain long enough to escape the resonator cavity and all modes of these lasers have the same polarization. 32
- 3.16 Some laser crystals are anisotropic and show higher gain for certain polarization states. 32
- 3.17 Many polarizing prisms have been invented by exploiting birefringent crystals and polarization upon reflection of dielectric materials. Most polarizing prisms produce highly polarized light, across a broad wavelength range. 34
- 4.1 *Left:* A wire grid polarizer is fabricated by aligning thin conducting wires, which preferentially absorb the electric field components parallel to the wire orientation. The wire width and spacing needs to be smaller than the wavelength of light for the polarizer to be efficient at blocking the unwanted polarization states. *Right:* In 1960, a wire grid polarizer for the near-infrared regime was fabricated by evaporating metal onto the ridges of a blazed diffraction grating. 36
- 4.2 Modern wire grid polarizers are typically made with aluminum wires ~ 74 nm wide and ~ 200 nm tall. This scanning electron micrograph shows the cross-section of a single pixel of a pixelated wire grid polarizer. 37

- 4.3 Simulated broadband performance of a modern wire grid polarizers, made from aluminum (Al), gold (Au), and a perfect electrical conductor (PEC). These polarizers are very efficient at transmitting the polarization states perpendicular to the wire direction (*Left*), and blocking the state parallel the wire direction (*Right*). These curves (especially the transmission of the desired state) show that the polarizer reaches optimum performance when the wavelength of light becomes about $10\times$ larger than the wire width, at $\lambda \approx 1\mu m$ 37
- 4.4 *Left*: A conventional wire grid polarizer was simulated in 2D by modeling an aluminum wire with a rectangular cross-section on an SiO_2 substrate. The light source originates inside the glass substrate $\sim 2\mu m$ above the wire. The reflected and transmitted components are measured $3\mu m$ and $5\mu m$ above and below the polarizer, respectively. The simulation uses periodic boundary conditions (orange vertical lines) in the $\pm\hat{x}$ directions, resulting in an infinitely repeating array of wires (*Right*). 41
- 4.5 We simulated structures using a wide range of mesh sizes, to determine when the structures were sufficiently resolved. We found that in 2D, simulations began to numerically converge when the simulation mesh was smaller than 4 nm. 42
- 4.6 The size of the smallest mesh cell determines how well the simulation reproduces the desired geometry. This effect can be seen in refractive index map of the simulated structures. Plots along the bottom of the figure show the profile of the refractive index of each wire. 42
- 4.7 *Left*: Our 2D simulations began to numerically converge when the mesh was smaller than 4 nm. *Right* Increasing the number of PML layers was effective at improving the estimation of the transmitted TE component (the state transmitted by the polarizer), but not of the TM component (the state reflected by the polarizer). 43
- 4.8 The numerical convergence of simulations can also be seen in the distribution of the amplitude of the electric field. This figure shows the electric fields for a TE pulse (which is mostly transmitted by the polarizer). High resolution simulations are required to model very localized regions of high electric field intensity (though this may not represent fabricated structures, if they lack similar definition). 44
- 4.9 *Left*: Transmission of the TE component for a wire grid polarizer with wire widths of 50 nm, 60 nm, 70 nm, 80 nm, 90 nm, 100 nm, 125 nm, 150 nm, 175 nm and 200 nm, with duty cycle and wire height fixed at 50% and 200 nm, respectively. In general, wire grids with thinner wires exhibit higher transmission at all wavelengths. Wires with widths >100 nm (solid black line) exhibit resonant behavior in the visible regime. *Right*: Reflection of the TE state increases with increasing wire width. 46

- 4.10 Electric field intensity cross-sections for 8 simulations of wires with increasing widths, for a TE pulse, which is mostly transmitted by the polarizer. Black rectangles correspond to the wire cross-section. These results are for light at a wavelength of 667 nm. The intensity is normalized by the source power and shown on a linear scale. The wire height is 200 nm and the spacing between the wires is equal to the wire width. 46
- 4.11 Left: Transmission of the TM component for a wire grid polarizer with wire widths of 50 nm, 60 nm, 70 nm, 80 nm, 90 nm, 100 nm, 125 nm, 150 nm, 175 nm and 200 nm, with duty cycle and wire height fixed at 50% and 200 nm, respectively. In general, wire grids with thinner wires transmit less light at all wavelengths. Right: Reflection of the TM state is not strongly affected by wire width; however, wires with thickness $> \sim 100$ nm exhibit resonant behavior at shorter wavelengths. 47
- 4.12 Electric field intensity cross-sections for 8 simulations of wires with increasing widths, for a TM pulse, which is mostly reflected by the polarizer. White rectangles are drawn to help outline the edges of the wires. These results are for light at a wavelength of 667 nm. The intensity is normalized by the source power and shown on a logarithmic scale. The wire height is 200 nm and the spacing between the wires is equal to the wire width. 47
- 4.13 Left: Transmission of the TE component for a wire grid polarizer with wire air gap width of 25 nm, 50 nm, 75 nm, 100 nm, 125 nm, 150 nm, 175 nm and 200 nm. In general, wire grids with larger air gaps exhibit higher transmission at all wavelengths. Right: Reflection of the TE state decreases with increasing wire separation. Wires with air gap widths < 50 nm (blue line) exhibit resonant behavior in the visible regime. 49
- 4.14 Electric field intensity cross-sections for 8 simulations of wires with increasing air gap widths, for a TE pulse, which is mostly transmitted by the polarizer. Black rectangles correspond to the wire cross-section. These results are for light at a wavelength of 667 nm. The intensity is normalized by the source power and shown on a linear scale. The wire height is 200 nm and the wire width is 75 nm. 49
- 4.15 Left: Transmission of the TM component for a wire grid polarizer with air gap widths of 25 nm, 50 nm, 75 nm, 100 nm, 125 nm, 150 nm, 175 nm and 200 nm. In general, wire grids with smaller air gaps exhibit lower transmission at all wavelengths. Simulations with a 25 nm gap predict extremely low transmission and a complex wavelength dependence, hinting at the emergence of numerical errors or more complex resonant behavior. Right: Reflection of the TM state increases with decreasing wire spacing, with the largest changes in the visible regime. 50
- 4.16 Electric field intensity cross-sections for 8 simulations of wires with increasing air gap widths, for a TM pulse, which is mostly reflected by the polarizer. White rectangles are drawn to help outline the edges of the wires. These results are for light at a wavelength of 667 nm. The intensity is normalized by the source power and shown on a logarithmic scale. The wire height is 200 nm and the wire width is 75 nm. 50

4.17	Left: Transmission of the TE component for a wire grid polarizer with wire heights of 25 nm, 50 nm, 75 nm, 100 nm, 125 nm, 150 nm, 175 nm, 200 nm, 250 nm, and 300 nm. In general, wire grids with taller wires exhibit lower transmission at all wavelengths; however, in the visible range two systematic patterns emerge, with a height of ~ 100 nm separating these two regimes. Right: Reflection of the TE state has a complex dependence on wire height.	51
4.18	Electric field intensity cross-sections for 8 simulations of wires with increasing height, for a TE pulse, which is mostly transmitted by the polarizer. Black rectangles correspond to the wire cross-section. These results are for light at a wavelength of 667 nm. The intensity is normalized by the source power and shown on a linear scale. The wire width is 74 nm and the duty cycle 50%.	52
4.19	Left: Transmission of the TM component for a wire grid polarizer with wire heights of 25 nm, 50 nm, 75 nm, 100 nm, 125 nm, 150 nm, 175 nm, 200 nm, 250 nm and 300 nm. In general, wire grids with taller wires exhibit lower transmission at all wavelengths. Right: Reflection of the TE state has a complex dependence on wire height.	53
4.20	Electric field intensity cross-sections for 8 simulations of wires with increasing height, for a TM pulse, which is mostly reflected by the polarizer. White rectangles are drawn to help outline the edges of the wires. These results are for light at a wavelength of 667 nm. The intensity is normalized by the source power and shown on a logarithmic scale. The wire width is 74 nm and the duty cycle 50%.	53
4.21	Right: We found that in 3D, simulations began to numerically converge when the simulation mesh was smaller than 4 nm. Left: We simulated structures and varied the number of layers in the absorbing PML boundary, to determine when the reflections from the PML were sufficiently suppressed. A significant decrease in relative error can be achieved by using ~ 26 layers in the PML.	55
4.22	Left: Transmission of the TE component for a wire grid polarizer with wire widths of 50 nm, 60 nm, 70 nm, 80 nm, 90 nm, 100 nm, 125 nm, 150 nm, 175 nm and 200 nm, with duty cycle and wire height fixed at 50% and 200 nm, respectively. In general, wire grids with thinner wires exhibit higher transmission at all wavelengths. Wires with widths > 100 nm (solid black line) exhibit resonant behavior in the visible regime. Right: Reflection of the TE state increases with increasing wire width.	56
4.23	Left: Transmission of the TM component for a wire grid polarizer with wire widths of 50 nm, 60 nm, 70 nm, 80 nm, 90 nm, 100 nm, 125 nm, 150 nm, 175 nm and 200 nm, with duty cycle and wire height fixed at 50% and 200 nm, respectively. In general, wire grids with thinner wires transmit less light at all wavelengths. Right: Reflection of the TM state is not strongly affected by wire width and the resonant behavior seen in 2D simulations is diminished.	57

-
- 4.24 Left: Transmission of the TE component for a wire grid polarizer with wire air gap width of 25 nm, 50 nm, 75 nm, 100 nm, 125 nm, 150 nm, 175 nm and 200 nm. In general, wire grids with larger air gaps exhibit higher transmission at all wavelengths. Right: Reflection of the TE state decreases with increasing wire separation. 58
- 4.25 Left: Transmission of the TM component for a wire grid polarizer with air gap widths of 25 nm, 50 nm, 75 nm, 100 nm, 125 nm, 150 nm, 175 nm and 200 nm. In general, wire grids with smaller air gaps exhibit lower transmission at all wavelengths. Simulations with a 25 nm gap predict extremely low transmission and a complex wavelength dependence, hinting at the emergence of numerical errors. Right: Reflection of the TM state increases with decreasing wire spacing, with the largest changes in the visible regime. 58
- 4.26 Left: Transmission of the TE component for a wire grid polarizer with wire heights of 25 nm, 50 nm, 75 nm, 100 nm, 125 nm, 150 nm, 175 nm, 200 nm, 225 nm, and 250 nm. In general, wire grids with taller wires exhibit lower transmission at all wavelengths; however, in the visible range two systematic patterns emerge, with a height of ~ 100 nm separating these two regimes. Right: Reflection of the TE state has a complex dependence on wire height. 59
- 4.27 Left: Transmission of the TM component for a wire grid polarizer with wire heights of 25 nm, 50 nm, 75 nm, 100 nm, 125 nm, 150 nm, 175 nm, 200 nm, 225 nm and 250 nm. In general, wire grids with taller wires exhibit lower transmission at all wavelengths. Right: Reflection of the TM state reaches the maximum after a wire height of ~ 75 nm. 60
- 4.28 We compare the results of 2D and 3D simulations of a single wire and a 3D simulation of a 50 wire region. All simulations show very similar results, even though the simulated region is very different in each case. It appears that 2D simulations can be an accurate representation of certain 3D structures, if one can exploit some symmetries (such as the length dimension of a long, skinny wire). 61
- 4.29 An SEM micrograph of the cross-section of a wire grid polarizer. The aluminum wires are approximately 74 nm wide, with a 50% duty cycle and a height of ~ 150 nm. It is clear from the micrographs that the fabricated polarizers do not have perfectly straight wires and their profiles are not strictly rectangular; furthermore, the height of the wires is not uniform 62
- 4.30 Left: The measured transmission of a wire grid polarizer is generally lower than the model prediction from our simulations. Furthermore, the measured data shows ringing in the near-infrared, which is likely due to the anti-reflective coating (that we don't simulate). Right: The actual polarizers are not as good at blocking the TM state as the simulated polarizers, especially in the near-infrared. 63

4.31	The real (Left) and imaginary (Right) components of the refractive index of aluminum found in the literature. The commonly used values from the book by Palik (1998) and CRC Handbook of Chemistry (Shiles et al., 1980), differ from more recent measurements of aluminum thin films by Lehmuskero et al. (2007) and McPeak et al. (2015).	64
5.1	a). A micro grid polarizer array fabricated by Moxtek, Inc. b) A scanning electron micrograph (SEM) of a set of 4 micro polarizer pixels. Lighter regions correspond to the wires and the darker regions are opaque aluminum. The wire orientations are, clockwise starting at top left: 0° , 45° , 90° , and -45° . c) An up-close image of a single micro polarizer.	67
5.2	left: A scanning electron micrograph of a pixelated polarizer. The grey regions represent aluminum and black gaps are air. Each polarizer is surrounded by an opaque aluminum border. The wires are $\sim 8\mu\text{m}$ long. Middle: The simulated pixelated polarizers were created by etching gaps in an aluminum layer to create wires of finite length. In this case, the wires had a length of $8\mu\text{m}$ and a height, width and air gap of 200 nm , 74 nm and 74 nm , respectively. The wires were surrounded by an opaque aluminum gap $0.5\mu\text{m}$ wide. Right: The pixelated polarizers are simulated using periodic boundary conditions in the \hat{x} and \hat{y} directions, to create an effectively infinite array of identical polarizers.	68
5.3	<i>Left:</i> Pixels with diagonal wires are more difficult to mesh using a rectangular grid. <i>Right:</i> These simulations converge at a similar rate as simulations of rectangular structures, but with a systematically higher relative error.	69
5.4	The transmission and reflection of the TE pulse for pixelated polarizers as compared to the conventional polarizer with similar wire parameters. The lower transmission of pixelated polarizers can be mostly explained by the non-uniform fill factor caused by the opaque border around each pixelated polarizer.	70
5.5	The transmission of pixelated polarizers as compared to the conventional polarizer with similar wire parameters, for TE (Left) and TM (Right) components. The lower transmission for both states can be mostly explained by the non-uniform fill factor caused by the opaque border around each pixelated polarizer; however, even after scaling the transmission by a constant to adjust for the fill factor (dashed line), the pixelated polarizer does not show identical performance to conventional polarizers.	71
5.6	The transmission and reflection of the TM pulse for pixelated polarizers as compared to the conventional polarizer with similar wire parameters.	72
5.7	<i>Left:</i> To model the performance of the whole MPA, pixels with different orientations were modeled at the same time. The simulated region included 4 pixels with $9\mu\text{m}$ pitch. The white dashed lines indicate the regions where cross-talk measurements were made (see Section 5.2.2). <i>Middle:</i> A cross-section of the simulated devices shows a setup similar to the one used in the simulations of individual pixels. <i>Right:</i> The periodic boundary conditions around the set of 4 pixels create an effective structure that is representative of real MPAs – a repeating pattern of “superpixels”	73

- 5.8 *Left:* A top-down view of the simulated region, showing the 4 micropolarizer pixels. *Right:* An isometric representation of the simulated region, showing the location of the electric field monitors. The glass substrate (which is on top of the blue micropolarizer layer) is not shown. 74
- 5.9 *Left:* The intensities recorded by monitors belonging to each pixel orientation show mostly expected behavior. The pixel with 90° wires transmits most of the 0° polarized light, while the 45° and 135° pixels transmit roughly half of that value. *Right:* The contrast ratio in simulations with all 4 pixels can be calculated using a single polarized pulse. Here, we show the ratio of the intensities measured by the 0° and 90° pixels monitors in response to a 0° polarized pulse. 75
- 5.10 *Left:* The pixel with 135° wires transmits most of the 45° polarized light, while the 0° and 90° pixels transmit roughly half of that value. *Right:* The contrast ratio of the intensities measured by the 135° and 45° pixels monitors in response to a 45° polarized pulse. 75
- 5.11 *Left:* To measure the diffraction pattern due to a micropolarizer array, we simulated an isolated micropolarizer surrounded by a large opaque border. *Right:* The electric field was recorded by a normal-sized monitor and an extended monitor, to show the diffracted light. 77
- 5.12 The electric field intensity (log scale) distribution for 400 nm (*Left*) and 2000 nm light (*Right*) transmitted by a 0° micropolarizer. The white dashed lines show the location of a $9\mu\text{m}\times 9\mu\text{m}$ region, $5\mu\text{m}$ below the micropolarizer. 77
- 5.13 Fraction of light measured by a central monitor directly below the micropolarizer and an extended monitor, which also captures the diffracted light (see Figure 5.11). Ideally, all light that passes through a single micropolarizer would remain in a region directly below that polarizer. 78
- 5.14 *Left:* Vertical monitors along the boundaries between individual pixels can be used to measure the crosstalk from diffraction directly. *Right:* The intensity of light passing through the vertical boundaries between the 45° polarizer and its neighbors accounts for most of the intensity measured by the 45° monitor. 78
- 6.1 Division of time polarimetry. The degree and angle of linear polarization can be determined by measuring the intensity through a polarizer oriented along several directions. This is typically accomplished by rotating a single polarizer (blue arrow indicates the polarizer axis) or by using several polarizers in a filter wheel (as in done on *The Hubble Space Telescope*). 81
- 6.2 Division of intensity polarimetry. Polarimeters that sample the electric field along several orientations simultaneously can be built using beam-splitting optics and several detectors. The incident light is split and imaged in two or more channels simultaneously. 82
- 6.3 *Left:* The Extreme Polarimeter (ExPo) uses beam splitters to record images polarized along two orthogonal directions simultaneously, on the same focal plane. *Right:* Two images of an object appear side-by-side on ExPo's single detector. Figure is adopted from Rodenhuis et al. (2012). ©SPIE. Used with Permission. 83

- 6.4 *Left:* In some instruments, like RoboPol, the 4 separate images are recorded by a single detector, resulting in a very crowded image plane (*Right*). Adopted from Fig. 1 and Fig. 2 of King et al. (2014). 83
- 6.5 The dual beam modulation scheme uses a retarder and a beam splitter to capture two polarization states simultaneously, with a single or multiple detectors. The retarder is used to switch the orientation of both beams for each successive measurement. 84
- 6.6 *Left:* a color filter array divides the focal plane into sets of 2×2 “superpixels” that determine the color of a section of a scene using the intensities measured by individual detector pixels. *Right:* A micropolarizer array-based polarimeter works in a fashion similar to a color sensor to measure polarization across a scene. Each polarizer pixel is matched spatially to a single detector pixel. Light passing through a polarizer pixel is modulated according to the polarizer’s orientation and the intensity is measured by the detector pixel. 85
- 6.7 Optimal sampling on the Poincaré sphere for linear (Left) and full Stokes (right) polarimetry. 88
- 6.8 The presence of Poisson noise results in a bi-variate distribution of the estimated Stokes parameter in the Q - U plane; here I show a set of 1000 synthetic measurements made with four ideal polarizers and non-ideal polarizers that are not perfectly characterized. The miscalibrated non-ideal polarimeter introduces systematic errors into the estimation. 92
- 6.9 Synthetic observations of an unpolarized source show the positive bias of the p estimator. Whereas q and u are distributed around a mean of 0, $\langle p \rangle = 0.0021$. The overestimation becomes worse as the scatter of q and u increases. 93
- 6.10 *Left:* The distance from the origin to a point in the q - u plane is an estimate of the fractional polarization p , while the angle made by this vector with respect to the q -axis is twice the estimated angle of linear polarization. *Right:* The distribution of the magnitudes, p , is given by the Rice distribution, which can be used to calculate the probability of measuring a value p for a source with intrinsic polarization p_0 . In the presence of noise, there is zero probability to measure a value $p/\sigma_p = 0$ 94
- 6.11 *Left:* The maximum likelihood estimator suggested by Simmons and Stewart (1985) is that value of p_0 that is a solution to equation $\frac{\partial F}{\partial p_0}(p, p_0) = 0$ (eq. 6.8); there is a threshold value of $p = 1.41$, below which the measured value of p is consistent with $p_0 = 0$. *Right:* The estimator suggested by Wardle and Kronberg (1974) is the value p_0 which solves equation 6.9. In this case, too, there is a threshold value of $p = 1$, below which the measured polarization is consistent with $p_0 = 0$ 95
- 6.12 *Left:* The variance for the q and u parameters can be used to estimate the noise associated with the measurement of q and u . *Right:* Similarly, the error associated with p and ψ can be estimated by determining the variance along (σ_p), and perpendicular (σ_ψ) the p vector. 97

- 7.1 *Left:* A wafer with several sensors ready to be diced and packaged (image: www-ccd.lbl.gov). *Middle:* A packaged CCD. The die has been cut from a wafer, attached to a ceramic carrier and wire-bonded to the metal pins of the carrier. *Right:* A microgrid polarizer on a thin glass substrate. 100
- 7.2 The imaging system used to determine MPA-CCD alignment is based on a compact microscope, CCD camera and a long working distance (LWD) microscope objective. The LWD objective is required because the alignment procedure requires imaging of the CCD through the polarizer substrate, which is 0.7 mm thick. This is much larger than the working distance of conventional objectives. 102
- 7.3 *Left:* A cross-section of the MPA-CCD pixels. From the top, down there are 5 distinct regions: glass polarizer substrate, the thin polarizer layer, a gap (filled with air or epoxy), a layer of CCD microlenses that demarcate the pixels of the CCD, a layer of gate electronics and the bulk epitaxial layer with the depletion region. *Right:* An isometric view of the MPA-CCD system, showing exact alignment between the grid formed by MPA pixels and the grid formed by CCD pixels. 103
- 7.4 Because the polarizer is at the focal plane of the optical system, it is illuminated using converging light. As the separation between the polarizer and the sensor (in this case with microlenses) increases, the projected area of the polarizer pixels decreases. This figure shows a converging beam of polarized light. The middle polarizer blocks all of the light, while its neighbors transmit light. As the polarizer is moved away from the sensor, light from the left and right pixels ends up in the middle pixel. This is one example of optical crosstalk. Source: figure is courtesy of Kenneth Fourspring, personal communication. 104
- 7.5 Setup for alignment of MPA to CCD sensor. The CCD is held in a aluminum chuck and is positioned in $\hat{x} - \hat{y} - \hat{\theta}$ using two linear stages stacked vertically on a rotation stage. The actuators of the stages are labeled in the figure. The z-distance between the polarizer and the CCD is controlled using another linear stage. The alignment of the MPA-CCD system is determined using a long working distance microscope objective and a CCD camera. The illumination source is fiber-coupled to the microscope system. 105
- 7.6 Close up of the assembly that holds the CCD and the micropolarizer array. 106
- 7.7 *Left:* An image acquired of the MPA at the physical edge of the MPA. The jagged substrate and square pixels of the polarizer are clearly seen. A line is created to indicate the alignment of the MPA. *Right:* An image of the same region, focused on the CCD that is below the polarizer. The CCD pixels appear as sets of bright and faint rectangles. The CCD grid can now be aligned with the line that indicates the MPA alignment. In this image, the CCD is slightly misaligned with the MPA grid. 106
- 7.8 First polarization-sensitive imager fabricated at RIT using the passive alignment technique. The silver square in the center is the micropolarizer array. Excess epoxy can be seen around the edges of the polarizer. 107

7.9	<i>Left:</i> The polarization sensitive focal planes were fabricated in a clean room at RIT. The micropolarizer arrays were aligned to a CCD sensor using a vacuum wand and computerized translation stages (<i>Right:</i>) A close-up of the illumination system. Alignment was monitored by illuminating the system with linearly polarized light and reading out the CCD.	108
7.10	<i>Left:</i> This alignment setup offered four degrees of motion - rotation in the plane of the sensor and $\hat{x} - \hat{y} - \hat{z}$ motion. <i>Right:</i> The micropolarizer array was held with a vacuum wand. This is a simple but problematic way to manipulate the micropolarizer.	109
7.11	<i>Left:</i> The translation stages used to manipulate the micropolarizer array and sensor were computer-controlled; however, the alignment process was not automated. <i>Right:</i> I built an interface to operate the camera, perform on-the-fly calibration, and provide real time feedback on the state of the alignment.	109
7.12	The 2nd generation prototype of a micropolarizer-based polarization sensor fabricated at RIT, using active alignment.	110
7.13	A carrier can be used to position the micropolarizer array above the sensor. This cross-section shows how a carrier can be used to avoid crushing the wire bonds that connect the CCD to the CCD carrier.	110
7.14	The 3rd generation prototype of a micropolarizer-based polarization sensor fabricated at RIT, using active alignment. This design uses an aluminum carrier to hold the micropolarizer suspended above the sensor, with an air gap between them.	111
8.1	The polarization sensors were characterized using a rotating linear polarizer and an integrating sphere. The filter is placed before the sphere to avoid any polarization from a tilted glass plate.	113
8.2	The median response for pixels oriented along 0° , 45° , 90° , and 135° to polarized light with a range of angles. The error bars show the standard deviation of pixels with the same orientation, at a particular angle. . . .	115
8.3	Full sensor area, uniformly illuminated by unpolarized light. The small, bright regions in the corners are uncovered areas of the sensor, which are used to calculate the throughput of the micropolarizer array (center). . .	117
8.4	<i>Left:</i> The camera head, with the front plate removed. The silver square in the middle is the micropolarizer array, surrounded by the white ceramic carrier. <i>Middle:</i> To avoid the polarizing effects of the carrier, I used a mask to baffle the sensor. <i>Right:</i> the baffle covers more of the edges than necessary, however, the resulting active area (yellow square) is still a large fraction of the sensor.	118
8.5	Histograms of the mean-normalized transmissions, t_k , for pixels of each orientation. The throughputs are systematically different for pixels with different orientations. There is a broad distribution of transmissions even for pixels of the same orientation.	119
8.6	Relative throughputs, t_k , for each pixel orientation, normalized by their own mean value. The regions of higher throughput correspond to areas of better alignment.	120

8.7	Histograms of the polarizer efficiency, e_k , for pixels of each orientation. The efficiency is similar for pixels with different orientations, with only the 135° pixels showing a systematic difference.	121
8.8	Spatial distribution of polarizer efficiency, ϵ_k for each pixel orientation, normalized by their own mean value. The spatial distribution of ϵ_k and t_k are only roughly similar (showing a top-down gradient) to the distribution of throughputs, t_k	122
8.9	Histograms of the polarizer orientations, ϕ_k , for pixels of each orientation.	123
8.10	Spatial distribution of polarizer orientation. The scale shows offsets from the nominal orientation.	124
8.11	<i>Left:</i> The initial Gaussian PSFs are generated in high resolution to allow precise shifts; presumably, this is what the electric field distribution looks like before it is sampled by the sensor. <i>Right:</i> The continuous image is sampled by the sensor, according to the magnification / plate scale of the imaging system.	126
8.12	<i>Left:</i> The total intensity PSFs are modulated by the micropolarizer array based on the intrinsic properties of the source. Weakly polarized stars appear relatively unchanged. <i>Right:</i> Highly polarized stars show a strong modulation pattern. For example, this object is polarized with an angle of 0° , so the 0° pixels appear brighter than the rest.	127
8.13	Synthetic stars generated to have 2, 4, and 8 superpixels across their full-width at half-maximum in the focal plane. Each star has the same total flux.	129
8.14	The estimation of q , for stars with intrinsic $q = 0, 0.05$, and 0.5 , using an ideal and non-ideal polarimeter. The total flux was held constant as the FWHM was increased (Figure 8.13). In each case, the scatter of the measurement is reduced by increasing the FWHM to 3 superpixels, with negligible gains seen with higher sampling.	130
8.15	The estimation of u , for stars with intrinsic $u = 0$, using an ideal and non-ideal polarimeter. The total flux was held constant as the FWHM was increased (Figure 8.13). In each case, the scatter of the measurement is reduced by increasing the FWHM to 3 superpixels, with negligible gains seen with higher sampling.	130
8.16	Synthetic stars generated to have 2, 4, and 8 superpixels across their full-width at half-maximum in the focal plane. Each star has the same peak intensity, but the total flux increases as the PSF grows larger.	131
8.17	The estimation of q , for stars with intrinsic $q = 0, 0.05$, and 0.5 , using an ideal and non-ideal polarimeter. The peak intensity at each sampling was held constant, allowing the total flux to increase (Figure 8.16). In each case, the scatter of the measurement is reduced by increasing the FWHM sampling to 5 superpixels, with negligible gains seen with higher sampling.	132
8.18	Synthetic stars generated to have 2, 4, and 8 superpixels across their full-width at half-maximum in the focal plane. Each star has the same peak intensity, but the total flux increases as the PSF grows larger.	132

8.19	Synthetic stars generated to have 4 superpixels across their full-width at half-maximum in the focal plane. Each star has a different peak intensity and, as a result, photometric SNR. Note that the high SNR images appear saturated because the scaling was chosen to ease comparison with the faint case.	133
8.20	Synthetic stars generated to have 4 superpixels across FWHM. The peak intensity of each star was increased to increase the shot-noise SNR. The scatter about the true value decreases significantly for stars with $\text{SNR} \gtrsim 300$.	134
8.21	Synthetic stars generated to have 4 superpixels across their FWHM. The peak intensity of each star was increased to increase the shot-noise SNR. The scatter about the true value decreases significantly for stars with $\text{SNR} \gtrsim 750$	134
8.22	The estimation of q , for stars with intrinsic $q = 0, 0.05, \text{ and } 0.5$, using an ideal and non-ideal polarimeter. The total flux was held constant as the FWHM was increased (Figure 8.13).	135
8.23	The estimation of u , for stars with intrinsic $u = 0$, using an ideal and non-ideal polarimeter. The total flux was held constant as the FWHM was increased (Figure 8.13).	136
8.24	The estimation of q , for stars with intrinsic $q = 0, 0.05, \text{ and } 0.5$, using an ideal and non-ideal polarimeter. The peak intensity at each sampling was held constant, allowing the total flux to increase (Figure 8.16). In each case, the scatter of the measurement is reduced by increasing the FWHM sampling to 5 superpixels, with negligible gains seen with higher sampling.	137
8.25	The estimation of u , for stars with intrinsic $u = 0$, and $q = 0, 0.05, \text{ and } 0.5$, using an ideal and non-ideal polarimeter. The peak intensity at each sampling was held constant, allowing the total flux to increase (Figure 8.16). In each case, the scatter of the measurement is reduced by increasing the FWHM sampling to 5 superpixels, with negligible gains seen with higher sampling.	137
8.26	The estimation of q , for stars with intrinsic $q = 0, 0.05, \text{ and } 0.5$, using an ideal and non-ideal polarimeter. The sampling was held constant at $\text{FWHM} = 4$ superpixels, and the SNR was varied, by increasing the peak intensity.	138
8.27	The estimation of u , for stars with intrinsic $u = 0$, and $q = 0, 0.05, \text{ and } 0.5$, using an ideal and non-ideal polarimeter. The sampling was held constant at $\text{FWHM} = 4$ superpixels, and the SNR was varied, by increasing the peak intensity.	138
8.28	The Stokes q estimation depends systematically on the position of the PSF center. The ideal polarimeter shows a consistent error with a period of 2 pixels and amplitude of $\sim 0.2\%$; however, the non-ideal polarimeter shows an additional error, likely due to imperfect calibration.	140
8.29	The non-ideal polarizer shows systematic errors that appear to be location-dependent. This is likely due to the way the device calibration is performed during data analysis (see Chapter 9).	141

8.30	The Stokes u estimation depends systematically on the position of the PSF center. The ideal polarimeter shows a consistent error with a period of 2 pixels and amplitude of $\sim 0.2\%$; however, the non-ideal polarimeter shows an additional error, likely due to imperfect calibration.	142
8.31	The non-ideal polarizer shows systematic errors that appear to be location-dependent. This can result from the way the device calibration is performed during data analysis (see Chapter 9).	142
8.32	An example of a simulated object blurred by seeing effects. This plot shows the raw intensity in counts.	143
8.33	<i>Left:</i> A synthetic modulated image showing the raw intensity for an object has uniform polarization degree and angle. <i>Right:</i> Here, only the darker features show significant polarization, so the modulation pattern is only seen in these regions.	144
9.1	<i>Left:</i> A raw image of the unpolarized standard star HD 90156. <i>Right:</i> Once the full image is divided into subframes with pixels of the same orientation, the flux can be measured using conventional aperture photometry.	148
9.2	A non-specular screen can be used to acquire unpolarized “dome flats”, as long as the screen is illuminated along the telescope’s axis. For example, lamps arranged symmetrically around the aperture of the telescope do a decent job. Note that the dome slit was only open to take this photograph.	149
9.3	<i>Left:</i> An unpolarized flat field image of RITPIC, showing large scale and small scale throughput nonuniformity on the order of $\pm 5\%$; some dust is also visible. <i>Right:</i> A histogram of the relative pixel throughputs for each pixel orientation. Each pixel orientation has a systematically different throughput from the other orientations. For example, the 0° pixels have lower throughput than 45° pixels.	150
9.4	<i>Left:</i> A Stokes I image of synthetic star with 5 superpixels across the FWHM; because this isn’t a raw image, each image pixel corresponds to a superpixel in the focal plane. <i>Right:</i> A schematic showing typical settings used for aperture photometry. The hashed region indicates the gap between the aperture around the star and the annulus used to estimate the sky background.	151
9.5	The mean-normalized properties of the 0° pixels, in a small region of the array; several percent deviations from the mean are common for t_k and ϕ_k	152
9.6	The estimation of Stokes q for stars with intrinsic polarization $q = 0, 0.05$ and 0.5 , made by ideal and non-ideal polarimeters, as a star is translated across the array.	153
9.7	The estimation of Stokes u for stars with intrinsic polarization $u = 0$ and $q = 0, 0.05$, and 0.5 as a star is translated across the array.	153
9.8	The subframes corresponding the four pixel orientations of a synthetically generated image. The two darker spots in the object are polarized, which is why they appear larger or smaller, depending on the subframe. The object is shifted ± 0.5 pixels in each frame, with respect to the other frames.	155

9.9	The estimation of Stokes q and u parameters for the object in Figure 9.8, without proper calibration. The two smaller spots have intrinsic values $q = 0.01$ and $u = 0$	156
9.10	The estimation of Stokes q and u parameters for the object in Figure 9.8, with image registration but no flat field correction.	156
9.11	The estimation of Stokes q and u parameters for the object in Figure 9.8, with image registration and flat field correction.	157
9.12	The estimation of Stokes q and u parameters for the object in Figure 9.8, with image registration and flat field correction.	157
10.1	<i>Left:</i> A mean-normalized flat field image in the Bessel B filter, showing the full focal plane of RITPIC. The bright orange areas correspond to the uncovered regions of the sensor, while the darker blue section corresponds to the area covered by the micropolarizer. Uneven distribution of the adhesive is easily seen near the top and bottom edge of the micropolarizer. <i>Right:</i> Looking only at the polarization-sensitive region, we see how the transmission varies. Features like dust and scratches on the polarizer substrate are also apparent. Note: The high-frequency vertical and horizontal lines are not real; the flats have high-frequency features which easily cause aliasing when displayed.	159
10.2	<i>Left:</i> A raw inverted intensity image of Jupiter and its two moons (Bessel B filter). Jupiter's disk shows the same aliasing effects seen in the flats, because the same structure is present in this not-yet flat-corrected image. <i>Right:</i> a flat-corrected image of Jupiter. The bright bands across the face of Jupiter appear red in this color map.	159
10.3	Polarization analysis of Jupiter data acquired with RITPIC. The polarization of the poles of Jupiter is immediately obvious. The face of Jupiter shows little polarization. Because the images are under-sampled, the polarimetric accuracy in these images is limited to ± 0.02 . Therefore, we find the poles to be polarized at the $9\% \pm 2\%$ level.	161
10.4	<i>Left:</i> RITPIC was mounted at the Cassegrain focus of the SMARTS 0.9 m telescope. The white spot in the upper left was used to acquire unpolarized dome flats. <i>Right:</i> RITPIC is a very compact imaging polarimeter.	162
10.5	<i>Left:</i> The sampling in the RITPIC focal plane was $0.12''$ per pixel and $0.24''$ per superpixel. <i>Right:</i> HD 90156 was observed using 5 different locations on the array. The dashed circles are centered on the location of each star and the numbers indicate the frame numbers that correspond to each location.	163
10.6	Estimation of the normalized Stokes parameters, q and u for each frame, using a flat field correction. The error bars on each measurement represent the photometric SNR.	164
10.7	Estimation of the fractional polarization and angle of polarization for each frame, using only a flat field correction. The error bars on each measurement represent the photometric SNR.	165

10.8	Estimation of the Stokes q and u parameters for each frame, using a combination of a flat field correction, as well as the efficiency and orientation data obtained in the lab.	166
10.9	Polarimetry performed by RITPIC for the unpolarized star HD 90156 using the broadband response of the CCD.	166
10.10	Normalized Stokes parameters q and u , measured by RITPIC for the polarized star HD 78344 in the V band. The error bars represent the scatter in the estimation (as 1 standard deviation).	167
10.11	Polarimetry performed by RITPIC for the polarized star HD 78344 in the V band.	168
10.12	Raw images of Venus, Jupiter and Saturn acquired with Gen 4 RITPIC at the 36" telescope at CTIO.	169
10.13	The Stokes q and u maps made using a median of 20 images of Jupiter in the Bessel R filter. The maximum polarization measured is $\sim q = 0.08$ and $u = -0.07$ in the instrumental reference frame.	170
10.14	The Stokes q and u maps aligned with the scattering plane, to match observations of Schmid et al. (2011). The maximum polarization measured is $\sim q = 0.08$	170
10.15	The uncertainty maps for the normalized Stokes parameters q and u , estimated using the variance-covariance of the linear least squares estimator and formal error propagation.	171
10.16	<i>Left:</i> The Stokes I "intensity" map of Jupiter in the Bessel R filter. <i>Right:</i> The fractional polarization of Jupiter, estimated using the degree of linear polarization. The polarization at the poles is $\sim 8\%$, and it rapidly and smoothly decreases towards the equator.	173
10.17	<i>Left:</i> Degree and angle of polarization shown with a vector plot. <i>Right:</i> Angle of polarization across the face of Jupiter shown as a colormap.	174
10.18	<i>Left:</i> Polarization at the poles and limbs of Jupiter, as a function of reciprocal wavelength, measured by Gehrels et al. (1969) in April 1960, with scattering angle $\alpha = -10.6^\circ$. Note that the asymmetry between the North and South pole polarization is minimal at ~ 500 nm. <i>Right:</i> The same measurements repeated in November and December 1963, with scattering angle $\alpha = 8.9^\circ$ and $\alpha = 9.8^\circ$, respectively. Note that the largest discrepancy is now at ~ 500 nm. ©AAS. Reproduced with permission.	175
10.19	The Stokes q and u maps made by Schmid et al. (2011) during the testing of the Zurich Imaging Polarimeter. The scale is set between 1% (white) and -1% (black). The lines in the Q/I image show the slit positions for spectropolarimetry performed with the EFOSC2 instrument on the ESO 3.6m telescope. Reprinted from Schmid et al. (2011), Copyright (2011), with permission from Elsevier.	176
10.20	A comparison of the North-South profile of the intensity and normalized Stokes parameter q for observations made with RITPIC (blue line) and ZIMPOL (black line). The ZIMPOL intensity profile was scaled to have the same peak value as the RITPIC profile.	177

10.21	A comparison of the East-West profile of the intensity and normalized Stokes parameter q for observations made with RITPIC (blue line) and ZIMPOL (black line). The ZIMPOL intensity profile was scaled to have the same peak value as the RITPIC profile.	178
10.22	Polarization of Saturn and its ring system in Stokes q and u . Although the overall polarization is low, some large scale features are clearly seen, such as the polarization of the rings, the northern and southern hemisphere and the south pole.	179
10.23	<i>Left:</i> A Stokes I “intensity” map of Saturn in the Bessel R band. <i>Right:</i> The fractional polarization of Saturn closely matches the Stokes q maps, because there is very little signal in u	180
10.24	The angle of linear polarization shows a complex, large scale pattern across the rings and disk of Saturn.	180
10.25	Polarization of Venus in Stokes q and u . The strongest polarization is seen in Stokes q , with a maximum near the poles and a minimum in the direction of the Sun.	181
10.26	<i>Left:</i> A Stokes I “intensity” map of Venus in the Bessel R band. <i>Right:</i> The fractional polarization of Venus, estimated using the degree of linear polarization. The polarization at the poles is $\sim 4\%$ and $\sim 1\%$ at the lower latitudes.	181
10.27	The polarization is oriented at $\sim -45^\circ$ with respect to the East-West direction across the entire disk of Venus.	182
10.28	Previous polarimetric observations of Venus and the models of Hansen and Hovenier (1974) for the Venereal atmosphere. The red circle shows the integrated polarization in Stokes q measured by RITPIC in the Bessel R band and the square shows the polarization at the equatorial point. This figure is adopted from Fig. 12 of Hansen and Hovenier (1974) ©American Meteorological Society. Used with permission.	183
10.29	Raw images of some planetary (and protoplanetary nebulae) acquired with Gen 4 RITPIC at the 36” telescope at CTIO. The scale is the same in all images.	184
10.30	Normalized Stokes parameters q and u calculated for Hen 401 using 5 300 second exposures in the R filter.	185
10.31	The R band Stokes I image and the degree of linear polarization map for Hen 401.	185
10.32	<i>Left:</i> <i>HST</i> imaging of Hen 401 from Ueta et al. (2007) showing the total (a) and polarized (b) flux. <i>Right:</i> Maps of the degree (c) and angle (d) of linear polarization. ©AAS. Reproduced with permission.	186
10.33	<i>Left:</i> The DOLP and AOLP of Hen 401 overlaid on the intensity image. <i>Right:</i> a detailed map of the angle of linear polarization shows good agreement with <i>HST</i> polarimetry.	186
10.34	Normalized Stokes parameters q and u calculated for Hen 404 using 9 300 second exposures, without any filters.	187
10.35	The Stokes I intensity and the degree of linear polarization for Hen 404 measured by RITPIC.	187

10.36	<i>Left:</i> <i>HST</i> imaging of Hen 404 from Ueta et al. (2007) showing the total (a) and polarized (b) flux. <i>Right:</i> Maps of the degree (c) and angle (d) of linear polarization. ©AAS. Reproduced with permission.	188
10.37	<i>Left:</i> The DOLP and AOLP of Hen 404 overlaid on the intensity image. <i>Right:</i> a detailed map of the angle of linear polarization shows good agreement with <i>HST</i> polarimetry. ©AAS. Reproduced with permission. . . .	189
10.38	The Stokes q and u polarization for Frosty Leo. Peak polarization is $\sim 40\%$ and -45% , respectively.	190
10.39	190
10.40	191
11.1	Several mechanisms for cross-talk exist in micropolarized-based sensors that use off-the-shelf devices.	193
11.2	The photometry of HD 90156 shows a standard deviation of $\sim 1\%$ about the mean. This scatter is due to shot noise and errors associated with device nonuniformity.	197

List of Tables

10.1 Comparison of the polarimetric analysis of two standard stars performed by RITPIC to previous measurements (DOLP_0), made by 1. Gil-Hutton and Benavidez (2003) and 2. Wiktorowicz et al. (2014).	168
---	-----

Abbreviations

AOLP	A ngle O f L inear P olarization
DOLP	D egree O f L inear P olarization
FDTD	F inite- D ifference T ime- D omain
MPA	M icro P olarizer A rray
PML	P erfectly M atched L ayer
RCWA	R igorous C oupled- W ave A nalysis
SEM	S canning E lectron M icroscope

To my parents
&
To John and Pete

Chapter 1

Introduction

On June 6, 1761, telescopes at observatories across Europe were pointed at the Sun to observe the transit of Venus across the solar disk. About two dozen scientists reported seeing the disk of Venus surrounded by “arcs of fire” as it crossed the solar limb and the appearance of “blisters” on the solar limb (which was otherwise quite sharp) as Venus began its egress. Several observers correctly attributed these phenomena to refraction through what must be Venus’s atmosphere, with the most rigorous observations (Figure 1.1) and analysis performed by Michael Vasil’evich Lomonosov ([Shiltsev, 2014](#)).

For the next 200 years, the nature of the Venusian atmosphere remained a mystery. Some suggested that the thick clouds consist of water vapor and hide a surface overgrown by a tropical jungle. Eventually, “progress at the Research Laboratory of the Eastman Kodak Company in sensitizing photographic plates to the [near]-infrared allowed” [Adams and Dunham \(1932\)](#) to obtain spectra that showed the first evidence for a large amount of CO₂ and very little H₂O; however, as CO₂ is transparent, the composition of the opaque clouds remained undetermined.

Debate continued into the 1960s and 1970s, with a wide range of constituents suggested for the cloud make-up, including, water ice, carbon dioxide ice, hydrated ferrous chloride, formaldehyde, hydrocarbons, hydrocarbon-amide polymers, ammonium nitride, aqueous

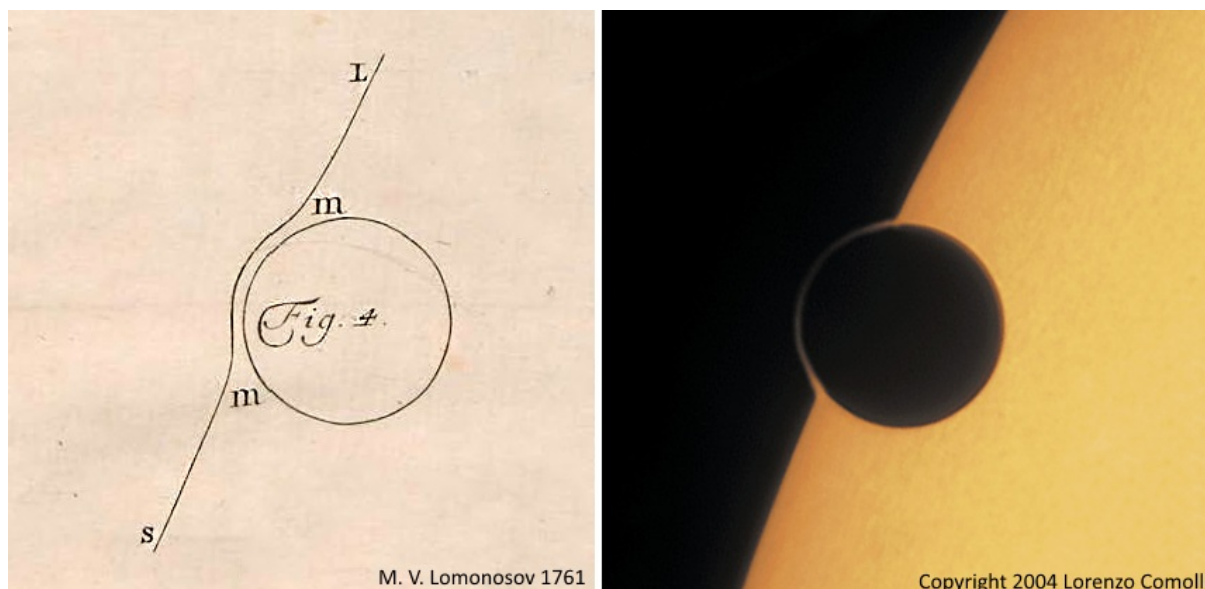


FIGURE 1.1: Left: A sketch by Lomonosov of a “fiery arc” surrounding Venus, caused by light refraction in the Venusian atmosphere. Right: a photo of the same phenomenon during the 2004 transit ©Lorenzo Comolli. Used with permission.

solutions of hydrochloric and sulfuric acid, mercury, and polywater¹. Spectroscopic features alone provided only ambiguous interpretations. For example, the features attributed to water ice could also be produced by gaseous CO₂. As a last resort, some began to look at the angular distribution of the light reflected by the Venusian clouds.

As Venus orbits the Sun, the reflected light arriving at the Earth samples a wide range of scattering angles. In the early 1970s, James E. Hansen and J. W. Hovenier developed radiative transfer models that accurately treat the effects of multiple scattering on polarization (Hansen, 1971; Hansen and Hovenier, 1971). Finally, Hansen and Hovenier (1974) used their models and the high quality polarimetric observations of Venus made by Lyot (1929), Coffeen and Gehrels (1969), and Dollfus and Coffeen (1970), to conclude that “the particle properties deduced from the polarization eliminate all but one of the cloud compositions which have been proposed for Venus. A concentrated solution of sulfuric acid (H₂SO₄-H₂O) provides good agreement with the polarization data.”

The characterization of the Venusian atmosphere is a spectacular example of the utility of polarimetry in the study of the microscopic properties of scattering particles. However, the measurement of polarization can also be used to infer the macroscopic geometry of

¹Polywater doesn't exist on Venus or anywhere else, because it turned out to be a hoax.

objects. This use of polarimetry was demonstrated by [Antonucci and Miller \(1985\)](#), who used spectropolarimetry of active galactic nuclei to show that Type 1 and Type 2 Seyfert galaxies probably host similar nuclei, containing an accretion disk surrounded by a dusty torus, but observed along different lines of sight. Polarimetry is also useful for spatially-resolved objects as a means of deriving depth information in a scene. This was elegantly shown by [Kervella et al. \(2014\)](#), who studied the polarization of light echoes reflected from the dusty shells around RS Puppis to determine a geometric distance estimate to this Cepheid variable. Measurements of polarization are responsible for discoveries in nearly all areas of astronomy, from solar system science and the study of planets around other stars, to the study of large scale structure of the universe.

On Earth, the applications of polarimetry are even more numerous. Measurements of polarization have been identified as a key tool in the study of the Earth’s own atmosphere and its aerosol content. Polarization can be exploited in microscopy and minimally invasive medical diagnostic imaging. In industrial settings, polarimetry can be used in product inspection and quality assurance systems. The amount of surface detail captured by infrared imaging systems can be significantly increased through the use of polarization.

Despite dozens of potential applications, the adoption of polarimetric techniques has been slow, because our most advanced detectors are insensitive to polarization. To determine the polarization of light, we are forced to use polarization-sensitive optics to modulate the intensity of light. However, these polarimeters rarely advance beyond temperamental prototypes built in research laboratories, and even the most polished systems cannot be easily adapted to perform a similar measurement in a different setting or field.

The relatively new class of imaging polarimeters based on micropolarizer arrays shows potential to be the first “general purpose” polarimeter, in sharp contrast to the highly specialized and idiosyncratic polarimeters of the past. In this work, I attempt to establish the level of precision and accuracy that can be achieved with these devices when imaging point sources and extended objects. To this end, I propose characterization and calibration techniques and describe several methods of data analysis. I also investigate the mechanisms which fundamentally limit the performance of these polarimeters.

In an attempt to make this work self-contained and consistent with existing conventions, the first few chapters provide an overview of the principles of polarization and polarimetry. A mathematical description of polarization and the Stokes formalism are introduced in Chapter 2. In Chapter 3 I describe some common sources and mechanisms that produce polarized light. The wire grid polarizer, which is the basic building block of polarization-sensitive detectors, is introduced in Chapter 4. Using high resolution numerical models I investigate the effects of wire shape and spacing on the polarizer's performance and explore the challenges associated with these simulations. In Chapter 5, I present high resolution 3D simulations of pixelated polarizers and micropolarizer arrays. A brief overview of techniques and instruments used for polarimetric measurements is given in Chapter 6. Efforts to fabricate polarimeters using micropolarizer arrays and CCDs at RIT are detailed in Chapter 7. In Chapter 8 I describe the method used to characterize sensors based on micropolarizer arrays and the software tools I developed to produce synthetic observations, which are used to study various sources of polarimetric errors. The data analysis process is described in Chapter 9. The results of the on-sky evaluation of the RIT Polarization Imaging Camera are presented in Chapter 10. Finally, I summarize the key results of this work in Chapter 11.

Chapter 2

Polarization of Light

Electromagnetic radiation is characterized by four fundamental properties: polarization, frequency, intensity and coherence (Figure 2.1). The term “polarization” can refer to the configuration of the electric field of a single photon, or the average preference of a collection of photons for a specific state. The electric field of each photon is configured at the time of emission such that the momentum of the photon-plus-emitter system is conserved. The polarization of a single photon is described by the direction of oscillation of the electric field in the plane perpendicular to the direction of propagation (Figure 2.2). If this angle, ψ , is constant, the photon is linearly polarized and its polarization is described by this angle of linear polarization (AOLP). If this angle changes (rotates) as the photon propagates, the photon can be described as having circular (or more generally elliptical) polarization. Without a mechanism that affects the emitters in some systematic way, the state of the electric field of one photon is independent from another. This is typical of systems that are well described by the Maxwell-Boltzmann distribution (e.g., black body radiators).

If a number of photons do not show a preference for a particular polarization state, we call this light unpolarized (or “randomly polarized”) and its degree of polarization, $p \ll 1$. Because our eyes are not sensitive to polarization, unpolarized light feels “natural”. However, in many situations the light we observe **is polarized** at some level. Some emission mechanisms (for example, many kinds of lasers) emit photons with a strong preference for a particular polarization state. Synchrotron radiation, which is emitted by

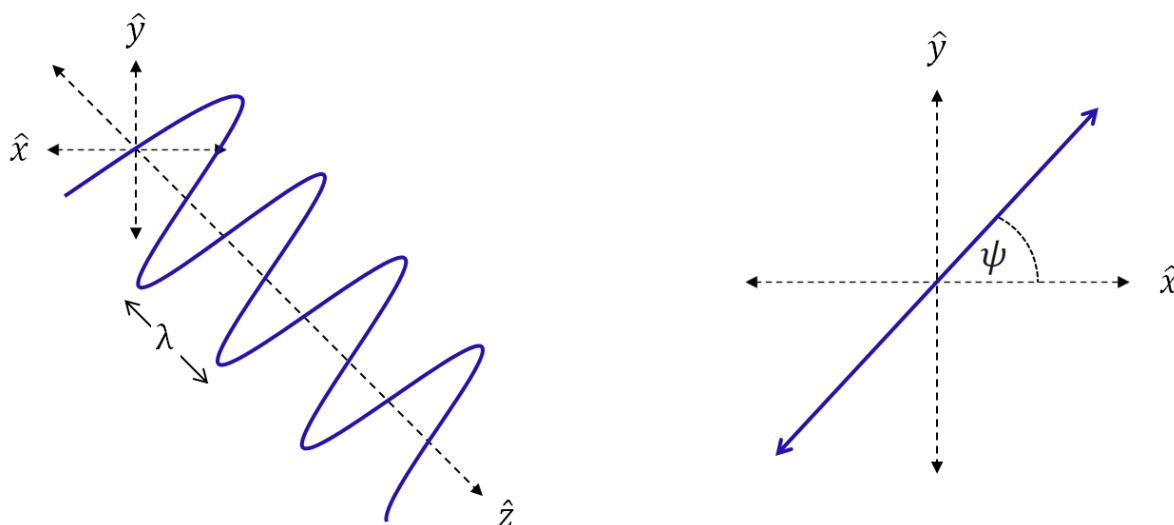


FIGURE 2.1: Left: Electromagnetic waves oscillate in a plane orthogonal to the direction of propagation. The frequency of oscillation is related to the energy of the photon and is often expressed in terms of the associated wavelength, λ . Right: The direction of oscillation in the plane of oscillation describes the polarization of a single photon. In this case, the photon is linearly polarized at 45° with respect to the x-axis.

relativistic particles accelerated in magnetic fields, is highly polarized and the preferred polarization state changes from linear to circular depending on the viewing geometry. Even sources that are traditionally treated as black body radiators (people, cars, etc) can emit polarized infrared radiation. Furthermore, there exist several processes that are efficient at polarizing light from sources with very little intrinsic polarization (See Chapter 3).

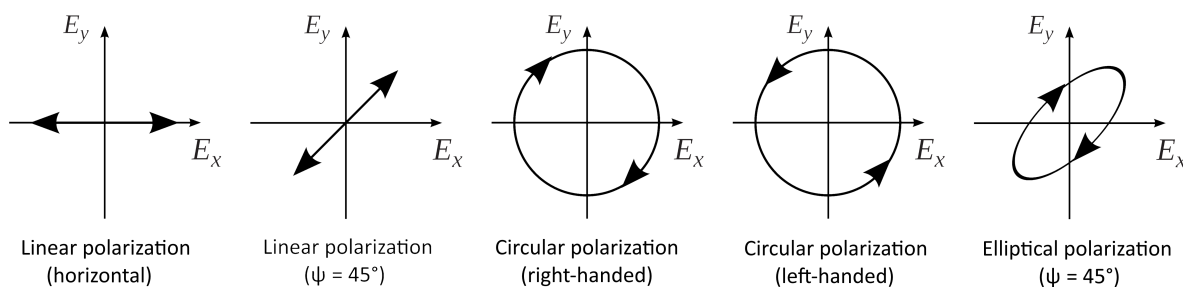


FIGURE 2.2: The polarization of a single photon, or the average polarization of a collection of photons, can be described by the path that is traced by the electric field vector in the $(\hat{x} - \hat{y})$ plane perpendicular to the direction of motion of the photon(s). The polarization can be purely linear, circular (a combination of two orthogonal linear states out of phase by $\frac{\pi}{2}$) or elliptical.

2.1 A Mathematical Description

The electric field of a single photon (Figure 2.1) can be expressed as the sum of its \hat{x} and \hat{y} components using the conventional wave equation solution as follows,

$$\vec{E}(z, t) = \vec{E}_x(z, t) + \vec{E}_y(z, t) \quad (2.1)$$

where

$$\vec{E}_x(z, t) = \hat{x} E_{0x} \cos(\kappa z - \omega t) \quad (2.2)$$

$$\vec{E}_y(z, t) = \hat{y} E_{0y} \cos(\kappa z - \omega t + \epsilon) \quad (2.3)$$

E_{0x} : electric field amplitude of the \hat{x} -component

E_{0y} : electric field amplitude of the \hat{y} -component

κ : wave number - $2\pi/\lambda$

ω : frequency - c/λ

ϵ : a phase shift between the \hat{x} and \hat{y} components

Using these equations, it is possible to produce any polarization state with the proper choice of the electric field amplitudes E_{0x} & E_{0y} and the phase difference between them, ϵ . Although the number of possible states is infinite, there exist several special cases worth noting (Figure 2.2). If $E_{0x} = 0$ or $E_{0y} = 0$, the light will be linearly polarized in the vertical or horizontal direction, respectively, regardless of the phase difference. If both electric field amplitudes are non-zero, phase shifts that are integer multiples of $\pm 2\pi$ or $\pm \pi$ will produce linearly polarized light. If $E_{0x} = E_{0y}$, and $\epsilon = \pm\pi/2 + 2m\pi$, where $m = 0, \pm 1, \pm 2, \dots$ the light will be circularly polarized. Any other choice of parameters will produce an elliptical state.

The Stokes Parameters

The simple mathematics in the previous section (Eq. 2.1-2.3) provide a straightforward way to determine the polarization state of a single photon (or monochromatic “waves”). In 1852, Sir G. G. Stokes invented a new formalism that allows one to add two (or more) photons (each with their own unique polarization state) and describe the polarization of the resulting light. The polarization state of each component and their sum is represented by the Stokes vector whose components are the four Stokes parameters,

$$\vec{S} = \begin{bmatrix} I \\ Q \\ U \\ V \end{bmatrix} \quad (2.4)$$

The Stokes parameters, I, Q, U, V are additive for different beams, allowing for simple computation of the new polarization state. This technique’s most attractive feature is the ability to describe the polarization state of partially polarized light. The definition of the Stokes parameters is very geometric and phenomenological, yet the arithmetic facilitated by the Stokes vector is precise and well behaved. In practice, the Stokes parameters can be measured by “filtering” the light using a series of polarizers and comparing the resulting intensities as follows,

$$I = i_{0^\circ} + i_{90^\circ} \quad (2.5)$$

$$Q = i_{0^\circ} - i_{90^\circ} \quad (2.6)$$

$$U = i_{+45^\circ} - i_{-45^\circ} \quad (2.7)$$

$$V = i_{RH} - i_{LH} \quad (2.8)$$

where i_{0° is the intensity of light having passed through a polarizer oriented at 0° , i_{90° is the intensity of light having passed through a polarizer oriented at 90° and so on; i_{RH} and i_{LH} represent the amount of light present with circular polarization that is right hand and left hand oriented. Although straightforward in concept, the measurement of Stokes

parameters is often complicated by systematic uncertainties related to the measurement apparatus and techniques (see Section 6).

The Stokes parameters can be calculated explicitly if the parameters of Eq. 2.1-2.3 are known or measured directly using their definitions:

I : total intensity

Q : overall preference for “horizontal” polarization states vs “vertical” states

U : overall preference for the $+45^\circ$ states vs -45° states

V : overall preference for the right circular vs left circular states

In addition to being determined experimentally, the Stokes parameters can be related explicitly to the properties of the electric field. Using the equations for the \hat{x} and \hat{y} electric field components,

$$\vec{E}_x(z, t) = \hat{x} E_{0x} \cos(\kappa z - \omega t)$$

$$\vec{E}_y(z, t) = \hat{y} E_{0y} \cos(\kappa z - \omega t + \epsilon)$$

we can express the Stokes parameters as follows (angle brackets indicate an average in time),

$$I = \langle E_{0x}^2 + E_{0y}^2 \rangle$$

$$Q = \langle E_{0x}^2 - E_{0y}^2 \rangle$$

$$U = \langle 2 E_{0x} E_{0y} \cos \epsilon \rangle$$

$$V = \langle 2 E_{0x} E_{0y} \sin \epsilon \rangle.$$

Even more useful than the ability to measure the Stokes parameters directly or to relate them to the properties of the electric field, is the ability to describe partially polarized light. Everything about the polarization state is described by the Stokes vector. However, it is often useful to express this information using three additional metrics: the degree of polarization, p , the angle of linear polarization, ψ , and the azimuthal angle on the Poincaré, sphere, χ , which is related to circular polarization. These properties can be

calculated using the Stokes parameters as follows,

$$\text{degree of polarization : } p = \frac{\sqrt{Q^2 + U^2 + V^2}}{I} \quad (2.9)$$

$$\text{angle of linear polarization : } \psi = \frac{1}{2} \arctan U/Q \quad (2.10)$$

$$\text{azimuthal angle : } \chi = \frac{1}{2} \arctan \frac{V}{\sqrt{Q^2 + U^2}} \quad (2.11)$$

If the light has no significant circular polarization (or if a measurement is only sensitive to linearly polarized components), the above relations reduce to the following,

$$\text{degree of linear polarization : } DOLP = \frac{\sqrt{Q^2 + U^2}}{I} \quad (2.12)$$

$$\text{angle of linear polarization : } AOLP = \frac{1}{2} \arctan U/Q \quad (2.13)$$

Note that equations 2.10 and 2.13 use the 360° arctan function.

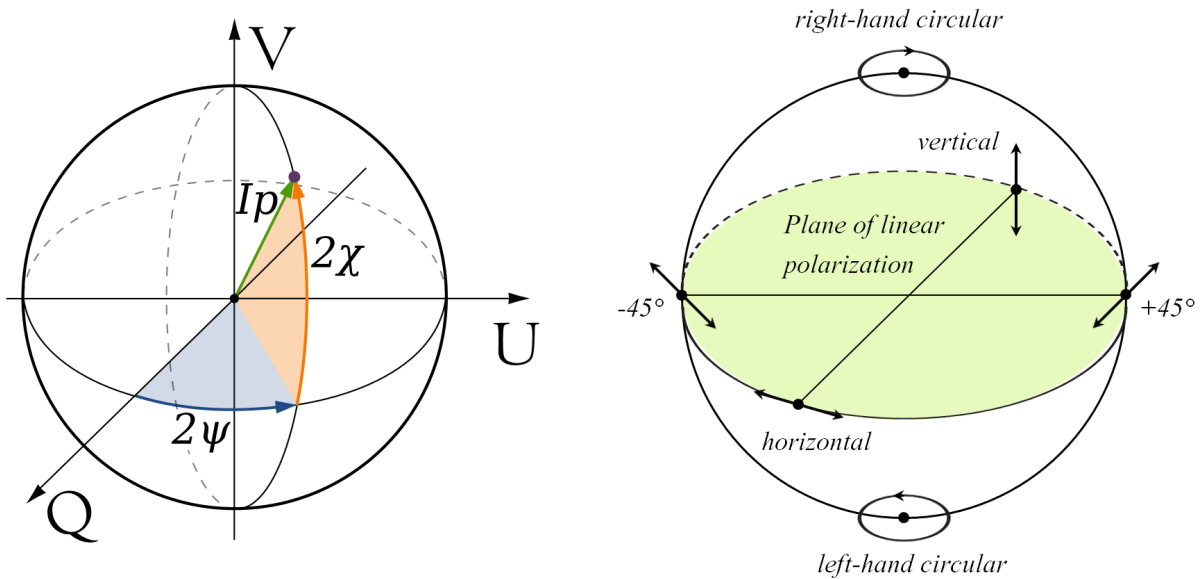


FIGURE 2.3: The Poincaré sphere can be used to specify the polarization state as a set of coordinates on its surface. Furthermore, it is a useful way to demonstrate the relationship between the Stokes parameters and the polarization state. Notice that polarization states that are purely linear or purely circular reside along the equator and at the poles, respectively. The rest of the surface corresponds to more general, elliptical states.

The metrics p , ψ , and χ , uniquely identify a location on the Poincaré sphere, which is a representation of all possible polarization states (Figure 2.3). In this way, the Stokes parameters can be thought of as coordinates on the surface of the Poincaré sphere. The

special cases of polarization (linear, horizontal, circular, etc) described in the beginning of this section reside in key places on the sphere. Completely linear polarization states reside along the equator and form a “plane of linear polarization”, where the degree of polarization is the radial coordinate. Conversely, completely circular states reside at the poles of the sphere ($\chi = \pm\frac{\pi}{4}$).

Chapter 3

Production of Polarized Light

Every photon has a well defined polarization state and every group of photons will show an average preference for a particular state of polarization; in other words, all light is polarized to some degree. Because our eyes, like the eyes of other mammals, cannot easily¹ distinguish the polarization state of photons the way we can distinguish colors, human perception of polarization is highly biased. Randomly polarized light seems “natural” and ubiquitous, while conditions for the production of strongly polarized light seem contrived. This bias creates the impression that polarized light and its measurement are restricted to a few isolated disciplines and can largely be ignored, when in fact, polarization is “a universal feature of our world” [Pye \(2001\)](#).

In this chapter, I will describe some mechanisms that produce polarized light, with a special emphasis on processes that are relevant to imaging applications in astronomy, terrestrial remote sensing and the biomedical disciplines. Furthermore, I will introduce some archetypal examples of man-made polarizers that exploit these phenomena to produce highly polarized light.

¹There appear to be no absolutes when it comes to polarization. There is some evidence that human eyes, specifically the macula, is somewhat sensitive to polarization, due to the dichroism of the xanthophyll pigment. This is the suggested cause for the phenomenon called Haidinger’s brush, where a faint yellow-blue cross pattern is sometimes seen when looking at highly polarized objects, like the twilight sky or an LCD monitor. Although fascinating, this sensitivity is too insignificant to be utilized the way other animals utilize their polarization-seeing eyes.

3.1 Polarization Upon Reflection

Although the Sun produces light with a very small degree of polarization, we encounter polarized light on a daily basis. Unpolarized light reflected by a surface can become highly polarized in the direction parallel to the surface (Figure 3.1). This effect is angle-dependent and maximally efficient when the light is incident at Brewster's angle, $\theta_B = \arctan(n_t/n_i)$, where n_i and n_t are the refractive indexes of the original medium and the surface medium, respectively. Polarized sunglasses exploit this effect to significantly reduce the glare from the surfaces of roads and bodies of water, by absorbing light with this “horizontal” polarization. The degree of polarization due to a reflection can be estimated using the Fresnel reflection coefficients for the electric field components parallel and perpendicular to the plane of incidence (see Hecht (2002) for a detailed discussion).

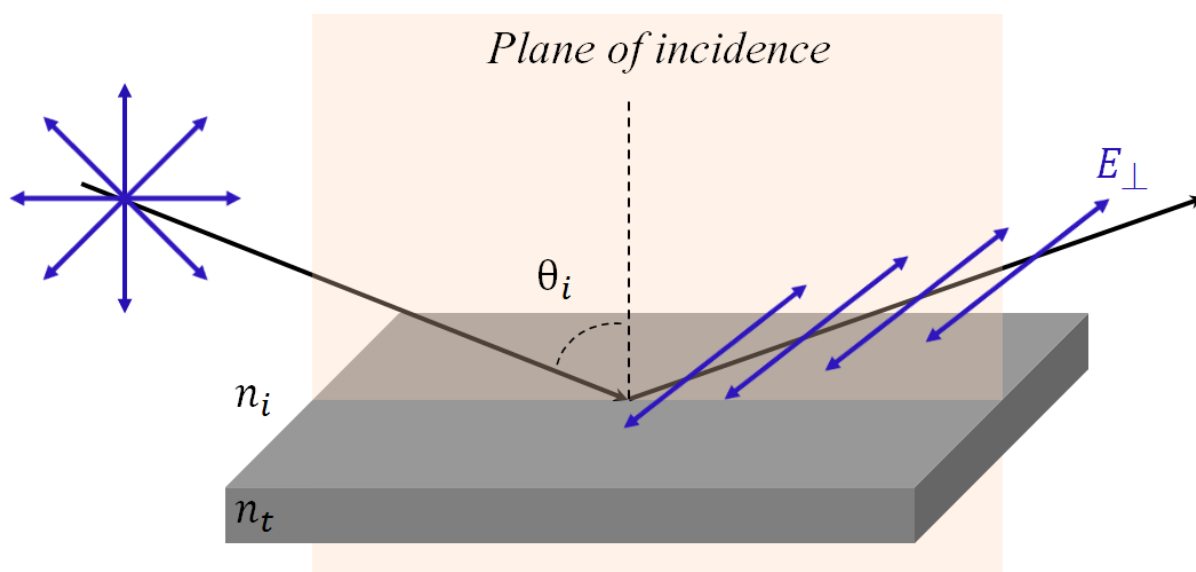


FIGURE 3.1: Randomly polarized light can become strongly polarized when reflected off a surface, with the angle of polarization parallel to the surface of reflection (and perpendicular to the plane of incidence).

3.1.1 Reflection from Dielectric Surfaces

For dielectric materials the Fresnel coefficients depend on the refractive indexes of the two media and the angle of incidence as follows,

$$r_{\perp} = \frac{n_i \cos \theta_i - n_t \cos \theta_t}{n_i \cos \theta_i + n_t \cos \theta_t} \quad (3.1)$$

$$r_{\parallel} = \frac{n_t \cos \theta_i - n_i \cos \theta_t}{n_i \cos \theta_t + n_t \cos \theta_i} \quad (3.2)$$

where r_{\perp} and r_{\parallel} are the amplitude coefficients for the electric field components perpendicular and parallel to the plane of incidence (which is normal to the reflecting surface by convention), n_i is the refractive index of the original medium, n_t is the refractive index of the surface medium, θ_i is the angle in the plane of incidence and θ_t is the angle of the transmitted light, which can be determined using Snell's law for refraction,

$$n_i \sin \theta_i = n_t \sin \theta_t. \quad (3.3)$$

The amplitude coefficients can be used to determine the total reflected power in each electric field component by calculating the corresponding reflection coefficients,

$$R_{\perp} = r_{\perp}^2$$

$$R_{\parallel} = r_{\parallel}^2$$

When light is incident on a dielectric surface close to the surface normal, the two orthogonal components of the electric field are reflected with the same intensity. However, as the angle of incidence increases and the numerator of Eq. 3.1, $n_i \cos \theta_i - n_t \cos \theta_t$, approaches zero, the electric field component parallel to the plane of incidence is significantly suppressed (Figure 3.2). At Brewster's angle, no electric field components parallel to the plane of incidence are reflected and the resulting light is very highly polarized parallel to the plane of the surface.

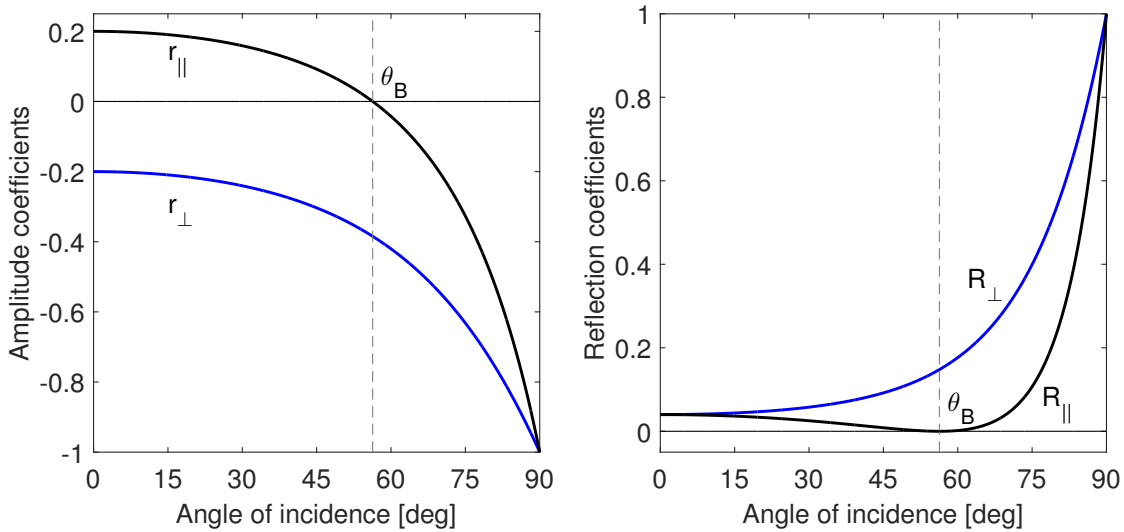


FIGURE 3.2: The reflection of light is highly dependent on the polarization of the incident radiation and the geometry of the reflection. The reflection coefficients for the amplitude of the electric field (given by Equations 3.1 & 3.2, $n_i = 1, n_t = 1.50$) depend highly on the angle of incidence. At Brewster’s angle, θ_B (dashed line), the amplitude coefficients and the reflection coefficients for electric field components parallel to the plane of incidence (perpendicular to the reflecting surface) reach zero and the reflected light is polarized parallel to the reflecting surface.

From the point of view of polarimetry, we can calculate the change in the Stokes parameters and the degree of linear polarization (DOLP), as a function of the angle on incidence (Figure 3.3). Near normal incidence, the reflection coefficients are equal and the Q parameter (which represents the difference between the horizontal and vertical polarization states) is zero. Q increases with increasing angle of incidence, until it becomes equal to the total reflected intensity. At this point, all reflected light is polarized in the “horizontal direction” and $DOLP = 1$. As the angle approaches grazing incidence, Q sharply decreases and the reflected light is, again, randomly polarized.

A Practical Note...

The calculations shown in Figure 3.2 and Figure 3.3 are for the case of perfectly collimated monochromatic light ($\lambda = 1.6 \mu\text{m}$) reflecting off a glass surface. In practice, light beams have some distribution of incidence angles and wavelengths, which result in a range of Brewster angles. Therefore, a single reflection cannot completely polarize a physical beam with a broad spectrum.

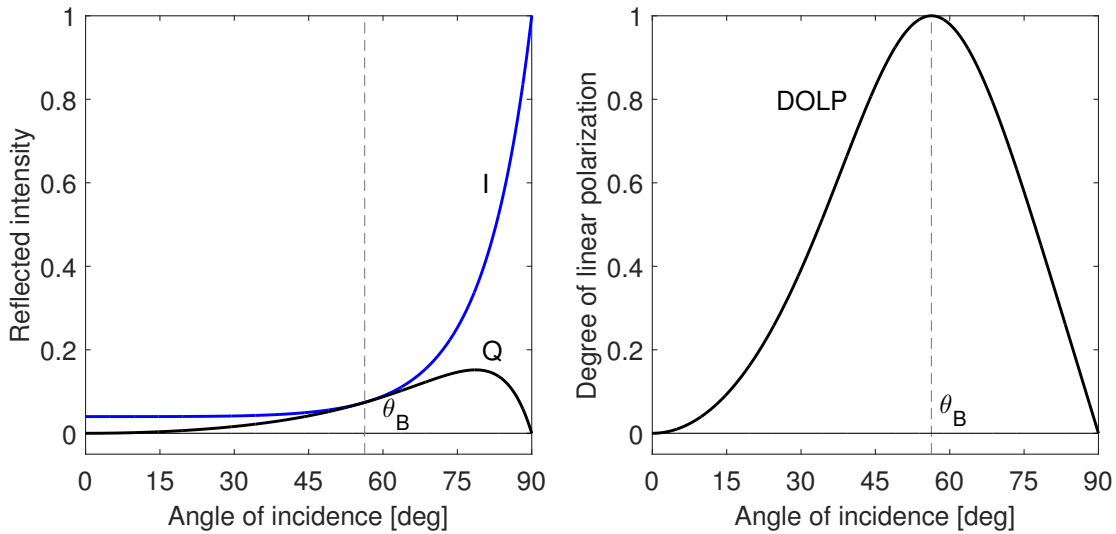


FIGURE 3.3: Left: The Stokes parameters I and Q describe how randomly polarized light can become highly polarized through a reflection from a dielectric material. At normal incidence, $Q = 0$ (the \hat{x} and \hat{y} components are reflected equally) and it increases with angle of incidence until $Q = I$ at Brewster's angle. In other words, at this point the intensity of light polarized parallel to the surface is equal to the total intensity and the $DOLP = 1$ (Right).

3.1.2 Reflection from Metal Surfaces

When light is reflected by a metal surface the behavior of reflected light is somewhat different. The Fresnel coefficients for the amplitude of the reflected components of the electric fields (Eq. 3.1-3.2) can be computed in a similar fashion to dielectrics; however, the complex refractive index must be used, to account for the non-negligible absorption of light in metals. The complex refractive index has the form,

$$\mathbf{n} = n + ik$$

where n is the real refractive index (which indicates the group velocity in the medium) and k is the *extinction coefficient*, whose sign is positive if there is absorption in the medium. With this form of the refractive index, the reflection coefficients for the amplitude of the electric field become,

$$r_{\perp} = \frac{n_i \cos \theta_i - (n_t + ik) \cos \theta_t}{n_i \cos \theta_i + (n_t + ik) \cos \theta_t} \quad (3.4)$$

$$r_{\parallel} = \frac{(n_t + ik) \cos \theta_i - n_i \cos \theta_t}{n_i \cos \theta_t + (n_t + ik) \cos \theta_i} \quad (3.5)$$

In this case, $\cos \theta_t$ is a complex number, given by,

$$\cos^2 \theta_t = \frac{1}{\mathbf{n}^2}(\mathbf{n}^2 - \sin^2 \theta_i).$$

Nevertheless, the coefficients for the reflected intensity of each component of the electric field can be closely approximated as follows,

$$R_{\perp} = \frac{(n - \cos \theta_i)^2 + k^2}{(n + \cos \theta_i)^2 + k^2} \quad (3.6)$$

$$R_{\parallel} = \frac{\left(n - \frac{1}{\cos \theta_i}\right)^2 + k^2}{\left(n + \frac{1}{\cos \theta_i}\right)^2 + k^2} \quad (3.7)$$

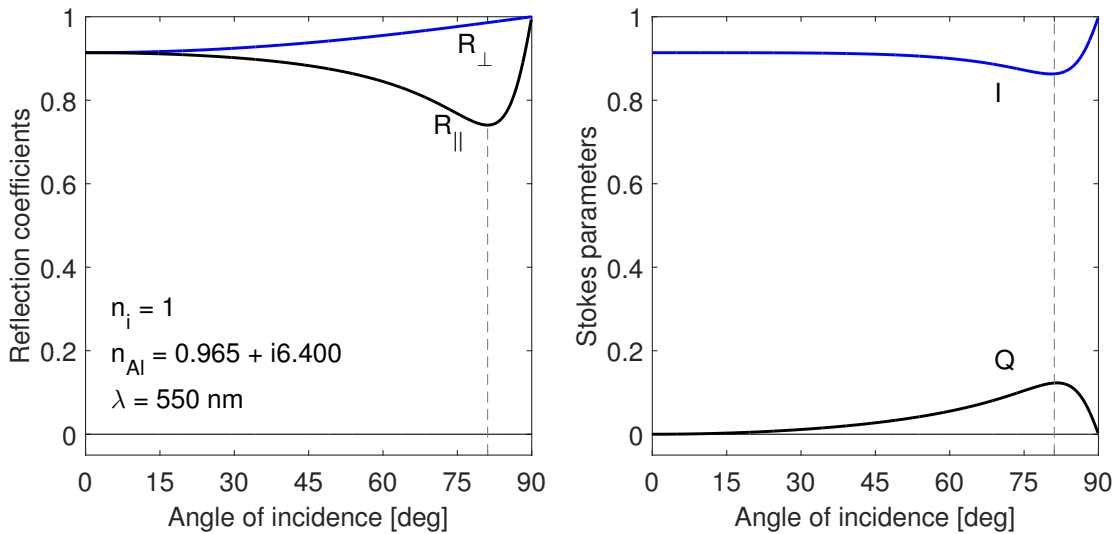


FIGURE 3.4: *Left:* Reflection coefficients for the electric field components perpendicular and parallel to the plane on incidence, for 550 nm light reflecting off an aluminum mirror. The parallel component is suppressed at large angles of incidence, but never reaches 0, like for dielectrics. The reflection is minimal at the angle of principal incidence, indicated by the vertical dashed line. *Right:* The Stokes parameters show the changes in the reflection coefficients by a decrease in the total intensity, I , and an increase in Q .

Unlike dielectrics, metals are very efficient reflectors at all angles of incidence. However, as the angle of incidence increases, the reflection coefficients for the two electric field components begin to diverge (Figure 3.4) and the reflection coefficient of the electric field parallel to the plane of incidence (and perpendicular to the reflecting surface) decreases, reaching a minimum at the *angle of principal incidence* ($\approx 81^\circ$ for 550 nm light and an aluminum mirror). This behavior is expressed by the Stokes parameters by a decrease in the total intensity, I and an increase in the Q parameter. The overall degree of polarization imparted on an unpolarized beam is not as large as that due to dielectrics, because there is no point at which one component is completely suppressed. However, the polarization is not insignificant (Figure 3.5) and a 45° fold mirror, a common optical component, will produce a $DOLP \approx 2.5\%$.

Although the magnitude of this effect is relatively small, it can be the source of many systematic errors in systems designed to measure polarization. For example, the 45° fold mirror is a critical component of Nasmyth telescopes, which make up the majority of large ground-based telescopes (Figure 3.5, *Right*). Conversely, a Cassegrain design is among the most benign for polarization measurement. However, even imaging systems without fold mirrors are susceptible to this effect, if the optical surfaces have sufficient curvature. Imaging systems that use small $f/\#$ “fast” optics are most vulnerable.

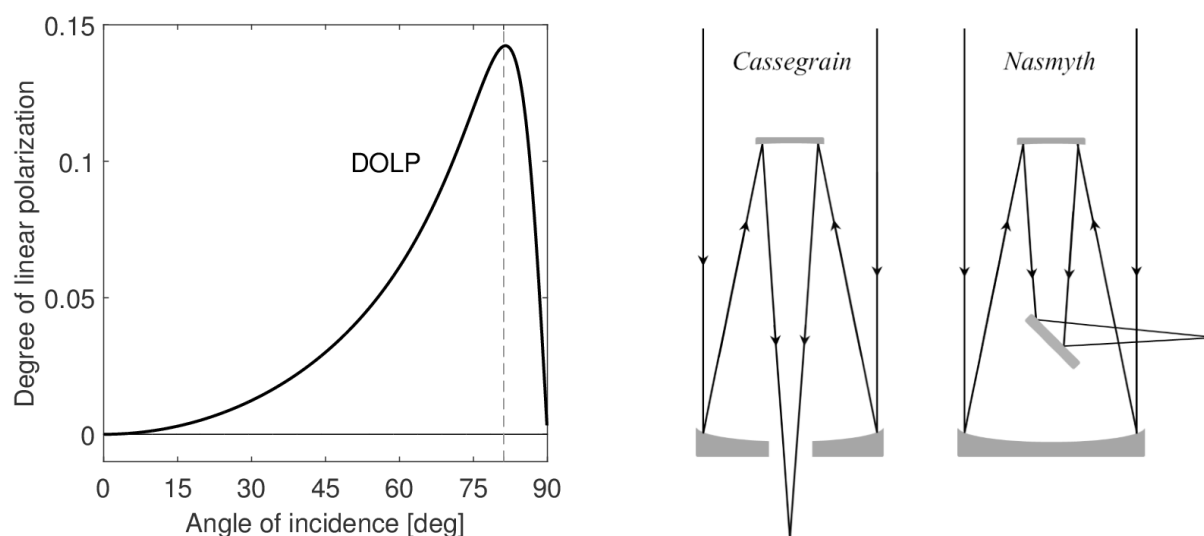


FIGURE 3.5: *Left*: The degree of polarization imparted to a randomly polarized beam during a reflection from a metal. *Right*: Telescopes with fold mirrors exhibit large instrumental polarization.

3.2 Polarization from Scattering

Polarization is fundamental to the interaction of light and matter. This is exemplified by the scattering of light from small, isolated particles. Electrons, atoms, molecules and even larger particles, like dust and smoke, are extremely efficient at producing polarized light, under the proper conditions. In this section, I provide a brief overview of the most practical aspects of several scattering processes and highlight the consequences for light polarization.

3.2.1 Rayleigh Scattering

The elastic scattering of light from particles with sizes smaller than the wavelength of light is well described by the theory developed by Lord Rayleigh (John William Strutt). This theory explains that for a spherical particle of a certain size, the scattering efficiency decreases as the wavelength increases. The Rayleigh approximation works best when the size of the scatterer is 10 - 100 times smaller than the wavelength of light. This is parametrized by the ratio,

$$x = \frac{2\pi r}{\lambda}$$

where r is the radius of the spherical particle and λ is the wavelength of light. When $x \ll 1$, the intensity of light scattered by any one particle is given by

$$I = I_0 \frac{1 + \cos^2 \theta}{2R^2} \left(\frac{2\pi}{\lambda} \right)^4 \left(\frac{n^2 - 1}{n^2 + 2} \right)^2 \left(\frac{d}{2} \right)^6 \quad (3.8)$$

I : scattered intensity

λ : wavelength of light

I_0 : incident intensity

n : refractive index of the particle

θ : scattering angle

d : diameter of the particle

R : distance to the particle

When the scattering particles are atoms or molecules, the scattering efficiency decreases like λ^{-4} . This is why the sky looks blue and it is this problem that led Rayleigh to develop his name sake theory. However, this scattering mechanism also produces a strong, angle-dependent polarization signature. This is due to the microscopic properties of the electric field and the macroscopic geometry of the light source and the scatterers, which is a recurrent theme in polarization measurement.

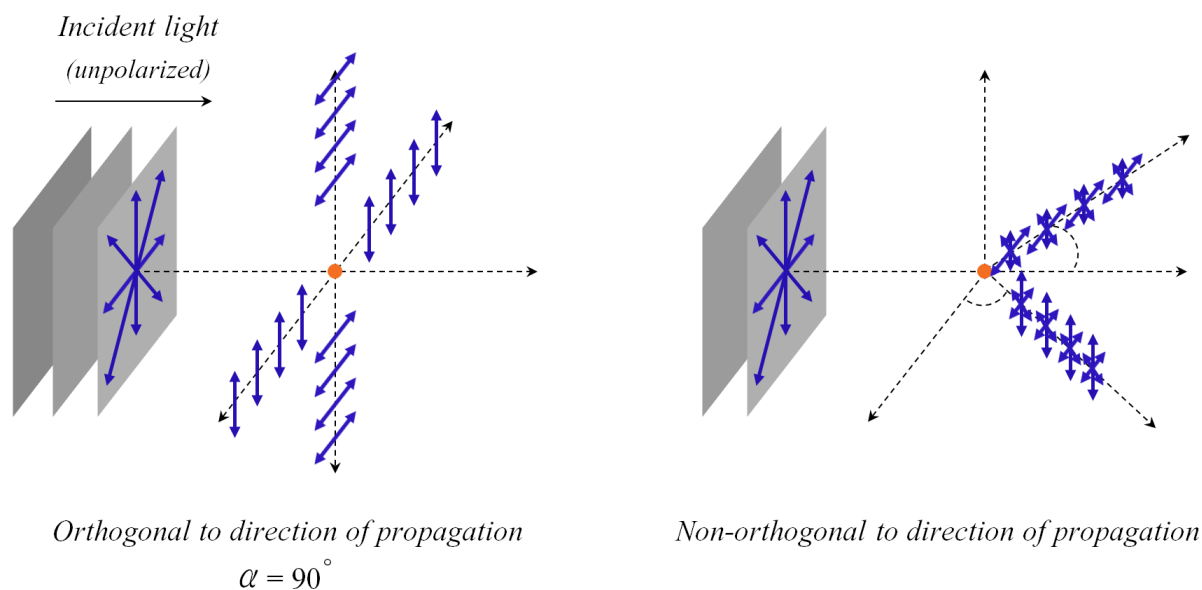


FIGURE 3.6: *Left:* When randomly polarized light interacts with an atom or molecule (orange circle in figure), the scattered photons will display a range of polarization states. The photons which are scattered in the plane orthogonal to the direction of propagation of the incident light will be completely linearly polarized. *Right:* Photons that are scattered at any other scattering angle will have a range of polarizations. Generally, the degree of polarization decreases as the scattering angle approaches $\alpha = 0^\circ$ or $\alpha = 180^\circ$.

When a photon interacts with an atom or a molecule, the scatterer is accelerated in the plane of the photon's electric field, which is always perpendicular to the direction of propagation (Figure 3.6). The scatterer is forced to oscillate in this plane, regardless of the photon's polarization state (because all linear polarizations exist in the same plane). The accelerated scatterer will radiate in a dipole pattern, with a range of polarization states which depend on the scattering angle, α . The photons which are scattered in the plane of oscillation ($\alpha = 90^\circ$) will be completely linearly polarized, perpendicular to their direction of propagation. In general, for Rayleigh scattering, the degree of linear

polarization depends on the scattering angle as follows,

$$DOLP = \frac{\sin^2 \alpha}{1 + \cos^2 \alpha} \quad (3.9)$$

where $DOLP$ is the degree of linear polarization and α is the scattering angle. In the Earth's atmosphere, the rays from the Sun appear parallel. This geometry creates very strong sky polarization along some lines of sight (for photons with scattering angle $\alpha \approx 90^\circ$). This geometry is shown in Figure 3.7.

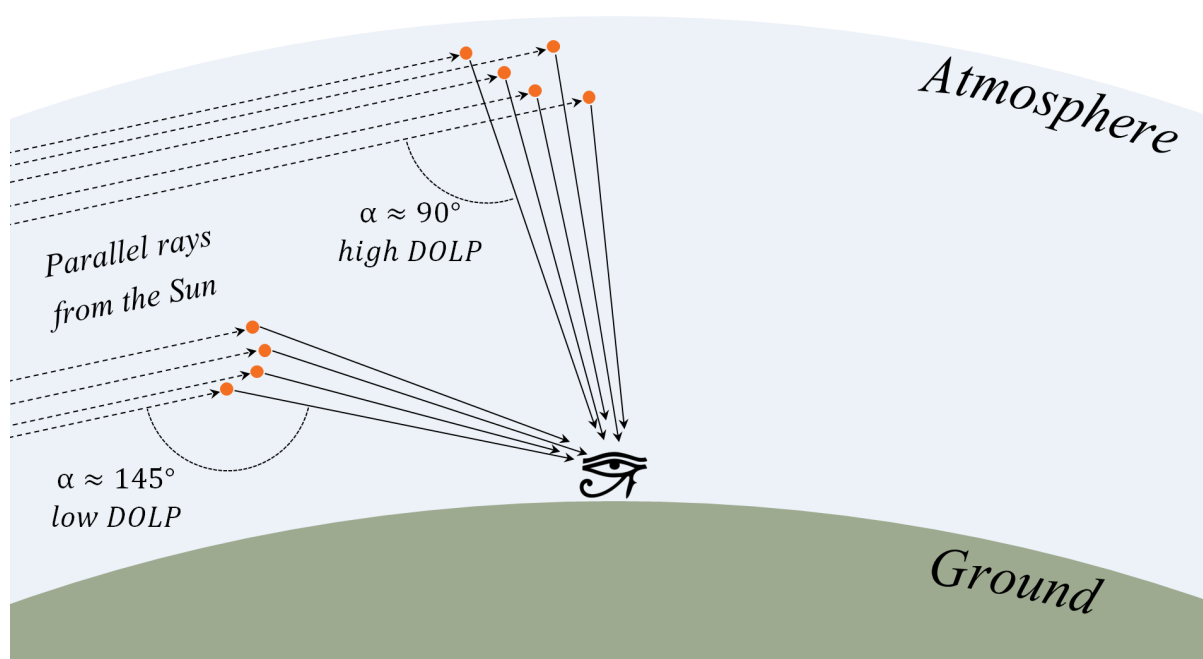


FIGURE 3.7: Because the Sun's rays are nearly parallel when they enter the Earth's atmosphere, there exist regions in the sky where many photons are scattered at an angle $\alpha \approx 90^\circ$, which creates very strong linear polarization along the line of sight toward those regions. This region of maximum polarization depends on the position of the Sun and it changes throughout the day and year. For example, at sunset and sunrise the sky near zenith is highly polarized.

The degree of polarization along a particular line of sight depends on the scattering angle, given by the relation in Eq. 3.9 (Figure 3.8). This pattern moves across the sky with the motion of the Sun, with the region of maximal polarization located in the direction $\approx 90^\circ$ away from the Sun and regions of minimal polarization in the solar and anti-solar direction ($\alpha = 0^\circ$ or 180°). Although Rayleigh scattering is an extremely efficient process for production of polarized light (100% efficient when $\alpha = 90^\circ$) the DOLP of the sky

is rarely above $\approx 80\%$. This is because a significant fraction of photons are scattered into the line of sight after several interactions. In general, multiple scattering events tend to reduce the maximum degree of polarization; however, sometimes these complex geometries can lead to unique phenomena, like production of circular polarization (need ref).

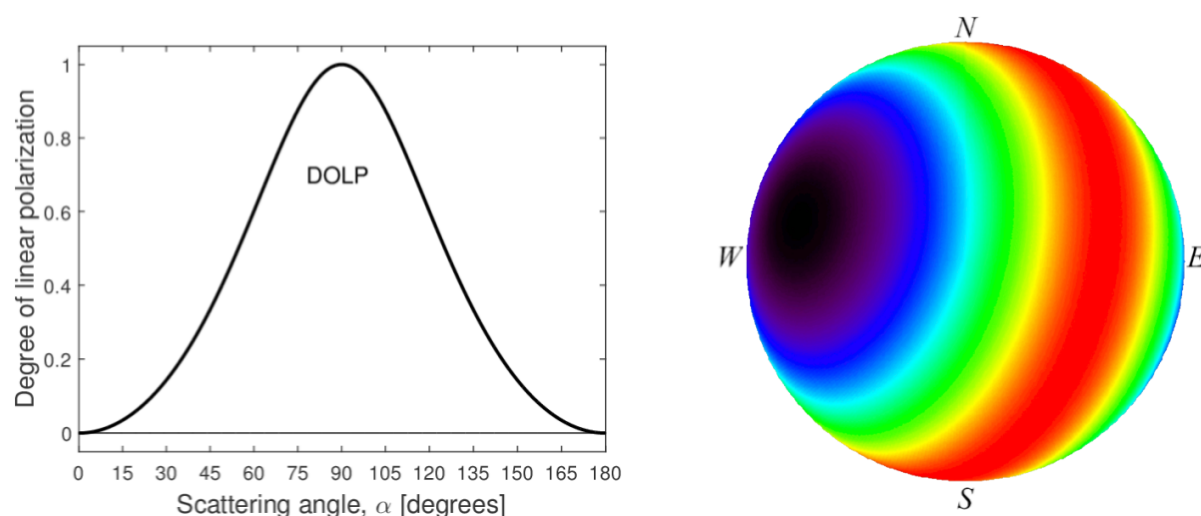


FIGURE 3.8: Rayleigh scattering produces primarily linearly polarized light, with the DOLP as a strong function of the scattering angle (*Left*). The DOLP is maximal for scattering angles near $\alpha = 90^\circ$, and minimal in the solar and anti-solar directions. In practice, multiple scattering in the atmosphere decreases the maximum observed DOLP to ~ 0.8 . The angle of linear polarization follows a circular pattern, centered on the Sun (*Right*).

3.2.2 Mie Scattering

The Rayleigh approximation (Eq. 3.8) is only accurate as long as the size of scattering particles is much smaller than the wavelength of light. When the size of the scatterers becomes comparable to the wavelength, a more precise solution of Maxwell's equation is needed to accurately describe the light-matter interaction. Mie theory provides a method for obtaining a solution to Maxwell's equations in the form of infinite series of spherical harmonic terms. In contrast to Rayleigh scattering, no generalized approximations (such as Eq. 3.8) exist in Mie scattering, because interactions in the Mie regime are highly

dependant on the wavelength of light and the specific scattering properties of the particles. Nevertheless, a few simple examples can be used to illustrate the importance of polarization in this regime.

The electric field of light scattered by a particle whose size is comparable to the wavelength of light can be calculated, using the formalism of [Hansen and Travis \(1974\)](#), from the electric field of the incident light and the scattering properties of the particle,

$$\begin{pmatrix} E_r^s \\ E_l^s \end{pmatrix} = \frac{e^{-ikR+ikz}}{ikR} \begin{pmatrix} S_1(\alpha, \phi) & S_4(\alpha, \phi) \\ S_3(\alpha, \phi) & S_2(\alpha, \phi) \end{pmatrix} \begin{pmatrix} E_r^i \\ E_l^i \end{pmatrix}. \quad (3.10)$$

Here, E_r^i and E_l^i are two orthogonal electric field components that describe the incident wave, which is propagating in the z direction with wave vector k and interacts with an object described by the scattering matrix, \mathbf{S} . The elements of \mathbf{S} are typically complex numbers, which depend on the scattering angle, α , and the azimuth angle, ϕ , which is measured about the direction of scatter. The electric field components of the scattered wave at a distance R are E_r^s and E_l^s . Often, one attempts to determine the scattering matrix, \mathbf{S} , by measuring the scattered field and assuming some form for the incident field.

In the case where the scattering particle is a homogeneous sphere, the scattering matrix has a simplified form,

$$\mathbf{S} = \begin{pmatrix} S_1(\alpha) & 0 \\ 0 & S_2(\alpha) \end{pmatrix},$$

and the matrix elements are given by two infinite series:

$$S_1 = \sum_{n=1}^{\infty} \frac{2n+1}{n(n+1)} [a_n \pi_n + b_n \tau_n]$$

$$S_2 = \sum_{n=1}^{\infty} \frac{2n+1}{n(n+1)} [b_n \pi_n + a_n \tau_n].$$

The coefficients π_n and τ_n are functions of only the scattering angle, α and have a simple relationship to the Legendre polynomials. Therefore, they can be easily calculated using

recursion relations; the first two terms (from Hansen and Travis (1974)) are,

$$\begin{aligned}\pi_1(\alpha) &= 1 & \tau_1(\alpha) &= \cos(\alpha) \\ \pi_2(\alpha) &= 3 \cos(\alpha) & \tau_2(\alpha) &= 3 \cos(2\alpha).\end{aligned}$$

The computation of the coefficients a_n and b_n is at the core of the Mie scattering problem. The coefficients a_n and b_n are functions of the complex refractive index, \mathbf{n} and the size parameter, $x = 2\pi r/\lambda$. The expressions for a_n and b_n involve spherical Bessel functions and can also be computed recursively. The considerations for appropriate numerical computation have been described by Dave (1969) and Bohren and Huffman (1983). Several numerical codes (like that of Wiscombe (1980)²) have been developed for this purpose.

The scattering of light by a homogeneous dielectric sphere with index of refraction $n = 1.5$ and diameter, $D = 1 \mu\text{m}$, for light with wavelength $0.5 \mu\text{m}$ and $1 \mu\text{m}$ is shown in Figure 3.9. The radiation pattern has a strong dependence on wavelength and the patterns for two orthogonal components of the electric field can be very different. Significant polarization will be observed along those lines of sight where the amplitude of the parallel and perpendicular components of the scattered electric field aren't equal. For example, strong polarization will be observed along 90° for $0.5 \mu\text{m}$ light and along 220° for $1 \mu\text{m}$ light (*Left* and *Right* panels of Figure 3.9, respectively).

The expected polarization for the two examples shown in Figure 3.9 is plotted in Figure 3.10. Here polarization is defined using the amplitudes of two orthogonal electric field components as follows,

$$P = \frac{|S_1|^2 - |S_2|^2}{|S_1|^2 + |S_2|^2},$$

where S_1 and S_2 are the elements of the scattering matrix in Eq. 3.10. In the case of a single scattering interaction, the polarization changes dramatically with the scattering angle. Multiple scattering tends to smooth out the extreme angular dependence of polarization and decrease the peak polarization. For example, multiple scattering in the thick

²At the time of writing in 2017, Scott Prahl maintains several Mie codes on this website at <http://omlc.org/software/mie/>, implemented in FORTRAN, C, and MATLAB, including that of Wiscombe (1980).

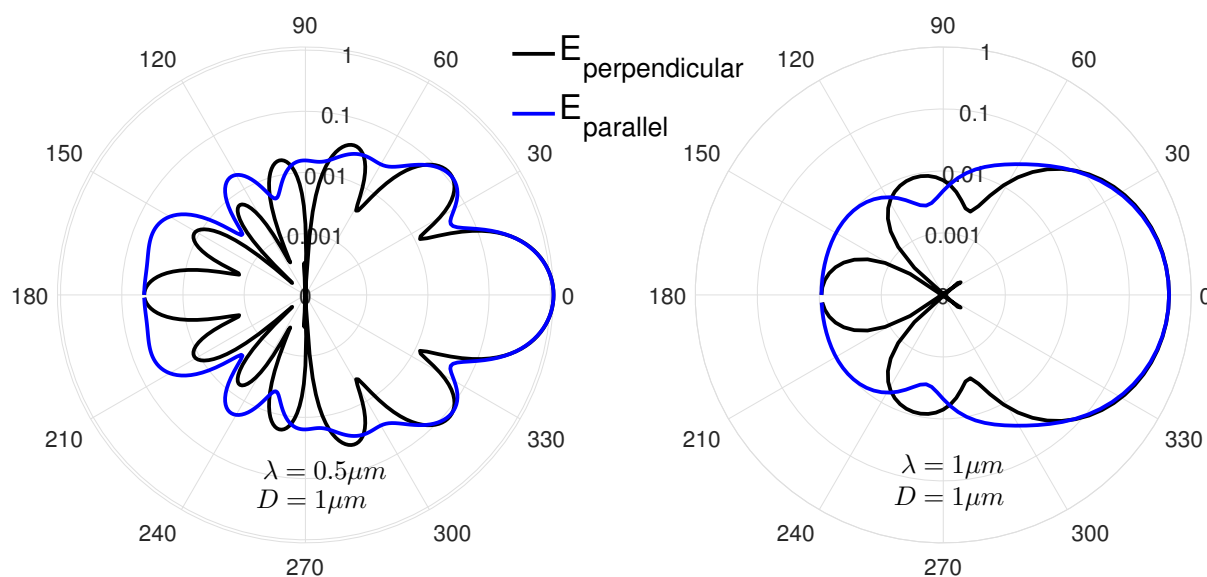


FIGURE 3.9: The radiation patterns for two orthogonal components of the electric field, for a wave scattered by a dielectric sphere with diameter of $1 \mu\text{m}$ can be very different. Here, the wave is incident from the left (180°) and the amplitude is shown on a logarithmic scale to emphasize the difference between the two components. The patterns also strongly depend on the wavelength of light. These patterns were calculated using Scott Prahl's convenient web-based Mie scattering calculator (http://omlc.org/calc/mie_calc.html).

Venereal clouds produces a peak polarization of -0.04 at scattering angle $\sim 40^\circ$ (Hansen and Hovenier, 1974)).

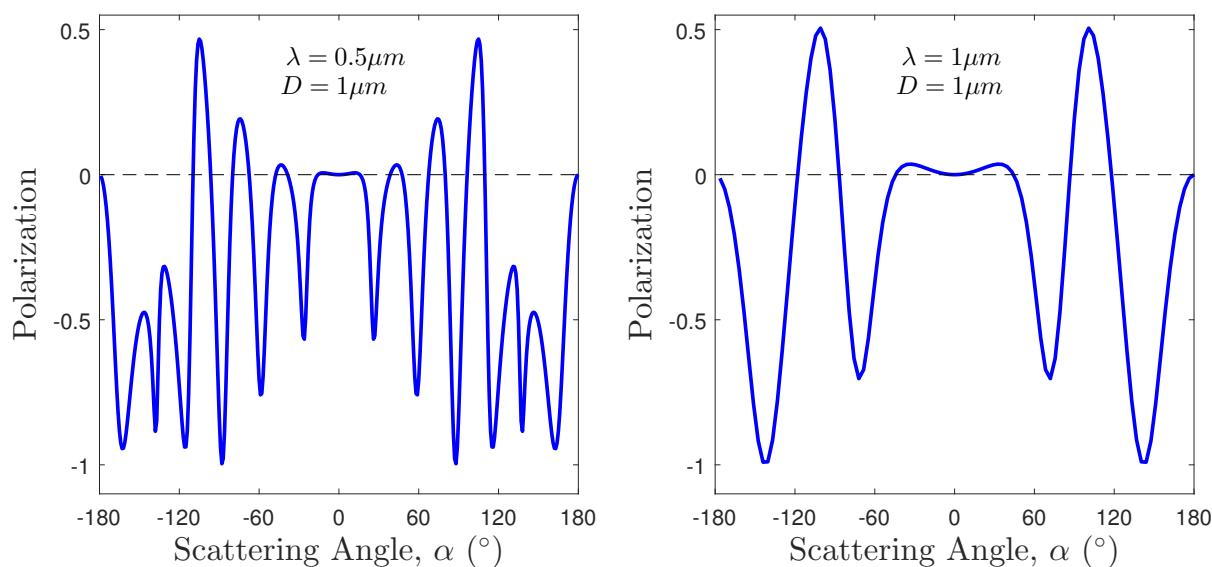


FIGURE 3.10: The polarization dependence on the scattering angle can be very complex for the case of a single scattering event and the exact pattern has a strong dependence on the wavelength of light, as well as the particle diameter.

3.3 Polarization from Anisotropic Materials

The production of polarized light requires some type of asymmetry. In the previous two sections, this asymmetry was created by the source of illumination and the reflecting or scattering surface. It shouldn't be surprising that the shape of the particles also plays an important role in the interaction of light and matter. In the scope of this work, the “dichroic” absorption of light (more accurately, *diattenuation*) is important in two contexts: the diattenuation of light by aligned non-spherical particles and man-made anisotropic materials, like the wire grid polarizer.

3.3.1 Diattenuation due to Aligned Asymmetric Particles

Non-spherical particles preferentially absorb electric field components parallel to the particle's “long” axis (Figure 3.11, *Left*). If these non-spherical particles are somewhat aligned, they will preferentially absorb photons of one polarization state and the transmitted light will be polarized in the orthogonal orientation.

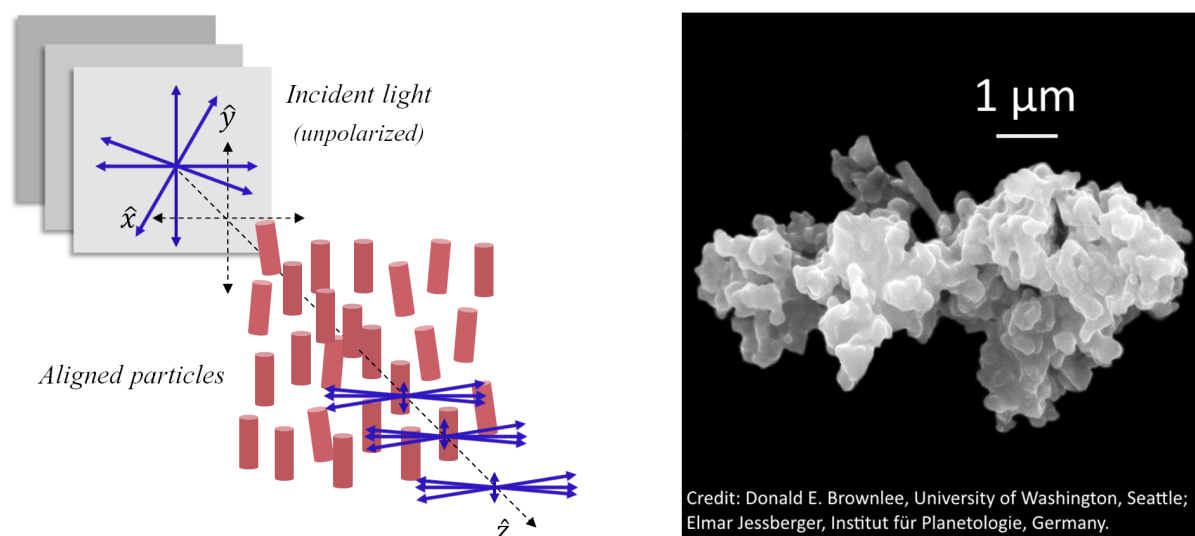


FIGURE 3.11: *Left*: Elongated dust grains preferentially absorb the electric field component parallel to their “long” axis. If there is a mechanism that aligns the dust grains, they can polarize the light from background objects. *Right*: Dust samples brought back to Earth from interplanetary space show strong evidence that these elongated dust grains exist throughout the Galaxy.

In contrast to the Rayleigh mechanism, this effect is seen along the line of sight towards the source of light. This effect was first seen in the polarization of stars in the Milky Way by [Hiltner \(1949\)](#), who correctly attributed it to diattenuation by elongated dust grains in interstellar space. Hiltner suggested that these dust grains could be aligned by a large scale Galactic magnetic field, the existence of which was hypothesized by Hannes Alfvén in 1937 ([Alfvén, 1937](#)). Hiltner's observations and hypothesis were supported by independent observations of [Hall \(1949\)](#).

Only two years later, [Davis and Greenstein \(1951\)](#) proposed a mechanism by which spinning elongated dust grains can be efficiently aligned by a large scale magnetic field. In short, paramagnetic absorption in the spinning dust grains generates a small nonconservative torque. This effective frictional force causes the dust grains to preferentially spin about their short axis, which ends up parallel to the magnetic field lines. The long axis of the grains, which is perpendicular to the magnetic field direction, preferentially absorbs electric field components to produce light which is polarized in the direction of the magnetic field.

Although there is still some debate regarding the details of the alignment mechanism, this effect is well measured for stars in the Milky Way. The fractional polarization due to anisotropic absorption ranges from $\sim 0.01\% - 5\%$, although polarization measurements $> 10\%$ have also been reported [Serkowski et al. \(1975\)](#). This mechanism produces polarization at all wavelengths in the visible range, but the maximal polarization typically occurs for red light. The presence of elongated dust grains in the Galaxy is further supported by dust samples retrieved from the solar system by the Stardust mission (Figure [3.11, Right](#)).

3.4 Intrinsically Polarized Sources

There are several mechanisms that produce light which is intrinsically polarized. Though less common than the scenarios described in the previous section, polarization is fundamental to these radiative mechanisms. The most significant of these is synchrotron radiation, which occurs naturally in several astrophysical sources and in synchrotrons on Earth.

3.4.1 Synchrotron Radiation

Electrons accelerated in circular orbits by strong magnetic fields radiate like dipoles (cyclotron radiation). When the electrons are relativistic ($v \sim c$), the radiation pattern becomes strongly beamed in the direction of motion (Figure 3.12). For electrons on instantaneous circular orbits, the radiated power as a function of frequency (integrated over the solid angle) is given by (Rybicki and Lightman, 1979),

$$P(\omega) = \frac{\sqrt{3}q^3 B \sin \alpha}{2\pi mc^2} F(\omega/\omega_c) \quad (3.11)$$

where,

$$F(\omega/\omega_c) \equiv \frac{\omega}{\omega_c} \int_{\frac{\omega}{\omega_c}}^{\infty} K_{\frac{5}{3}}(\xi) d\xi$$

and

ω : gyration frequency

ω_c : critical frequency

K : modified Bessel function

q : particle charge

B : magnetic field strength

α : cone opening angle

m : particle mass

c : speed of light

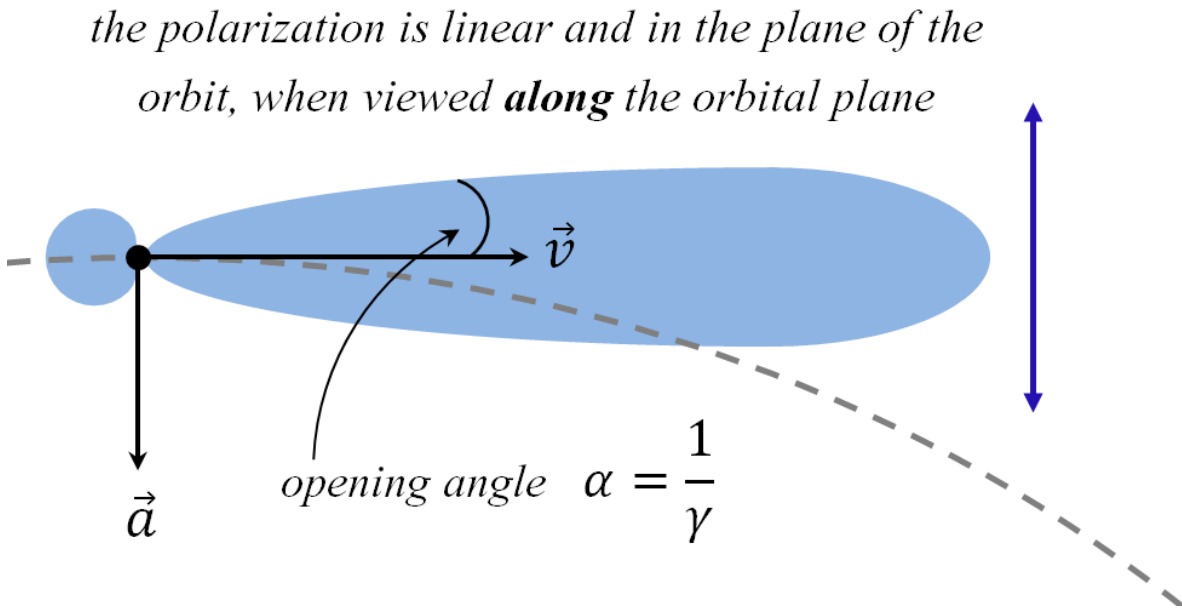


FIGURE 3.12: Relativistic charged particles that are accelerated into circular orbits by magnetic fields emit synchrotron radiation. The polarization of this light depends strongly on the direction of radiation; for example, light emitted in the plane of the orbit is linearly polarized in that plane.

To look at the polarization of synchrotron radiation, it's useful to separate the power into orthogonal components with respect to the particle's orbital plane. The perpendicular and parallel components are given by,

$$P_{\perp}(\omega) = \frac{\sqrt{3}q^3 B \sin \alpha}{2\pi mc^2} \left[F(\omega/\omega_c) + G(\omega/\omega_c) \right] \quad (3.12)$$

$$P_{\parallel}(\omega) = \frac{\sqrt{3}q^3 B \sin \alpha}{2\pi mc^2} \left[F(\omega/\omega_c) - G(\omega/\omega_c) \right] \quad (3.13)$$

with,

$$G(\omega/\omega_c) \equiv \frac{\omega}{\omega_c} K_{\frac{2}{3}}(\omega/\omega_c).$$

We can now define the degree of polarization (as a function of frequency) as follows,

$$p(\omega) = \frac{P_{\perp}(\omega) - P_{\parallel}(\omega)}{P_{\perp}(\omega) + P_{\parallel}(\omega)} = \frac{G(\omega/\omega_c)}{F(\omega/\omega_c)}.$$

The functions F , G , and the polarization, $p(\omega)$ are shown in Figure 3.13. Note that F and G decrease asymptotically as a function of frequency, which causes the polarization to approach $p = 1$. In practice, an object emitting synchrotron light will have a distribution

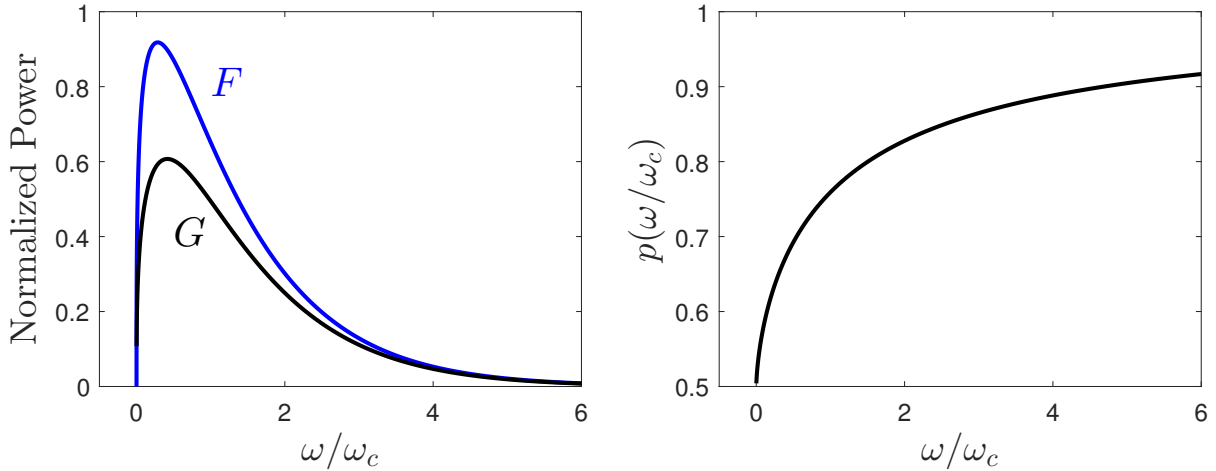


FIGURE 3.13: Relativistic charged particles that are accelerated into helical orbits by magnetic fields emit synchrotron radiation. The polarization of this light depends strongly on the direction of radiation; for example, light emitted in the plane of the instantaneous circular orbit is linearly polarized in that plane.

of electrons, gyrating with a broad range of frequencies. To estimate the polarization that we would measure, we must integrate F and G over all frequencies,

$$\bar{p} = \frac{\int_0^\infty G(\eta) d\eta}{\int_0^\infty F(\eta) d\eta} \approx 0.75.$$

This is the maximum fractional polarization we should expect to measure for a typical synchrotron source; however, such high polarization can only be practically observed for structures with very uniform magnetic fields. If the magnetic fields (and the resulting electron orbits) are twisted, polarization components measured along the line of sight will tend to average out through superposition, which decreases the measured fractional polarization. A similar averaging occurs due to finite spatial resolution of telescopes.

Nevertheless, large fractional polarizations have been measured for galactic and extragalactic synchrotron sources. In 1954, V. A. Dombrovsky, of Byurakan Observatory, reported the first measurement of strong polarization in the Crab Nebula. A year earlier, I. S. Shklovsky suggested that the Crab could be powered by the synchrotron mechanism and that polarization should be expected. The polarization measurement was confirmed and expanded by Baade (1956a), Oort and Walraven (1956), and Hiltner (1957). The magnetic fields in the Crab Nebula are produced by the Crab Pulsar, which was the first pulsar to be associated with a supernova remnant (Reifenstein et al., 1969).

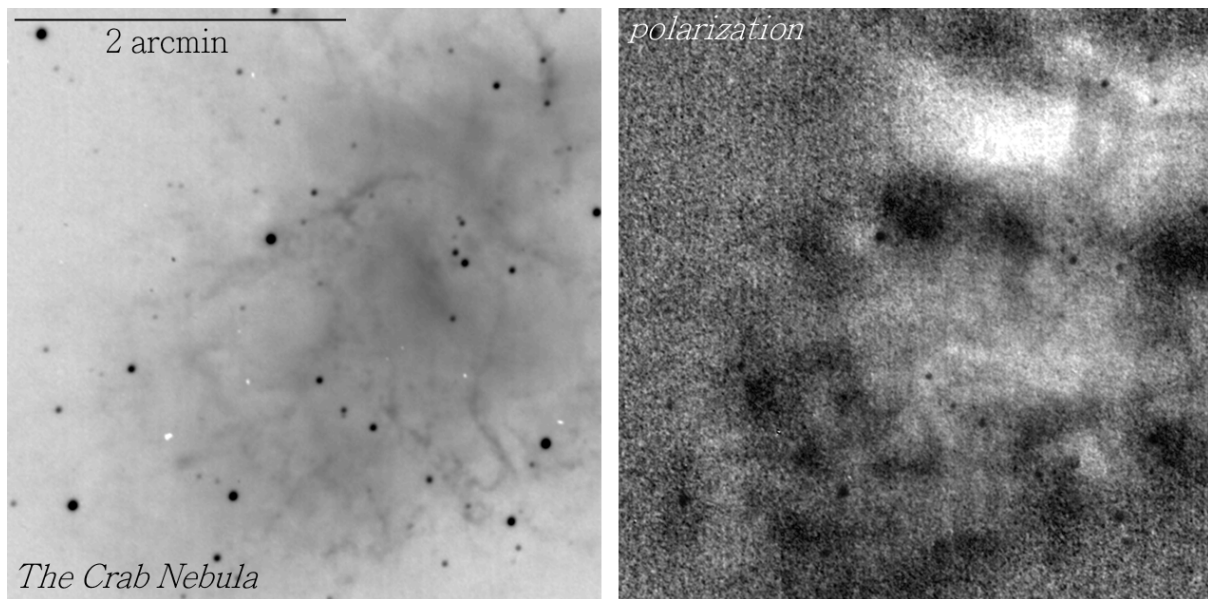


FIGURE 3.14: *Left:* The Crab Nebula is a large remnant of a supernova that was observed in 1054 CE. This is a map of the flux in the visible V band. *Right:* The Crab Nebula shows a strong and complex polarization pattern (white corresponds to large polarization), with peak fractional polarization of $\sim 30\%$. Observations of D. Vorobiev, made using the SMARTS 0.9 m telescope at Cerro Tololo Inter-American Observatory.

Once the connection between astronomical synchrotron sources and polarization was made in the Crab Nebula, it was suggested that the jet in the active galaxy Messier 87 may be another example of synchrotron radiation. The polarization of M87's jet was first reported by Baade (1956b), who estimated that the fractional polarization reached $\sim 30\%$. More recently, Perlman et al. (1999) studied the M87 jet using high resolution polarimetry performed with the *Hubble Space Telescope* in the visible range and the *Very Large Array* at 15 GHz. The jet contains several “knots” that show polarization of $\sim 30\%$ - 40%, which suggests a very ordered magnetic field in these regions. Spatially-resolved polarimetry in the optical and radio bands is one of the few tools available to astronomers to map the magnetic field structure of distant sources.

3.4.2 Lasers

Many lasers produce highly polarized light. In some cases, this is due to the presence of polarization-dependent optics in the amplifier of the resonator. For example, the discharge tube of many gas lasers is terminated by Brewster windows (Figure 3.15), which have very low reflection losses for the parallel polarization states (see Figure 3.2). Because the laser light bounces around in the resonator many times before escaping through the partially transparent mirror, only the photons with parallel polarization survive. In these lasers, all modes have the same polarization.

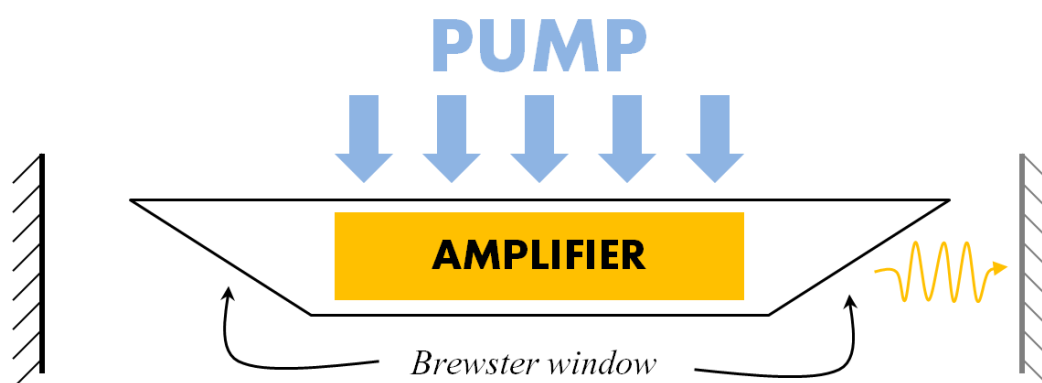


FIGURE 3.15: Some lasers use Brewster windows, due to their extremely low reflectivity for the parallel polarization states. Only these states remain long enough to escape the resonator cavity and all modes of these lasers have the same polarization.

In some lasers, the gain mechanism itself is polarization dependent. Some laser crystals, like Nd:YVO₄ and Nd:YLF are naturally birefringent. For example, Nd:YVO₄ has a tetrahedral lattice, with one short axis (the c-axis). Typically, the crystal is cut such that the rod's axis is orthogonal to the c-axis (Figure 3.16). The absorption (and gain) is highest for light polarized along the c-axis.

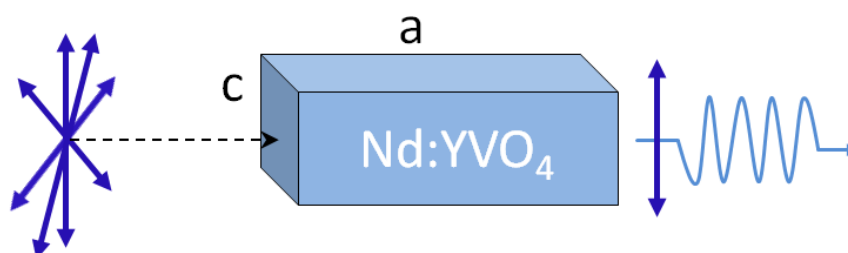


FIGURE 3.16: Some laser crystals are anisotropic and show higher gain for certain polarization states.

3.5 Polarizers

Devices that create polarized light (from a randomly polarized source) can be broken down into three categories: prisms based on birefringent crystals, anisotropic materials that use diattenuation to only transmit one polarization state, and non-birefringent dielectrics that use Brewster's angle to produce polarized light. Whereas the first two types of polarizers produce highly polarized light with high overall throughput, the glass plate is rarely used in polarimeters. Instead, it is a very powerful method of producing polarized light with an arbitrary degree of linear polarization, from 0 at normal incidence to 1 at Brewster's angle (Figure 3.3).

3.5.1 Polarizing Prisms

The first high quality polarizers for visible and infrared light were created using combinations of birefringent crystals like calcite and quartz. Because these crystals are anisotropic, orthogonal polarization states of the incident beam take different paths through the crystal and physically separate. A single birefringent crystal already performs this function, however the amount of divergence between the beams is small. To make these polarizers more useful, several crystals are aligned in various configurations to increase the separation of the outgoing beams (Nicol prism, Wollaston prism, Rochon prism, Glan-Focault prism), increase the acceptance angle (Glan-Thompson prism), create parallel outgoing beams (Savart plate), or allow use with very intense beams (Glan-Taylor, Glan-laser) (Figure 3.17). A great advantage of polarizing beam-splitters is that both polarization states can be used; however, when used in a polarimeter two separate images must be formed and analyzed.

3.5.2 Polarizers Based On Diattenuation

The second important class of polarizers are devices that use diattenuation to transmit light of only 1 polarization state, while absorbing or reflecting the orthogonal state; usually this is accomplished by creating an asymmetry in the material. Today, there are

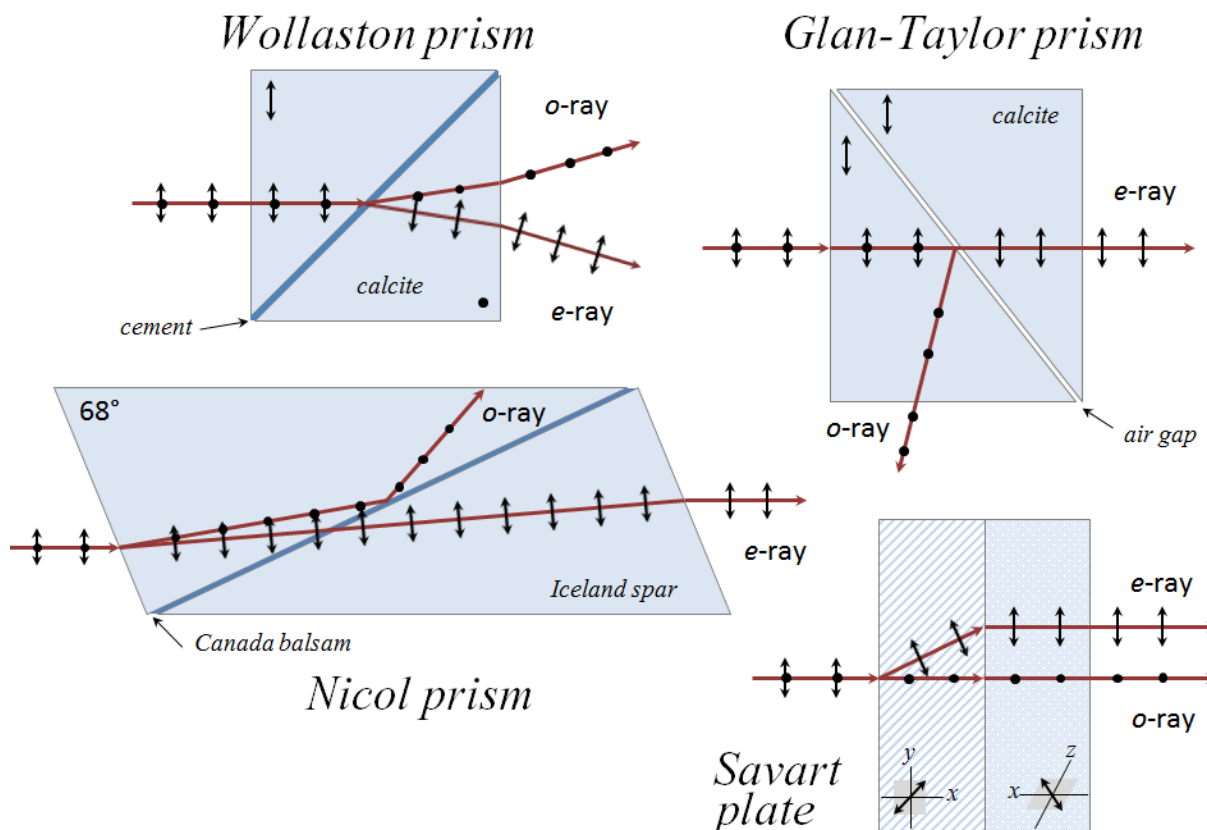


FIGURE 3.17: Many polarizing prisms have been invented by exploiting birefringent crystals and polarization upon reflection of dielectric materials. Most polarizing prisms produce highly polarized light, across a broad wavelength range.

two kinds of polarizers that use diattenuation. The Polaroid-type polarizers absorb the unwanted state, while the wire grid polarizer reflects the unwanted light. In this section, I briefly describe the absorptive Polaroid-type filters; the wire grid polarizer is discussed in great detail in the next chapter.

3.5.2.1 Absorptive Polarizers

The Polaroid filters developed by E. H. Land were the first high efficiency polarizers not based on prisms. The first polarizers, known as *J-Sheet*, were made of nitrocellulose film doped with aligned iodoquinine sulphate crystals. The crystals were dichroic and preferentially absorbed electric field components parallel to their long axis. Land later improved the Polaroid filters with the *H-Sheet*, which was made with polyvinyl alcohol polymers doped with iodine. The iodine made the polymer chains conductive, and the chains were aligned by stretching the sheet.

Chapter 4

The Wire Grid Polarizer

A wire grid polarizer consists of an array of parallel, thin, closely spaced, conducting “wires”; usually, the wire material is a metal, such as aluminum or gold (Figure 4.1). As the incident wave impinges on the wire grid, the electric field can be decomposed into components parallel and perpendicular to the metal wires. The electric field components parallel to the wires interact with the electrons in the metal and drive them to oscillate along the wires. As a result, two processes occur. As the electrons travel through the metal wire, they collide with the lattice atoms and heat is generated in the wires. Thus, energy is transferred from the electric field into heating the grid. The accelerated electrons also radiate in the forward and backward directions. The re-radiated forward-propagating wave cancels with the original incident forward-traveling wave via superposition and the re-radiated backward-propagating field appears as the reflected wave. In this fashion, the component of the field parallel to the wires is not allowed to pass through the wire grid. Conversely, the electric field perpendicular to the wires cannot accelerate the electrons a long enough distance for them to become efficient radiators and the electric field passes through the grid essentially unaltered.

Modern wire grid polarizers are fabricated using photolithography to create “wires” as thin as ~ 74 nm (Figure 4.2). These devices are very important because they operate over a large range of wavelengths and incidence angles (Figure 4.3). The operation range is typically limited by the transmission of the substrate on which the wires are fabricated. As such, wire grid polarizers can be easily fabricated for operation in the visible and

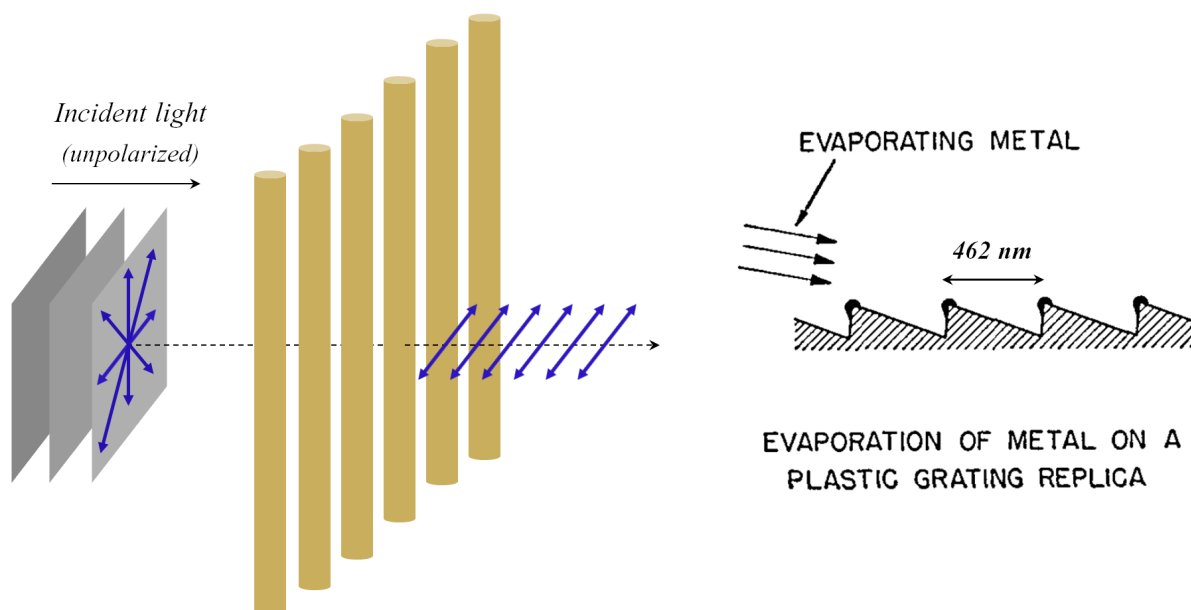


FIGURE 4.1: *Left:* A wire grid polarizer is fabricated by aligning thin conducting wires, which preferentially absorb the electric field components parallel to the wire orientation. The wire width and spacing needs to be smaller than the wavelength of light for the polarizer to be efficient at blocking the unwanted polarization states. *Right:* In 1960, a wire grid polarizer for the near-infrared regime was fabricated by evaporating metal onto the ridges of a blazed diffraction grating.

near-infrared regimes on sapphire substrates ($0.4\ \mu\text{m}$ - $5.0\ \mu\text{m}$) or on silicon for use in the infrared wavelengths ($1\ \mu\text{m}$ - $10\ \mu\text{m}$).

Wire grid polarizers, like other kinds of polarizers, are the heart of polarimeters - instruments used to measure polarization of light (see Chapter 6). Wire grid polarizers are also the fundamental building block of micropolarizer arrays (see Chapter 5), which can be used to construct a specific kind of polarimeter, based on the division-of-focal plane measurement technique. The design, fabrication, and evaluation of these polarimeters is the focus of this dissertation.

Although I am primarily concerned with the performance of micropolarizer arrays (ie pixelated wire grid polarizers), I use this chapter to present 2D and 3D models of non-pixelated wire grid polarizers for two reasons. First, the wire grid polarizer is the basis for micropolarizer arrays and an interesting sub-wavelength optical device in its own right. Second, these relatively simple devices provide a good example to introduce the simulation methods used in this work and point out some of the nuances of high resolution simulations.

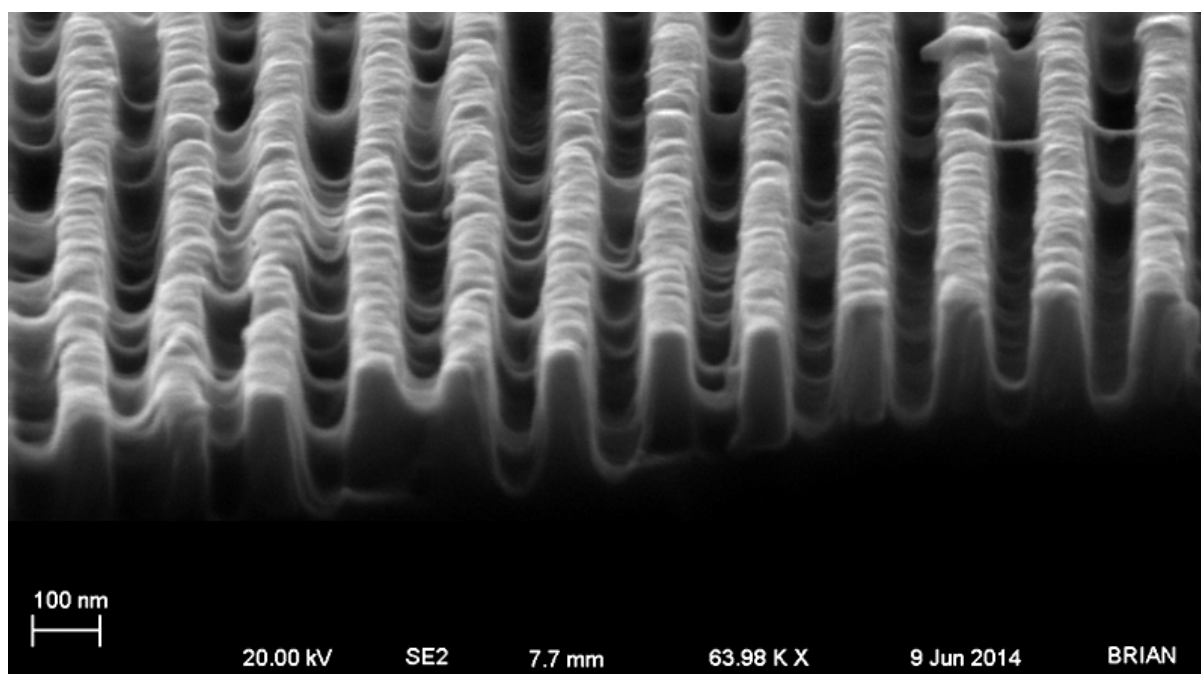


FIGURE 4.2: Modern wire grid polarizers are typically made with aluminum wires ~ 74 nm wide and ~ 200 nm tall. This scanning electron micrograph shows the cross-section of a single pixel of a pixelated wire grid polarizer.

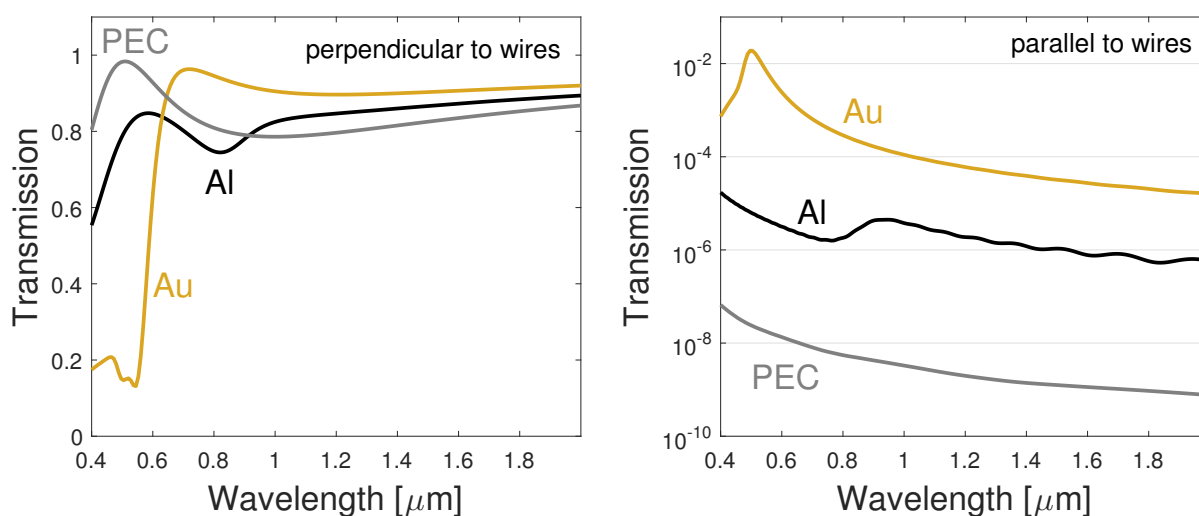


FIGURE 4.3: Simulated broadband performance of a modern wire grid polarizers, made from aluminum (Al), gold (Au), and a perfect electrical conductor (PEC). These polarizers are very efficient at transmitting the polarization states perpendicular to the wire direction (*Left*), and blocking the state parallel the wire direction (*Right*). These curves (especially the transmission of the desired state) show that the polarizer reaches optimum performance when the wavelength of light becomes about $10\times$ larger than the wire width, at $\lambda \approx 1\mu\text{m}$.

4.1 Simulations of Wire Grid Polarizer Performance

Several groups have attempted to simulate wire grid polarizers, to better understand the effects of polarizer design and fabrication defects on the polarizer's performance. To efficiently reject the unwanted polarization states, wire grid polarizers must be fabricated with highly conductive wires whose width is smaller than the wavelengths of interest. For example, the current generation of wire grid polarizers designed for use in the visible regime use wires with a width of ~ 74 nm. Such small features, as well as the large magnitude of the complex refractive index of metals, require a very fine mesh to accurately model the structure, resulting in calculations which require significant memory and computing resources.

To circumvent the problems associated with large simulations, wire grid polarizers (and other sub-wavelength structures) are often modeled in 2D using finite-difference time domain (FDTD) schemes or rigorous coupled wave analysis (RCWA). For example, [Lin et al. \(2016\)](#) use 2D RCWA simulations to predict the performance of a wire grid polarizer on a glass substrate with 125 nm-wide wires and investigate the effects of varying the thickness (or "height") of the wires. Similarly, [Raisanen et al. \(2012\)](#) investigate the effect of wire width and spacing ("pitch") using 2D finite element simulations.

These 2D simulations are useful to study general trends associated with wire shape and polarizer performance, and their results generally agree: polarizers that use thinner and taller wires are predicted to have better performance. However, it's not obvious how well these simulations represent the structures that are actually fabricated. For example, nearly all simulations (even ones presented in this work) use perfectly rectangular, straight, identical wires, which is not what real polarizers look like (see [Figure 4.2](#)). Noting that most simulations predict much better performance than that of actual devices, and that fabricated polarizer wires rarely show sharp corners, [Mélen et al. \(2015\)](#) model the wires as trapezoids, using the 2D RCWA method. Their models show that the slope of the wire "walls" has a significant effect on the polarizer performance. [Ryu et al. \(2008\)](#) push the 2D RCWA technique to its extreme, by simulating a repeating pattern of non-uniform "jagged" wires. Their simulations show that the modeled surface roughness tends to decrease the polarizer transmission.

The 2D simulations described above study various aspects of wire design (width, height, spacing, and shape profile) using a variety of techniques. However, no one has yet performed a systematic analysis of these parameters using a consistent methodology. Furthermore, these 2D studies ignore the finite length of the wires. It's plausible that the wires can be treated as having infinite length; however, to our knowledge, no one has validated this assumption with 3D models. Similarly, errors associated with numerical accuracy and resolution are rarely discussed in the existing literature.

We performed high resolution 2D and 3D FDTD simulations of non-pixelated wire grid polarizers to determine the appropriate mesh resolution for each case and to see how the 2D models compare with the full 3D solution. This chapter describes a rigorous suite of simulations of wire grid polarizers, with a special emphasis on numerical accuracy.

4.1.1 Simulation Methods

Our simulations of wire grid polarizers were carried out using the FDTD Solutions software from Lumerical. The simulations use the finite-difference time-domain scheme to solve Maxwell's equations in 3D. Because the aluminum wires that make up the polarizers have a width of ~ 74 nm and the source wavelengths are in the visible range (~ 400 nm - 2000 nm), we paid special attention to numerical accuracy and performed extensive convergence testing.

Spatial Resolution

Through extensive convergence testing, we found that a spatial resolution of ~ 5 nm provided sufficient numerical accuracy, without requiring an insurmountable amount of computing resources.

Boundary Conditions

The simulations used periodic boundary conditions in the X and Y directions and perfectly matched layer (PML) absorbing boundaries in the Z direction (direction of light propagation). We found that the PML boundaries reflect light at a level of 1 part in

10^6 . Reflections from the PML become the most significant factor limiting numerical convergence below a resolution of ~ 4 nm.

Light Source

The simulations used a planar light source with spectral range of 400 nm - 1000 nm or 400 nm - 2000 nm, depending on the simulation. The pulse width was ~ 2.66 fs. Each structure is simulated twice, using a source with TE polarization and TM polarization. In the TE mode, the electric field is perpendicular to the wires and the light is mostly transmitted by the polarizer. Conversely, in the TM mode the electric field is parallel to the wires and the light is mostly rejected (reflected) by the polarizer.

4.1.2 2D Simulations - Setup and Convergence Testing

We simulated conventional wire grid polarizers in 2D by constructing a single rectangular aluminum wire on a SiO_2 substrate (Figure 4.4). The simulated region uses periodic boundary conditions in the $\pm\hat{x}$ directions and absorbing PML boundaries in the $\pm\hat{y}$ directions. The effective simulated structure is an infinite series of rectangular aluminum wires extending in the $\pm\hat{x}$ directions. A polarized light pulse is propagated in the $-\hat{y}$ direction (from the top, down); two simulations are performed to propagate pulses polarized along the polarizer's axis and orthogonal to the polarizer's axis. The transmitted and reflected components are measured $5\ \mu\text{m}$ and $3\ \mu\text{m}$ below and above the polarizer, respectively.

4.1.2.1 Testing Numerical Convergence in 2D

Numerical schemes to efficiently solve Maxwell's equations for waves interacting with complex geometries, such as FDTD, are vulnerable to many sources of computational errors. More troubling, it is often impossible to accurately quantify the error associated with a calculation because an exact analytic solution is unavailable for comparison. To determine the accuracy of our calculations, we performed rigorous testing of various simulation parameters to look for numerical convergence of the results. We compare the

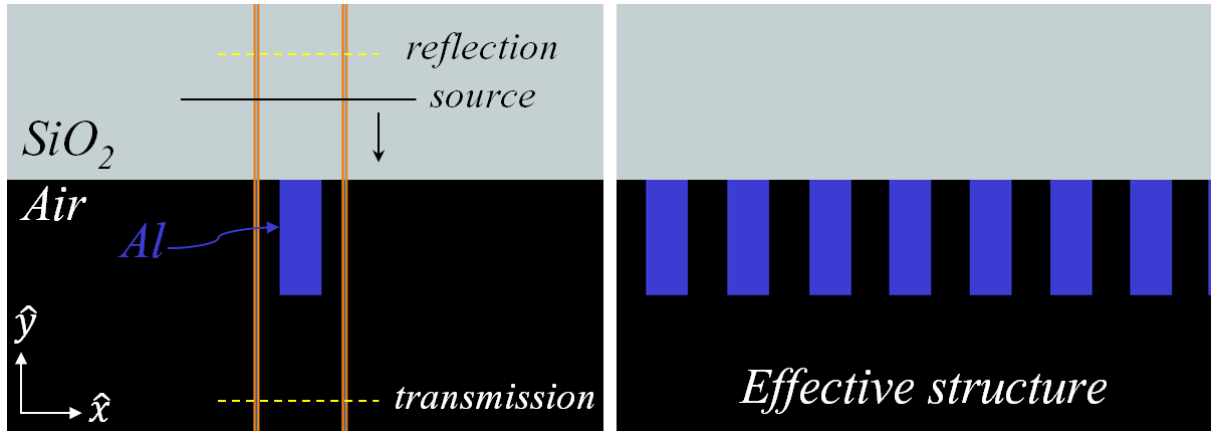


FIGURE 4.4: Left: A conventional wire grid polarizer was simulated in 2D by modeling an aluminum wire with a rectangular cross-section on an SiO_2 substrate. The light source originates inside the glass substrate $\sim 2\ \mu\text{m}$ above the wire. The reflected and transmitted components are measured $3\ \mu\text{m}$ and $5\ \mu\text{m}$ above and below the polarizer, respectively. The simulation uses periodic boundary conditions (orange vertical lines) in the $\pm\hat{x}$ directions, resulting in an infinitely repeating array of wires (Right).

results from successive simulations that use increasing amounts of computing resources to more exactly model the structures we’re interested in. We quantify the relative error, dS , of each simulation by determining how much it differs from a slightly less accurate simulation as follows,

$$dS(i) = \sqrt{\frac{\int (s_i - s_{i-1})^2 d\lambda}{\int \frac{1}{2}(s_i + s_{i-1})^2 d\lambda}} \quad (4.1)$$

Most often, FDTD simulations are limited by the size of the smallest mesh element used to resolve the structure (Figure 4.5). In general, simulations that use shorter wavelengths of light and materials with a higher refractive index require a finer mesh. We simulated a single aluminum wire on a glass substrate using a several meshes and varied the smallest cell size from $\sim 13.7\ \text{nm}$ to $\sim 2.4\ \text{nm}$. The effect of mesh size on the geometry that is actually simulated can be seen by studying the refractive index of the simulated structures (Figure 4.6). When the mesh is too coarse, structures appear “fuzzy”, totally lacking sharp boundaries. Indeed, even the position of objects becomes uncertain, as evidenced by the wire embedded in the SiO_2 substrate in the simulation using a $13.6\ \mu\text{m}$ or $7.8\ \mu\text{m}$ mesh.

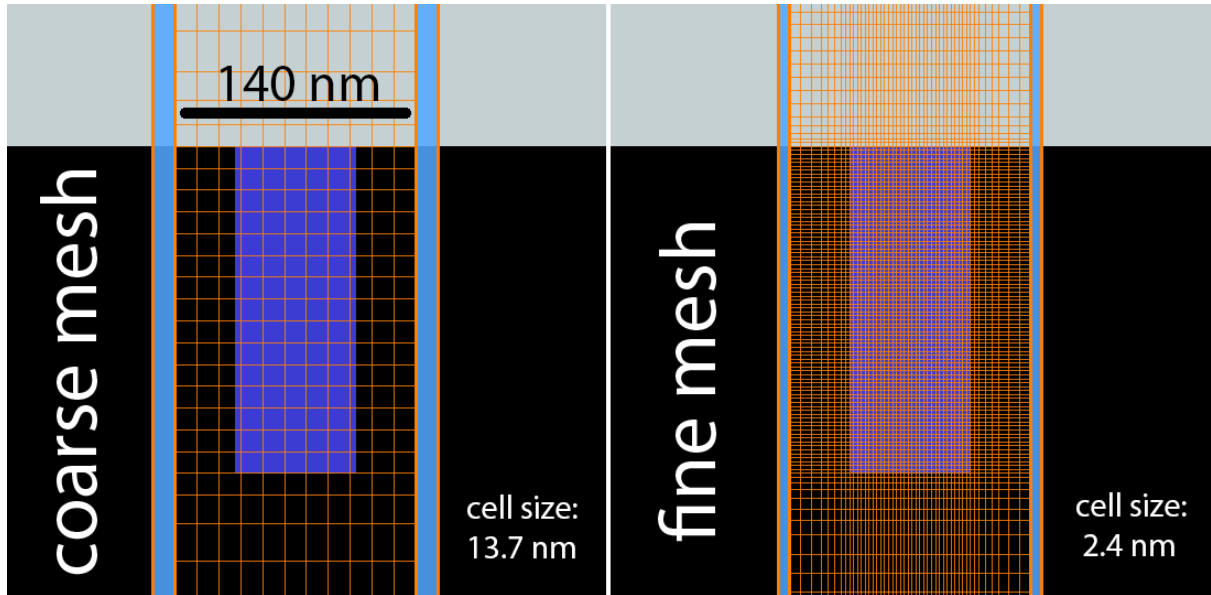


FIGURE 4.5: We simulated structures using a wide range of mesh sizes, to determine when the structures were sufficiently resolved. We found that in 2D, simulations began to numerically converge when the simulation mesh was smaller than 4 nm.

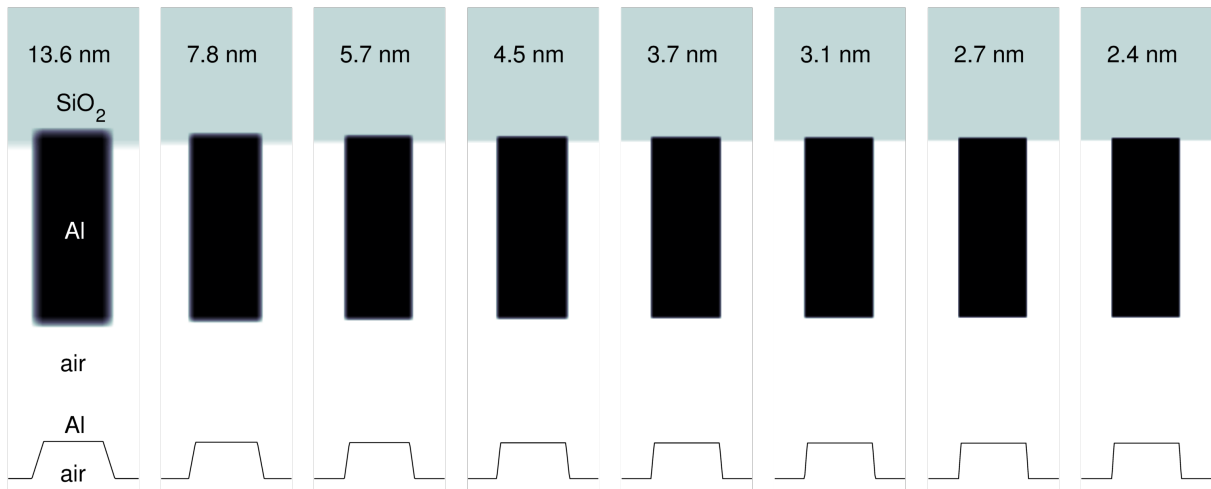


FIGURE 4.6: The size of the smallest mesh cell determines how well the simulation reproduces the desired geometry. This effect can be seen in refractive index map of the simulated structures. Plots along the bottom of the figure show the profile of the refractive index of each wire.

To quantify convergence, we calculated the relative error, dS (Eq. 4.1), for the transmitted TE and TM components (Figure 4.7, Right). We found that simulations began to converge when the mesh size was ~ 4 nm, for both TE and TM components. Results for simulations with a ~ 3.7 nm mesh were similar to those with a ~ 4.5 nm mesh at the 3% and 0.2% level, for the TM and TE modes, respectively. This convergence can also be seen in the distribution of the electric field intensity (Figure 4.8).

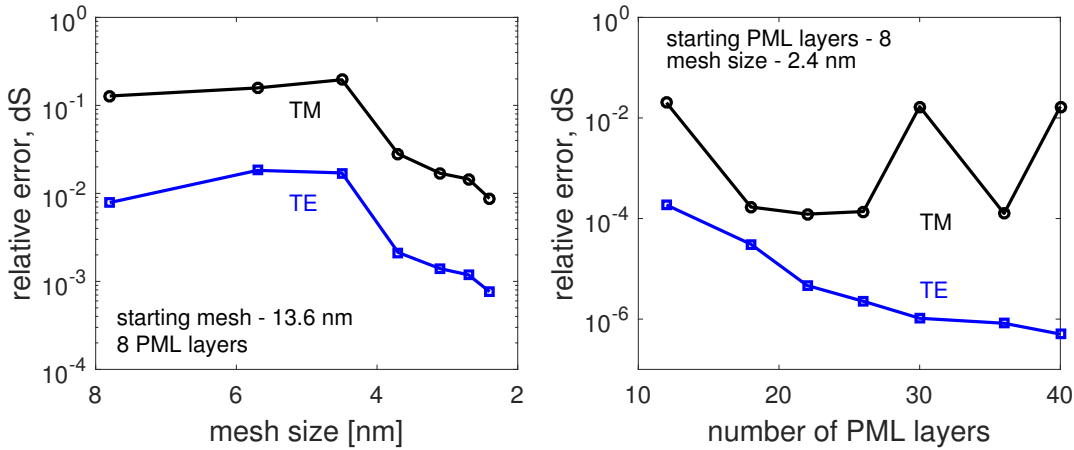


FIGURE 4.7: *Left*: Our 2D simulations began to numerically converge when the mesh was smaller than 4 nm. *Right* Increasing the number of PML layers was effective at improving the estimation of the transmitted TE component (the state transmitted by the polarizer), but not of the TM component (the state reflected by the polarizer).

Another important source of numerical errors in these simulations is the reflections from the perfectly matched layer (PML) boundary, which isn't exactly perfectly absorbing. To test the effect of the PML reflections, we performed simulations similar to those we used to test the mesh size. To minimize the effects of the mesh, we used a very fine mesh with a size of 2.4 nm and varied the number of PML layers from 8 to 40 (Figure 4.7, Left). We found that the transmitted component of the TE polarization (the component transmitted by the polarizer) is affected by the PML, whereas the TM component (which is supposed to be blocked by the polarizer) appears to be limited by some other mechanism. For example, the mesh requirements to properly model the TM and TE modes may be different, as the reflection of the TM component involves the re-radiation of light. This process may be more sensitive to errors that arise with the varying resolution of the adaptive mesh.

Summary After extensive testing, we found that 2D simulations (that span the 400 nm - 2000 nm range) begin to converge when the mesh size is ~ 4 nm. At this resolution, reflections from the PML boundaries begin to become important sources of numerical error for the (transmitted) TE states. For the 2D simulations presented in the rest of this

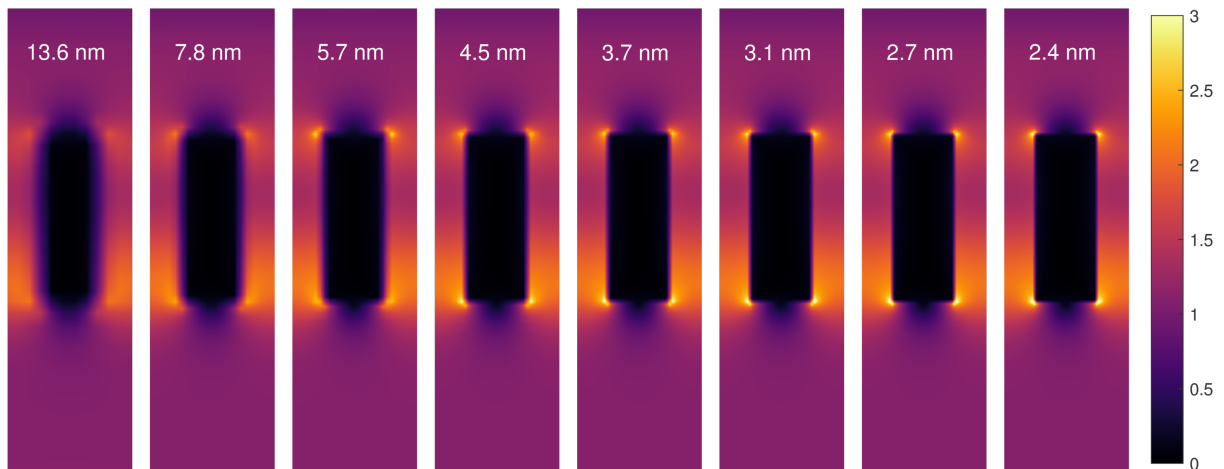


FIGURE 4.8: The numerical convergence of simulations can also be seen in the distribution of the amplitude of the electric field. This figure shows the electric fields for a TE pulse (which is mostly transmitted by the polarizer). High resolution simulations are required to model very localized regions of high electric field intensity (though this may not represent fabricated structures, if they lack similar definition).

work, we used a mesh size of ~ 2.4 nm and 40 layers in the PML boundary, even though the increase in simulation accuracy is marginal.

4.1.3 2D Simulations - Effects of Wire Shape and Spacing

The performance of a wire grid polarizer depends on the ability of the wires to efficiently absorb and re-radiate the incident light. This efficiency is largely dictated by the shape, spacing, and material properties of the wires. Many important wire shape parameters that have to do with the wire profile (or “cross-section”) can be studied in 2D and there is a growing body of work concerned with these effects (Lin et al., 2016; Mélen et al., 2015; Jourlin et al., 2014; George et al., 2013; Ryu et al., 2008). We studied the effects of wire shape in 2D on the performance of the wire grid polarizer, by modeling the transmission and reflection of TE and TM polarized light, and the electric field distribution, for a variety of designs.

4.1.3.1 Effects of Wire Width

Wire grid polarizers begin to work well when the size and spacing of the wires is much smaller than the wavelength of light. To study the effects of wire width on the performance of wire grid polarizers, we simulated polarizers with widths of 50 nm, 60 nm, 70 nm, 80 nm, 90 nm, 100 nm, 125 nm, 150 nm, 175 nm and 200 nm. The width of the air gap was set equal to the wire width, i.e., a 50% duty cycle. The height of the wires was 200 nm.

Several trends can be seen in the simulations. First, polarizers with thin wires transmit more of the desired state across all wavelengths (Figure 4.9, Left), even though the duty cycle remains fixed at 50%. As the wire width begins to increase, the amount of transmitted light decreases and the reflection of the TE component increases (Figure 4.9, Right). Second, simulations with wire widths >100 nm (solid black line) begin to show resonant behavior in the visible regime, as evidenced by the low transmission and high reflection of the TE components. This behavior coincides with the growth of high electric field intensity regions around the ribs (corners) of the wires (Figure 4.10) for simulations with widths of 150 nm, 175 nm and 200 nm. The polarizer’s ability to reflect/reject the TM state also decreases with increasing wire width (Figure 4.12). Again, several trends emerge. First, polarizers with thinner wires transmit more light at all wavelengths (Figure 4.11, Left). Second, for most wire widths the ability to reject the TM state

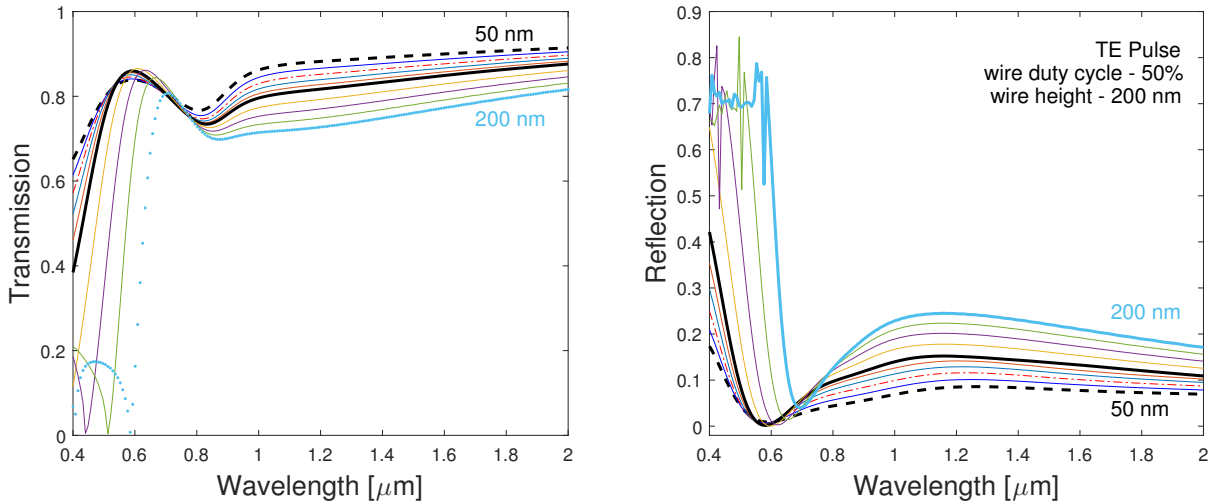


FIGURE 4.9: Left: Transmission of the TE component for a wire grid polarizer with wire widths of 50 nm, 60 nm, 70 nm, 80 nm, 90 nm, 100 nm, 125 nm, 150 nm, 175 nm and 200 nm, with duty cycle and wire height fixed at 50% and 200 nm, respectively. In general, wire grids with thinner wires exhibit higher transmission at all wavelengths. Wires with widths >100 nm (solid black line) exhibit resonant behavior in the visible regime. Right: Reflection of the TE state increases with increasing wire width.

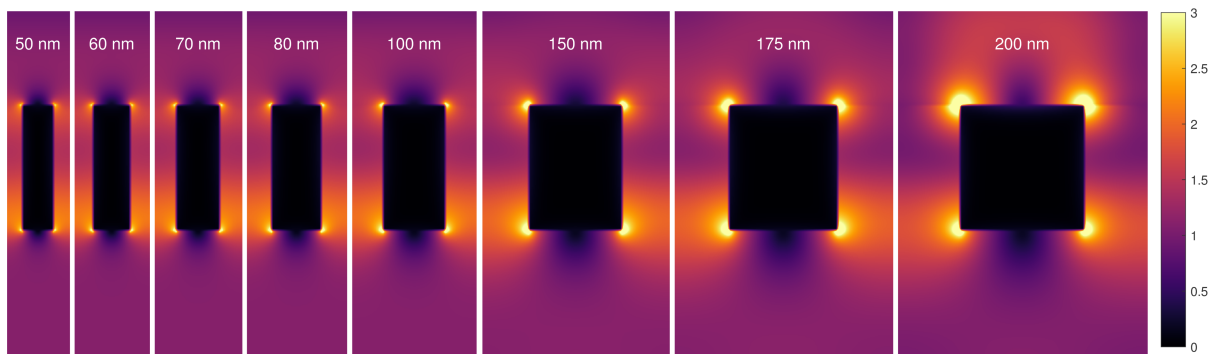


FIGURE 4.10: Electric field intensity cross-sections for 8 simulations of wires with increasing widths, for a TE pulse, which is mostly transmitted by the polarizer. Black rectangles correspond to the wire cross-section. These results are for light at a wavelength of 667 nm. The intensity is normalized by the source power and shown on a linear scale. The wire height is 200 nm and the spacing between the wires is equal to the wire width.

improves as the wavelength of light increases. However, this trend weakens as the wires become thinner. For example, 25 nm and 50 nm wires have roughly similar performance at 400 nm and 2000 nm, whereas the performance of 200 nm wires improves 100 times over this range. This suggests that there is a critical wire width at which the polarizer becomes sufficiently smaller than the source wavelengths and further reductions in wire width provide increasingly smaller performance gains. The reflection of the TM state (Figure 4.11, Right) is similar for the wire widths simulated; however, the resonant behavior seen

for the TE states emerges once again for wires with widths >100 nm.

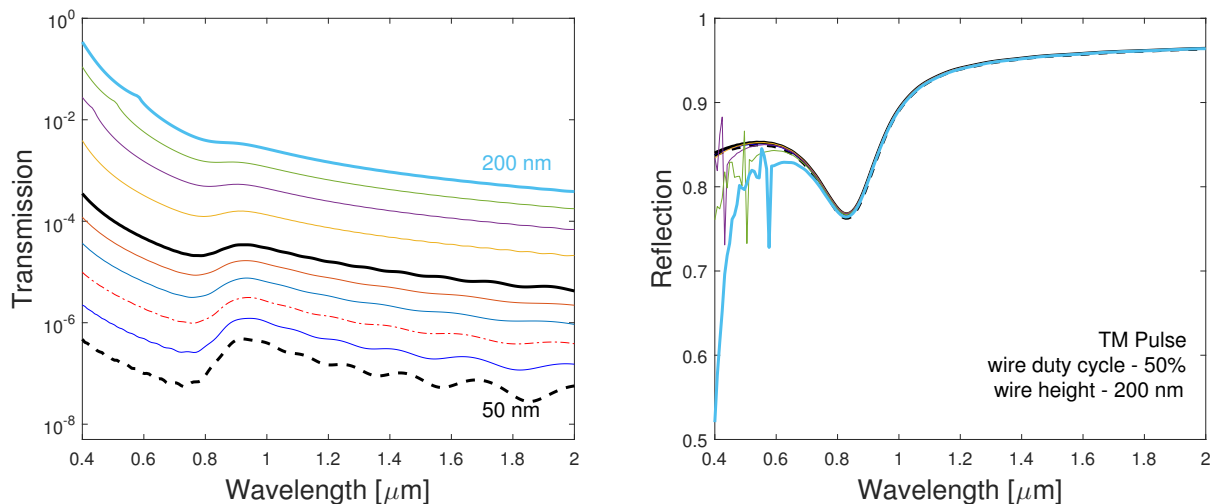


FIGURE 4.11: Left: Transmission of the TM component for a wire grid polarizer with wire widths of 50 nm, 60 nm, 70 nm, 80 nm, 90 nm, 100 nm, 125 nm, 150 nm, 175 nm and 200 nm, with duty cycle and wire height fixed at 50% and 200 nm, respectively. In general, wire grids with thinner wires transmit less light at all wavelengths. Right: Reflection of the TM state is not strongly affected by wire width; however, wires with thickness $> \sim 100$ nm exhibit resonant behavior at shorter wavelengths.

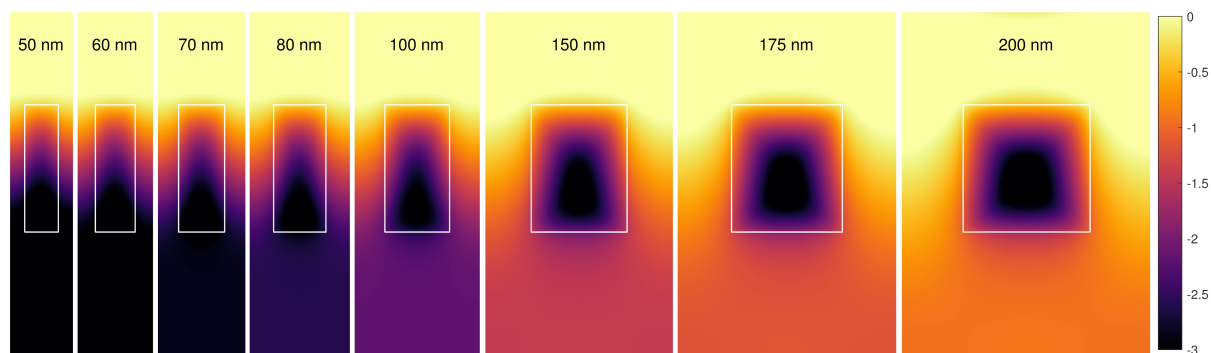


FIGURE 4.12: Electric field intensity cross-sections for 8 simulations of wires with increasing widths, for a TM pulse, which is mostly reflected by the polarizer. White rectangles are drawn to help outline the edges of the wires. These results are for light at a wavelength of 667 nm. The intensity is normalized by the source power and shown on a logarithmic scale. The wire height is 200 nm and the spacing between the wires is equal to the wire width.

4.1.3.2 Effects of Wire Spacing

In the previous section, we explored the effects of changing wire width on polarizer performance. Because we held the duty cycle constant, we also changed the width of the air gap between wires and (as a result) the pitch of the wires. Here, we fix the wire width and look at the effect wire separation has on the transmission and reflection of TE and TM states. We performed simulations of wire grid polarizers with wire widths of 75 nm, height of 200 nm and air gap widths of 25 nm, 50 nm, 75 nm, 100 nm, 125 nm, 150 nm, 175 nm and 200 nm.

First, we look at the transmission and reflection of the TE state (which is mostly transmitted by the polarizer). As the spacing between the wires increases, the polarizer transmits more light across all wavelengths (Figure 4.13, Left). Also, the transmission dip near 800 nm, which corresponds to a drop in the refractive index of aluminum, becomes less pronounced as the wire spacing increases and the effective index of the structure becomes less like that of pure aluminum. Unsurprisingly, the reflection of the TE component (Figure 4.13, Right) decreases as the wire spacing increases. The high reflection predicted for simulations with a 25 nm gap appears to be related to resonant behavior. This is also hinted at by the intense electric fields seen in the 25 nm and (to a lesser extent) 50 nm simulations (Figure 4.14).

The spacing of the wires has a significant effect on the transmission of the TM state (which is mostly reflected by the polarizer). Decreasing the air gap between wires dramatically decreases the transmission of the TM state (Figure 4.15). Simulations with the smallest air gaps (25 nm and 50 nm) begin to show signs of numerical error; the wavy structure seen in the 50 nm simulation (blue line) is characteristic of reflections from the PML boundary, which is even more pronounced in the 25 nm simulations. As with simulations of wire width, the reflection of the TM component is only moderately affected by changing the wire spacing, with the largest changes seen in the visible range, where the polarizer is closer to the boundary of the sub-wavelength regime.

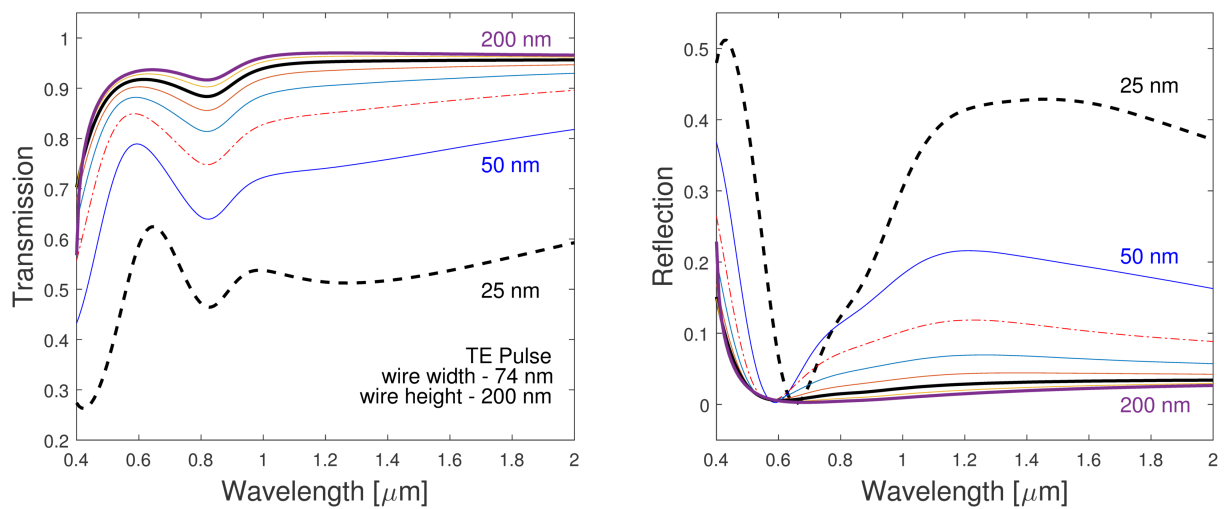


FIGURE 4.13: Left: Transmission of the TE component for a wire grid polarizer with wire air gap width of 25 nm, 50 nm, 75 nm, 100 nm, 125 nm, 150 nm, 175 nm and 200 nm. In general, wire grids with larger air gaps exhibit higher transmission at all wavelengths. Right: Reflection of the TE state decreases with increasing wire separation. Wires with air gap widths < 50 nm (blue line) exhibit resonant behavior in the visible regime.

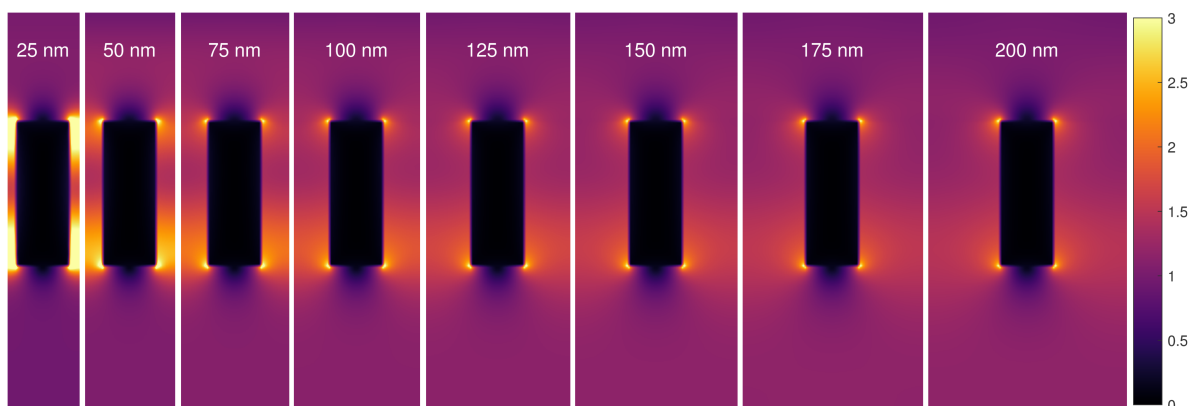


FIGURE 4.14: Electric field intensity cross-sections for 8 simulations of wires with increasing air gap widths, for a TE pulse, which is mostly transmitted by the polarizer. Black rectangles correspond to the wire cross-section. These results are for light at a wavelength of 667 nm. The intensity is normalized by the source power and shown on a linear scale. The wire height is 200 nm and the wire width is 75 nm.

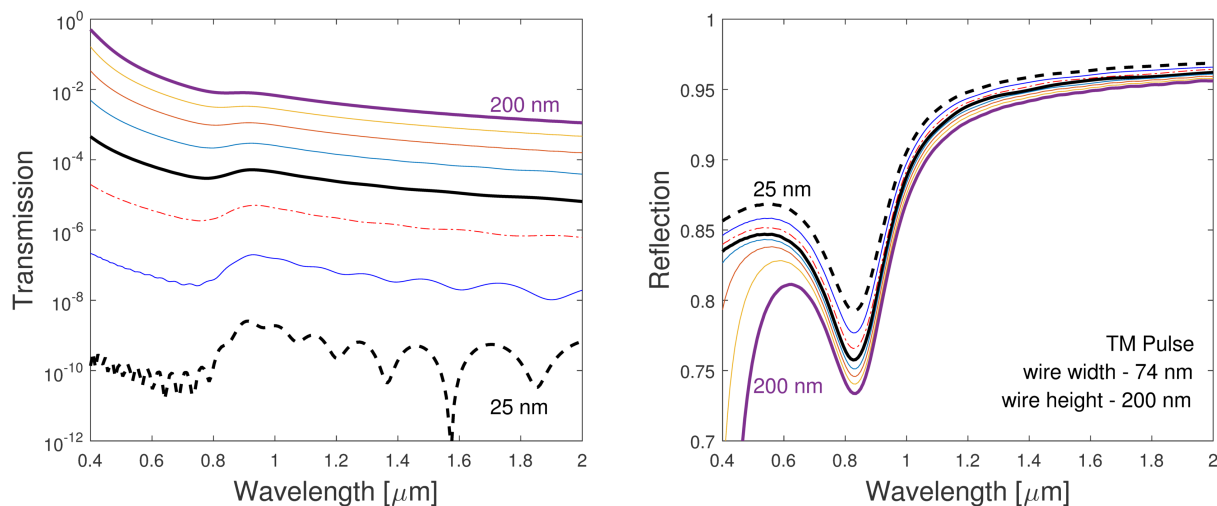


FIGURE 4.15: Left: Transmission of the TM component for a wire grid polarizer with air gap widths of 25 nm, 50 nm, 75 nm, 100 nm, 125 nm, 150 nm, 175 nm and 200 nm. In general, wire grids with smaller air gaps exhibit lower transmission at all wavelengths. Simulations with a 25 nm gap predict extremely low transmission and a complex wavelength dependence, hinting at the emergence of numerical errors or more complex resonant behavior. Right: Reflection of the TM state increases with decreasing wire spacing, with the largest changes in the visible regime.

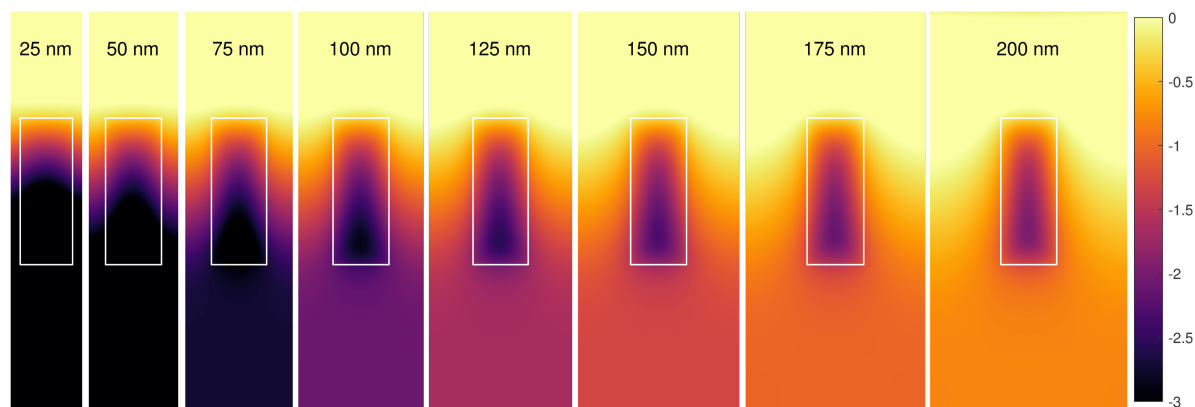


FIGURE 4.16: Electric field intensity cross-sections for 8 simulations of wires with increasing air gap widths, for a TM pulse, which is mostly reflected by the polarizer. White rectangles are drawn to help outline the edges of the wires. These results are for light at a wavelength of 667 nm. The intensity is normalized by the source power and shown on a logarithmic scale. The wire height is 200 nm and the wire width is 75 nm.

4.1.3.3 Effects of Wire Height

Once the width and spacing of the wires is chosen such that the polarizer structure is sufficiently far in the sub-wavelength regime, it is worthwhile to look at the effects of wire height. We simulated wires with width of 74 nm, a 50% duty cycle and heights of 25 nm, 50 nm, 75 nm, 100 nm, 125 nm, 150 nm, 175 nm, 200 nm, 250 nm and 300 nm. Changing the wire height produces a rich variety of results, suggesting the presence of complex and competing resonant behaviors.

The height of the wires has a strong effect on the transmission and reflection of the TE state (which is mostly transmitted by the polarizer). As the wire height increases from 25 nm to 300 nm, the transmission of the TE state generally decreases (Figure 4.17, Left). However, several systematic trends appear to emerge. The transmission for wires shorter than ~ 100 nm decreases monotonically for shorter wavelengths. Simulations of wires taller than ~ 100 nm show a different response, with a slightly better transmission at shorter wavelengths and a noticeable “800 nm dip.” Once the height reaches 250 nm, more complex behavior is predicted by the simulations. The reflection of the TE pulse follows similar trends as the transmission curves (Figure 4.17, Right).

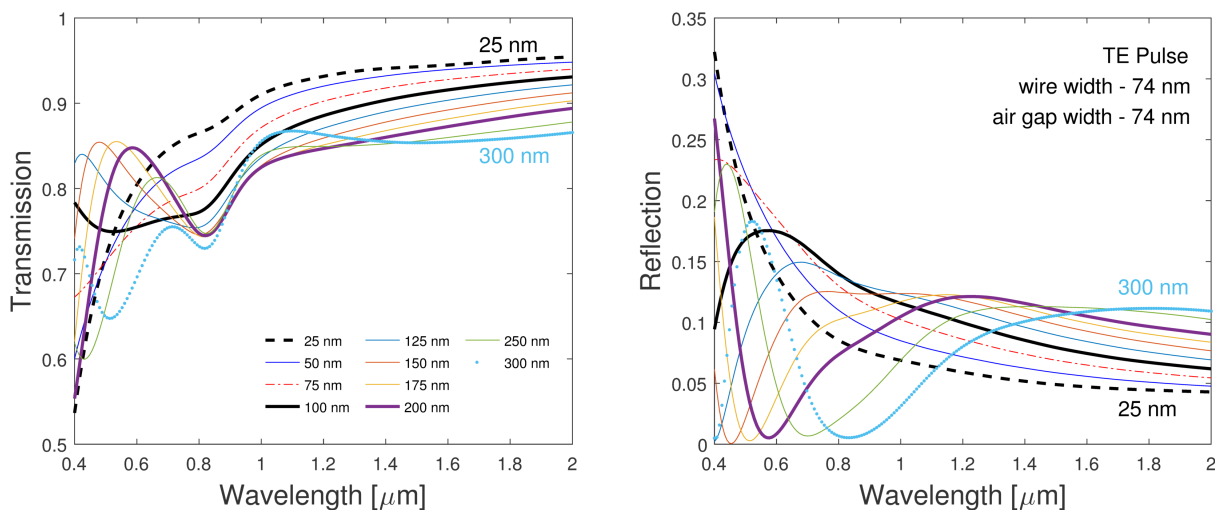


FIGURE 4.17: Left: Transmission of the TE component for a wire grid polarizer with wire heights of 25 nm, 50 nm, 75 nm, 100 nm, 125 nm, 150 nm, 175 nm, 200 nm, 250 nm, and 300 nm. In general, wire grids with taller wires exhibit lower transmission at all wavelengths; however, in the visible range two systematic patterns emerge, with a height of ~ 100 nm separating these two regimes. Right: Reflection of the TE state has a complex dependence on wire height.

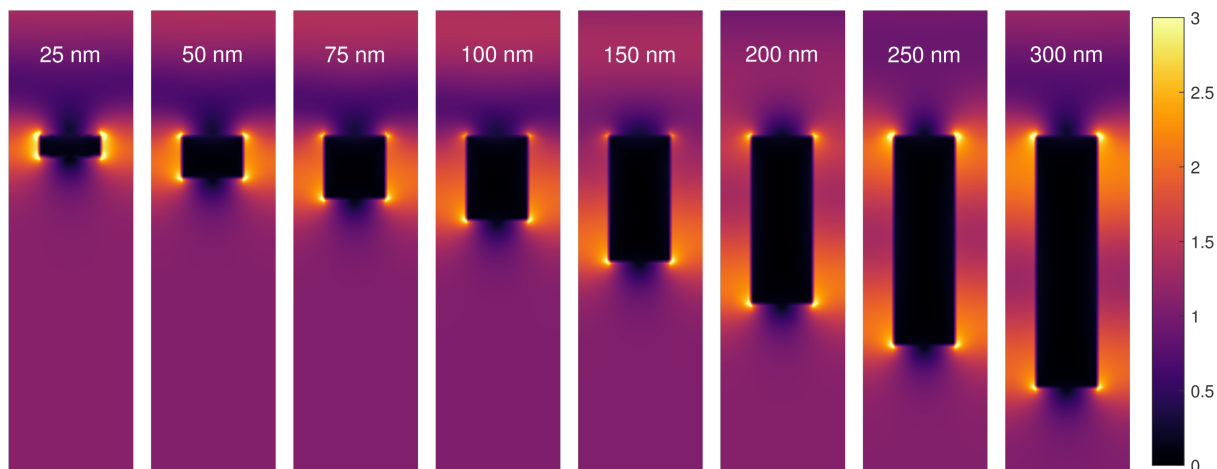


FIGURE 4.18: Electric field intensity cross-sections for 8 simulations of wires with increasing height, for a TE pulse, which is mostly transmitted by the polarizer. Black rectangles correspond to the wire cross-section. These results are for light at a wavelength of 667 nm. The intensity is normalized by the source power and shown on a linear scale. The wire width is 74 nm and the duty cycle 50%.

The effect of wire height on the transmission and reflection of the TM states is less dramatic than for the TE state. Overall, the ability of the polarizer to reflect the TM state improves as the wire height increases, as is clearly shown by the decrease in the transmitted light (Figure 4.19, Left). The tallest wires we simulated (250 nm and 300 nm) predicted extremely low transmissions, at a level where the PML reflections start to become prominent and appear as wavy interference patterns in the transmission curves. The reflection of the TM component (Figure 4.19, Right) is not strongly affected by the wire height, except when the wires become very short, with heights of ~ 25 nm.

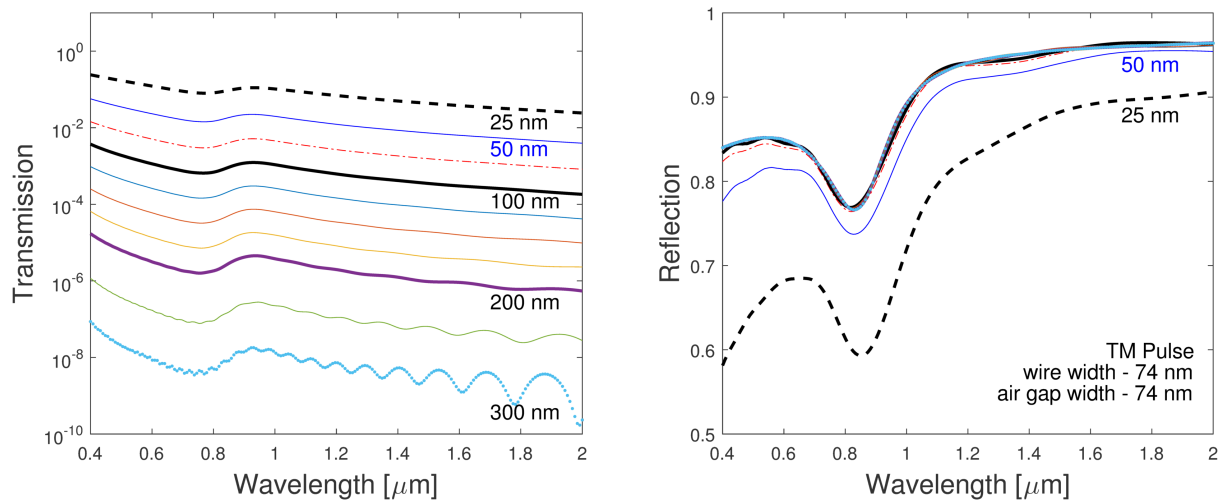


FIGURE 4.19: Left: Transmission of the TM component for a wire grid polarizer with wire heights of 25 nm, 50 nm, 75 nm, 100 nm, 125 nm, 150 nm, 175 nm, 200 nm, 250 nm and 300 nm. In general, wire grids with taller wires exhibit lower transmission at all wavelengths. Right: Reflection of the TE state has a complex dependence on wire height.

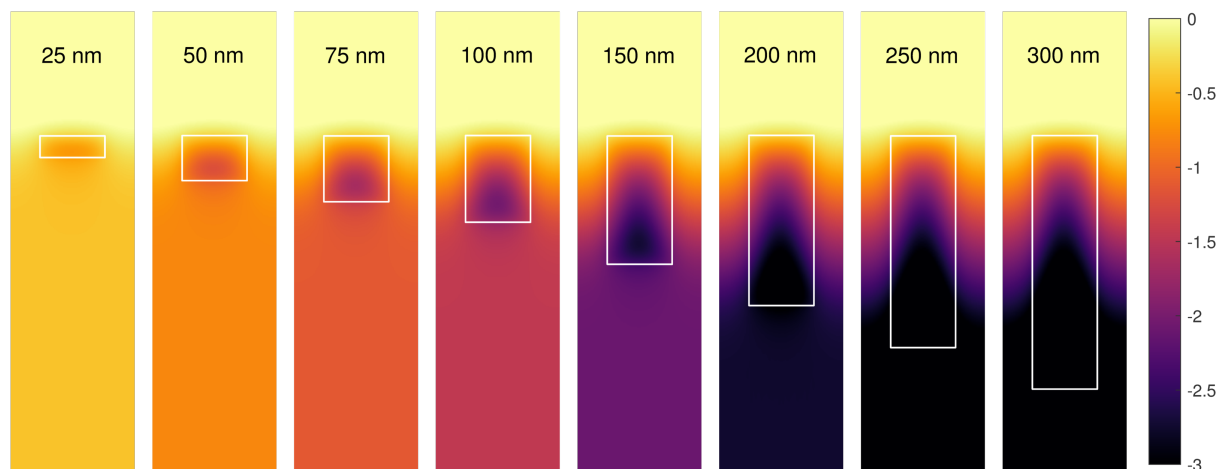


FIGURE 4.20: Electric field intensity cross-sections for 8 simulations of wires with increasing height, for a TM pulse, which is mostly reflected by the polarizer. White rectangles are drawn to help outline the edges of the wires. These results are for light at a wavelength of 667 nm. The intensity is normalized by the source power and shown on a logarithmic scale. The wire width is 74 nm and the duty cycle 50%.

4.1.4 3D Simulations - Effects of Wire Shape and Spacing

As we have shown in the previous section, many properties of wire grid polarizers can be simulated in 2D. Approximating the length dimension to be infinite is natural, because conventional wire grid polarizers consist of wires whose length is much greater than their width or height. However, 2D simulations prevent 2D plasmon modes from developing on the surface of the polarizers and preclude the modeling of more complex geometric effects, like surface roughness. To investigate the effect of the 3rd dimension on models of wire grid polarizers, we performed 3D simulations of conventional non-pixelated wire grid polarizers and compared the results to those of our 2D models and to measurements of actual devices.

4.1.4.1 Testing Numerical Convergence in 3D

Most studies of these structures are performed in 2D because 3D simulations require significantly more computing resources and computing time. Furthermore, the complex behaviors that only exist in 3D simulations can have a detrimental effect on numerical convergence. As such, we performed convergence testing for 3D simulations to determine a sufficient mesh resolution and identify other potential sources of numerical error. Our simulations consisted of a single aluminum wire on a SiO₂ substrate, with a width of 74 nm, height of 200 nm and a length of 8 μ m. The simulation used periodic boundary conditions in the width and length dimensions to create an infinite array of wires of infinite length, i.e., a large wire grid polarizer. As in the 2D case, we propagated a planar source that originated in the SiO₂ substrate, down, through the wire grid; the direction of propagation was bounded by PML regions, which absorbed most of the light.

First, we simulated the polarizers using several mesh refinement levels to study the effects of mesh size in 3D simulations. The size of the smallest cell in each simulation was 13.6 nm, 7.8 nm, 5.7 nm, 4.5 nm, 3.7 nm, 3.1 nm, 2.7 nm, and 2.4 nm (as in the 2D simulations). We quantify the level of convergence using the difference between successive simulations using the relative error, dS (Eq. 4.1). Our tests show (Figure 4.21, Right) that these simulations begin to converge numerically when the smallest cell size is \sim 4 nm. As before, we look

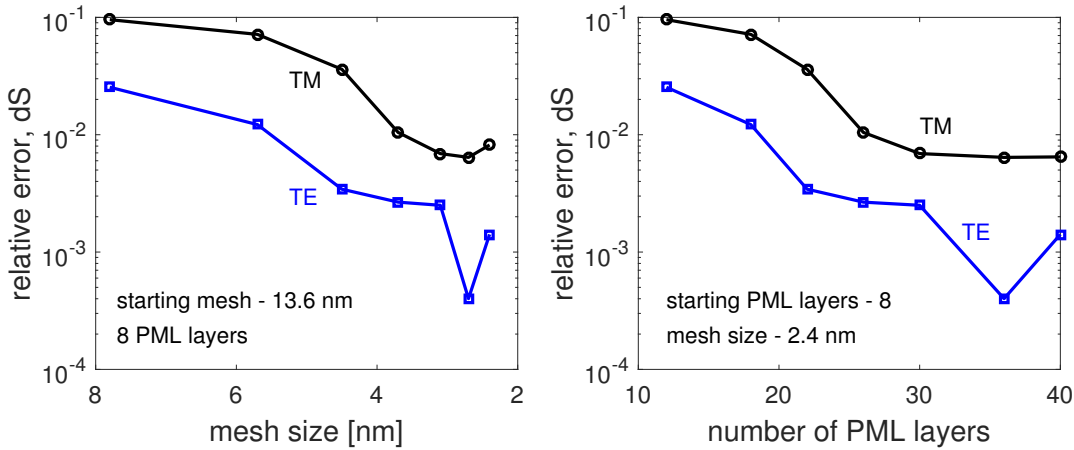


FIGURE 4.21: Right: We found that in 3D, simulations began to numerically converge when the simulation mesh was smaller than 4 nm. Left: We simulated structures and varied the number of layers in the absorbing PML boundary, to determine when the reflections from the PML were sufficiently suppressed. A significant decrease in relative error can be achieved by using ~ 26 layers in the PML.

at the effect the PML boundaries have on numerical accuracy, because this is typically the most significant source of error, after mesh size. We simulated the same structures using a high resolution mesh, with smallest cell size of 2.7 nm and varied the number of layers in the PML boundary from 8 to 40 (4.21, Left). We found significant improvements in relative error when the number of layers in the PML was increased from 8 to ~ 26 layers. Beyond this, additional layers had only marginal effects on the simulation results, suggesting that a different mechanism becomes the dominant source of numerical errors.

4.1.4.2 Effects of Wire Width

To study the effects of wire width on polarizer performance in 3D, we performed a suite of simulations with similar parameters as in the 2D case (Section 4.1.3.1). We simulated wires with widths of 50 nm, 60 nm, 70 nm, 80 nm, 90 nm, 100 nm, 125 nm, 150 nm, 175 nm and 200 nm. The duty cycle was set to 50% and the wire height was fixed at 200 nm. As before, we look at the transmission and reflection of TE and TM polarizer light to determine the polarizer's performance.

When the incident light is TE polarized, a strong trend emerges with increasing wire width. The transmission of the TE state (Figure 4.22, Left) in the visible range has a

sharp cut-off, that moves to shorter wavelengths as the wires become thinner. In fact, the ratio between the cut-off wavelength and the wire width is roughly constant ($\sim 3:1$) for the 3 simulations where the cut-off is visible, which is suggestive of resonant behavior. If we look at the local peak in transmission near 580 nm, we see that it begins to shift to longer wavelengths for the thicker wires. Specifically, the peak is at approximately 580 nm for wires of width 50 nm, 60 nm, 70 nm, 80 nm, 90 nm, 100 nm and it shifts to 608 nm, 640 nm, 657 nm, and 695 nm for wire widths of 125 nm, 150 nm, 175 nm, and 200 nm, respectively. The shifts begin when the ratio of the peak wavelength to wire width drops below $\sim 6:1$. Similar behavior is seen in the reflection curves (Figure 4.22, Right).

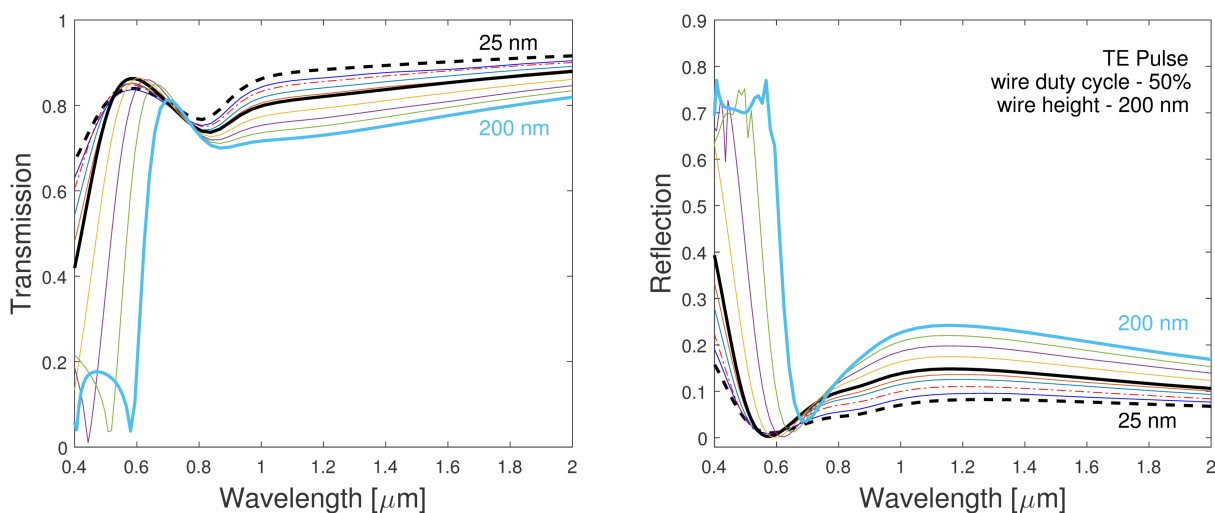


FIGURE 4.22: Left: Transmission of the TE component for a wire grid polarizer with wire widths of 50 nm, 60 nm, 70 nm, 80 nm, 90 nm, 100 nm, 125 nm, 150 nm, 175 nm and 200 nm, with duty cycle and wire height fixed at 50% and 200 nm, respectively. In general, wire grids with thinner wires exhibit higher transmission at all wavelengths. Wires with widths >100 nm (solid black line) exhibit resonant behavior in the visible regime. Right: Reflection of the TE state increases with increasing wire width.

The polarizer’s response to TM-polarized light in 3D is similar to the 2D case. In general, the polarizer becomes much better at blocking the TM states as the wires become thinner (Figure 4.23, Left). As before, the ability of a polarizer of a certain wire width to block TM-polarized light increases with increasing wavelength and the rate of improvement decreases as the wires become thinner. This suggests that there exists a regime where the width of the wires is sufficiently small compared to the wavelength of light, a “deep sub-wavelength regime”, where decreasing the wire width or increasing the wavelength

of light has marginal effects. This regime is important to understand because it represents the beginning of diminishing returns in terms of performance improvement vs. complexity of fabrication. The reflection of the TM component (Figure 4.23, Right) follows similar trends: wires with widths $> \sim 150$ nm show poor performance for the shortest wavelengths we simulated, suggesting that these structures are outside the “deep sub-wavelength regime.”

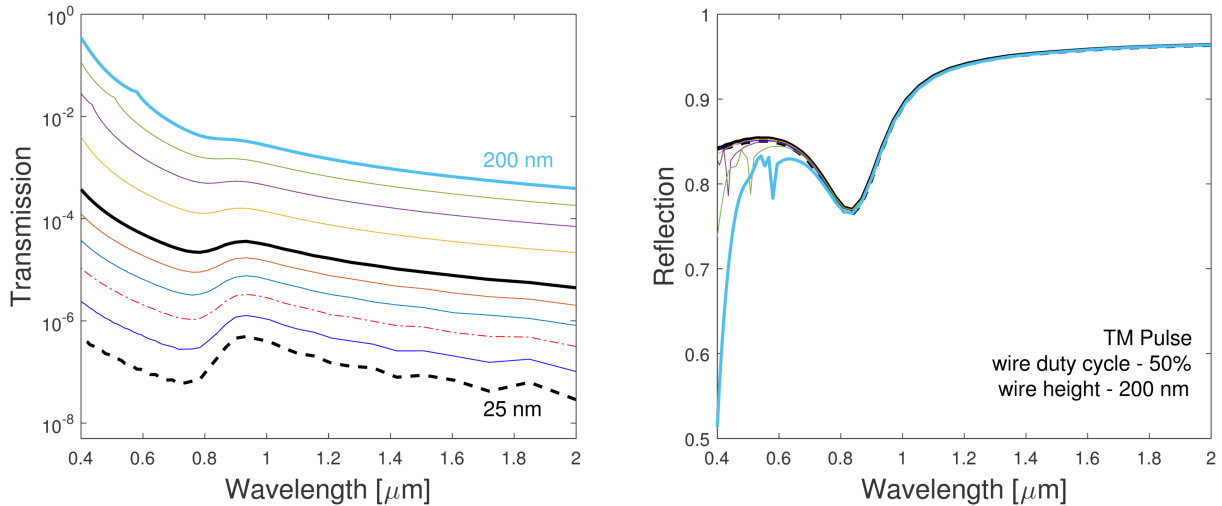


FIGURE 4.23: Left: Transmission of the TM component for a wire grid polarizer with wire widths of 50 nm, 60 nm, 70 nm, 80 nm, 90 nm, 100 nm, 125 nm, 150 nm, 175 nm and 200 nm, with duty cycle and wire height fixed at 50% and 200 nm, respectively. In general, wire grids with thinner wires transmit less light at all wavelengths. Right: Reflection of the TM state is not strongly affected by wire width and the resonant behavior seen in 2D simulations is diminished.

4.1.4.3 Effects of Wire Spacing

Our 3D simulations of polarizer performance and the effects of wire spacing (or duty cycle) yield results that are similar to the 2D simulations. In general, the transmission of TE polarized light (Figure 4.24, Left) improves as the gap between the wires increases. However, increasing the gap between the wires also increases the transmission of TM polarization states (Figure 4.25, Left), reducing the contrast (or “extinction ratio”) of the polarizer. Polarizers with wide gaps between the wires also show the lowest reflection for both TE (Figure 4.24, Right) and TM (Figure 4.25, Right) polarization states. From this we can conclude that polarizers begin to suffer performance degradation related to poor contrast when the wire spacing becomes larger than ~ 100 nm and show reduced

transmission for the desired (TE) state when the spacing becomes smaller than ~ 75 nm. In other words, optimal wire spacing appears to be in the range of 50 nm - 100 nm, depending on whether high transmission or high contrast are more desirable.

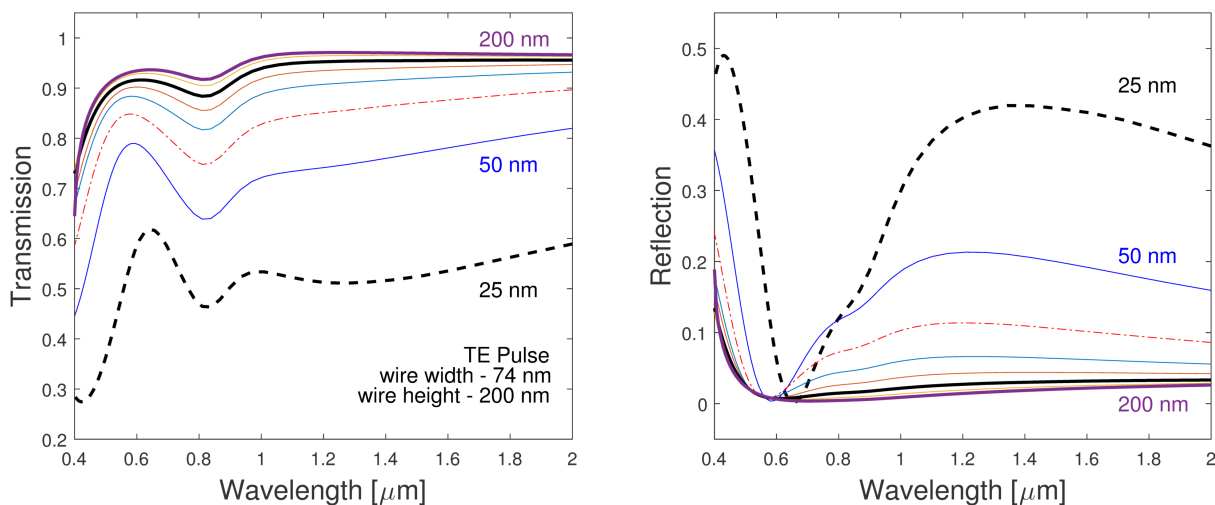


FIGURE 4.24: Left: Transmission of the TE component for a wire grid polarizer with wire air gap width of 25 nm, 50 nm, 75 nm, 100 nm, 125 nm, 150 nm, 175 nm and 200 nm. In general, wire grids with larger air gaps exhibit higher transmission at all wavelengths. Right: Reflection of the TE state decreases with increasing wire separation.

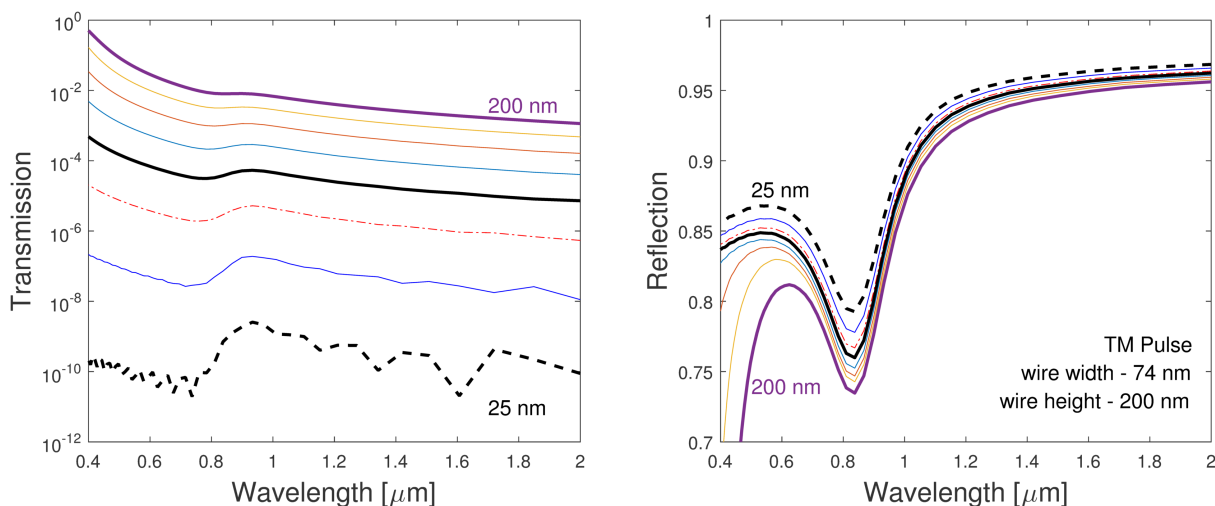


FIGURE 4.25: Left: Transmission of the TM component for a wire grid polarizer with air gap widths of 25 nm, 50 nm, 75 nm, 100 nm, 125 nm, 150 nm, 175 nm and 200 nm. In general, wire grids with smaller air gaps exhibit lower transmission at all wavelengths. Simulations with a 25 nm gap predict extremely low transmission and a complex wavelength dependence, hinting at the emergence of numerical errors. Right: Reflection of the TM state increases with decreasing wire spacing, with the largest changes in the visible regime.

4.1.4.4 Effects of Wire Height

Finally, we investigate the effects of wire height on polarizer performance in 3D. As in the 2D case, we simulated wires with width and spacing of 74 nm and heights of 25 nm, 50 nm, 75 nm, 100 nm, 125 nm, 150 nm, 175 nm, 200 nm, 225 nm, and 250 nm. The results are similar to those obtained in the 2D simulations.

As the wire height increases, the polarizer’s ability to transmit the TE polarized light decreases (Figure 4.26, Left). As before, a wire height of ~ 100 nm appears to be a boundary case between two regimes: shorter wires show a slow, monotonic decrease in transmission towards shorter wavelengths, while taller wires develop the “800 nm aluminum dip” and a shorter drop-off in transmission in the blue and ultraviolet regime. This behavior is also evident in the reflection curve for the TE source (Figure 4.26, Right).

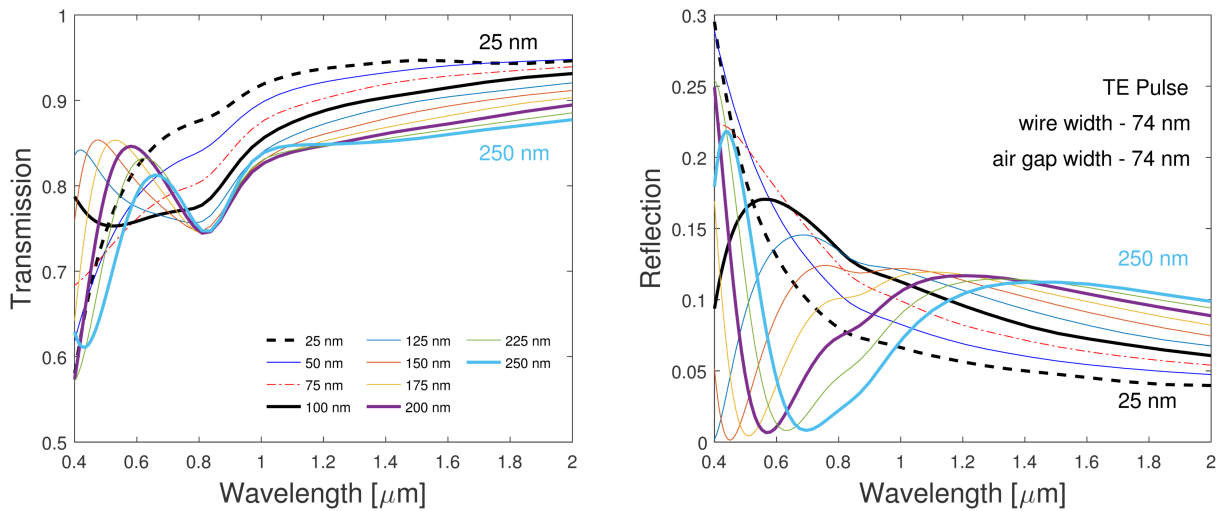


FIGURE 4.26: Left: Transmission of the TE component for a wire grid polarizer with wire heights of 25 nm, 50 nm, 75 nm, 100 nm, 125 nm, 150 nm, 175 nm, 200 nm, 225 nm, and 250 nm. In general, wire grids with taller wires exhibit lower transmission at all wavelengths; however, in the visible range two systematic patterns emerge, with a height of ~ 100 nm separating these two regimes. Right: Reflection of the TE state has a complex dependence on wire height.

The wire height has a more straightforward effect on the ability of the polarizer to transmit and reflect TM polarized light. As the wire height increases, the transmission of the TM state decreases (Figure 4.27, Left), resulting in a polarizer that is much more efficient at blocking this “un-wanted” state. The reflection of TM polarized light (Figure 4.27,

Right) also improves; however, a point of diminishing returns is reached for a height of ~ 75 nm.

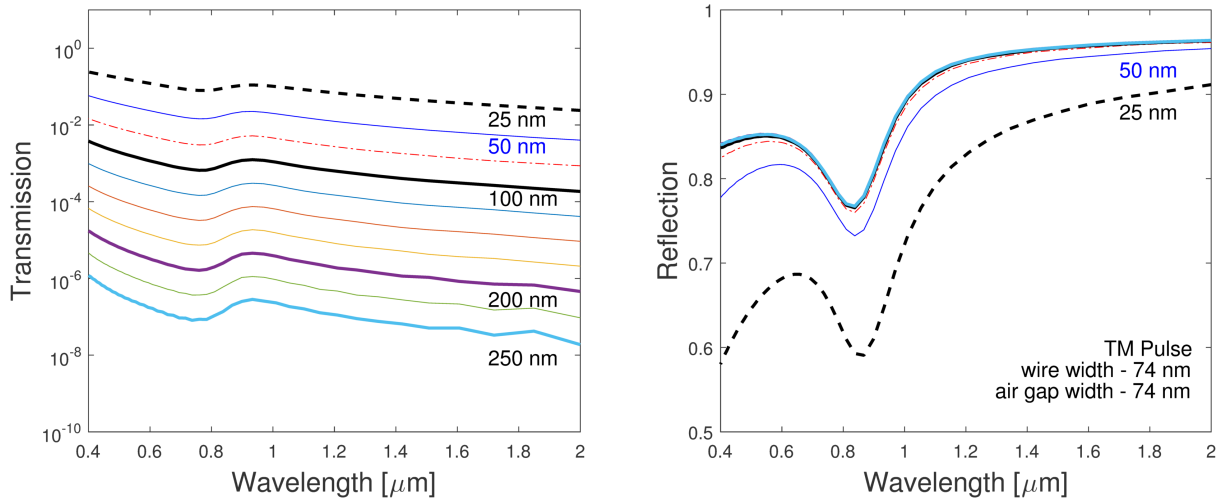


FIGURE 4.27: Left: Transmission of the TM component for a wire grid polarizer with wire heights of 25 nm, 50 nm, 75 nm, 100 nm, 125 nm, 150 nm, 175 nm, 200 nm, 225 nm and 250 nm. In general, wire grids with taller wires exhibit lower transmission at all wavelengths. Right: Reflection of the TM state reaches the maximum after a wire height of ~ 75 nm.

4.1.5 A Comparison of 2D and 3D Simulations

The 2D and 3D simulations we presented in this section produced very similar results. In this subsection, we compare several of these simulations directly and discuss the implications for future models of these structures. Specifically, we look at a wire grid polarizer with a wire width and spacing of 74 nm and height of 200 nm. The first two simulations model this structure using a single wire in 2D and 3D, using periodic boundary conditions to create an effectively infinite array of such wires. The third simulation models 54 wires simultaneously, again using periodic boundary conditions to create an infinite array of this larger simulation region.

The calculated transmission of the TE and TM polarized sources in these 3 simulations is nearly identical (Figure 4.28). This is a result of the many symmetries present in our setup (and a credit to the accuracy of the periodic boundary condition implementation). In other words, 2D simulations are sufficient to accurately model an infinite array of straight wires with some arbitrary cross-section. One might expect this to be true, but it

is nevertheless remarkable just how much the simulations agree. For wire grid polarizers, this makes 2D simulations sufficient to study the effects of profile shape and material properties on polarizer performance. The low computational requirements associated with even the highest resolution 2D simulations make them an important tool, even in the face of full 3D models. For example, the 2D and 3D simulations of a single wire and the 3D simulation of many wires required 16 MB, 8,000 MB and 420,000 MB of RAM, respectively.

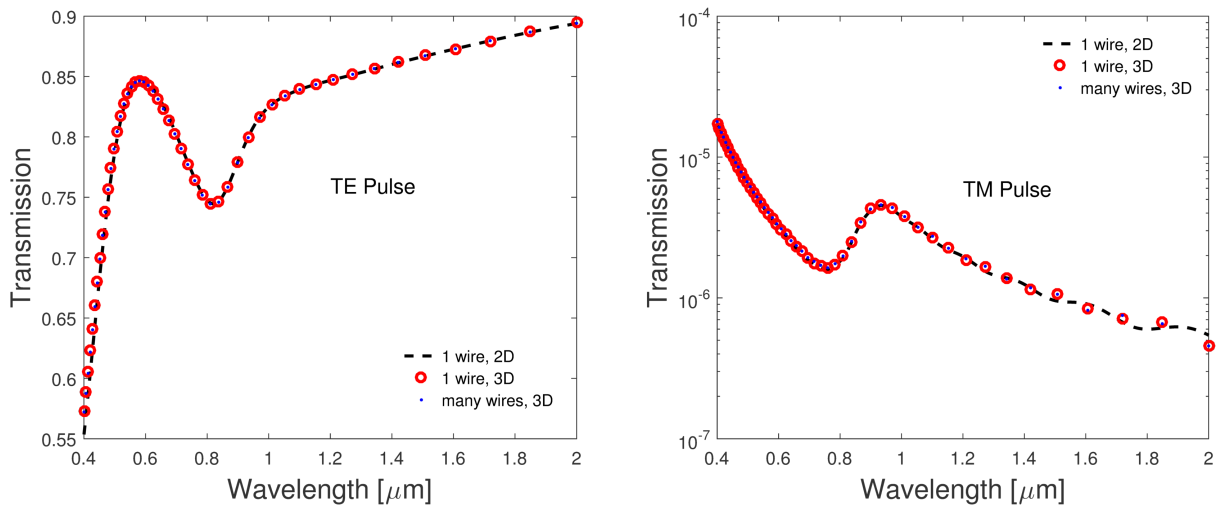


FIGURE 4.28: We compare the results of 2D and 3D simulations of a single wire and a 3D simulation of a 50 wire region. All simulations show very similar results, even though the simulated region is very different in each case. It appears that 2D simulations can be an accurate representation of certain 3D structures, if one can exploit some symmetries (such as the length dimension of a long, skinny wire).

4.1.6 Comparing Simulations to Experimental Results

In this section we presented 2D and 3D simulations of “infinite” wire grid polarizers and investigated the effects of wire width, spacing and height on the ability of the polarizer to efficiently transmit the desired polarization states (TE states) and reject the unwanted polarization components (TM states). These simulations represent an idealized version of wire grid polarizers, by forcing each wire to be identical and, in the case of 2D simulations, perfectly straight and infinitely long. We conclude this section with a comparison of simulated polarizers to experimental results obtained from commercially available wire grid polarizers.

To compare the simulated polarizers to fabricated devices, we look at the transmission of the TE and TM polarizations for a single polarizer. The simulated structures consisted of straight aluminum wires on a SiO₂ substrate, with wire width and spacing of 74 nm and a height of 150 nm. These parameters were chosen to match the dimensions of fabricated structures, determined from scanning electron micrographs (Figure 4.29).

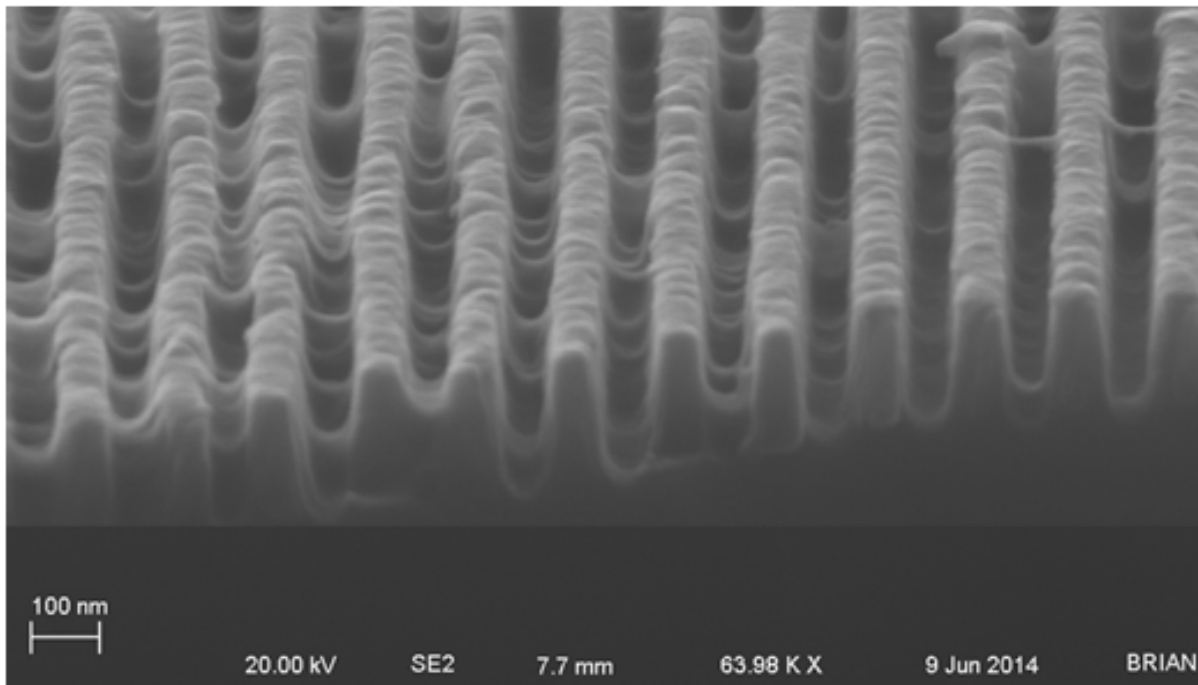


FIGURE 4.29: An SEM micrograph of the cross-section of a wire grid polarizer. The aluminum wires are approximately 74 nm wide, with a 50% duty cycle and a height of ~ 150 nm. It is clear from the micrographs that the fabricated polarizers do not have perfectly straight wires and their profiles are not strictly rectangular; furthermore, the height of the wires is not uniform

First, we compare the ability of the simulated and fabricated polarizers to transmit the TE states (Figure 4.30, Left). Overall, the fabricated devices are not as transmissive as the model predictions, especially in the near-infrared. Also, the measured polarizers show a “ringing” response in the near-IR, which is likely caused by the anti-reflection coating (which we do not simulate). Nevertheless, the shape of the transmission curve matches the measured response well, considering how sensitive the models are to the various structure parameters (see Figure 4.22, Figure 4.24 and Figure 4.26).

Next, we look at the transmission of the TM states for the model and measured device (Figure 4.30, Right), i.e., the ability of the polarizer to reject the unwanted states. The

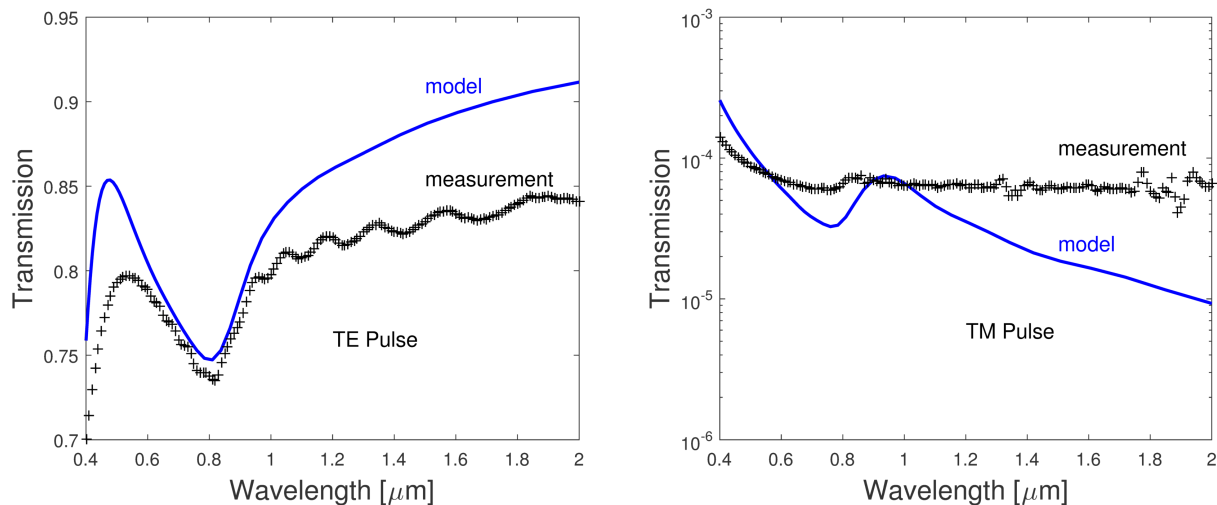


FIGURE 4.30: Left: The measured transmission of a wire grid polarizer is generally lower than the model prediction from our simulations. Furthermore, the measured data shows ringing in the near-infrared, which is likely due to the anti-reflective coating (that we don’t simulate). Right: The actual polarizers are not as good at blocking the TM state as the simulated polarizers, especially in the near-infrared.

model does not approximate the measured response as well as for the TE case. At shorter wavelengths, the measured device shows a lower transmission than the model prediction; however, this is likely due to the overall lower efficiency in the UV (e.g., this is also true for the TE state). At longer wavelengths, the contrast of the measured device does not improve in the way that the model predicts, but remains roughly constant. We explore the possible reasons for disagreement between the simulated structures and measured structures in the next section.

4.1.6.1 Common Sources of Disagreement

In most cases when the model predictions do not agree with the measured results, the source of the error is frustratingly simple: either the simulated structure is not a faithful representation of the real device or not all of the relevant physics are included in the simulation. In this case, both factors are at play. First, it is evident from the SEM micrographs (Figure 4.29) that actual polarizer wires do not have perfectly rectangular profiles, but have a rounded trapezoidal shape. Furthermore, the wires are not smooth, but show a “lumpy” surface, with undulations with a period of ~ 20 nm. Finally, the etch depth does not appear uniform, which results in a height variation across the polarizer.

Without more detailed modeling, it is difficult to guess to what degree these features can affect the results, though some recent 2D models have shown that these effects can be significant [Ryu et al. \(2008\)](#); [Mélen et al. \(2015\)](#). Our 3D simulations are well posed to study these geometric effects and they are the focus of future work.

The second source of disagreement stems from the way the relevant physics are implemented in the simulation. The FDTD solver used for this work prescribes most of the physics using the refractive index of the materials at the appropriate source wavelengths. As such, accurately specifying the refractive index (both real and complex) is as important as choosing an accurate geometry. However, the refractive index for most materials is typically measured for “bulk” materials, and it’s not clear how well these bulk measurements apply to sub-wavelength structures and thin films, which are deposited using nano-fabrication techniques. For example, there is a wide range in the reported refractive index of aluminum (Figure 4.31). Indeed, the refractive index appears highly dependent on the thickness of the metal layer and on the quality of the deposition process. In our simulations we used the [Palik \(1998\)](#) data; however, it is not clear which choice best models these polarizers.

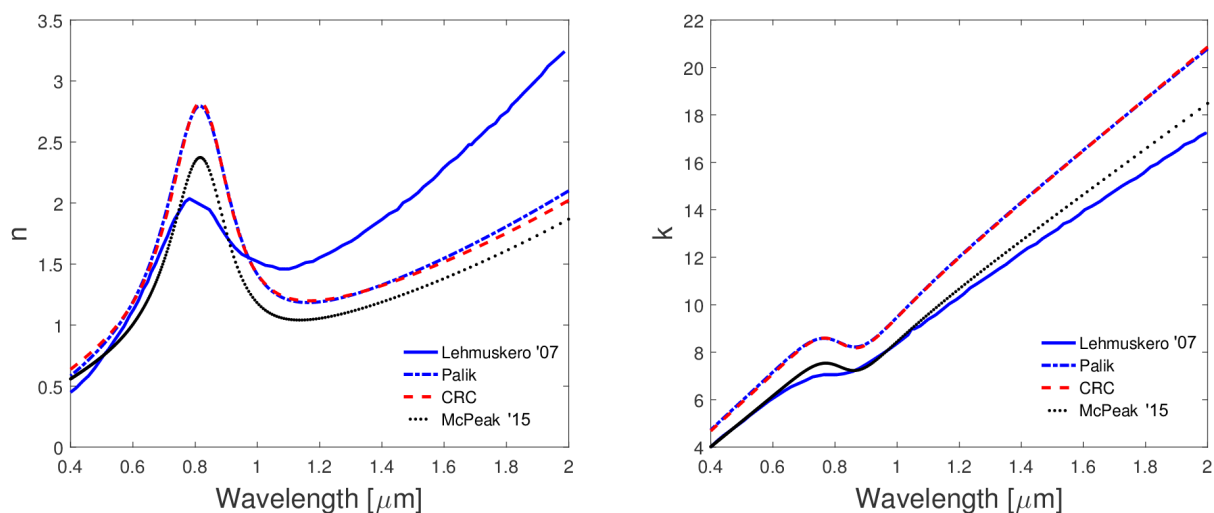


FIGURE 4.31: The real (Left) and imaginary (Right) components of the refractive index of aluminum found in the literature. The commonly used values from the book by [Palik \(1998\)](#) and CRC Handbook of Chemistry ([Shiles et al., 1980](#)), differ from more recent measurements of aluminum thin films by [Lehmuskero et al. \(2007\)](#) and [McPeak et al. \(2015\)](#).

4.1.7 Summary of Wire Grid Polarizer Simulations

In this section, we described 2D and 3D simulations of conventional “infinite” wire grid polarizers, which explore the effects of wire geometry on the polarizer’s performance. We find that in the 400 nm - 2000 nm regime, the simulations numerically converge when the mesh size is ~ 4 nm, resulting in simulations with an accuracy of $\sim 1\%$. Our key findings can be summarized as follows:

- The ability of a wire grid polarizer to block the unwanted polarization states depends most strongly on wire height and wire spacing. Increasing the wire height and reducing the gap between wires dramatically decreases the transmission of the TM states. Reducing the width of the wires also improves performance, but not as much as adjusting height and spacing.
- The transmission of the TE state (the desired state) also decreases as the wire height and width are increased (though not nearly as quickly as the transmission of the TM state). Wire spacing has the most effect on TE transmission.
- 2D and 3D simulations of wire grid polarizers show very similar results. The “infinite wire” approximation used in 2D simulations appears extremely suitable for wire grid polarizers and simulations of semi-infinite 3D wires did not exhibit any significant new interactions. 2D simulations appear sufficient to study the effects of wire profile (height, width, spacing, shape).
- Great care must be taken when attempting to model real devices, because these simulations are extremely sensitive to the input geometry and material properties. Depending on the structure, the infinite/semi-infinite approximations used by 2D and 3D simulations may not be good representations of reality.

Chapter 5

Micropolarizer Arrays

The micropolarizer array (MPA) (Figure 5.1) is a pixelated wire grid polarizer (Nordin et al. (1999)), with each pixel being a wire grid polarizer oriented along a particular direction. Most often, the pixels are linear polarizers, however, some pixel designs have been proposed and fabricated for passing only the circular polarizations (Peltzer et al. (2012)). Micropolarizer arrays are analogous to color filter arrays, which are used to create color-sensitive imaging sensors. Whereas non-pixelated polarizers are “general purpose” optical elements that can be used in a wide range of optical systems, micropolarizer arrays are used almost exclusively with conventional imaging sensors to create polarization-sensitive imagers, i.e., imaging polarimeters.

The accuracy, precision and optical throughput of an imaging polarimetric system based on a micropolarizer array (MPA) is ultimately limited by the performance of the micropolarizer array itself and any cross-talk effects that arise during the fabrication of the MPA + sensor system. Using finite-element and analytical techniques, we investigated two regimes of micropolarizer array performance:

1. Parameters of the micropolarizer array that affect the contrast ratio and throughput of the MPAs
2. Effects of contrast ratio, pixel orientation and throughput on the accuracy and precision of the polarimetric measurement

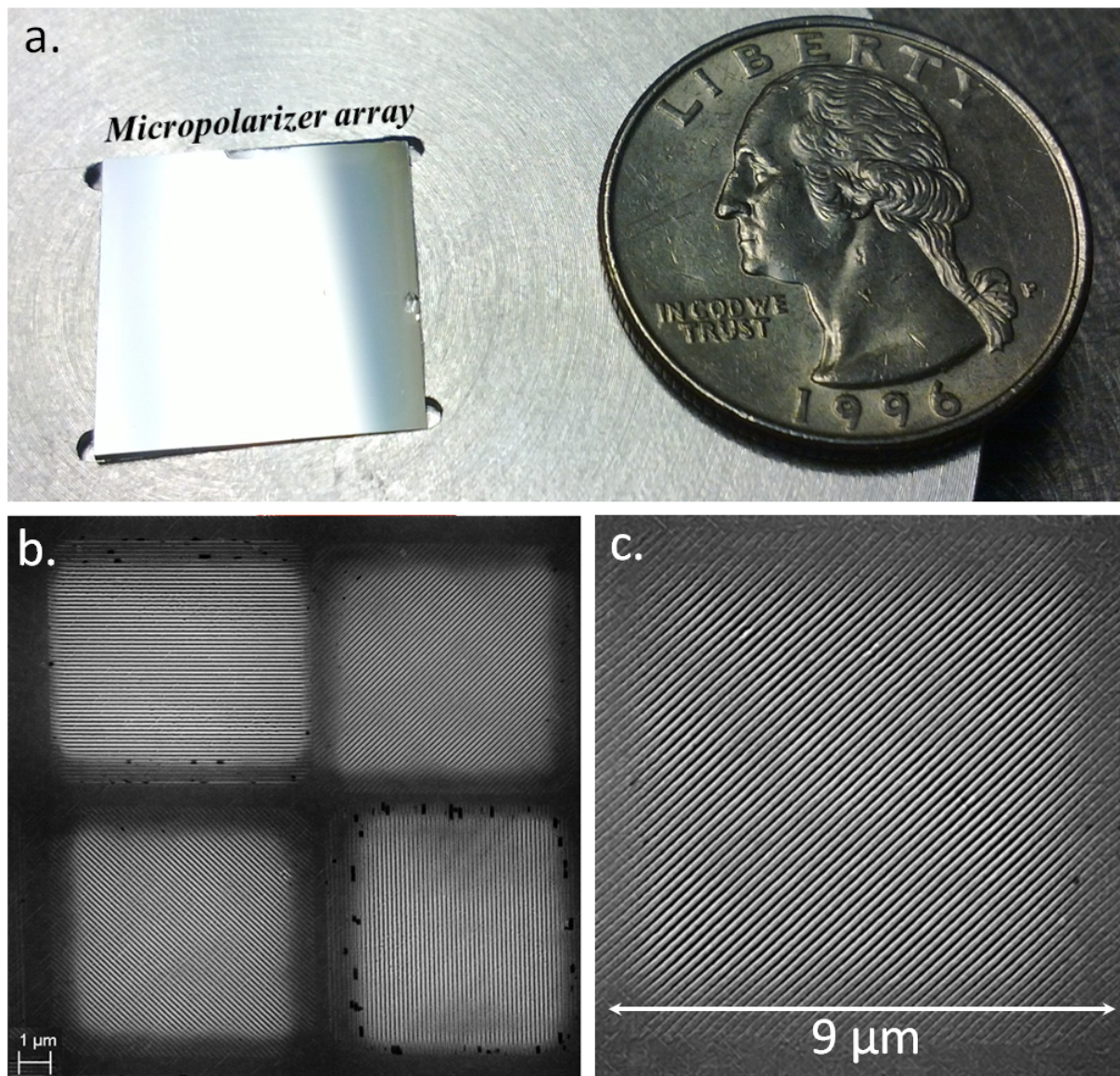


FIGURE 5.1: a). A micro grid polarizer array fabricated by Moxtek, Inc. b) A scanning electron micrograph (SEM) of a set of 4 micro polarizer pixels. Lighter regions correspond to the wires and the darker regions are opaque aluminum. The wire orientations are, clockwise starting at top left: 0° , 45° , 90° , and -45° . c) An up-close image of a single micro polarizer.

5.1 Simulations of Pixelated Wire Grid Polarizers

Pixelated polarizers, which are the base element of micropolarizer arrays (Figure 5.1), can only be modeled using full 3D simulations, because the size of the polarizers is on the order of $\sim 10\ \mu\text{m}$ and the assumption of infinite wire length is no longer appropriate (Figure 5.2, Left). Additionally, each polarizer is typically surrounded by an opaque border of variable width, which must also be faithfully simulated. In this section, we

simulate pixelated polarizers with several designs, to better understand the effects of finite wire length on polarizer performance; we compare the performance of pixelated polarizers to the conventional “bulk” polarizers discussed in the previous section.

5.1.1 Simulation Setup

We construct the pixelated polarizers by creating an aluminum film on an SiO_2 substrate and creating air gaps (that is, regions of refractive index $n = 1$), which then define the aluminum wires (Figure 5.2, Middle). This allows us to easily create opaque aluminum gaps around the pixels. As with the conventional polarizer simulations, the light source originates several microns above the aluminum layer (inside the SiO_2 substrate) and propagates downward, through the polarizer. The resulting wires have a length of $8\ \mu\text{m}$, height of $200\ \text{nm}$, width of $74\ \text{nm}$ and are separated by an airgap of $74\ \text{nm}$; these parameters are similar to those used in the “bulk” polarizer simulations.

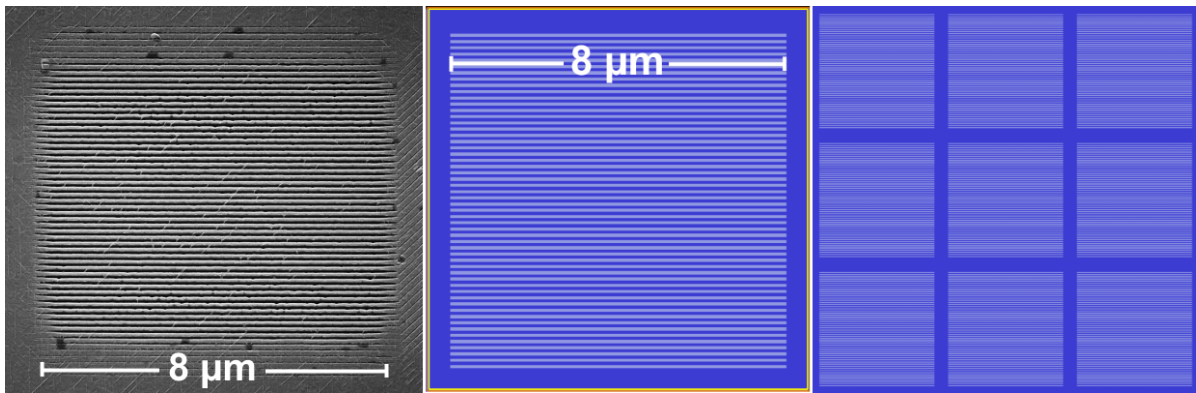


FIGURE 5.2: left: A scanning electron micrograph of a pixelated polarizer. The grey regions represent aluminum and black gaps are air. Each polarizer is surrounded by an opaque aluminum border. The wires are $\sim 8\ \mu\text{m}$ long. Middle: The simulated pixelated polarizers were created by etching gaps in an aluminum layer to create wires of finite length. In this case, the wires had a length of $8\ \mu\text{m}$ and a height, width and air gap of $200\ \text{nm}$, $74\ \text{nm}$ and $74\ \text{nm}$, respectively. The wires were surrounded by an opaque aluminum gap $0.5\ \mu\text{m}$ wide. Right: The pixelated polarizers are simulated using periodic boundary conditions in the \hat{x} and \hat{y} directions, to create an effectively infinite array of identical polarizers.

The simulated region is $9\ \mu\text{m} \times 9\ \mu\text{m} \times 7\ \mu\text{m}$, which includes a $0.5\ \mu\text{m}$ wide opaque aluminum border around each pixel (indicated by the blue border in Figure 5.2, Middle). The simulation uses periodic boundary conditions in the \hat{x} and \hat{y} directions and absorbing

boundaries in the $\pm\hat{z}$ directions. This creates an infinite grid of identical pixelated polarizers, separated by an opaque gap aluminum gap of $1\ \mu\text{m}$ (see Figure 5.2, Right). The smallest mesh cells were set to be $3.7\ \text{nm}$, which provides sufficient numerical accuracy (see Section 4.1.4.1). The resulting simulated volume consisted of ~ 6 billion mesh nodes and required $370\ \text{GB}$ of RAM to run.

5.1.2 Convergence of Non-rectilinear Structures

Full 3D simulations allow modeling of structures that do not line up neatly with the simulation mesh, such as pixels with wires tilted at some angle other than 0° or 90° (Figure 5.3). In these cases, the meshing algorithm does not conform to the boundary of the structure as efficiently as for the rectilinear case, which has been most commonly studied in the past. To investigate the effects of this mesh-structure mismatch, I performed convergence testing on pixels with wires tilted at 45° (Figure 5.3, Right).

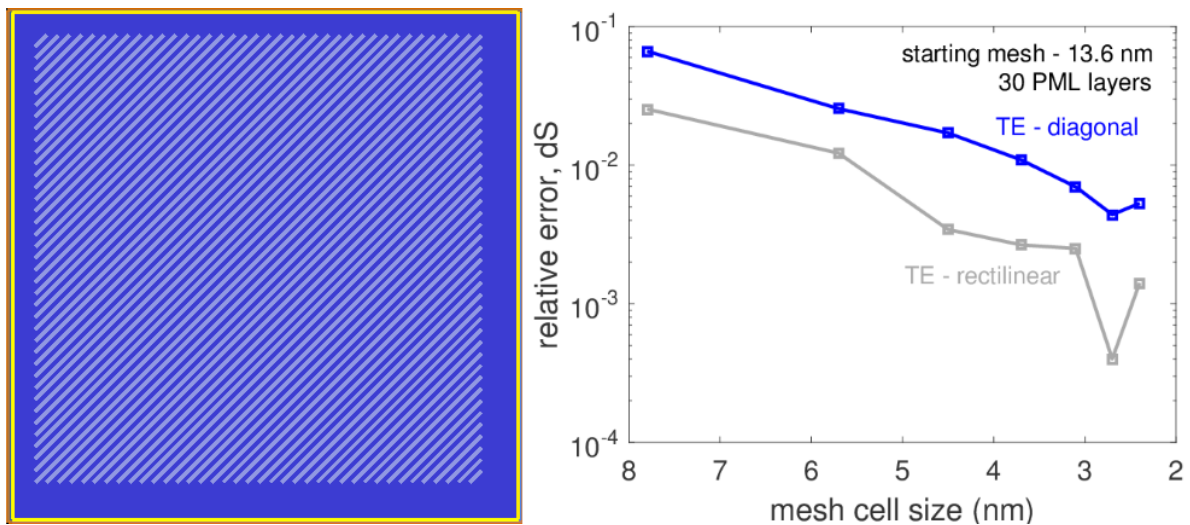


FIGURE 5.3: *Left:* Pixels with diagonal wires are more difficult to mesh using a rectilinear grid. *Right:* These simulations converge at a similar rate as simulations of rectilinear structures, but with a systematically higher relative error.

Simulations with diagonal wires do not converge as quickly as the rectilinear case of 0° wires (Figure 5.2). Nevertheless, simulations with mesh cells smaller than $5\ \text{nm}$ produce results that agree at the 1% level or better. For example, decreasing the cell size from $3.7\ \text{nm}$ to $3.1\ \text{nm}$ changes the results by only 0.6%. Therefore, my previous choice to use a mesh with cell size of $3.7\ \text{nm}$ remains adequate in this case. However, this illustrates the

need for careful convergence testing of all geometries that are being simulated, especially when the mesh size is relatively coarse.

5.1.3 Performance of Pixelated Polarizers

We characterize the performance of pixelated polarizers (as for the “bulk” polarizers) by propagating TE and TM polarized plane wave pulses and measuring the ability of the polarizers to transmit the desired components and reject the unwanted states. First, we consider a polarizer design that consists of wires with uniform lengths, as in Figure 5.2.

The transmission of pixelated polarizers is less than that of conventional polarizers for the TE state (Figure 5.4). This drop in transmission is mostly a result of non-uniform fill factor due to the opaque border around each polarizer. The pixelated polarizers were designed with an effective area of $8\ \mu\text{m} \times 8\ \mu\text{m}$, which is only 79% of the $9\ \mu\text{m} \times 9\ \mu\text{m}$ simulation region. If we account for this geometric fill factor effect, the $8\ \mu\text{m}$ long wires of pixelated polarizers appear to work almost as well as the conventional “infinite” polarizers (Figure 5.5).

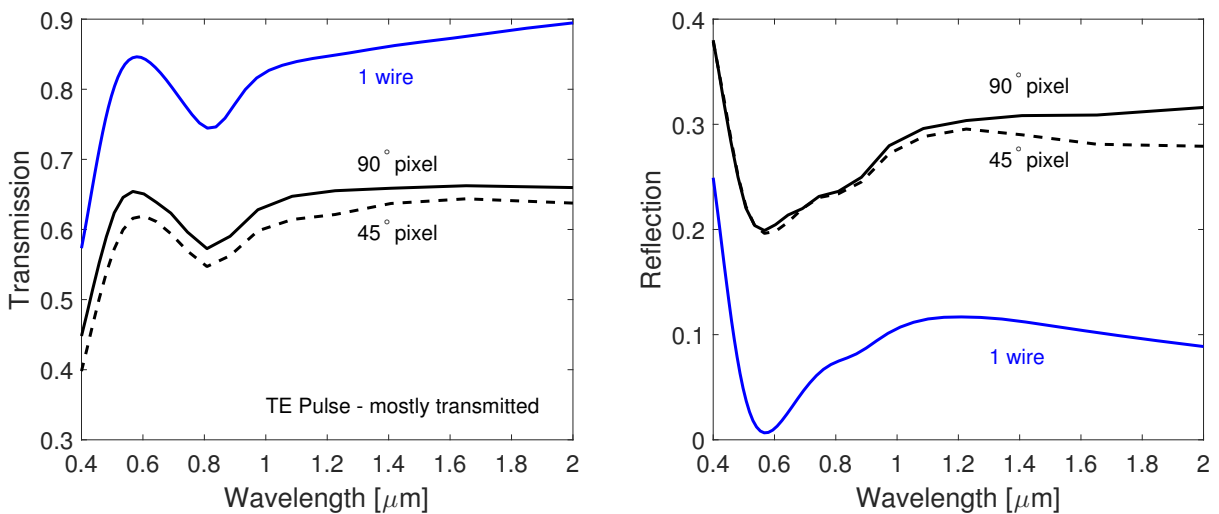


FIGURE 5.4: The transmission and reflection of the TE pulse for pixelated polarizers as compared to the conventional polarizer with similar wire parameters. The lower transmission of pixelated polarizers can be mostly explained by the non-uniform fill factor caused by the opaque border around each pixelated polarizer.

However, even the transmission curves that are “adjusted for fill factor” do not exactly match the predictions for conventional polarizers. Pixelated polarizers still show a slightly

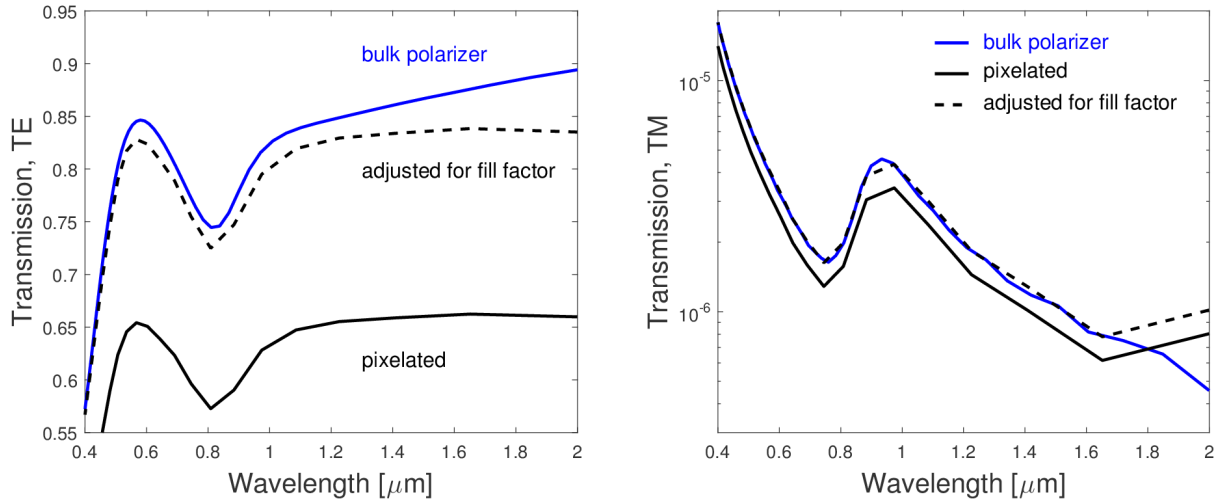


FIGURE 5.5: The transmission of pixelated polarizers as compared to the conventional polarizer with similar wire parameters, for TE (Left) and TM (Right) components. The lower transmission for both states can be mostly explained by the non-uniform fill factor caused by the opaque border around each pixelated polarizer; however, even after scaling the transmission by a constant to adjust for the fill factor (dashed line), the pixelated polarizer does not show identical performance to conventional polarizers.

lower transmission across all wavelengths; furthermore, the improvement in throughput (and rejection) at longer wavelengths seen in conventional polarizers is not seen for pixelated polarizers. This may be a sign that the finite size of pixelated polarizers becomes important when the wavelength of light begins to approach the size of the polarizer itself. Another possibility is that the opaque aluminum borders absorb a substantial fraction of the longer wavelength light.

The ability of pixelated polarizers to block the TM state also differs from conventional polarizers (Figure 5.6). The 90° pixelated polarizer blocks slightly more light than a bulk wire grid. This can be attributed to the lower fill factor, just as for the TE transmission. However, the 45° pixelated polarizer is significantly worse at blocking the TM state. This may indicate that the shorter wires in the corners of these polarizers are less effective.

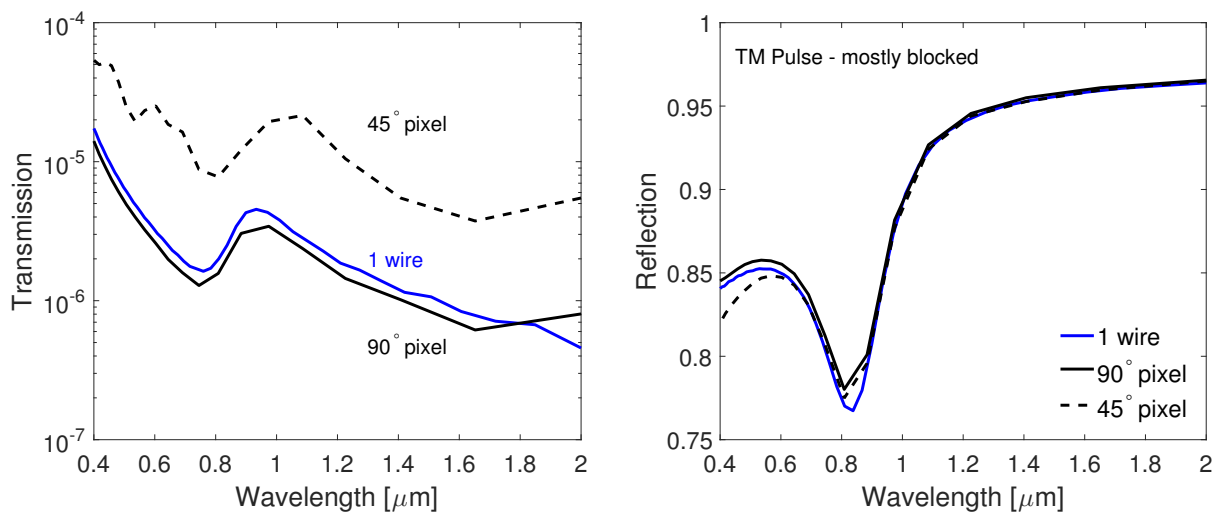


FIGURE 5.6: The transmission and reflection of the TM pulse for pixelated polarizers as compared to the conventional polarizer with similar wire parameters.

5.2 Performance of Micropolarizer Superpixels

The simulations presented in the previous sections are of individual micropolarizer pixels. This kind of study is useful to determine the effect of the physical pixel parameters on the pixel’s performance. However, real micropolarizer arrays consist of many pixels and the performance of the MPA as a whole can only be modeled with simulations of the entire array structure. This is because simulations of individual polarizer pixels (or, worse yet, semi-infinite wires) do not take into account the cross-talk that arises due to diffraction and multiple reflections in the device. To model these effects, we simulated 2×2 sets of polarizer pixels with orientations of 0° , 45° , 90° and 135° at the same time (Figure 5.7). The \hat{x} - and \hat{y} -direction boundary conditions were made periodic, so the effective structure that was modeled was a repeating pattern of the 2×2 set (Figure 5.7, *Right*), which is a good representation of the real devices (Figure 5.1).

The simulated superpixels consisted of polarizer pixels with a $9 \mu\text{m}$ pitch and $1 \mu\text{m}$ wide opaque region, which separated the individual pixels. This resulted in individual pixels with effective dimensions of $8 \mu\text{m} \times 8 \mu\text{m}$, as before. The wires had width and spacing of 74 nm and height of 200 nm ; note that aliasing effects in Figure 12 give the impression of non-uniform wire spacing, which is not the case.

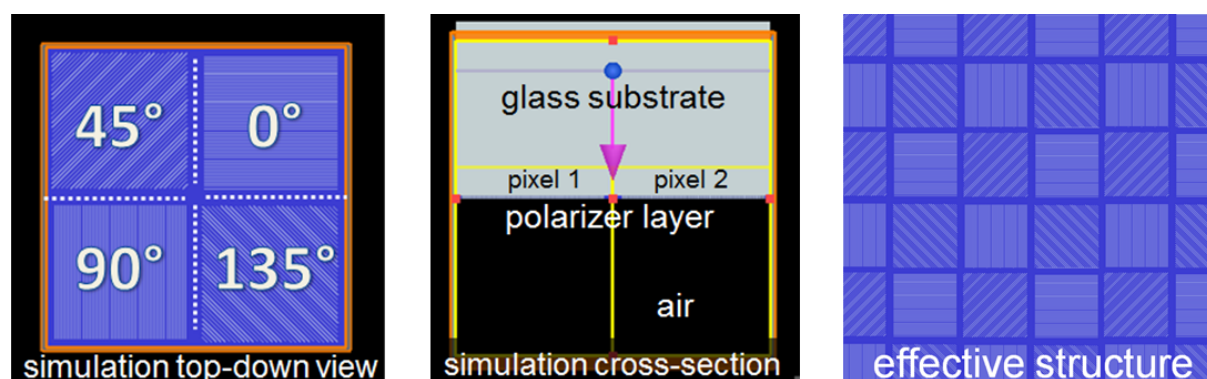


FIGURE 5.7: *Left*: To model the performance of the whole MPA, pixels with different orientations were modeled at the same time. The simulated region included 4 pixels with $9 \mu\text{m}$ pitch. The white dashed lines indicate the regions where cross-talk measurements were made (see Section 5.2.2). *Middle*: A cross-section of the simulated devices shows a setup similar to the one used in the simulations of individual pixels. *Right*: The periodic boundary conditions around the set of 4 pixels create an effective structure that is representative of real MPAs – a repeating pattern of “superpixels”

The electric field $5\ \mu\text{m}$ below each pixel is recorded with a monitor with dimensions of $9\ \mu\text{m} \times 9\ \mu\text{m}$ (Figure 5.8). Using 4 separate monitors allows a relatively straightforward prediction of total flux incident on the detector pixel below a particular micropolarizer pixel. Additional monitors were placed “vertically” (perpendicular to the plane of the micropolarizer) in the regions between each pixel, to measure any cross-talk between pixels (indicated by white dashed lines in Figure 5.7, *Left*).

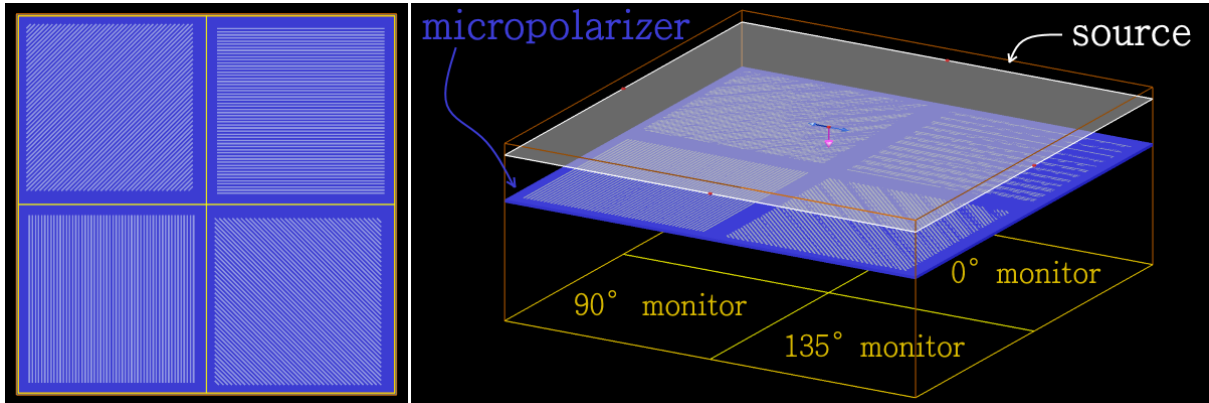


FIGURE 5.8: *Left*: A top-down view of the simulated region, showing the 4 micropolarizer pixels. *Right*: An isometric representation of the simulated region, showing the location of the electric field monitors. The glass substrate (which is on top of the blue micropolarizer layer) is not shown.

5.2.1 Simulation Results

The performance of the MPA superpixels was characterized by the transmission and the contrast ratio of the individual pixels in the superpixel. Because we simulate pixels of different orientations at the same time, it is possible to calculate the contrast ratio using a single simulation: the transmission of a 0° pulse through a 0° pixel and 90° pixel can be used to calculate the contrast ratio. Similarly, a 45° pulse can be used to characterize the 45° and 135° pixels. .

First, let’s consider the propagation of a pulse polarized at 0° (Figure 5.9). The 90° micropolarizer transmits most of this pulse (because the polarization is perpendicular to the wires), while the 0° micropolarizer reflects most of the light. The transmission of the 0° micropolarizer increases from $\sim 10^{-3}$ in the blue wavelengths to $\sim 10^{-2}$ in the near-infrared regime. This results in a contrast ratio of ~ 250 , which rapidly decreases as the

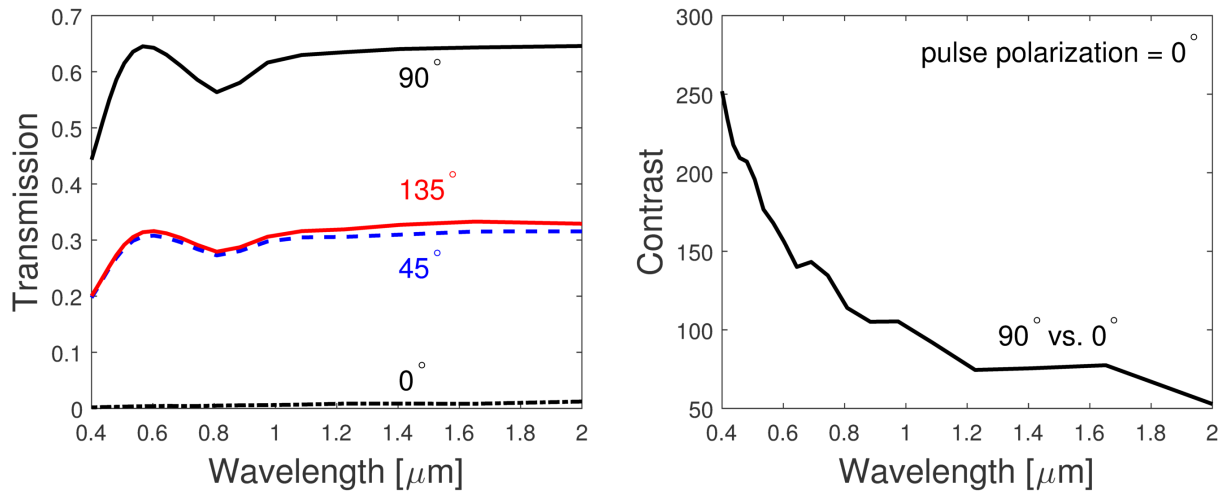


FIGURE 5.9: *Left:* The intensities recorded by monitors belonging to each pixel orientation show mostly expected behavior. The pixel with 90° wires transmits most of the 0° polarized light, while the 45° and 135° pixels transmit roughly half of that value. *Right:* The contrast ratio in simulations with all 4 pixels can be calculated using a single polarized pulse. Here, we show the ratio of the intensities measured by the 0° and 90° pixels monitors in response to a 0° polarized pulse.

wavelength of light increases. As expected, the micropolarizers oriented at 45° and 135° show transmissions roughly half that of the 90° polarizer. Next, we show the transmission of a pulse polarized at 45° (Figure 5.10). The results are similar to the previous case: the 135° , 90° , and 0° , behave as expected, while the 45° micropolarizer appears to transmit more light than we would expect based on simulations of individual micropolarizers (see Section 5.1.3).

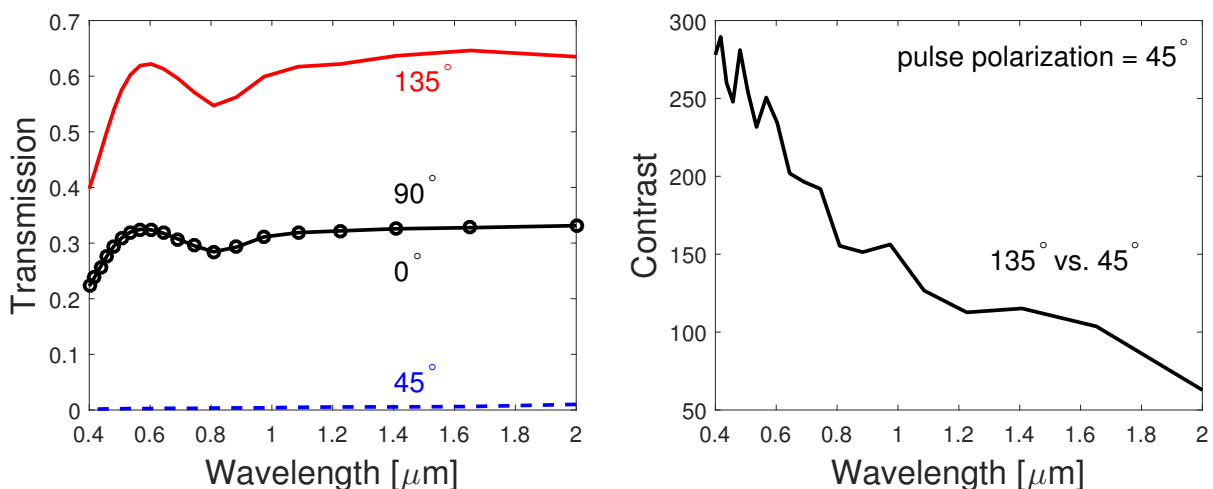


FIGURE 5.10: *Left:* The pixel with 135° wires transmits most of the 45° polarized light, while the 0° and 90° pixels transmit roughly half of that value. *Right:* The contrast ratio of the intensities measured by the 135° and 45° pixels monitors in response to a 45° polarized pulse.

This “extra light” measured by the electric field monitors belonging to the 0° and 45° pixels has several possible sources. First of all, the ability of these pixels to reject polarization states parallel to their wire directions may be poor; this is not likely to be the case, because the simulations of individual pixels presented in Section 5.1.3 show that pixels with these physical parameters transmit, at most, $\sim 10^{-4}$ of these unwanted states. Secondly, there could exist a mode of cross-talk that allows light from neighboring micropolarizers to be recorded by these monitors. The most plausible mechanism for this would be diffraction of light which occurs at the edges of each pixel. Finally, in a real device there could exist reflections between the polarizer layer and the top surface of the glass substrate, which could cause stray light to be scattered or directly reflected into these monitors. The simulations we present in this work only allow us to study the diffraction mechanism, which we investigate in the next section.

5.2.2 Analysis Of Diffraction-induced Cross-talk

To study how a micropolarizer diffracts light, we simulated an isolated micropolarizer, surrounded by a large opaque region (Figure 5.11). This allows us to study the near-field diffraction pattern, for a wide range of wavelengths. The intensity of the electric field (on a logarithmic scale) as recorded by the extended monitor is shown in Figure 5.12, for the shortest and longest wavelength we simulate. As one might expect, the micropolarizer produces a near-field diffraction pattern similar to that of a rectangular aperture. The amount of light diffracted outside the $9\ \mu\text{m} \times 9\ \mu\text{m}$ region which defines the micropolarizer pitch increases at longer wavelengths. We can compare the amount of light within the central $9\ \mu\text{m} \times 9\ \mu\text{m}$ region to the total intensity transmitted by the micropolarizer (Figure 5.13).

Because our simulations are 3D, we can use vertical monitors at the boundaries of each micropolarizer to estimate how much flux can be expected to end up in a pixel due to light diffracted by its neighbors. Let’s consider the simulation of 4 micropolarizers using a 45° polarized source (Figure 5.14, *Left*). The 45° micropolarizer is surrounded by 0° and 90° polarizers. Because the polarizers diffract mostly along their edges (see Figure

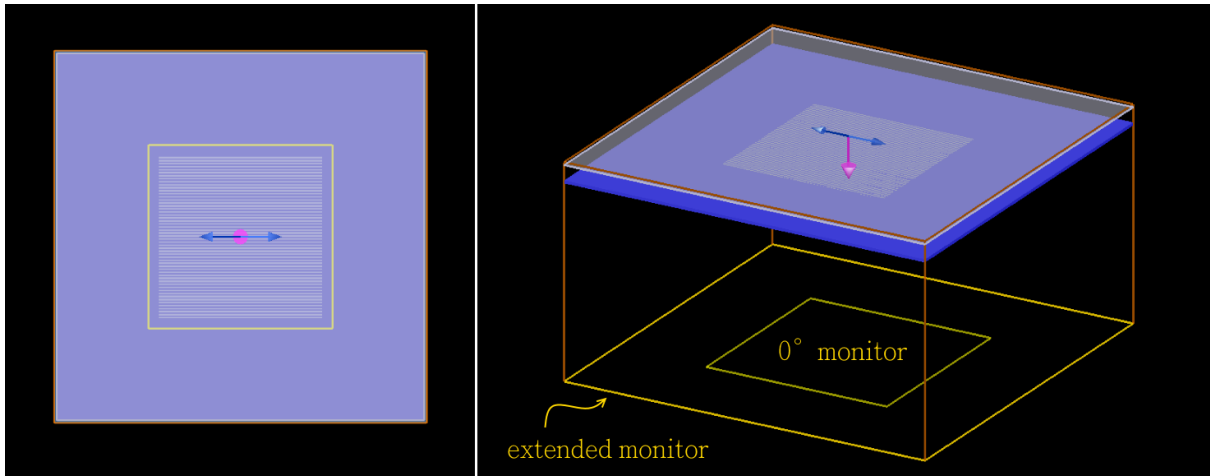


FIGURE 5.11: *Left*: To measure the diffraction pattern due to a micropolarizer array, we simulated an isolated micropolarizer surrounded by a large opaque border. *Right*: The electric field was recorded by a normal-sized monitor and an extended monitor, to show the diffracted light.

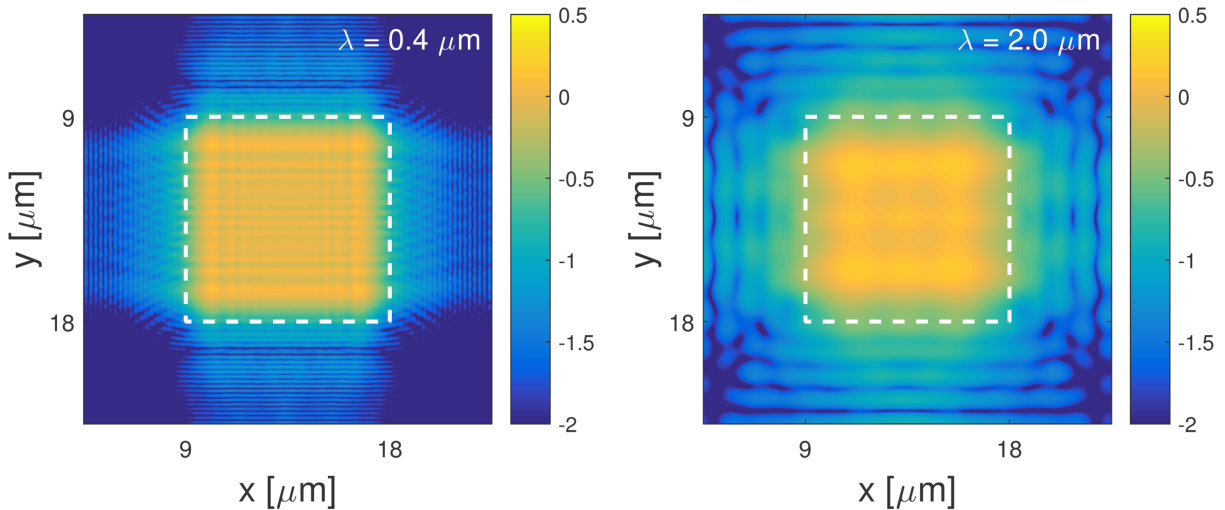


FIGURE 5.12: The electric field intensity (log scale) distribution for 400 nm (*Left*) and 2000 nm light (*Right*) transmitted by a 0° micropolarizer. The white dashed lines show the location of a $9\ \mu\text{m} \times 9\ \mu\text{m}$ region, $5\ \mu\text{m}$ below the micropolarizer.

5.12), we can expect that most of the light diffracted into the 45° monitor will be from the 0° and 90° polarizers.

Using the monitors along the $45^\circ - 90^\circ$ boundary and the $45^\circ - 0^\circ$ boundary, we can measure how much light was diffracted into the 45° monitor. The intensities recorded by the crosstalk monitors passing through these boundaries are shown in Figure 5.14 (Right). For reference, we also show the intensity recorded by the 45° monitor. We can account for most of the flux measured by the 45° monitor by adding up the flux passing through the

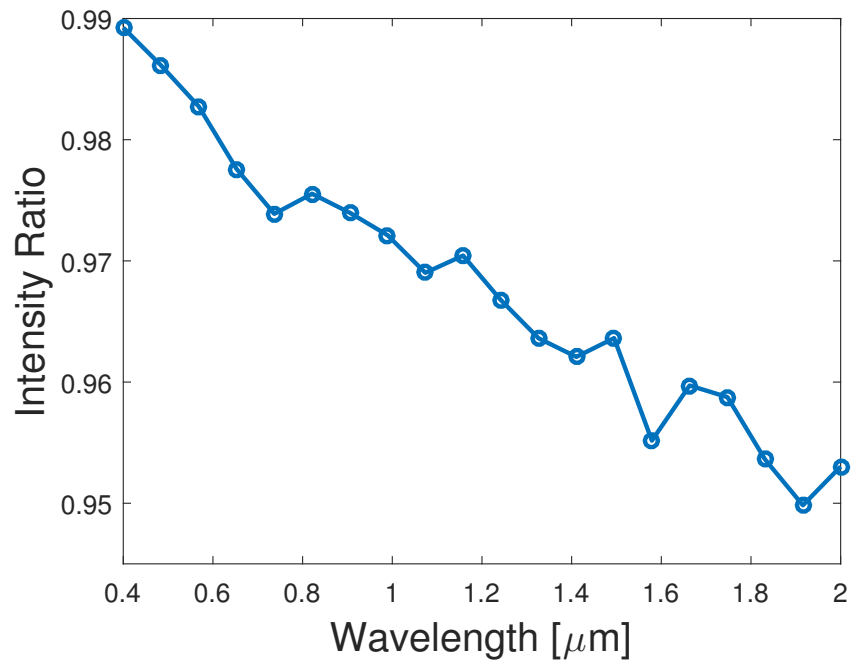


FIGURE 5.13: Fraction of light measured by a central monitor directly below the micropolarizer and an extended monitor, which also captures the diffracted light (see Figure 5.11). Ideally, all light that passes through a single micropolarizer would remain in a region directly below that polarizer.

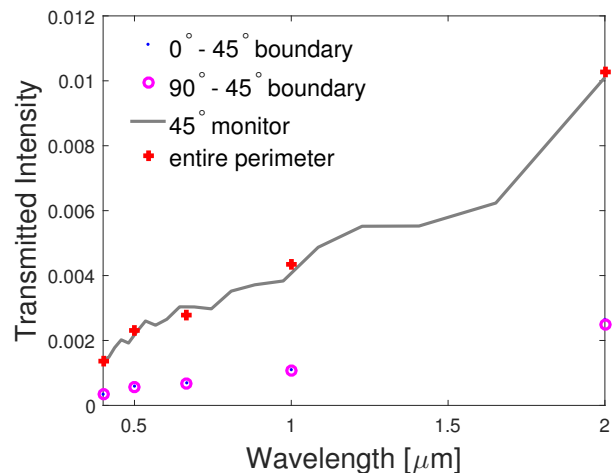
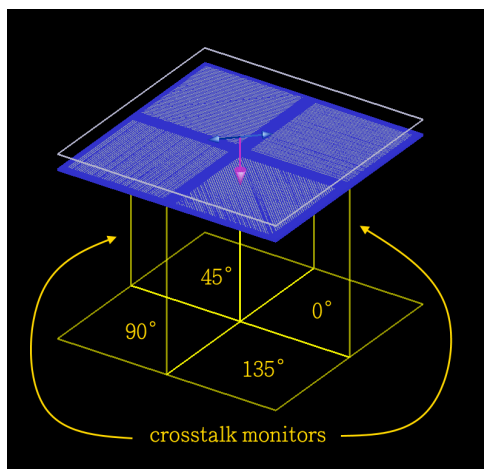


FIGURE 5.14: *Left*: Vertical monitors along the boundaries between individual pixels can be used to measure the crosstalk from diffraction directly. *Right*: The intensity of light passing through the vertical boundaries between the 45° polarizer and its neighbors accounts for most of the intensity measured by the 45° monitor.

boundaries of the 45° polarizer (and multiplying by 2, to account for the other 2 sides). In this way, we can directly study the process by which diffraction degrades the contrast of micropolarizer arrays.

5.2.3 Summary of Pixelated Polarizer Simulations

The unique advantage of fully 3D simulations is the ability to simulate pixels with different wire orientations at the same time. This allows simulations to properly model effects of cross-talk, which are present in real devices and cannot be simulated in 2D models. We modeled 2×2 sets of 0° , 45° , 90° , and 135° pixels and found that the contrast ratio for this configuration is much lower than the contrast ratio of individual polarizers, as is seen in real devices. We investigated the effect of diffraction around the pixel edges and found that it can be a significant channel for cross-talk. Specifically we find:

1. Simulations of individual pixelated polarizers show similar transmission and contrast ratios to that of “bulk” conventional wire grid polarizers. Opaque borders around micropolarizers, naturally, decrease transmission; however, the finite length ($\sim 8 \mu\text{m}$) of the conducting wires does not seem to have a large effect on polarizer performance in the $0.4 \mu\text{m} - 2 \mu\text{m}$ regime.
2. Simulations of 2×2 sets of polarizers show much lower contrast ratios ($\sim 250 - 50$) than simulations of the same structures, individually. Furthermore, the contrast ratio decreases as the wavelength of light becomes longer, whereas the individual polarizers tend to work better at longer wavelengths. This suggests that the mechanism that lowers the contrast of micropolarizer arrays is cross-talk due to diffraction of light at the pixel edge (which is stronger for longer wavelength light).
3. Using 3D models and electric field monitors at the boundaries of each micropolarizer, we have confirmed that the loss of contrast can be directly attributed to the cross-talk that results from the diffraction of light by a pixel’s neighbors.

Chapter 6

Measurement of Polarization

The polarization of light is challenging to measure due to a lack of detectors with inherent sensitivity to the state of polarization. Modern photon detectors, such as charge-coupled devices (CCDs), active pixel sensors (CMOS), photodiodes, bolometers, photomultiplier tubes (PMTs) and photographic film, only measure the intensity of light and do not differentiate between different polarizations. This means polarization measurement must be accomplished through a scheme that modulates the intensity of radiation, based on its polarization state. This intensity modulation can then be measured and demodulated to recover the polarization state of the source. Over the years, several different methods to modulate the intensity have been developed. The modulation can occur in the spatial, temporal and spectral domains; see reviews by [Tyo et al. \(2006\)](#) and [Snik et al. \(2014\)](#). Typically, the intensity is modulated using one of a number of polarizers.

6.1 Polarimetry With a Single Polarizer

The most simple device to measure polarization, a *polarimeter*, can be constructed using a single polarizer and a photodetector. When the detector is the human eye, these devices are called polariscopes. The polarizer is used to sample the electric field components along several angles, to derive the Stokes parameters (Figure 6.1). A typical approach is to measure the intensity of the source with the polarizer oriented at 0° , 45° , 90° , and

-45° and calculate the Stokes parameters using the relations from Chapter 2,

$$I = i_{0^\circ} + i_{90^\circ}$$

$$Q = i_{0^\circ} - i_{90^\circ}$$

$$U = i_{+45^\circ} - i_{-45^\circ}$$

Division of time polarimetry

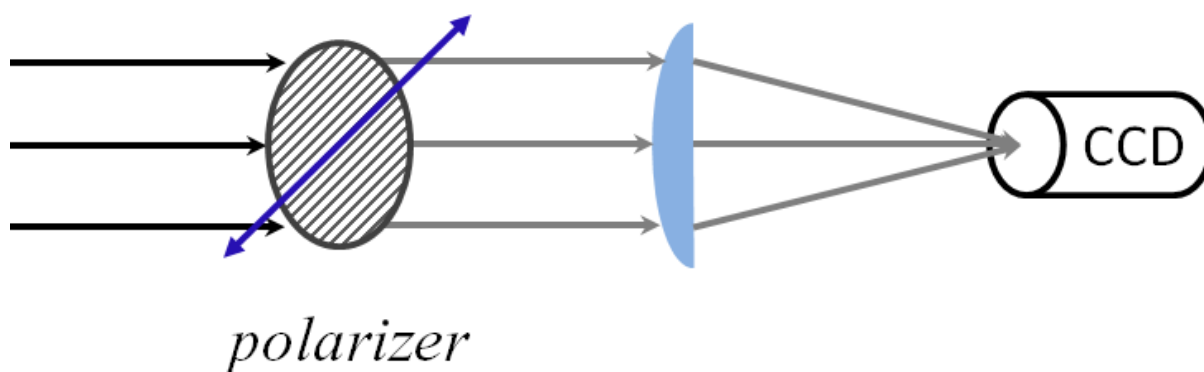


FIGURE 6.1: Division of time polarimetry. The degree and angle of linear polarization can be determined by measuring the intensity through a polarizer oriented along several directions. This is typically accomplished by rotating a single polarizer (blue arrow indicates the polarizer axis) or by using several polarizers in a filter wheel (as in done on *The Hubble Space Telescope*).

Division of time schemes are straightforward and require only simple hardware. Accurate, high precision polarimetry is possible with these systems, if the source/scene being observed does not change in the time it takes to acquire the needed intensity measurements. In practice, this is rarely the case and the (mis)registration of images becomes a large source of polarimetric errors. If the scene/target changes substantially quickly, either due to motion with respect to the imaging system or due to intrinsic brightening and dimming, polarimeters that can measure several electric field orientations in the same exposure should be used.

6.2 Snapshot Polarimeters

The polarimetric information in a scene can be obtained with a single exposure, if the electric field is sampled along several directions simultaneously (Figure 6.2). The first systems of this kind used polarizing beamsplitters (see Section 3.5.1). This technique allows high speed polarimetry with only a moderate increase in instrument complexity as compared to division-of-time polarimeters; also, the frugal observer can use all of the light in a scene.

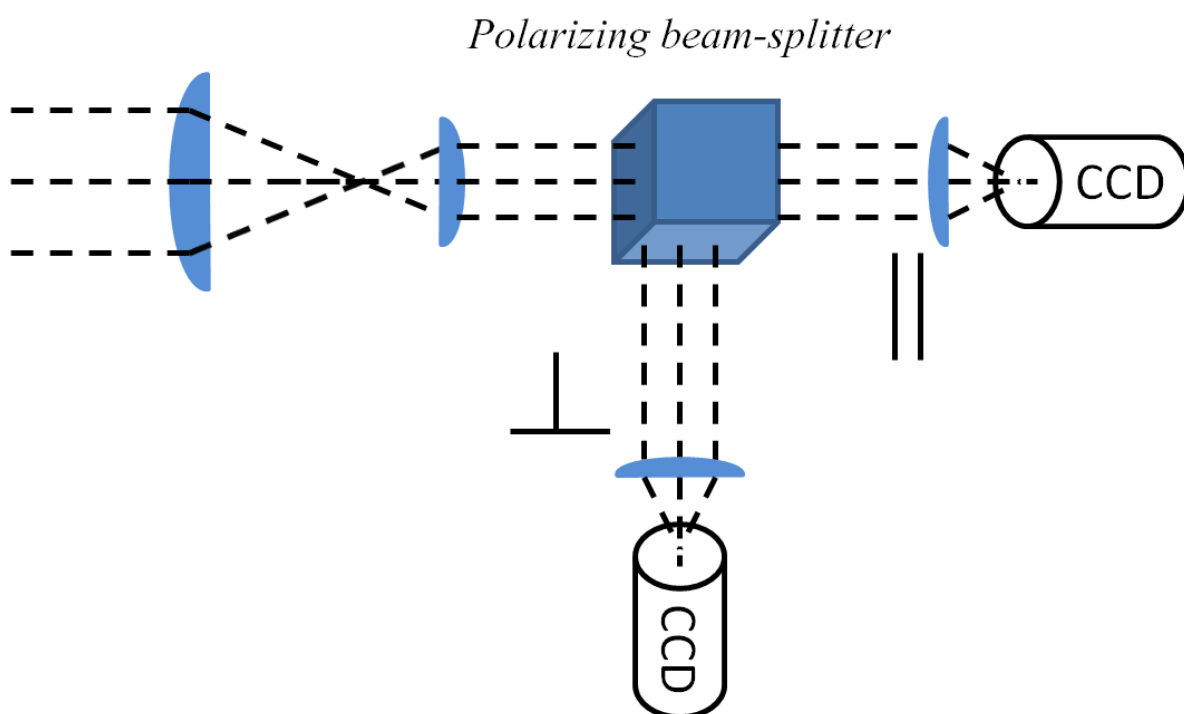


FIGURE 6.2: Division of intensity polarimetry. Polarimeters that sample the electric field along several orientations simultaneously can be built using beam-splitting optics and several detectors. The incident light is split and imaged in two or more channels simultaneously.

The disadvantages of this approach stem from the need for extra optics and detectors. Because the system forms several different images, they must be acquired by different cameras or the images have to be overlaid in the same focal plane and separated in post-processing. The extra weight, size and power requirements of these polarimeters are especially problematic for deployment on people, land vehicles, ships, aircraft, and spacecraft. Finally, these polarimeters are not totally rid of the problem of image registration.

6.2.1 Division of Focal Plane Polarimetry

Area format detectors (like CCDs and CMOS arrays) allow a way to perform the intensity modulation in the focal plane. One important implementation of the division of focal plane technique is utilized by snapshot polarimeters that use beam splitting optics to project 2 or 4 separate images onto the focal plane of a single detector. Some systems, like the Durham polarimeter (Scarrott et al., 1983) and Extreme Polarimeter (Rodenhuis et al., 2012), project two images side by side (Figure 6.3). Other designs, like the RoboPol instrument (King et al., 2014), have much smaller separations between the modulated images (Figure 6.4).

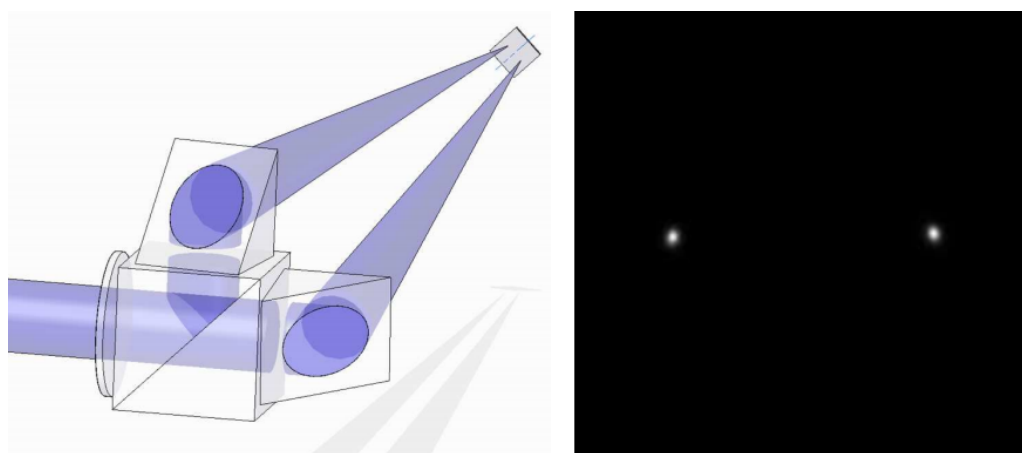


FIGURE 6.3: *Left:* The Extreme Polarimeter (ExPo) uses beam splitters to record images polarized along two orthogonal directions simultaneously, on the same focal plane. *Right:* Two images of an object appear side-by-side on ExPo's single detector.

Figure is adopted from Rodenhuis et al. (2012). ©SPIE. Used with Permission.

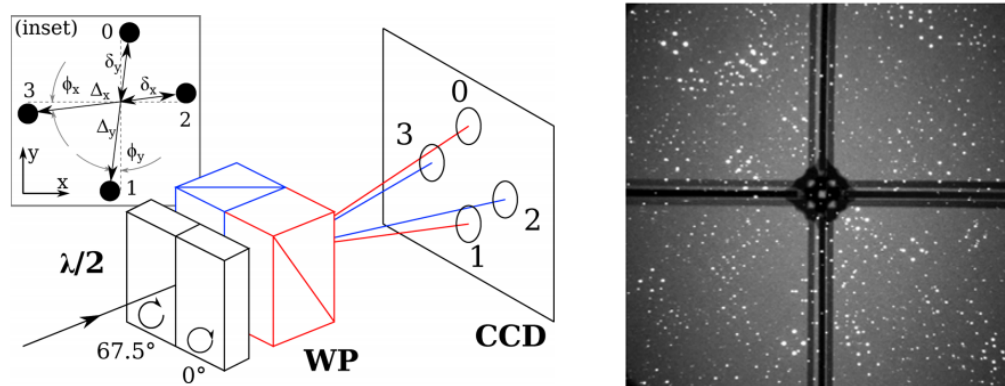


FIGURE 6.4: *Left:* In some instruments, like RoboPol, the 4 separate images are recorded by a single detector, resulting in a very crowded image plane (*Right*). Adopted from Fig. 1 and Fig. 2 of King et al. (2014).

6.3 The Dual-Beam Technique

Most high precision polarimeters use some elements from all of the aforementioned modulation schemes. For example, the state of the art polarimeters in the Gemini Planet Imager (Macintosh et al., 2006) and the SPHERE-ZIMPOL (Roelfsema et al., 2010) instrument use rapidly switching wave plates, beam splitters, and project multiple images onto a single focal plane. Through a combination of several modulation schemes, these advanced polarimeters are designed to use the “dual beam” or “beam exchange” modulation technique (Donati et al., 1990; Semel et al., 1993). In its simplest implementation, the dual beam method uses a retarder and a polarizing beam splitter to produce two images of the source, with orthogonal polarization. The retarder is then used to change the orientation of each beam, for successive measurements (see Figure 6.5).

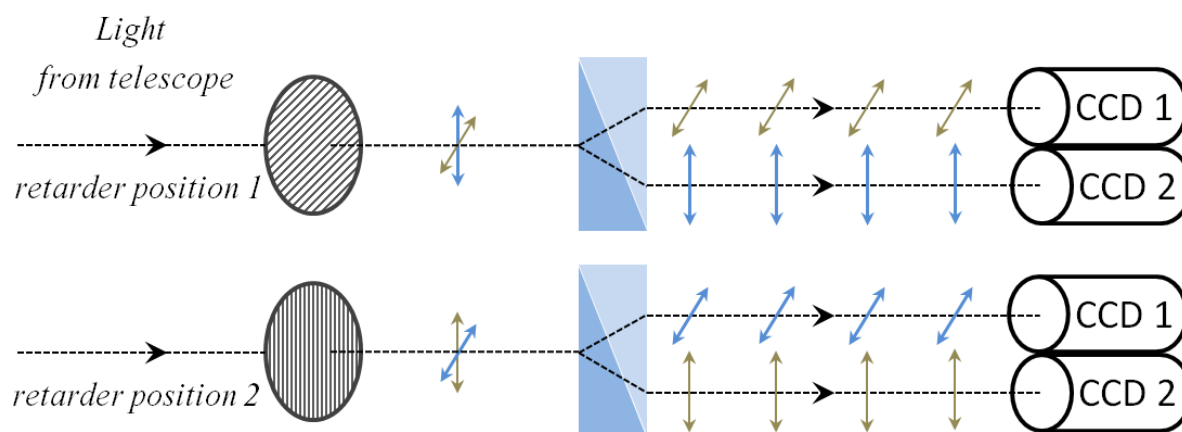


FIGURE 6.5: The dual beam modulation scheme uses a retarder and a beam splitter to capture two polarization states simultaneously, with a single or multiple detectors. The retarder is used to switch the orientation of both beams for each successive measurement.

This technique is extremely powerful, because the same detector (or the same pixels in an imaging sensor) are used to measure the intensity of both polarization states. Furthermore, this is still a “snapshot” technique, because two states are captured simultaneously. Because the same detector is used to measure both states, this measurement is truly “relative” and many systematic and instrumental effects can be dramatically suppressed.

6.4 Polarization-Sensitive Detectors

One of the most recent innovations in the field of polarimetry is the development of imaging sensors that perform the intensity modulation entirely at the sensor level. These polarization-sensitive imaging detectors operate in an analogous fashion to color-sensitive imaging arrays. These devices are capable of snapshot polarimetry with a single focal plane, across a broad wavelength range and are a radical departure from previous polarimeters.

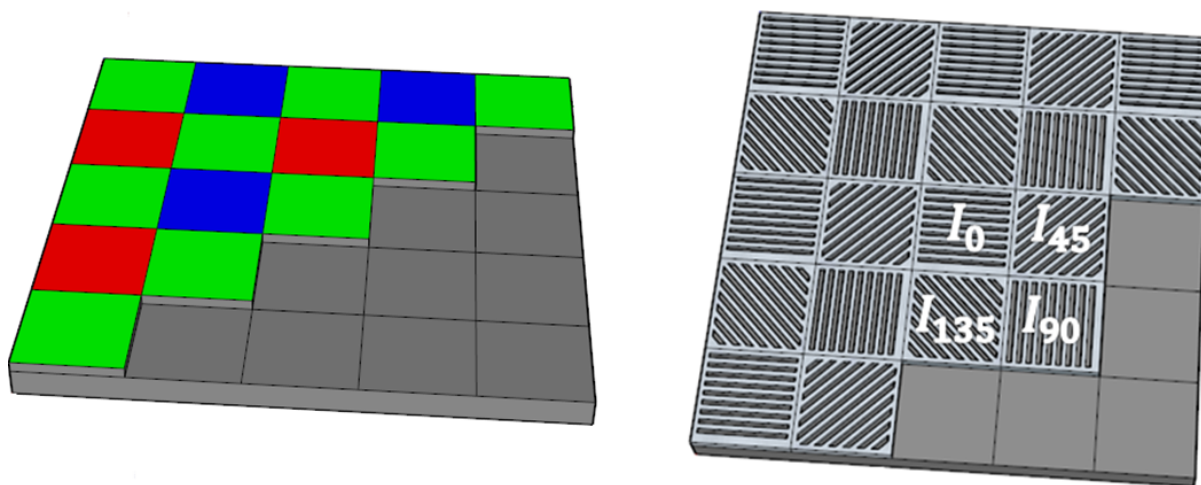


FIGURE 6.6: *Left:* a color filter array divides the focal plane into sets of 2×2 “super-pixels” that determine the color of a section of a scene using the intensities measured by individual detector pixels. *Right:* A micropolarizer array-based polarimeter works in a fashion similar to a color sensor to measure polarization across a scene. Each polarizer pixel is matched spatially to a single detector pixel. Light passing through a polarizer pixel is modulated according to the polarizer’s orientation and the intensity is measured by the detector pixel.

Polarization-sensitive sensors are the first true “general purpose” polarimeters. Most conventional polarimeters have been built for very specific measurements, and the idiosyncrasies of their designs prevented them from being adopted for other measurements in other fields. This precluded the spread of polarimetric techniques into many fields that may otherwise benefit from polarimetry.

Polarization-sensitive detectors offer many attractive features, as compared to the polarimeters described above. Polarization-sensitive focal plane arrays are extremely compact, light weight, mechanically robust, and require no moving parts. Furthermore, these

devices are permanently aligned (the micropolarizer array does not move with respect to the imaging sensor), which allows for reliable and long-lasting calibration.

Despite their many advantages, these devices suffer from two important drawbacks, which stem from the problem of “instantaneous field of view” of each pixel (Tyo et al., 2006). Because each pixel sees a different part of the scene, polarimetric errors can arise due to intrinsic intensity differences seen by two pixels. More importantly, the polarimetric information is derived using intensities measured by four different pixels (in contrast to polarimeters which use the division of time or dual-beam technique). This means that any pixel-to-pixel response variations (due to differences in quantum efficiency, gain, etc.) may introduce errors into the polarimetric analysis. As such, the performance of these detectors is limited by systematic and instrumental effects and the quality of the device characterization. These issues are explored in depth in Chapter 8.

6.5 Polarimetry With Non-ideal Polarizers

The conceptual definition of the Stokes parameters (Eq. 2.5 - 2.8) provides a phenomenological and intuitive description of polarization, however, this form is not especially useful for general purpose polarimetry. Furthermore, this definition of the Stokes parameters assumes that the measurements are made with perfect polarizers, which is never the case. In this section, I introduce the notation and mathematical tools developed for the measurement of polarization.

Astronomers (Sparks and Axon, 1999) generalized the definition of the linear Stokes parameters, Q and U , as a function of degree of linear polarization, p , and angle of linear polarization, ψ , as follows,

$$Q = Ip \cos(2\psi) \quad (6.1)$$

$$U = Ip \sin(2\psi) \quad (6.2)$$

where I is the total intensity (i.e., Stokes I). This definition of the Stokes parameters forces Q and U to follow the Rice distribution (see Section 6.5.2). This leads to a biased estimation of Q and U , especially when the polarimetric signal-to-noise ratio is low. However, this form is very convenient for specifying the state of light produced by a polarizer during the characterization process (see Section 8.1), where the signal-to-noise can be made sufficiently high that the bias is minimized.

These linear Stokes parameters can be determined using a minimum of three independent measurements with polarizers oriented at three different angles; a minimum of four measurements are need to measure the fourth parameter, Stokes V . It has been shown that by choosing a set of angles with minimal correlation, the sensitivity of the measurement to polarizer misalignment or fluctuations in source intensity can be minimized (Ambirajan and Look, 1995; Sabatke et al., 2000; Tyo, 2002). When considering only linear polarization, this means choosing angles that are evenly spaced along the equator of the Poincaré sphere, forming an equilateral triangle in the equatorial plane when measuring linear polarization (Figure 6.7). In the case of a “full Stokes” polarimeter, the choice of measurements would optimally inscribe a tetrahedron inside the Poincaré sphere.

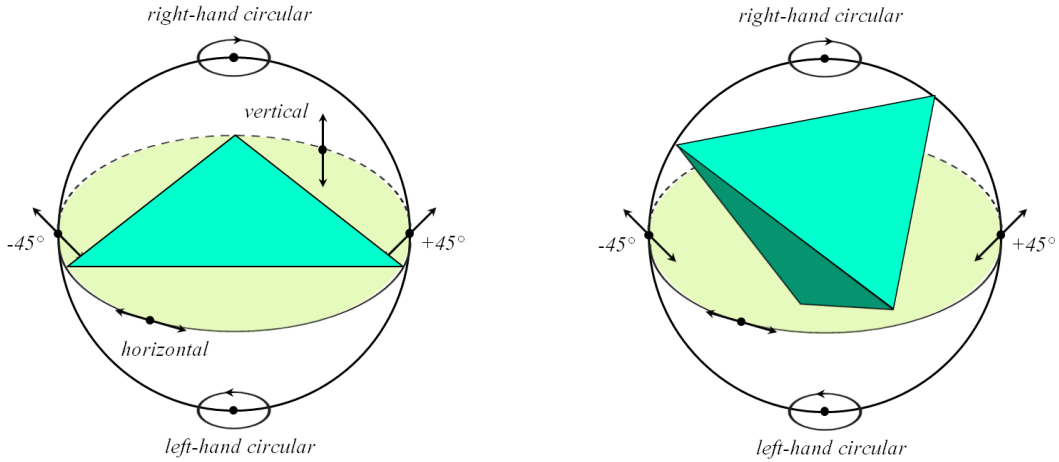


FIGURE 6.7: Optimal sampling on the Poincaré sphere for linear (Left) and full Stokes (right) polarimetry.

The intensity transmitted by a polarizer oriented at a particular angle in a set of k measurements depends on the polarization state of the incident radiation and the properties of the polarizer in the following way (Sparks and Axon, 1999; Hines et al., 2000),

$$S_k = A_k I + \epsilon_k (B_k Q + C_k U), \quad (6.3)$$

where I , Q , and U are the linear Stokes parameters, ϵ_k is the polarizer's efficiency and A_k , B_k , and C_k are transmission coefficients defined as

$$A_k = \frac{t_k}{2}(1 + l_k), \quad B_k = A_k \cos 2\phi_k, \quad C_k = A_k \sin 2\phi_k. \quad (6.4)$$

These transmission coefficients depend on the throughput of the polarizer for 100% polarized light input aligned with the polarizer axis, t_k , and a “leak” term, l_k , which is the throughput of the polarizer for 100% polarized light perpendicular to the polarizer axis; the coefficients B_k and C_k also depend on the polarizer orientation, ϕ_k . The polarizer efficiency is determined by the leak term as,

$$\epsilon_k = \frac{1 - l_k}{1 + l_k}.$$

This formalism is extremely powerful, because it provides a way to calibrate the polarimetric system, through the characterization of the polarizer's properties: t_k , ϵ_k , and

ϕ_k . If these coefficients are known, equation 6.3 can be used to determine the Stokes parameters.

If three measurements are used (for example, at polarizer angles of 0° , 60° , and 120°), the resulting system of equations can be solved directly:

$$\begin{aligned} S_{0^\circ} &= A_{0^\circ}I + \epsilon_{0^\circ}(B_{0^\circ}Q + C_{0^\circ}U) \\ S_{60^\circ} &= A_{60^\circ}I + \epsilon_{60^\circ}(B_{60^\circ}Q + C_{60^\circ}U) \\ S_{120^\circ} &= A_{120^\circ}I + \epsilon_{120^\circ}(B_{120^\circ}Q + C_{120^\circ}U) \end{aligned}$$

6.5.1 Using Linear Least Squares

If more than three measurements are made (for example at 0° , 45° , 90° , and 135°), the system of equations (6.3) becomes over-constrained. In this case, the Stokes parameters can be determined using the linear least squares method. This approach is especially useful because it leverages the redundancy that comes with using more than three angles to determine the Stokes parameters. Furthermore, the linear least squares problem can be formulated using matrix multiplication, which can be efficiently implemented in many programming languages/environments.

The system of equations that describes four intensity measurements made at four angles can be expressed in matrix form as follows¹,

$$\begin{aligned} S_0 &= A_0I + \epsilon_0(B_0Q + C_0U) \\ S_{45} &= A_{45}I + \epsilon_{45}(B_{45}Q + C_{45}U) \\ S_{90} &= A_{90}I + \epsilon_{90}(B_{90}Q + C_{90}U) \\ S_{135} &= A_{135}I + \epsilon_{135}(B_{135}Q + C_{135}U) \end{aligned} \iff \begin{bmatrix} A_0 & \epsilon_0 B_0 & \epsilon_0 C_0 \\ A_{45} & \epsilon_{45} B_{45} & \epsilon_{45} C_{45} \\ A_{90} & \epsilon_{90} B_{90} & \epsilon_{90} C_{90} \\ A_{135} & \epsilon_{135} B_{135} & \epsilon_{135} C_{135} \end{bmatrix} \begin{bmatrix} I \\ Q \\ U \end{bmatrix} = \begin{bmatrix} S_0 \\ S_{45} \\ S_{90} \\ S_{135} \end{bmatrix}$$

¹Note that I drop the use of the degree symbol here, to improve readability.

The matrix equation above can be solved for the vector of Stokes parameters by inverting the coefficient matrix,

$$\begin{bmatrix} I \\ Q \\ U \end{bmatrix} = (\mathbf{X}^T \mathbf{X})^{-1} \mathbf{X}^T \begin{bmatrix} S_0 \\ S_{45} \\ S_{90} \\ S_{135} \end{bmatrix}, \quad \mathbf{X} = \begin{bmatrix} A_0 & \epsilon_0 B_0 & \epsilon_0 C_0 \\ A_{45} & \epsilon_{45} B_{45} & \epsilon_{45} C_{45} \\ A_{90} & \epsilon_{90} B_{90} & \epsilon_{90} C_{90} \\ A_{135} & \epsilon_{135} B_{135} & \epsilon_{135} C_{135} \end{bmatrix}. \quad (6.5)$$

6.5.2 Distribution of the Stokes Parameters

Once the Stokes parameters have been determined, it is critical to determine the uncertainty of this estimate. In the presence of noise, the measured Stokes parameters, I , Q , and U , are scattered about the “true” intrinsic values of I_0 , Q_0 , and U_0 . For example, Q and U can be described with a bi-variate normal distribution (Figure 6.8) with the form,

$$g(Q, U) = \frac{1}{2\pi\sigma_Q\sigma_U\sqrt{1-R^2}} \cdot \exp\left\{-\frac{1}{2(1-R^2)}\left[\frac{(Q-Q_0)^2}{\sigma_Q^2} + \frac{(U-U_0)^2}{\sigma_U^2} - 2R\frac{(Q-Q_0)(U-U_0)}{\sigma_Q\sigma_U}\right]\right\},$$

where

σ_Q : standard deviation of Q

σ_U : standard deviation of U

$R = \sigma_{QU}^2/\sigma_Q\sigma_U$: the correlation coefficient between Q and U.

The Stokes parameters Q and U can be scaled by the total intensity Stokes I to obtain the *normalized Stokes parameters*, q and u , which are also normally distributed:

$$q = Q/I$$

$$u = U/I$$

The precision of the Stokes parameter estimation can be determined directly from the distribution of Q , U , and I , by calculating their respective variances. However, in practice there are rarely enough measurements to determine these variances directly. Because the Stokes parameters are normally distributed, the uncertainty can be estimated from the uncertainty of the individual intensity measurements, S_0 , S_{45} , S_{90} , etc. The uncertainty of the intensity measurements is affected by the traditional factors: shot noise, read noise, dark noise and the uncertainty associated with the flat field calibration.

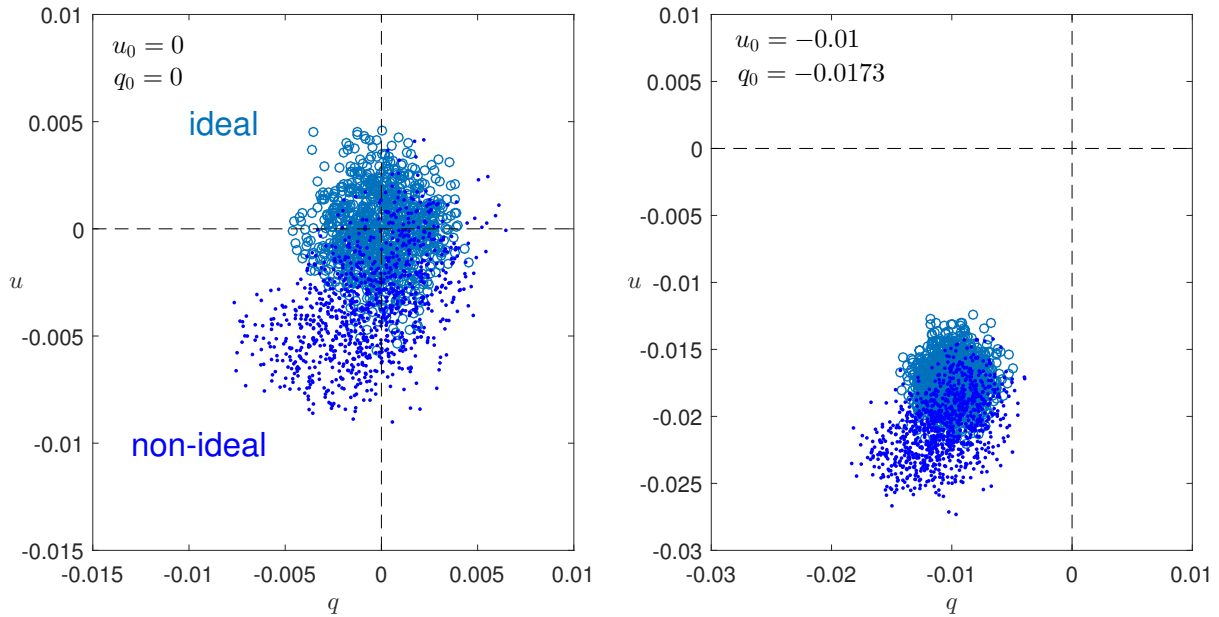


FIGURE 6.8: The presence of Poisson noise results in a bi-variate distribution of the estimated Stokes parameter in the Q - U plane; here I show a set of 1000 synthetic measurements made with four ideal polarizers and non-ideal polarizers that are not perfectly characterized. The miscalibrated non-ideal polarimeter introduces systematic errors into the estimation.

The uncertainty of the normalized Stokes parameters, $\sigma_{q,u}$ can be estimated using formal (linear) error propagation and errors associated with the photometry in each exposure. To first order, the uncertainty scales with the total number of photons, N . The dependence on N can be divided into three regimes, based on the photon signal-to-noise ratio (Hines et al., 2000):

1. very low light levels, $N \lesssim 10^3$

Read noise dominates σ_S , the uncertainty on the signal, S_k . As a result, the uncertainty on the Stokes parameters, $\sigma_{q,q} \propto N^{-1}$.

2. shot-noise dominated regime, $10^3 \gtrsim N \lesssim 10^5$

$$\sigma_S \propto \sqrt{N} \text{ and } \sigma_{q,u} \propto N^{-0.5}$$

3. very high signal levels, $N \gtrsim 10^5$

The uncertainty is dominated by the precision of the flat field correction and the polarizer characterization.

6.5.3 Bias of Polarization Estimators

The Stokes parameters themselves completely describe the polarization state of a light source; however, people are often interested in the fractional polarization and the angle of the polarized light. The most common estimators used are the degree of linear polarization and angle of linear polarization discussed in Chapter 2. When considering only the linear polarization states, it's possible to redefine the degree of polarization, p , to be equal to the degree of linear polarization,

$$p = \sqrt{\langle q \rangle^2 + \langle u \rangle^2}. \quad (6.6)$$

Although the degree of linear polarization (DoLP) is ubiquitous, especially outside of astronomy, it is a biased estimator of the fractional polarization, especially in the presence of noise, when $p/\sigma_p \lesssim 4$. It is clear from the form of equation 6.6 that p can never be negative, unlike q and u . This causes p to overestimate the true degree of polarization. Furthermore, because p does not have a normal distribution (see following section), the value of p determined using an average value of q and u ($\langle q \rangle$ and $\langle u \rangle$, respectively) will be different than $\langle p \rangle$. This overestimation is most evident in the polarimetry of very weakly polarized or “unpolarized” sources. In the presence of noise, p will never be zero.

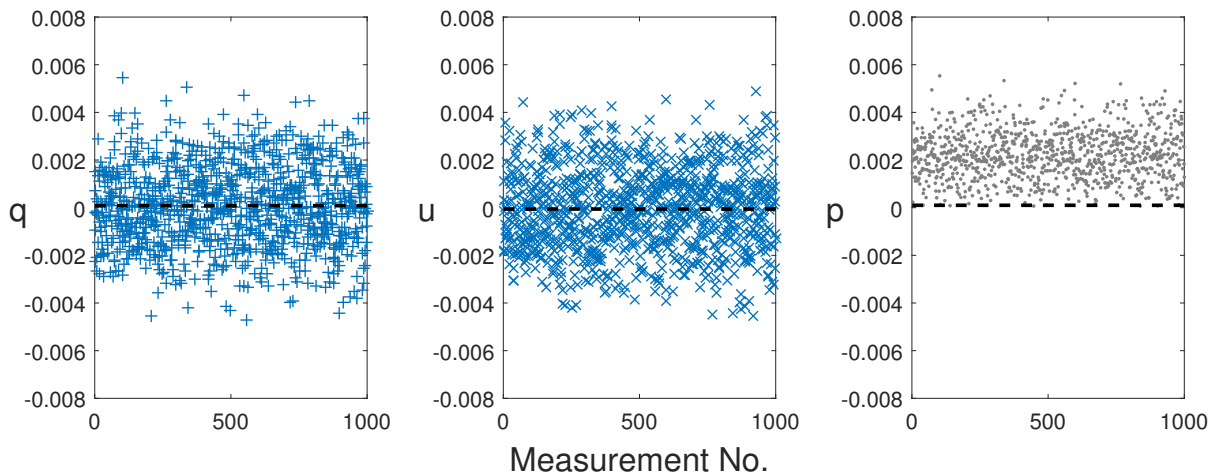


FIGURE 6.9: Synthetic observations of an unpolarized source show the positive bias of the p estimator. Whereas q and u are distributed around a mean of 0, $\langle p \rangle = 0.0021$. The overestimation becomes worse as the scatter of q and u increases.

This is demonstrated in Figure 6.9, which shows 1000 synthetic measurements of an unpolarized source. The q and u parameters are distributed around a mean of 0 and using $\langle q \rangle$ and $\langle u \rangle$ to estimate p gives the correct value; however, estimating p from individual measurements of q and u results in a distribution centered on a mean value of $p = 0.0021$. This effect becomes much stronger as the uncertainty on q and u becomes larger.

The positive bias of p exists because p is not normally distributed. Instead, p is described by the Rice distribution (Serkowski, 1958), which describes the length of a vector from the origin, to a point in a bi-variate normal distribution around some mean. In the context of polarimetry, the Rice distribution describes the distance from the origin, to values in the q - u plane (Figure 6.10). The Rice distribution can be used to determine the probability of measuring a fractional polarization p , given an intrinsic fractional polarization p_0 and measurement uncertainty σ_p (Simmons and Stewart, 1985),

$$F\left(\frac{p}{\sigma_p}, \frac{p_0}{\sigma_p}\right) = \frac{p}{\sigma_p} \exp\left\{-\frac{(p/\sigma_p)^2 + (p_0/\sigma_p)^2}{2}\right\} I_0\left(i \frac{p}{\sigma_p} \frac{p_0}{\sigma_p}\right), \quad (6.7)$$

where I_0 is the zeroth order modified Bessel function of the first kind.

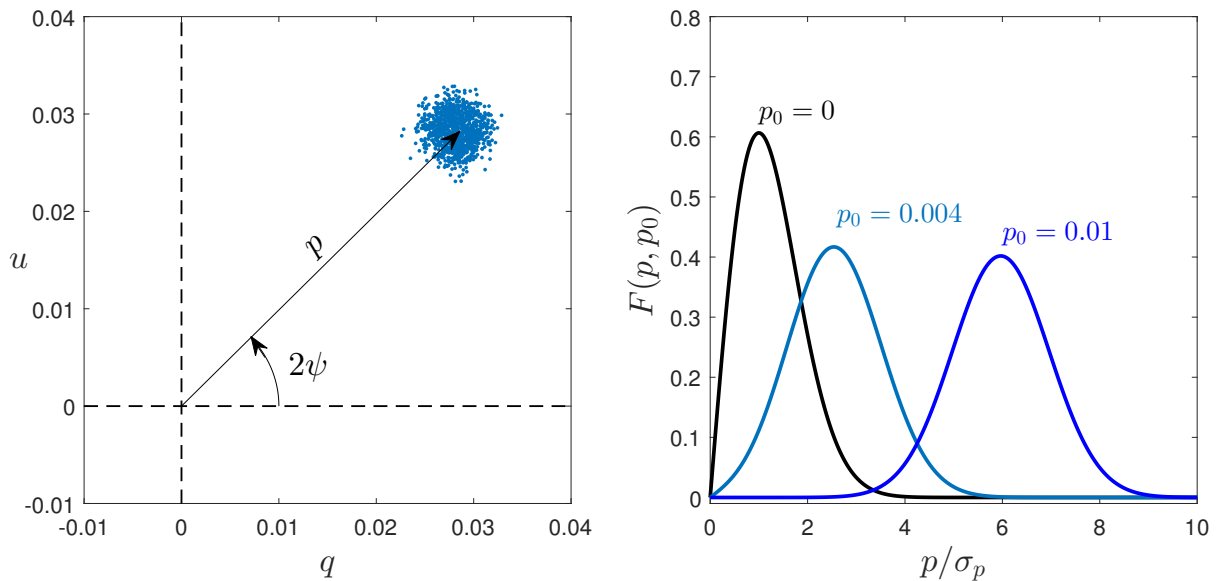


FIGURE 6.10: *Left:* The distance from the origin to a point in the q - u plane is an estimate of the fractional polarization p , while the angle made by this vector with respect to the q -axis is twice the estimated angle of linear polarization. *Right:* The distribution of the magnitudes, p , is given by the Rice distribution, which can be used to calculate the probability of measuring a value p for a source with intrinsic polarization p_0 . In the presence of noise, there is zero probability to measure a value $p/\sigma_p = 0$.

With the distribution in hand, several estimators of the fractional polarization have been developed; [Simmons and Stewart \(1985\)](#) have summarized the four most straightforward options:

- i. \hat{p}_{ML} - the maximum likelihood estimator of p_0 , is the value of p_0 which maximizes $F(p, p_0)$ for a given observed polarization, p . This value can be found by solving the equation,

$$\frac{\partial F}{\partial p_0}(p, p_0) = -p \exp\left\{\frac{-(p^2 + p_0^2)}{2}\right\} \left(p_0 I_0(ipp_0) + ip I_1(ipp_0)\right) = 0, \quad (6.8)$$

where p and p_0 are the normalized values, $p = p/\sigma_p$, $p_0 = p_0/\sigma_p$.

There is a threshold value, $p = 1.41$, below which the only solution to equation 6.8 is $p_0 = 0$ (Figure 6.11, Left); in other words, no significant fractional polarization can be measured, given the scatter in the data.

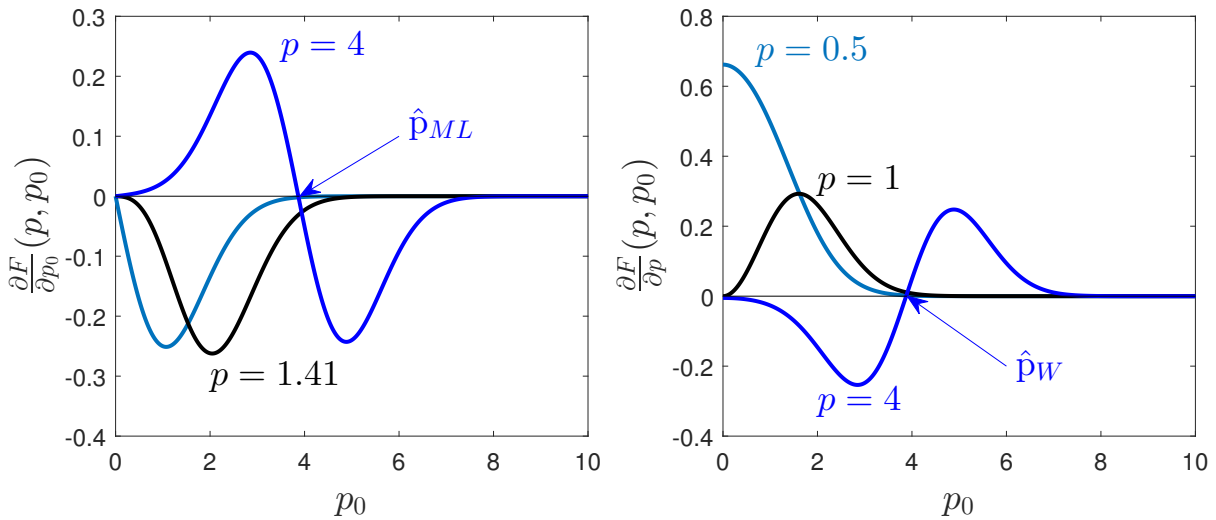


FIGURE 6.11: *Left:* The maximum likelihood estimator suggested by [Simmons and Stewart \(1985\)](#) is that value of p_0 that is a solution to equation $\frac{\partial F}{\partial p_0}(p, p_0) = 0$ (eq. 6.8); there is a threshold value of $p = 1.41$, below which the measured value of p is consistent with $p_0 = 0$. *Right:* The estimator suggested by [Wardle and Kronberg \(1974\)](#) is the value p_0 which solves equation 6.9. In this case, too, there is a threshold value of $p = 1$, below which the measured polarization is consistent with $p_0 = 0$.

ii. \hat{p}_W - the estimator developed by [Wardle and Kronberg \(1974\)](#), defined by the value of p_0 for which the observed polarization, p is a maximum of the distribution $F(p, p_0)$. This is equivalent to finding p_0 that solves the equation,

$$\frac{\partial F}{\partial p}(p, p_0) = -p \exp\left\{\frac{-(p^2 + p_0^2)}{2}\right\} [p_0 I_0(ip p_0) + ip I_1(ip p_0)] = 0. \quad (6.9)$$

As in the previous case, there is a threshold value of \hat{p}_W below which the measured polarization is consistent with 0 (Figure 6.11, Right). This value can be found by setting $p_0 = 0$ in equation 6.9 and solving for p . In this case, the threshold value is $p = 1$.

iii. \hat{p}_M - the median estimator, defined as the value of p_0 for which the observed value p is the median of the distribution $F(p, p_0)$. Again, there is a threshold value of $p = 1.18$, with p_M given by the equation,

$$\int_0^p F(p', \hat{p}_M) = 0.5.$$

iv. \hat{p}_S - the mean estimator, used by [Serkowski \(1958\)](#), is defined as the value of p_0 for which the observed value of p is the mean of the distribution $F(p, p_0)$. Here, the threshold value is $p = 1.25$ and for values greater than this, \hat{p}_S can be found by solving the equation,

$$\int_0^\infty p' F(p', \hat{p}_S) = p.$$

v. $\hat{p} = p$ this estimator uses the measured p at face value, without attempting to correct for any bias. This is the least accurate estimator, but also the one most commonly used.

A direct comparison between these five estimators shows that the maximum likelihood estimator \hat{p}_{ML} has the least bias when the measured polarization is small ($p_0 \lesssim 0.7$), while \hat{p}_M has the least bias for larger values ($p_0 \gtrsim 0.7$). However, all five estimators agree asymptotically, so the choice of estimator is only critical at small values of $p = p/\sigma_p$. Full details of this analysis and calculations of the threshold values can be found in [Simmons and Stewart \(1985\)](#).

6.5.4 Estimation of Uncertainty

The estimation of uncertainty is a critical part of the measurement process. Polarimetric measurements are susceptible to several sources of measurement error: random errors due to a low signal-to-noise ratio; systematic errors due to an imperfect calibration of instrumental effects; and bias associated with the mathematical form of an estimator, like the kind described in the previous section. Rigorous error analysis requires one to consider all three mechanisms. I propose a multi-stage process, which begins with a bare-minimum measure of the uncertainty and builds to a more complete analysis.

Stage 1. Uncertainty of the Stokes Parameters

One can gain some idea of the measurement uncertainty by determining the variance of the q and u distributions. Ideally, enough measurements have been performed that this can be calculated directly from the data, by constructing a plot in q - u space (Figure 6.12, *Left*). The standard deviations, σ_q and σ_u can be used as noise terms to calculate polarimetric signal-to-noise ratios (SNR), q/σ_p and u/σ_u . Taking this idea one step further, one may also calculate a noise term for the estimation of p and ψ , σ_p and σ_ψ , respectively.

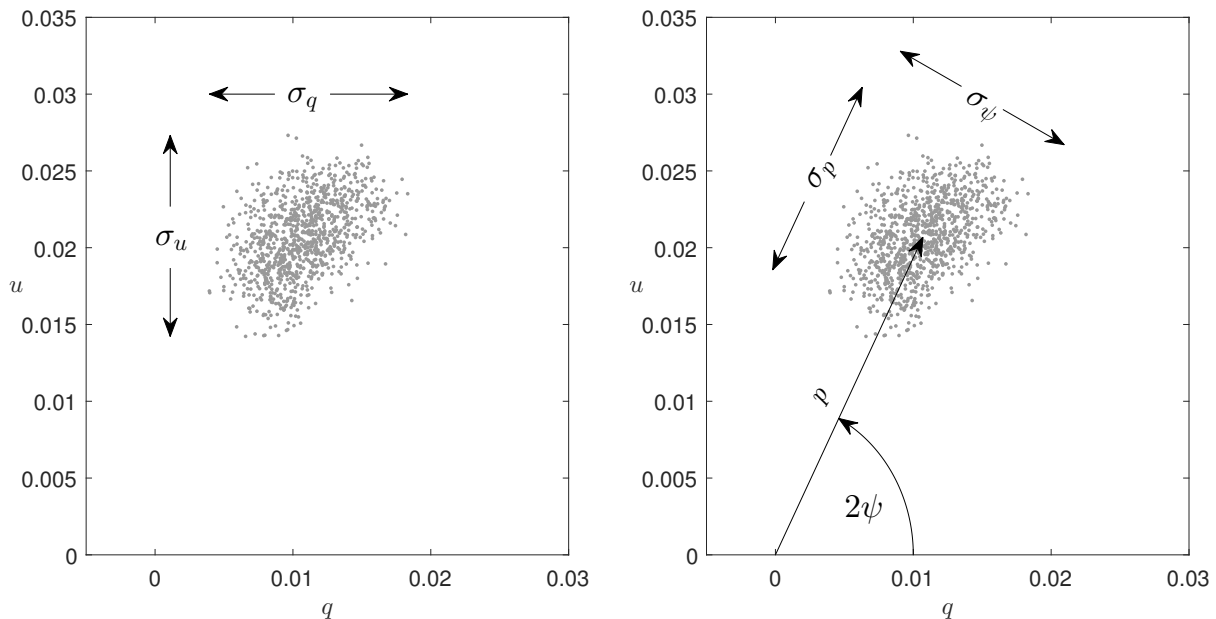


FIGURE 6.12: *Left*: The variance for the q and u parameters can be used to estimate the noise associated with the measurement of q and u . *Right*: Similarly, the error associated with p and ψ can be estimated by determining the variance along (σ_p), and perpendicular (σ_ψ) the p vector.

If there are only a few measurements in q - u space and the noise terms σ_q and σ_u cannot be determined directly, one can fall back on formal error propagation. Using the photometric errors associated with the individual intensity measurements S_0 , S_{45} , S_{90} , etc, it's possible to estimate the expected variance of Q , U and I . Once the noise terms σ_q and σ_p have been obtained, they can be mathematically projected into p - ψ space as follows (Sparks and Axon, 1999),

$$\begin{aligned}\sigma_p^2 &= \sigma_q^2 \cos^2 \psi + \sigma_u^2 \sin^2 \psi + R\sigma_q\sigma_u \sin 2\psi \\ 2\sigma_\psi^2 &= \sigma_q^2 \sin^2 \psi + \sigma_u^2 \cos^2 \psi - R\sigma_q\sigma_u \sin 2\psi,\end{aligned}$$

where R is the correlation coefficient between q and u . Unfortunately, it may be impossible to determine the value of R from the data and some assumption has to be made, such as $R = 0$. For cases where the polarimetric signal-to-noise ratio is sufficiently high ($\text{SNR}_p \gtrsim 10$), this type of analysis might be sufficient; especially if the polarimetric system is relatively free of systematic effects.

Stage 2. Understanding the Measurement Bias

Once the polarimetric SNR has been estimated, it may be important to consider any systematic effects that may be present due to an imperfect calibration of the polarimetric system or bias due to a particular estimator (see section 6.5.3).

Stage 3. Modeling the System's Response

A powerful and convenient way to determine the performance of a polarimetric system is through characterization and simulated observations. This allows one to estimate, with a good deal of confidence, the response of the system to inputs whose properties are known *a priori*. First, an accurate model of the polarimetric system must be constructed. For this, it is crucial to accurately determine the throughput, efficiency and orientation terms described in section 6.5. Then, these parameters can be used to modulate an input signal, using its intensity and polarization properties. Finally, these synthetic observations must be processed with the same analysis used for actual data. This is the process I use to estimate RITPIC's performance and I describe it in Chapter 8.

Chapter 7

Fabrication of Micropolarizer Array-based Polarimeters

An area format detector can be made sensitive to polarization using a pixel mask which consists of polarizers ([Vorobiev and Ninkov \(2014\)](#), [Zhao et al. \(2010\)](#), [Myhre et al. \(2012\)](#), [Brock et al. \(2011\)](#)), retarders or both ([Hsu et al. \(2014\)](#)). This approach is analogous to the use of color filter arrays (CFAs) to create color-sensitive imaging sensors (Figure 6.6). The fabrication of polarization-sensitive focal planes has closely followed the development of color filter arrays. As with CFAs, the micropolarizer array (MPA) can be fabricated on a separate substrate and hybridized with an off-the-shelf imaging sensor or be deposited directly onto the sensor.

7.1 Fabrication of Polarization-Sensitive Sensors

We envision 5 strategies for the fabrication of polarization-sensitive imaging sensors:

1. The polarizer pixels are fabricated at the wafer level as part of the imaging sensor. For example, the polarizer pixels can occupy the region typically used for color filter arrays. If successfully fabricated, these devices should exhibit the lowest crosstalk, because the filtering of different polarization orientations happens within a pixel,

and not some distance away. At the time of writing, no group has announced any efforts to employ this procedure.

2. The polarizer pixels are fabricated as a thin layer on top of a wafer (Figure 7.1, Left) of conventional sensors, which have not yet been diced and packaged. This process should provide similar results to the first, however, past attempts show poor device contrast ratio.
3. The packaged CCD (Figure 7.1, Middle) and a cut MPA (Figure 7.1, Right) can be aligned using a flip-chip bonder (a tool typically used to bond sensors to carriers) and adhered using some kind of adhesive (for example, an optical grade epoxy or a wax). This requires the fabrication of specialized adapters, because flip-chip bonders are not designed to hold a wide range of objects.
4. The MPA and sensor can be aligned using an opto-mechanical system that aligns features on the MPA to features on the sensor and adheres the device when proper alignment is achieved.
5. The MPA can be aligned with a CCD that is housed in an operating camera. As the camera looks at a target and takes images, the MPA can be aligned with the CCD pixels, using the camera images for real-time feedback. Once proper alignment has been determined, the MPA is adhered to the sensor.

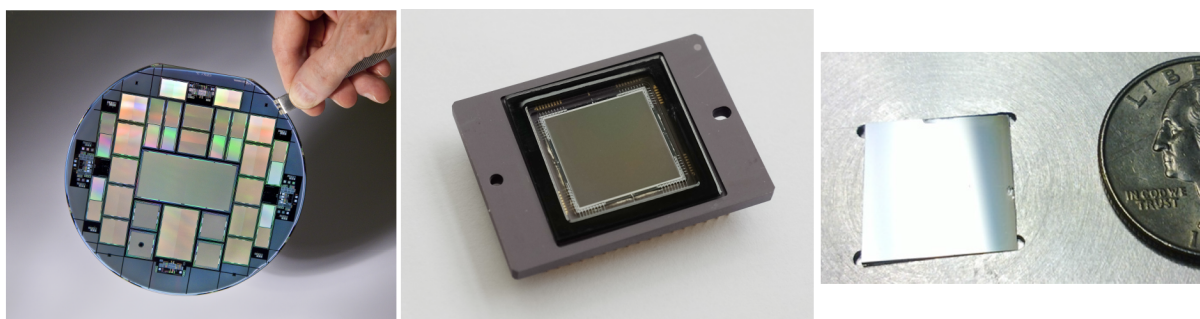


FIGURE 7.1: *Left:* A wafer with several sensors ready to be diced and packaged (image: www-ccd.lbl.gov). *Middle:* A packaged CCD. The die has been cut from a wafer, attached to a ceramic carrier and wire-bonded to the metal pins of the carrier. *Right:* A microgrid polarizer on a thin glass substrate.

The first two techniques require a significant commitment from a semiconductor foundry and the development of many new procedures. Nevertheless, mass-production of these

devices will eventually require polarizer integration at the wafer level. Approaches 3, 4, and 5 are able to work with commercially available devices. Packaged sensors are readily available and even unpackaged dies can be obtained from some manufacturers. A flip-chip bonder can be automated, especially when aligning die-to-wafer, and the process should be very repeatable. Dozens of units should be possible to fabricate in a span of several weeks. Similarly, a custom apparatus can be fabricated to position and align the MPA and the packaged sensor.

The last approach uses the sensor itself to confirm proper alignment. Whereas the previous approaches use “passive” alignment techniques, this active approach provides extremely useful information about the actual optical response of the system. This approach is attractive for devices in the visible range, but is impractical for infrared devices, which must be operated at very low (80K and below) temperatures to reduce the high dark current that is characteristic of infrared detectors. This requires that the opto-mechanical equipment must be housed in a large dewar and also cooled. This is problematic, because positioning stages that operate at such low temperatures are extremely expensive and large cryogenic setups are difficult to develop and operate.

7.1.1 Fabrication at RIT - Passive Alignment

The fabrication of the MPA-CCD polarimeter is simple in principle, but it presents some key engineering challenges. The fabrication process consists of two key stages: alignment of the micropolarizer array and the imaging array and fixing the alignment in place.

Alignment Strategy

Whereas wafers are created with precisely positioned alignment target marks to allow easy alignment of two wafers, diced dies and packaged sensors lack these features. The first challenge is determining when proper alignment between the MPA and the sensor is achieved. At RIT, a high magnification imaging system was built to monitor the position and orientation of the sensor and the MPA (Figure 7.2). The imaging system is able to move in \hat{x} , \hat{y} , and \hat{z} directions (independently of the MPA-CCD positioning system) and examine the system alignment without disturbing it.

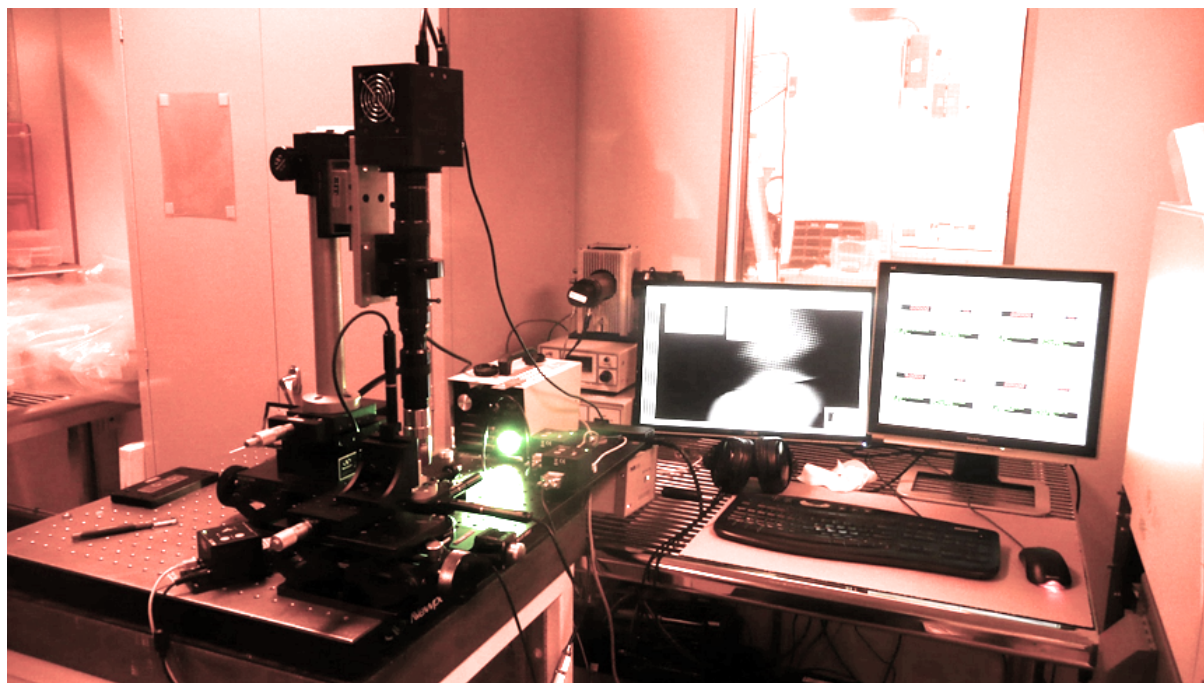


FIGURE 7.2: The imaging system used to determine MPA-CCD alignment is based on a compact microscope, CCD camera and a long working distance (LWD) microscope objective. The LWD objective is required because the alignment procedure requires imaging of the CCD through the polarizer substrate, which is 0.7 mm thick. This is much larger than the working distance of conventional objectives.

Because the CCD and MPA lack actual alignment marks, the pixels of the devices are used for alignment of the system. Figure 7.3 shows a 3D model of the MPA-CCD system. The MPA is positioned with the polarizer surface pointed towards the CCD surface. In this case, a small gap exists between the polarizer and the CCD surface (which is defined by the layer of microlenses). This gap will exist if the MPA is adhered to the CCD with a layer of epoxy. As long as the polarizer doesn't cover the entire area of the sensor, the sensor grid will create a border around the polarizer.

The pixels of the MPA must be precisely aligned with the pixels of the sensor. This requires precise positioning capability with 6 degrees of freedom: \hat{x} , \hat{y} , \hat{z} , $\hat{\theta}$ (rotation the $\hat{x} - \hat{y}$ plane), as well as pitch and yaw to maintain the MPA and sensors parallel. The dead space between CCD pixels determines the tolerance in $\hat{x} - \hat{y}$ positioning. For these devices, this is approximately $1 \mu m$. Ray-tracing models of the MPA-CCD pixels using converging beams of light suggest a maximum separation between the CCD surface and MPA of $10 \mu m$ in the \hat{z} -direction. After this point, geometric cross-talk effects become significant. That is, the angle of incidence of the beam near the focal plane causes light

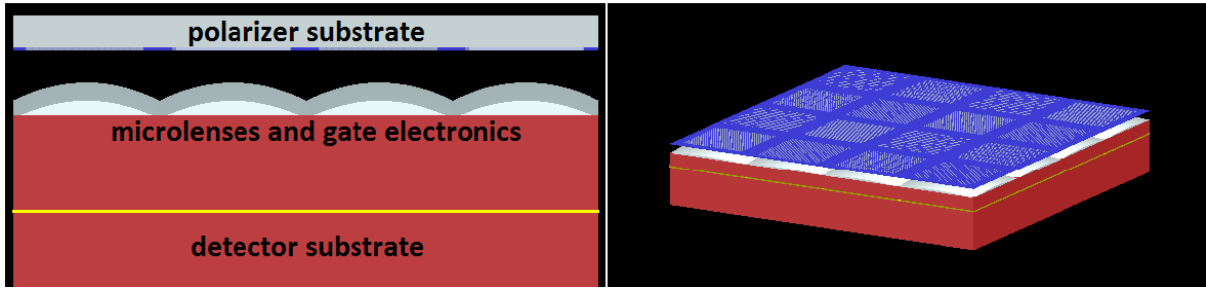


FIGURE 7.3: *Left:* A cross-section of the MPA-CCD pixels. From the top, down there are 5 distinct regions: glass polarizer substrate, the thin polarizer layer, a gap (filled with air or epoxy), a layer of CCD microlenses that demarcate the pixels of the CCD, a layer of gate electronics and the bulk epitaxial layer with the depletion region. *Right:* An isometric view of the MPA-CCD system, showing exact alignment between the grid formed by MPA pixels and the grid formed by CCD pixels.

rays that pass through a particular pixel to end up in a neighboring CCD pixel (Figure 7.4).

The CCD used in the initial alignment uses $9\ \mu\text{m}$ pixels and is an array of 1536×1024 pixels with linear dimensions $13.8\ \text{mm} \times 9.2\ \text{mm}$ for the active imaging area. A $1\ \text{mum}$ deviation over a distance of $6.9\ \text{mm}$ (half-length of the sensor, assuming rotation about the center) imposes a tolerance of 30 arcseconds for θ misalignment. The pitch and yaw requirements are similar to rotational ones. To meet these stringent requirements, an $\hat{x} - \hat{y} - \hat{z} - \hat{\theta}$ positioning system was built using motorized translation stages, purchased with funds awarded by the RIT Center for Imaging Science Research Micro-Grant. The system is capable of $\hat{x} - \hat{y} - \hat{z}$ positioning with precision better than $0.1\ \mu\text{m}$ and $\theta < 10$ arcseconds (Figure 7.5).

Alignment Procedure

The alignment process consisted of four stages: initial positioning; epoxy application; precise alignment; final placement and epoxy curing. Because the separation in the z -direction between the MPA and the CCD must be kept minimal, the CCD and MPA surfaces must be kept clean and free from dust particles, which are often 10's of microns in size. To prevent contamination of the devices, the fabrication of the device took place in a Class 1000 clean room at the RIT SMFL.

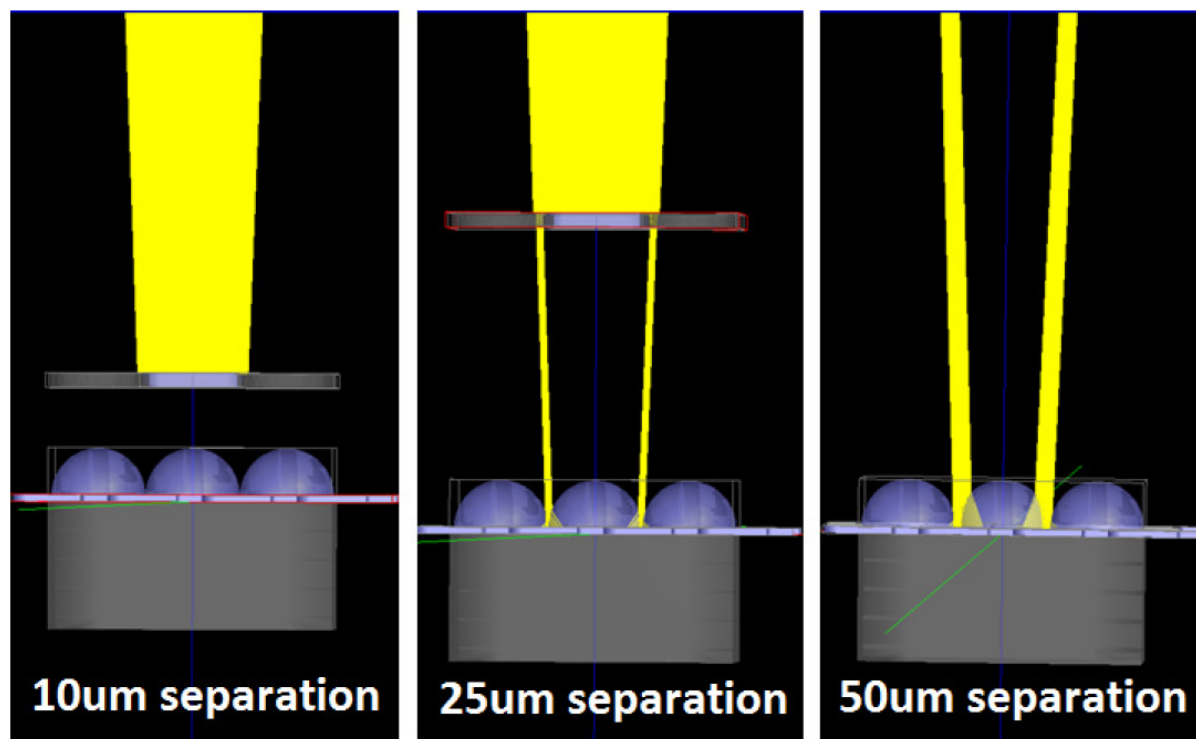


FIGURE 7.4: Because the polarizer is at the focal plane of the optical system, it is illuminated using converging light. As the separation between the polarizer and the sensor (in this case with microlenses) increases, the projected area of the polarizer pixels decreases. This figure shows a converging beam of polarized light. The middle polarizer blocks all of the light, while its neighbors transmit light. As the polarizer is moved away from the sensor, light from the left and right pixels ends up in the middle pixel. This is one example of optical crosstalk. Source: figure is courtesy of Kenneth Fourspring, personal communication.

Initial Positioning

First, the packaged CCD was secured in an aluminum chuck, which was machined to keep the sensor fixed with respect to the $\hat{x} - \hat{y} - \hat{z}$ coordinate system created by the 2 translation stages and the rotation stage. The MPA was then placed face-down onto the CCD surface. This step is critical because it sets the planarity of the MPA-CCD system. A set of “fingers” designed to hold the MPA are then lowered on a vertical translation stage (\hat{z} -axis in Figure 7.5). The fingers are adjusted to grab the MPA at opposite corners and engaged by tightening the mounting bolts. Figure 7.6 shows two views of the CCD chuck, the CCD itself, the square MPA, the MPA holder and the microscope objective.

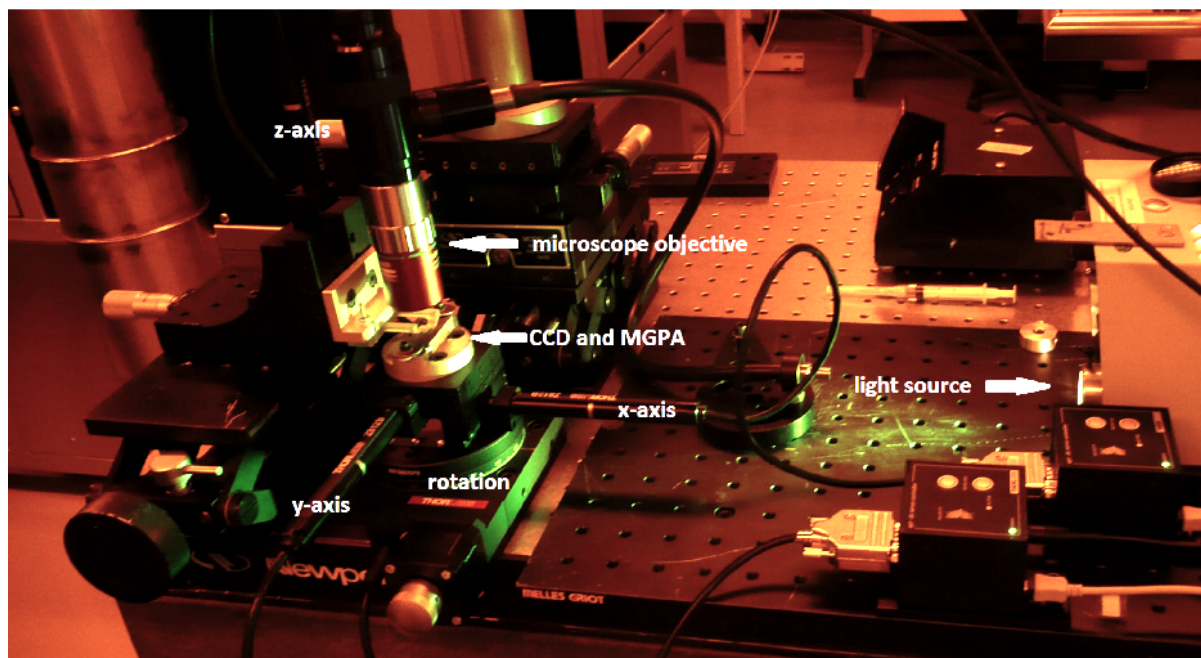


FIGURE 7.5: Setup for alignment of MPA to CCD sensor. The CCD is held in an aluminum chuck and is positioned in $\hat{x} - \hat{y} - \hat{\theta}$ using two linear stages stacked vertically on a rotation stage. The actuators of the stages are labeled in the figure. The z -distance between the polarizer and the CCD is controlled using another linear stage. The alignment of the MPA-CCD system is determined using a long working distance microscope objective and a CCD camera. The illumination source is fiber-coupled to the microscope system.

Epoxy Application

Once the MPA is firmly held, it is raised 7 mm by the z -axis translation stage. A small amount of optical grade Norland 61 epoxy is then deposited onto the CCD surface using a syringe and needle. The epoxy is designed to only cure if exposed to ultraviolet light and will stay runny indefinitely, allowing plenty of time for alignment.

Precise Alignment

After the epoxy is deposited, the MPA is lowered again 6.9 mm, leaving a $100 \mu\text{m}$ gap between the MPA and the CCD. This allows the CCD to be moved without any danger of moving the MPA, which is held fixed during alignment. The imaging system is positioned to look at the edge of the MPA - note the small spot of light near the polarizer edge in Figure 7.6 (Right). The microscope is then focused on the MPA pixels to determine the alignment of the MPA grid. An image is acquired and a line is drawn in software to indicate the direction of rows perpendicular to the MPA edge (Figure 7.7, Left). The

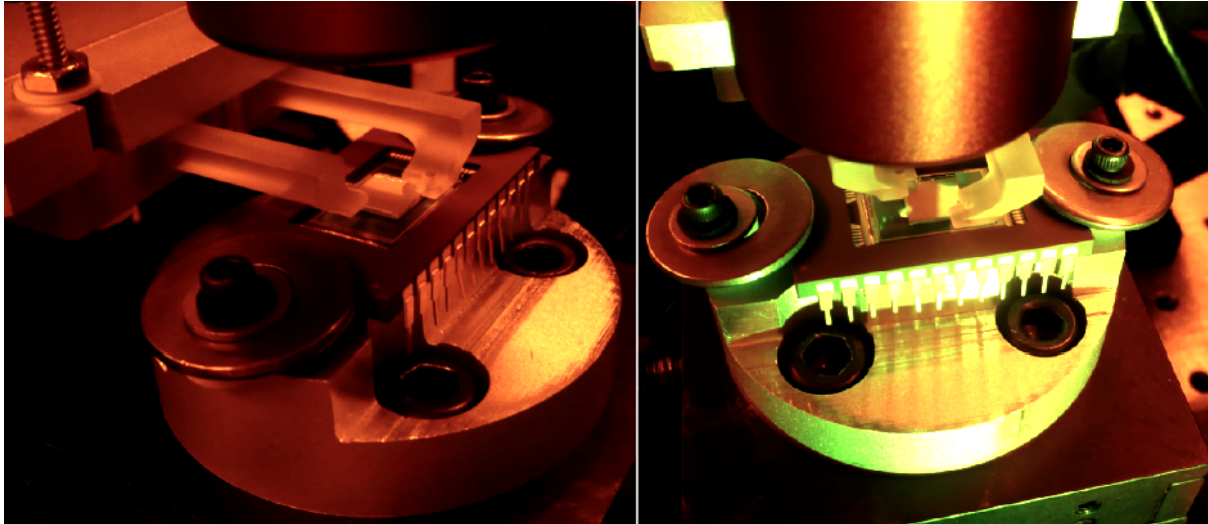


FIGURE 7.6: Close up of the assembly that holds the CCD and the micropolarizer array.

line preserves the alignment of the MPA while the microscope is focused on the CCD array. This way, the grid formed by the CCD pixels can be registered with the MPA grid (Figure 7.7, *Right*).

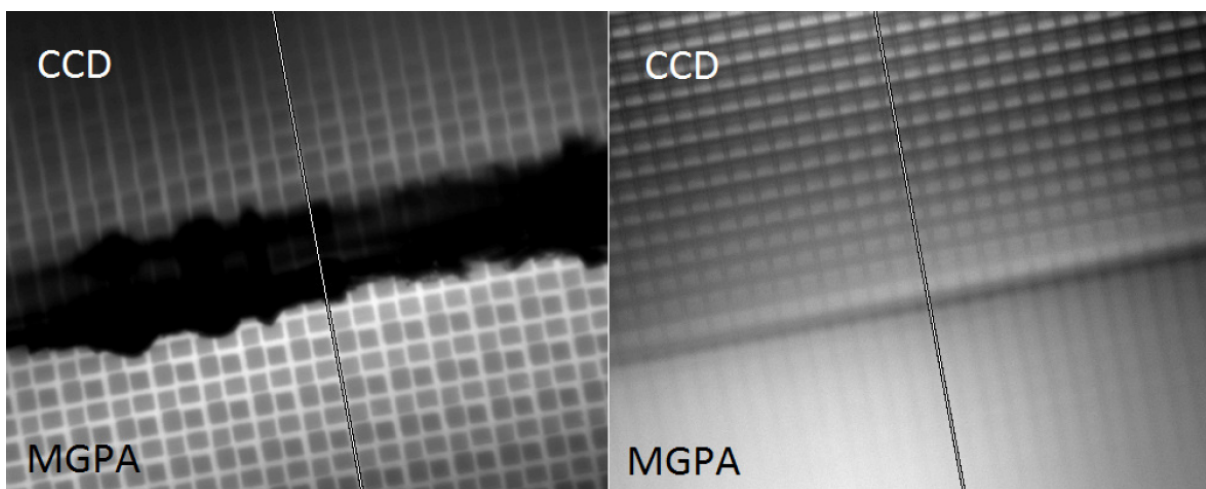


FIGURE 7.7: *Left*: An image acquired of the MPA at the physical edge of the MPA. The jagged substrate and square pixels of the polarizer are clearly seen. A line is created to indicate the alignment of the MPA. *Right*: An image of the same region, focused on the CCD that is below the polarizer. The CCD pixels appear as sets of bright and faint rectangles. The CCD grid can now be aligned with the line that indicates the MPA alignment. In this image, the CCD is slightly misaligned with the MPA grid.

First, the CCD is rotated until its pixel grid is parallel to the MPA grid. Then, the CCD is translated until the grid (in this case, the gaps between pixels) coincides with the grid of the MPA (which is indicated by the white line). Because the two grids are made to be

parallel, the system can be aligned independently in the \hat{x} and \hat{y} directions. Once one direction is aligned, the microscope moves to an orthogonal edge and the procedure is repeated.

Final Placement and Epoxy Curing

Once satisfactory alignment has been achieved, the MPA is lowered the final $100\ \mu\text{m}$ in increments of $10\ \mu\text{m}$. The MPA height is monitored by the translation stage encoder and by maintaining focus in the microscope. As the MPA is lowered, excess epoxy is squeezed out and a thin layer remains. After the alignment is confirmed one last time, a mercury lamp is used to cure the epoxy. After an hour long cure, the holder is disengaged and the device fabrication is complete (Figure 7.8).

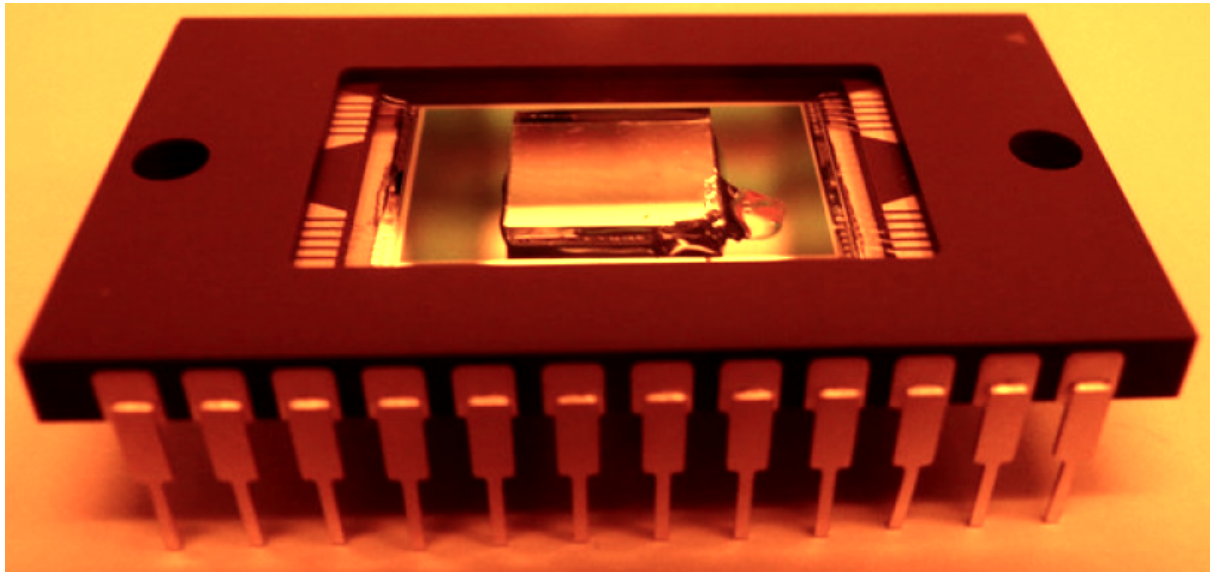


FIGURE 7.8: First polarization-sensitive imager fabricated at RIT using the passive alignment technique. The silver square in the center is the micropolarizer array. Excess epoxy can be seen around the edges of the polarizer.

7.1.2 Fabrication at RIT - Active Alignment

The polarization-sensitive focal planes were fabricated at RIT's Semiconductor & Microsystems Fabrication Laboratory using a custom alignment apparatus (Figure 7.9). The micropolarizer arrays (fabricated by Moxtek, Inc.) and the KAF-1603 CCD both have pixels with $9\ \mu\text{m}$ pitch. The micropolarizer was held with a vacuum wand and manipulated with computerized translation stages until desired alignment was achieved. The alignment was monitored by illuminating the sensor-plus-polarizer system with polarized light.

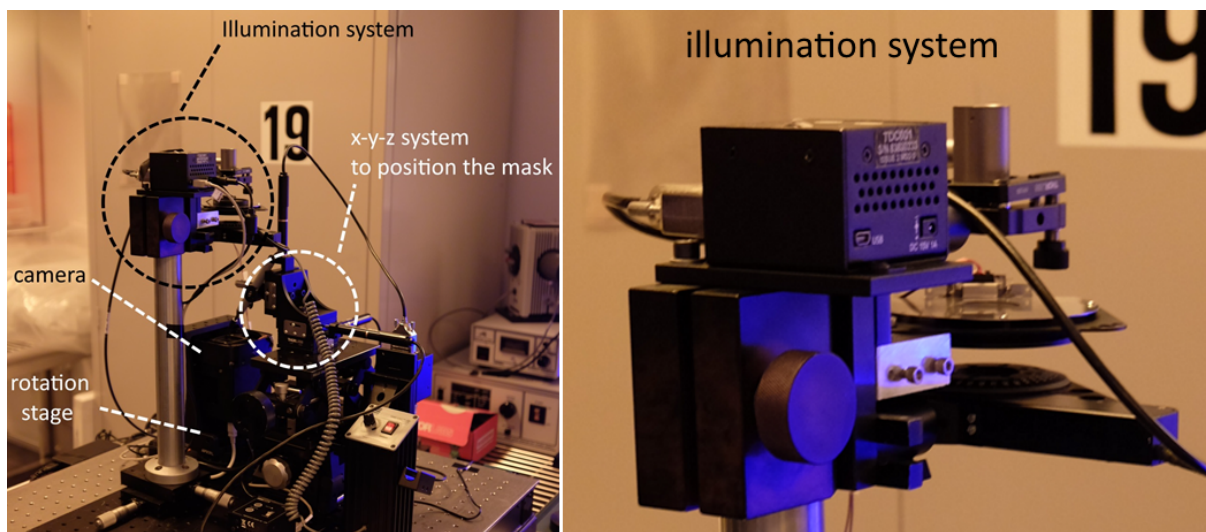


FIGURE 7.9: *Left:* The polarization sensitive focal planes were fabricated in a clean room at RIT. The micropolarizer arrays were aligned to a CCD sensor using a vacuum wand and computerized translation stages (*Right:*) A close-up of the illumination system. Alignment was monitored by illuminating the system with linearly polarized light and reading out the CCD.

I was able to achieve good, sub-pixel, alignment with this system. The instantaneous alignment can be easily determined by reading out the sensor and attempting to estimate the degree of polarization of the incident light (Figure 7.11). When the micropolarizer array and the sensor are severely misaligned, strong “beat” patterns can be seen across the array. By adjusting the alignment to reduce the frequency of these beats, it’s possible to achieve very good alignment. Once this “coarse” alignment is achieved, the estimation of the degree of polarization can be used to fine-tune the alignment.

The vacuum wand presented several critical problems for the fabrication process. First, it blocked a large fraction of the sensor area, leaving only the edges to be used for feedback.

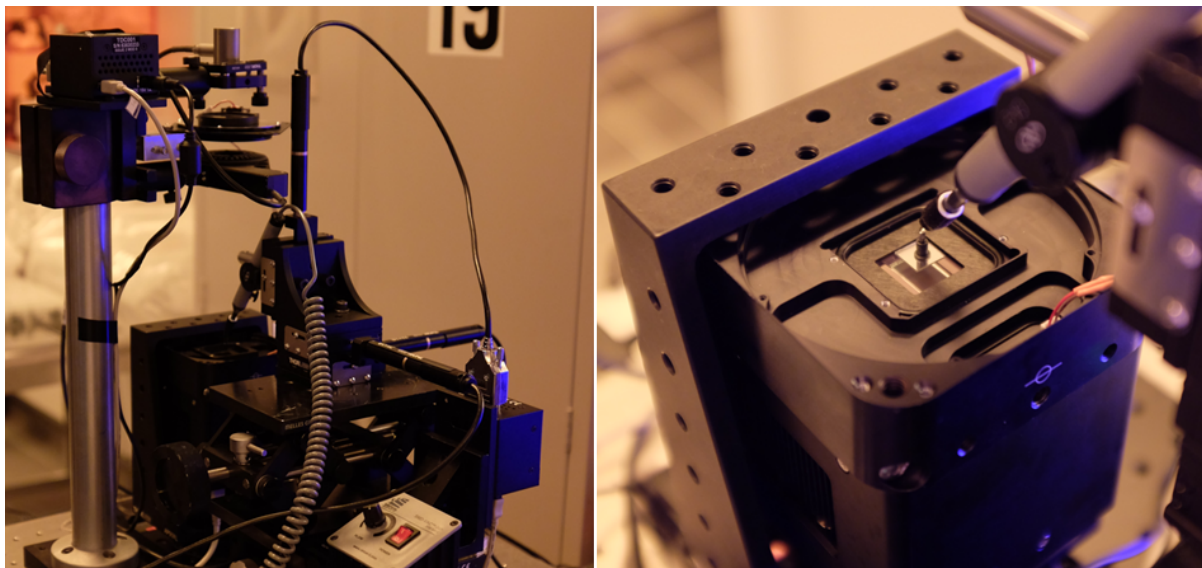


FIGURE 7.10: *Left:* This alignment setup offered four degrees of motion - rotation in the plane of the sensor and $\hat{x} - \hat{y} - \hat{z}$ motion. *Right:* The micropolarizer array was held with a vacuum wand. This is a simple but problematic way to manipulate the micropolarizer.

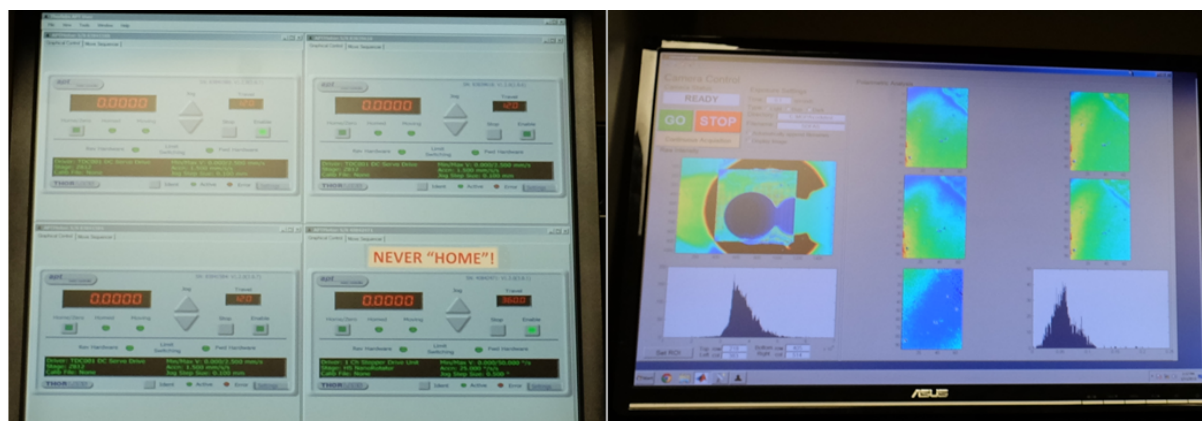


FIGURE 7.11: *Left:* The translation stages used to manipulate the micropolarizer array and sensor were computer-controlled; however, the alignment process was not automated. *Right:* I built an interface to operate the camera, perform on-the-fly calibration, and provide real time feedback on the state of the alignment.

This is more of an inconvenience, because if the edges are aligned, the center should be aligned, too. Most crucially, the rubber cup (as well as the rest of the wand+translation mechanism) is not mechanically robust enough to prevent movement while the epoxy cures and fixates the alignment. Therefore, some misalignment is unavoidable with this system. Nevertheless, the 2nd generation prototype fabricated with this system showed better alignment than the 1st generation prototype (Figure 7.12).

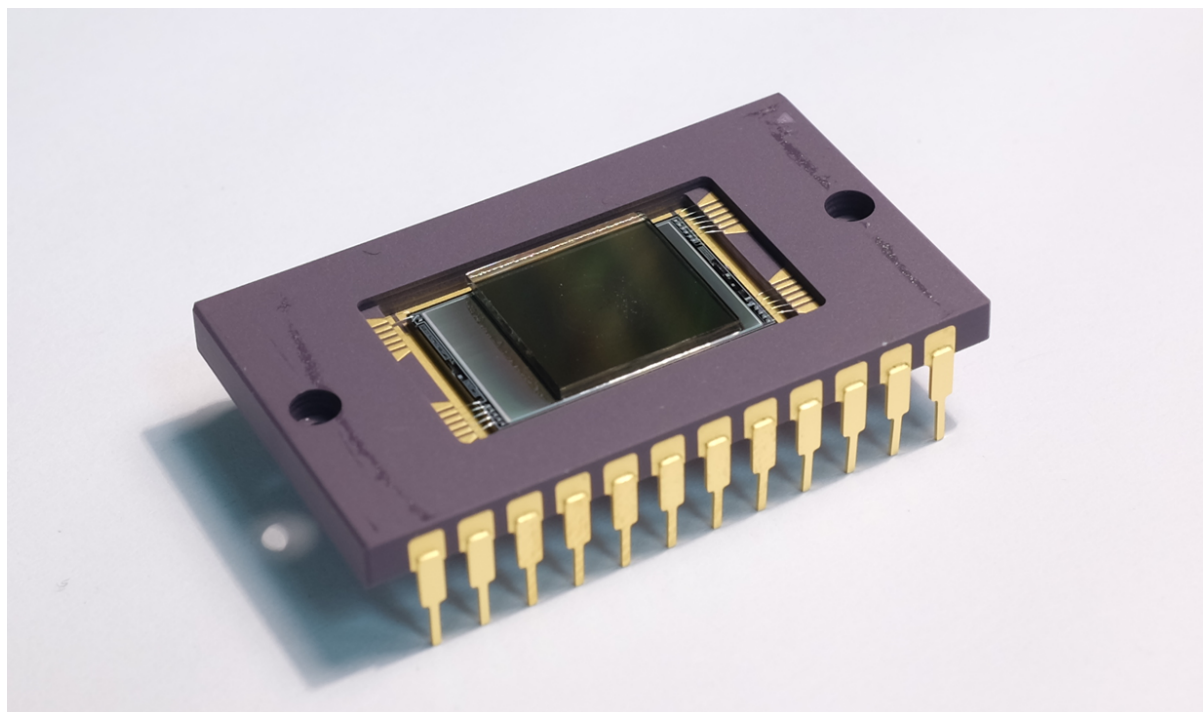


FIGURE 7.12: The 2nd generation prototype of a micropolarizer-based polarization sensor fabricated at RIT, using active alignment.

7.1.3 Alignment Using A Carrier

To solve some of the problems associated with the vacuum wand, the next variation of the active alignment process used a custom machined aluminum carrier (Figure 7.13). Rather than holding the polarizer itself, the vacuum wand held onto the edge of the carrier. This way, the suction cup no longer blocked the usable area.

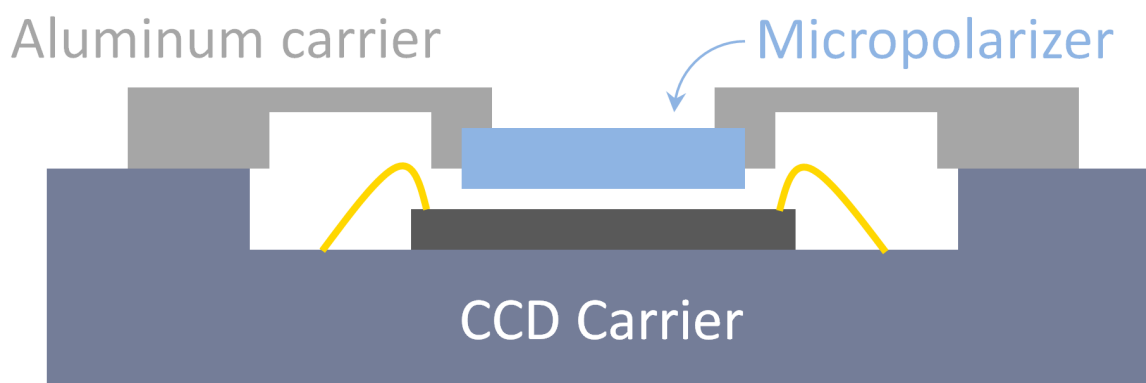


FIGURE 7.13: A carrier can be used to position the micropolarizer array above the sensor. This cross-section shows how a carrier can be used to avoid crushing the wire bonds that connect the CCD to the CCD carrier.

However, the issues with mechanical instability remained. Nevertheless, the use of a carrier allows great flexibility in the alignment process, because the carrier is much easier to interface with, than the micropolarizer array itself. The carrier-based prototype is shown in Figure 7.14.

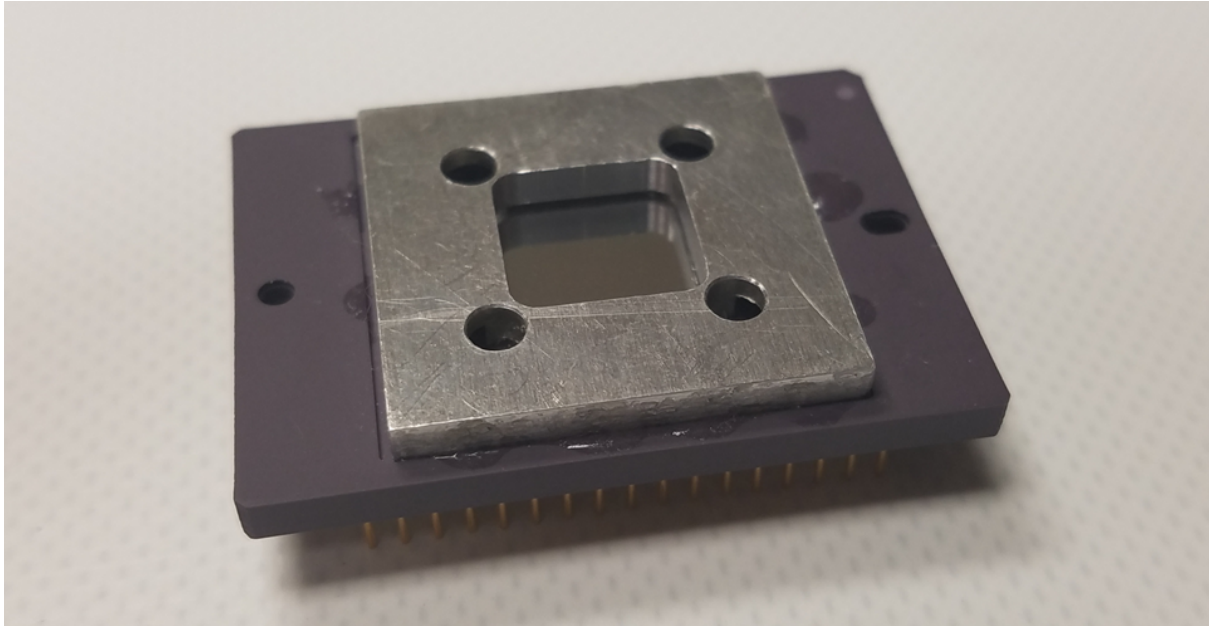


FIGURE 7.14: The 3rd generation prototype of a micropolarizer-based polarization sensor fabricated at RIT, using active alignment. This design uses an aluminum carrier to hold the micropolarizer suspended above the sensor, with an air gap between them.

7.2 Fabrication at 4D Technologies

The latest prototype was fabricated at 4D Technology Corporation in Tucson, AZ. 4D has fabricated similar sensors in the past, for use in their interferometers. For RIT, they modified their apparatus to fabricate a scientific grade sensor which can be temperature controlled and used for low light level imaging. This is the prototype used for the on-sky evaluation at CTIO.

Chapter 8

Performance and Calibration

The physical properties of the polarizer - such as the geometry of the conductive wires - largely determine the performance of the polarizer, which is commonly specified by two metrics: the contrast ratio and the throughput of the polarizer. When a polarizer is used to construct a polarimeter, the performance of the polarimeter is largely determined by the contrast ratio and throughput of the polarizer. However, the performance of the polarimeter is also affected by the measurement method and the corresponding uncertainties. In other words, a perfect polarizer does not guarantee a perfect polarimeter. Conversely, a high precision polarimeter can be made with less-than-perfect polarizers.

In this chapter, I describe the characterization procedure I used to determine the transmission, efficiency, and orientation for each pixel in the polarization-sensitive imager. Accurate characterization of these properties is critical to the performance of these devices, because the data acquisition and analysis methods typically used with these sensors do not allow for convenient calibration methods, like the dual-beam double-difference technique.

8.1 Characterization of Device Properties

In these polarimeters, each pixel of an imaging sensor is covered with a single pixelated wire grid polarizer. The throughput, efficiency, and orientation of each polarizer must be determined so the intensities measured by the sensor pixels can be accurately demodulated (see Chapter 6). To determine these parameters, the polarization sensor was installed in a Finger Lakes Instruments Microline camera - the Rochester Institute of Technology Polarization Imaging Camera (RITPIC). The sensor was uniformly illuminated with linearly polarized light, by polarizing the output of an integrating sphere (Figure 8.1). The integrating sphere was fed by a stable broadband light source and broadband filters (Bessel UBVR set). In this section I only show the V-band results, because the UBRI data is similar.

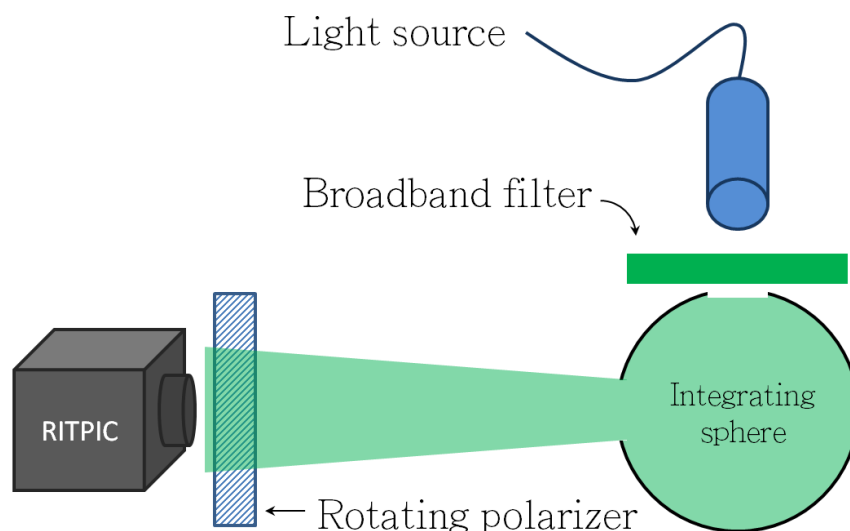


FIGURE 8.1: The polarization sensors were characterized using a rotating linear polarizer and an integrating sphere. The filter is placed before the sphere to avoid any polarization from a tilted glass plate.

This setup produces polarized “flat field” images, which are commonly used in astronomy to characterize and calibrate sensors and imaging systems. The linear wire grid polarizer used in this setup (Thorlabs part [WP25M-VIS](#)) produces highly polarized light (99.8% polarized at 500 nm), over a broad range of wavelengths and incidence angles. A computerized rotation stage is used to change the polarizer’s orientation, such that polarized flats can be collected for a broad range of incidence angles, such as 0° to 210° , in increments of

1°. Typically, multiple frames are acquired at each orientation to improve signal-to-noise ratio (especially for pixels orthogonal to this “analyzer” polarizer’s orientation, which receive very little light) and to filter out cosmic rays. At the end of this process, the response of every pixel to polarized light over a broad range of angles is known.

Although a Wollaston prism, or another polarizing prism, would produce light with much higher polarization purity, the wire grid polarizer was used to produce a more stable and repeatable measurement system. A wire grid polarizer is straightforward to align and rotate, without introducing “beam wobble”, which could change the illumination pattern on the sensor.

8.1.1 Modeling the System Response

The response of a single pixel in these polarimeters to polarized light describes the modulation of intensity based on the polarimetric properties of incident light, which is the basis of all polarimetric measurement schemes. For example, Figure 8.2 shows the median response of pixels with four orientations to polarized light over the angle range 0° to 210°, using the Bessel V filter (broadband “green” light). It’s possible to describe some properties of the system, qualitatively, from these raw curves alone. For example, the 45° pixels appear to have a lower overall throughput than pixels with the other three orientations. The response curves appear offset from each other in increments of roughly 45°. Also, the ratio between the minimum and maximum signal measured for pixels of a certain orientation is indicative of the contrast or efficiency of these polarizers (and it ranges from ~ 30:1 - 40:1).

Once the response of each pixel to polarized light has been measured, the properties of each pixel can be determined using a model of the system. The signal measured by each pixel for light of a certain polarization can be described with equation 6.3,

$$S_k = A_k I + \epsilon_k (B_k Q + C_k U),$$

where S_k is the measured signal, I , Q , and U are the Stokes parameters which describe the state of the incident light and A_k , B_k , C_k , and ϵ_k are transmission and efficiency terms

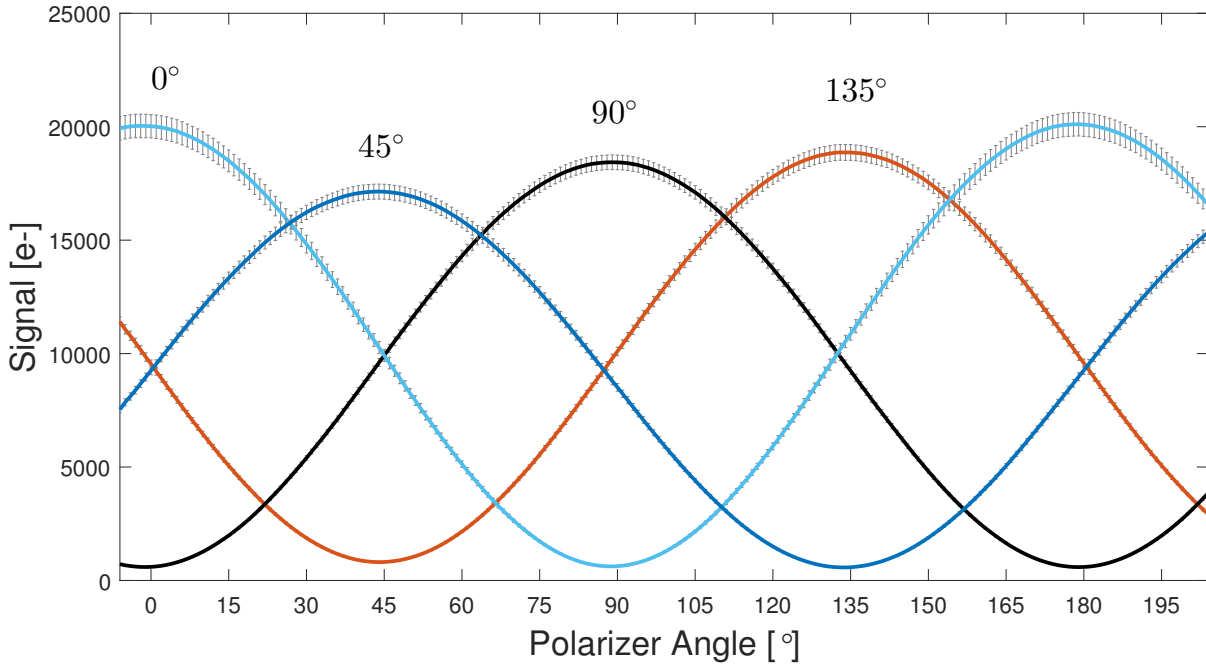


FIGURE 8.2: The median response for pixels oriented along 0° , 45° , 90° , and 135° to polarized light with a range of angles. The error bars show the standard deviation of pixels with the same orientation, at a particular angle.

that describe each polarizer. Using the relations between degree of polarization and the stokes parameters, the above equation can be expressed as follows,

$$S_k = A_k I + \epsilon_k (B_k I p \cos 2\psi + C_k I p \sin 2\psi),$$

where I is the total intensity, p is the fractional polarization, and ψ is the polarization angle. Next, the transmission terms A_k , B_k , and C_k are written in terms of a generic throughput, t_k and polarizing efficiency ϵ_k ,

$$S_k = I \frac{1}{2} t_k + \frac{1}{2} t_k \epsilon_k I p \cos 2\phi_k \cos 2\psi + \frac{1}{2} t_k \epsilon_k I p \sin 2\phi_k \sin 2\psi.$$

Collecting terms and using a value of $p = 1$, we arrive at the response equation,

$$S_k = \frac{1}{2} t_k I \left[1 + \epsilon_k (\cos 2\phi_k \cos 2\psi + \sin 2\phi_k \sin 2\psi) \right]. \quad (8.1)$$

This model can be fit to the response curves in Figure 8.2 to determine the transmission, t_k , efficiency, ϵ_k , and orientation, ϕ_k , of every polarizer. To determine the value

of t_k and ϕ_k absolutely, the incident flux, I and angles ψ must be known with high accuracy. These absolute measurements are needed to determine the Stokes parameters, I , Q , and U . However, the measurement of the normalized Stokes parameters, q and u , fractional polarization, p and the angle of linear polarization, ψ , only needs the relative transmissions and orientations between the polarizers. In this case, the absolute transmission cancels out, and the t_k terms act like a conventional flat field correction. Similarly, the absolute orientation of the polarizers does not matter - only the relative orientation between polarizers is important.

8.1.2 Pixel Throughput

The throughput of each polarimeter pixel can be described as the absolute throughput to unpolarized and polarized light or as a relative throughput, to specify throughput differences between each pixel; in this case, the throughput values act like a traditional flat field correction. The full field of view of RITPIC is shown in Figure 8.3. The light blue areas correspond to parts of the imaging sensor covered by the micropolarizer array. The dark blue strips along the bottom and the right edges are due to the opaque ceramic carrier which holds the micropolarizer array. The three small bright regions in the corners correspond to unmasked areas of the imaging sensor.

Determining the absolute throughput of the micropolarizer array is difficult, because it is attached to the imaging sensor. Therefore, measuring its throughput must be performed the way the quantum efficiency is characterized. These kinds of absolute measurements are quite challenging and rarely have accuracy better than 1% - 2%. However, the uncovered regions on the sensor (small bright areas in the corners of Figure 8.3) can be used to estimate the throughput of the array in a relative way. Assuming the illumination is uniform across the entire sensor, the throughput of the micropolarizer array, relative to the signal measured at the corners can be determined.

Using the flux in the uncovered areas, the throughput of the micropolarizer array to unpolarized is estimated to be $\sim 30\%$. This might seem very low, but a perfect polarizer

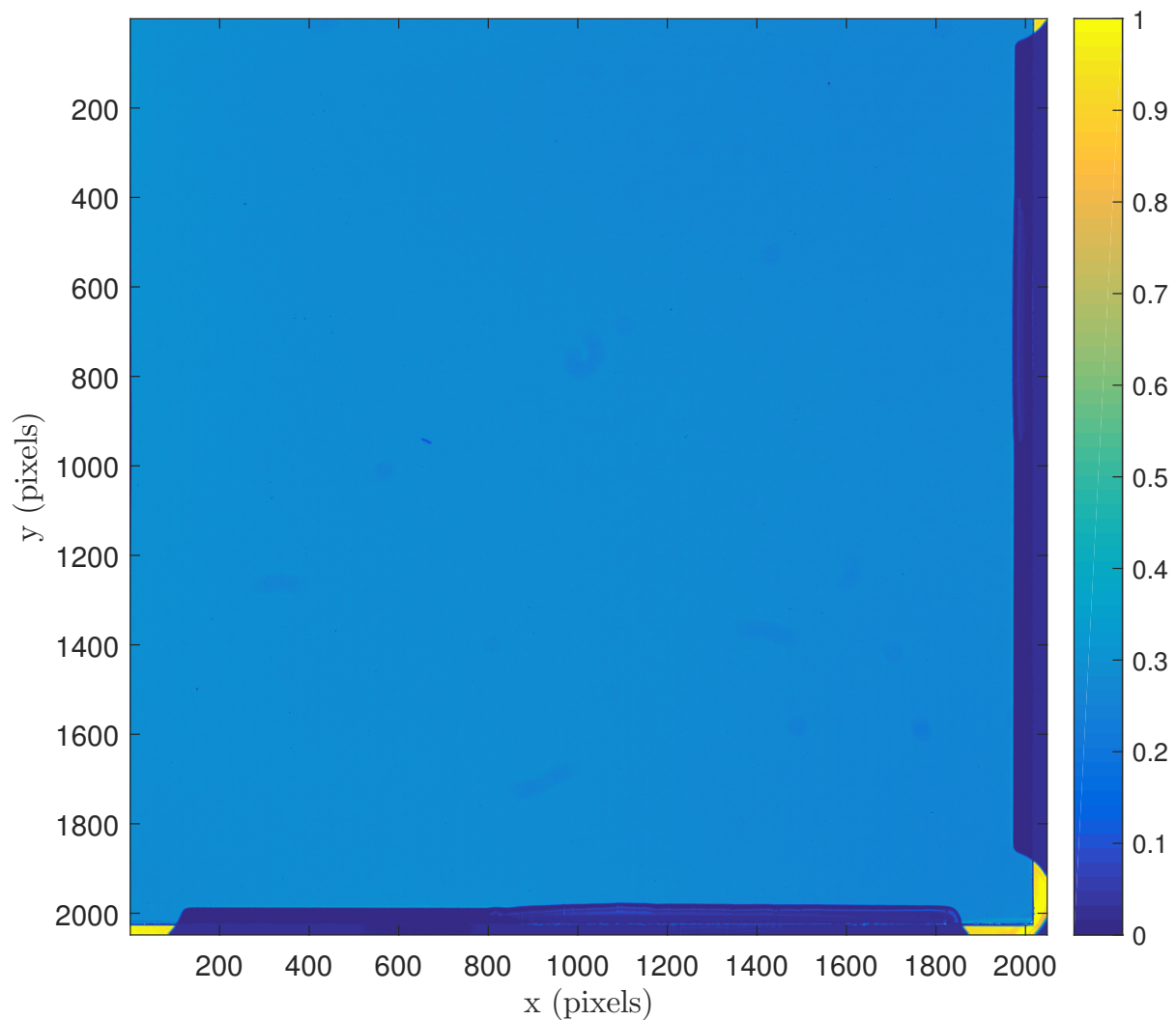


FIGURE 8.3: Full sensor area, uniformly illuminated by unpolarized light. The small, bright regions in the corners are uncovered areas of the sensor, which are used to calculate the throughput of the micropolarizer array (center).

has only 50% throughput to unpolarized light. Several effects contribute to the additional 20% loss:

- opaque regions around each micropolarizer pixel reflect $\sim 10\%$ of the light (see section 5.1.3)
- absorption due to the aluminum layer (see section 5.1.3)
- reflection due to the glass micropolarizer substrate
- absorption in the micropolarizer substrate

The absolute transmission is useful to estimate the required exposure time for an observation and is critical for absolute photometry. However, accurate polarimetry does not need depend on knowing the absolute transmission of the micropolarizer pixels. Instead, we must measure the differences in transmission of the pixels, relative to each other. This is analogous to a flat field correction in conventional differential photometry. These values are given by fitting the polarizer model to a series of polarized flat field images, which is described in the previous section. The relative transmissions, t_k , show systematic transmission differences between pixels of different orientations, as well as broad variation for the same kind of pixel.

8.1.3 Relative Transmission - t_k

To measure the relative transmissions, t_k , the sensor was uniformly illuminated with polarized light, using the setup shown in Figure 8.1). Furthermore, the edges of the sensor were masked off using a baffle in front of the camera window. This was done to mitigate the instrumental polarization caused by the micropolarizer carrier. The resulting usable area is a 1400×1400 pixel region near the center of the sensor (Figure 8.4). This is a very conservative mask, because the illumination from the integrating sphere has a relatively large divergence. For an actual imaging system with a given $f/\#$, an effective baffle can be designed with a minimal loss of usable area.

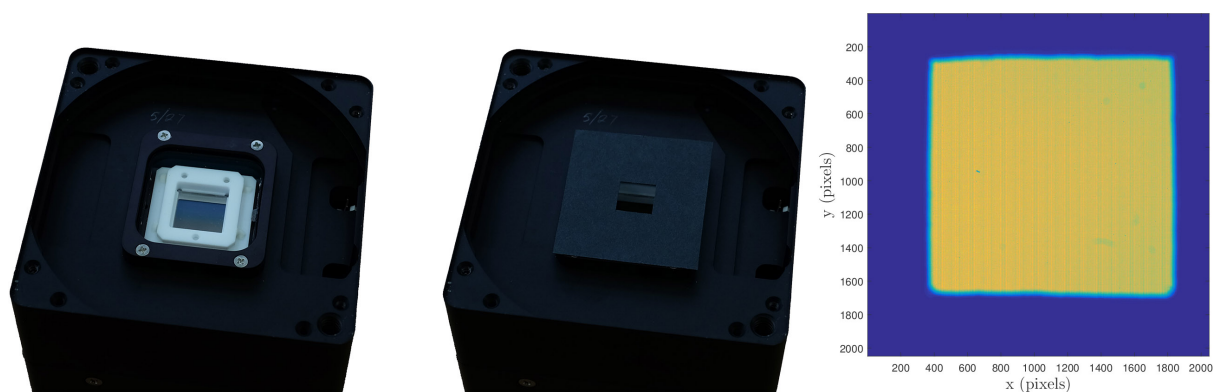


FIGURE 8.4: *Left:* The camera head, with the front plate removed. The silver square in the middle is the micropolarizer array, surrounded by the white ceramic carrier. *Middle:* To avoid the polarizing effects of the carrier, I used a mask to baffle the sensor. *Right:* the baffle covers more of the edges than necessary, however, the resulting active area (yellow square) is still a large fraction of the sensor.

The histograms of the relative transmissions are shown in Figure 8.5. In this figure, the transmission values of all pixels of a certain orientation are normalized by the mean transmission of all pixels. This clearly shows the systematic differences between pixels of different orientations. For example, on average, 0° pixels have roughly 20% higher throughput than 45° pixels. Furthermore, the pixels of a single orientation do not show uniform throughput, with a typical standard deviation of $\sim 5\%$ about the mean.

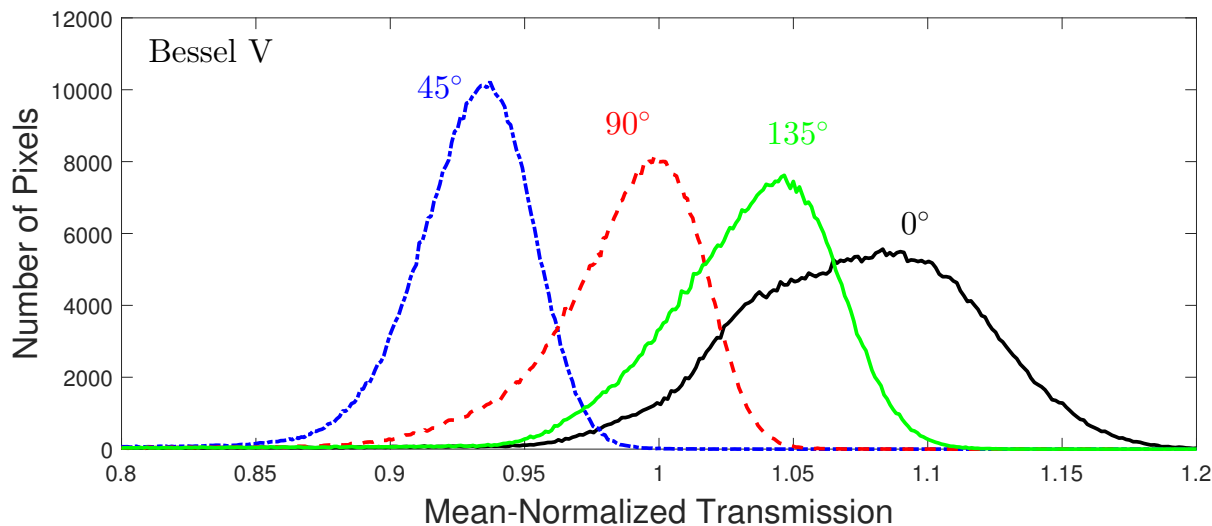


FIGURE 8.5: Histograms of the mean-normalized transmissions, t_k , for pixels of each orientation. The throughputs are systematically different for pixels with different orientations. There is a broad distribution of transmissions even for pixels of the same orientation.

The distribution of transmission values for pixels of a certain orientation are significant. Furthermore, pixels with lower or higher transmission are not distributed randomly on the array. Instead, regions of higher or lower throughput can be seen for each orientation (Figure 8.6).

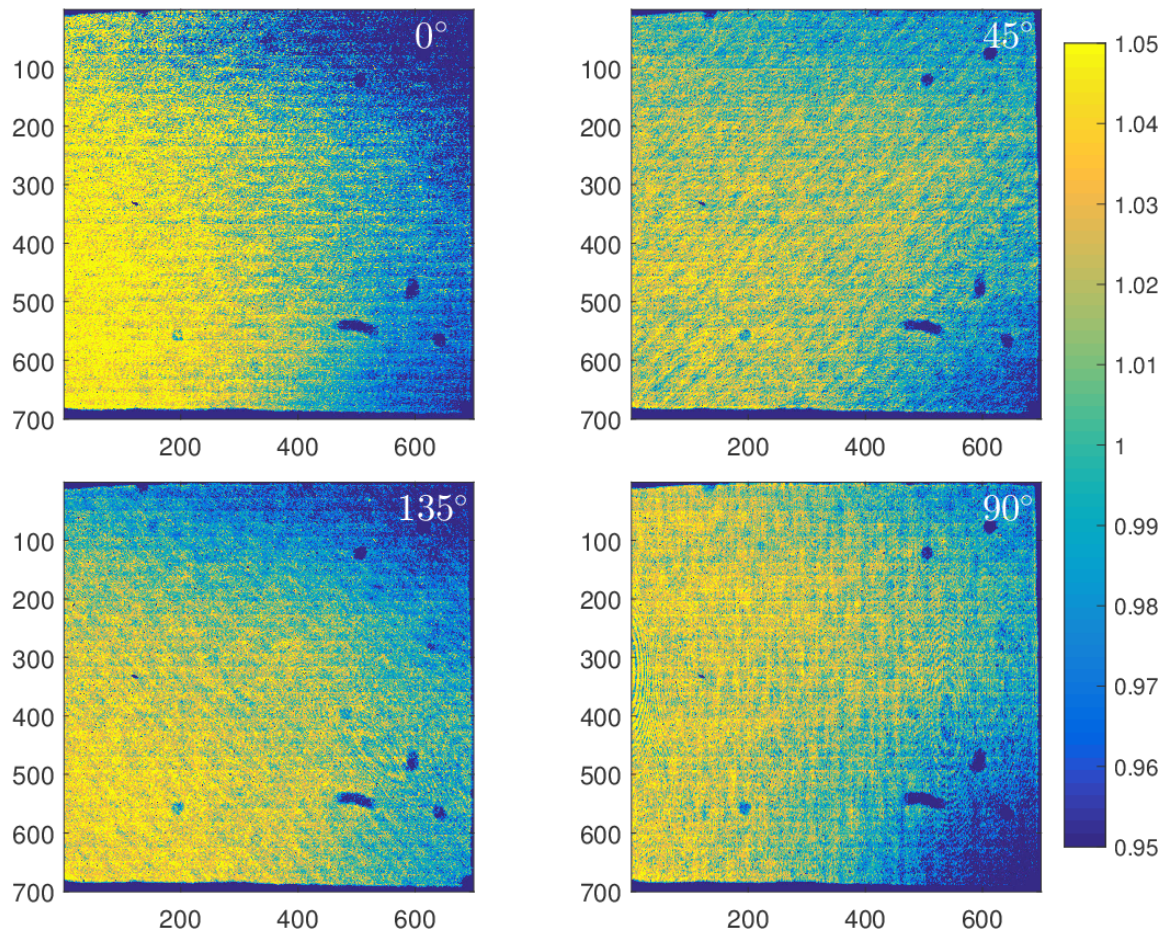


FIGURE 8.6: Relative throughputs, t_k , for each pixel orientation, normalized by their own mean value. The regions of higher throughput correspond to areas of better alignment.

8.1.4 Polarizer Efficiency - ϵ_k

The efficiency of the polarizer, ϵ_k , describes its ability to reject the unwanted polarization states. The efficiency can be expressed using a “leak” term, l_k , which is the throughput of the polarizer for light oriented perpendicular to the polarizer’s axis,

$$\epsilon_k = \frac{1 - l_k}{1 + l_k}.$$

An efficiency of ~ 0.94 corresponds to a leak of $l_k \sim 0.03$. This roughly agrees with a contrast of $\sim 30:1$. As I mentioned in Chapter 5, this low contrast appears to be due to cross-talk from nearby pixels, as the efficiency of an individual pixelated polarizer is significantly higher than this.

The pixels of RITPIC do not show dramatic systematic differences in efficiency, which is seen in the throughput, t_k , except for 135° pixels. Furthermore, the range of efficiency for pixels of the same orientation are more narrow than that of t_k (Figure 8.7). However, the spatial distribution of efficiency is not random, and there are clear regions of high and low efficiency (Figure 8.8). Curiously, the areas of highest throughput do not correspond to areas of highest efficiency. They may be because areas of low throughput also show very low amounts of “leaked” light.

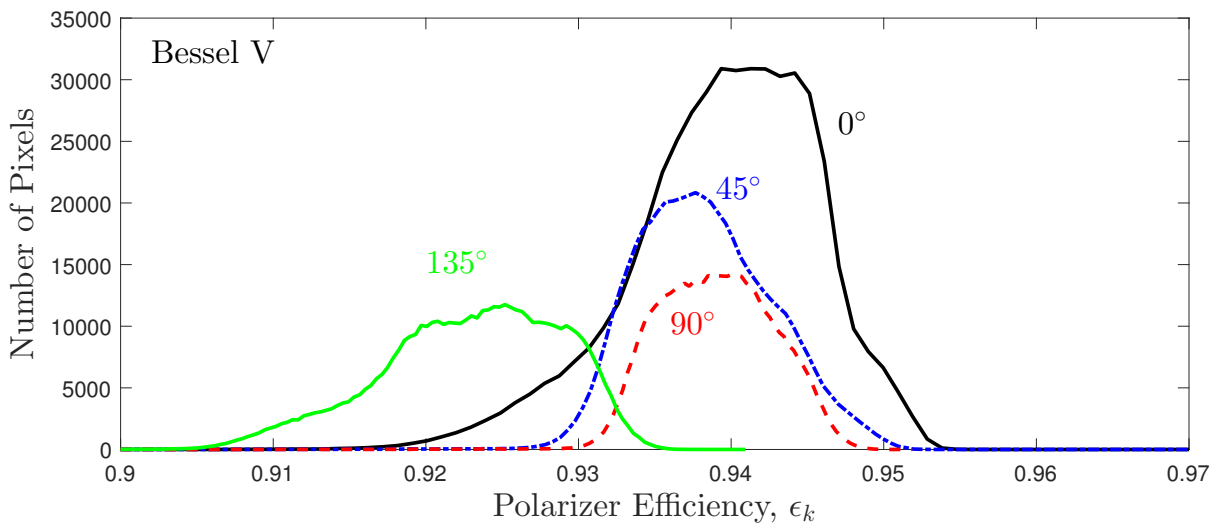


FIGURE 8.7: Histograms of the polarizer efficiency, e_k , for pixels of each orientation. The efficiency is similar for pixels with different orientations, with only the 135° pixels showing a systematic difference.

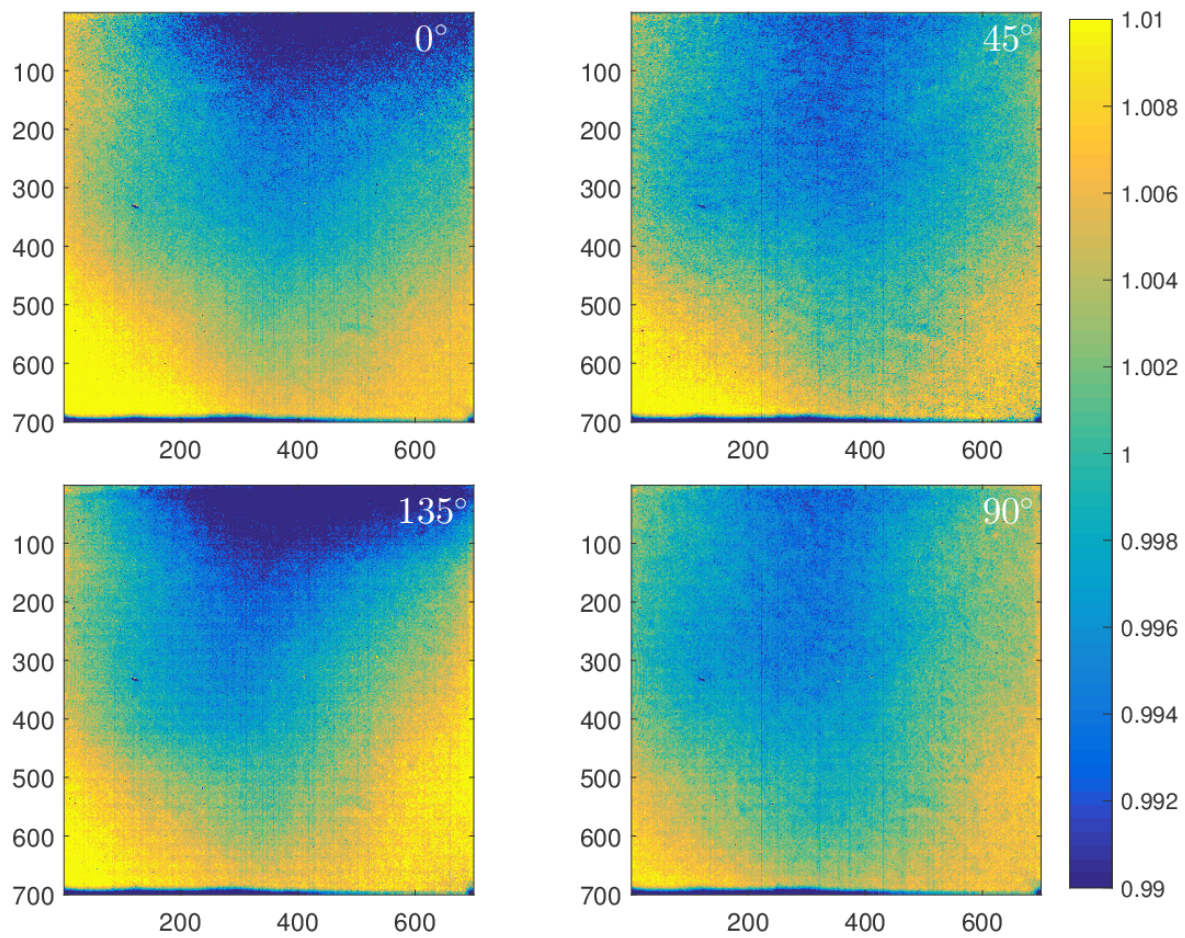


FIGURE 8.8: Spatial distribution of polarizer efficiency, ϵ_k for each pixel orientation, normalized by their own mean value. The spatial distribution of ϵ_k and t_k are only roughly similar (showing a top-down gradient) to the distribution of throughputs, t_k .

8.1.5 Pixel Orientation - ϕ_k

The last parameter needed to describe a polarizer is its orientation, ϕ_k . In polarimetry, the relative orientations between polarizers must be known with high accuracy, because the orientation contributes to the transmission coefficients B_k and C_k in equation 6.3. Fitting the polarizer model to the response curves allows one to determine the relative orientations between pixels with high precision. The distributions of orientations for each pixel orientation are shown in Figure 8.9.

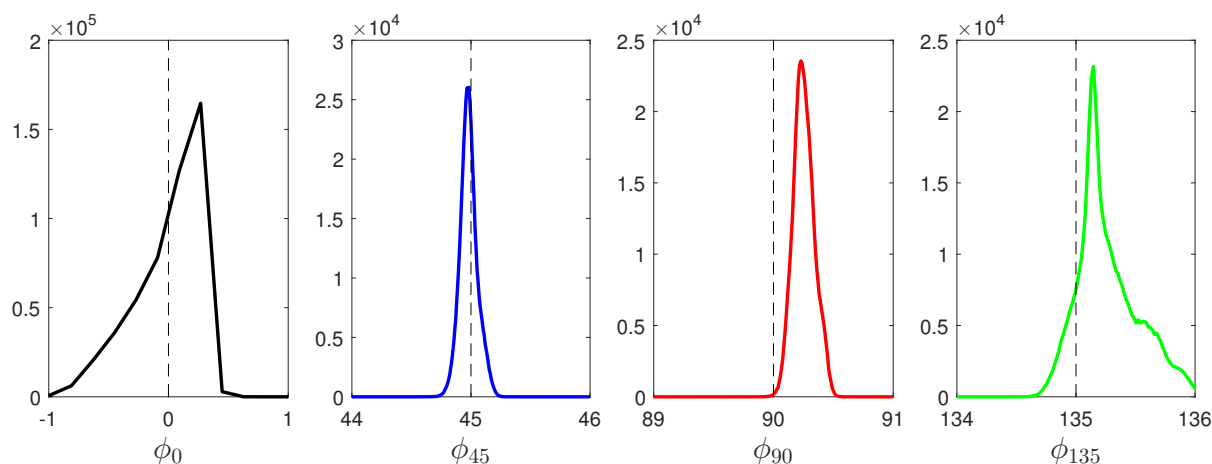


FIGURE 8.9: Histograms of the polarizer orientations, ϕ_k , for pixels of each orientation.

On average, RITPIC's pixels are close to their nominal orientations. However, some pixels show relatively broad distributions of orientation. For example, there are hundreds of 0° and 135° pixels that are 1° away from their nominal position.

These orientations may not exactly reflect the physical direction of the micropolarizer wires. Instead, they are an “effective” orientation. That is, these polarizers behave as having these orientations. This is important to note, because the effective orientation can be affected by the alignment between the micropolarizer and the CCD (which is never perfect). Also, this means the effective orientation can change across the sensor. Indeed, maps of the spatial distribution of pixel orientation show large scale patterns (Figure 8.10).

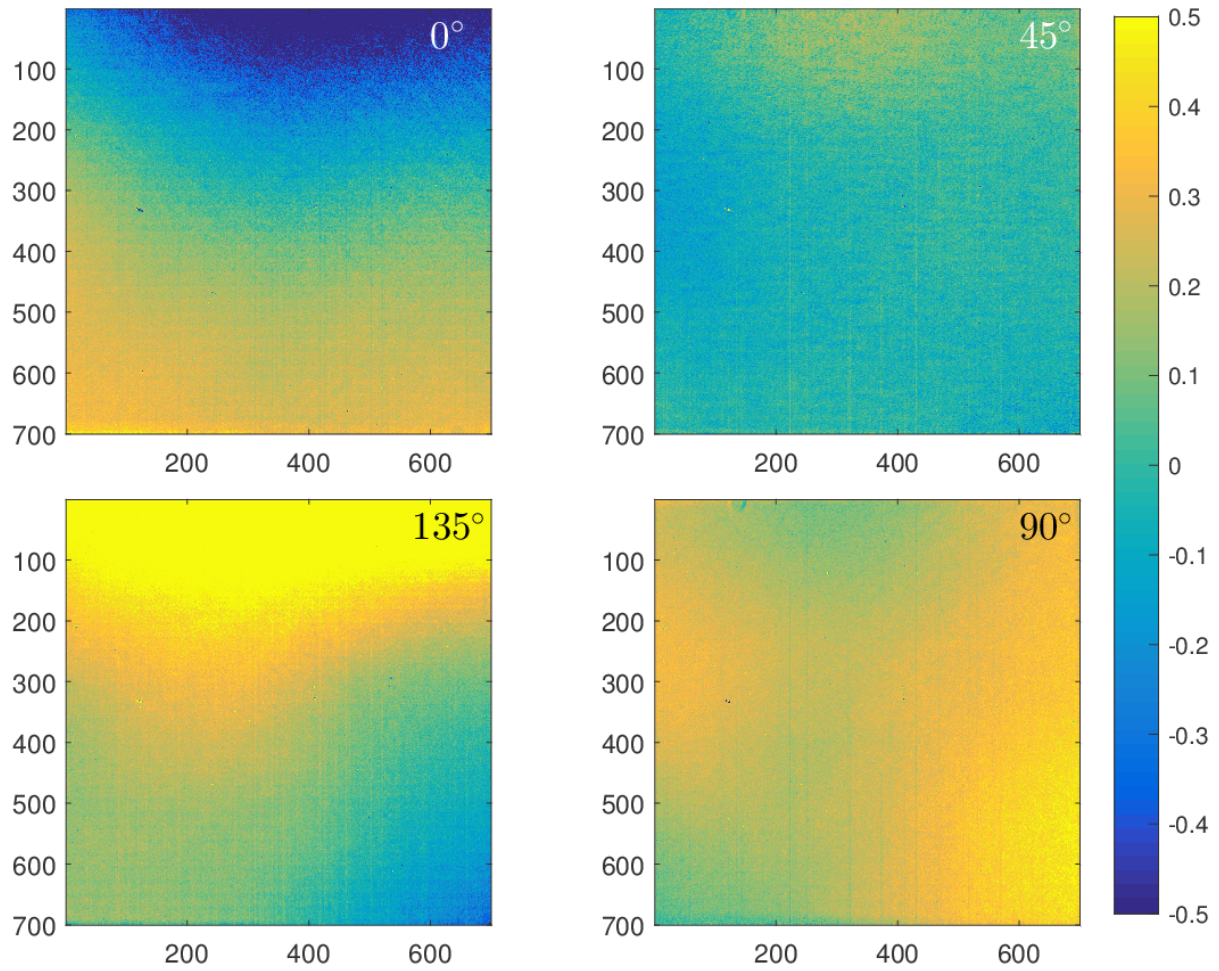


FIGURE 8.10: Spatial distribution of polarizer orientation. The scale shows offsets from the nominal orientation.

8.2 Simulating the Polarimetric Performance

Once the device has been characterized, the polarimetric accuracy and the presence of systematic effects can be investigated using synthetic observations. This is a critical tool for device calibration and estimation of measurement uncertainty. In this section, I describe the procedure I developed to generate synthetic observations of point sources using RITPIC.

8.2.1 Simulated Observations of Point Sources

The observation of unresolved “point” sources, which can be stars or fluorescent molecules, is one of two main observational regimes that polarimeters like RITPIC are suited for - the other being imaging of scenes/resolved objects. The simulated images are generated in two steps: first, the point spread function (PSF) is generated, given a certain shape and peak intensity; second, the PSF is modulated at the pixel level, based on the specified fractional polarization p , angle of polarization, ψ , as well as pixel throughput, efficiency, and orientation.

8.2.1.1 Step 1. Generation of the Point Spread Function

To generate the PSF, one must specify the peak intensity, shape, and the sampling in the focal plane. In general, the shape will be determined by the optical system and any “seeing effects” due to the observing medium, like the atmosphere. The more the modeled PSF resembles the actual PSF, the more accurate the results of this analysis will be. It’s common to model the PSF as a 2D Gaussian. A more robust approach might involve building a library of PSFs using actual observations with the system. For now, I use the simple Gaussian model (Figure 8.11). First, the Gaussian is created in high resolution and then it is down-sampled to achieve the desired sampling in the focal plane. The high resolution Gaussian can be translated with high precision, to simulate sub-pixel shifts in the sampled image.

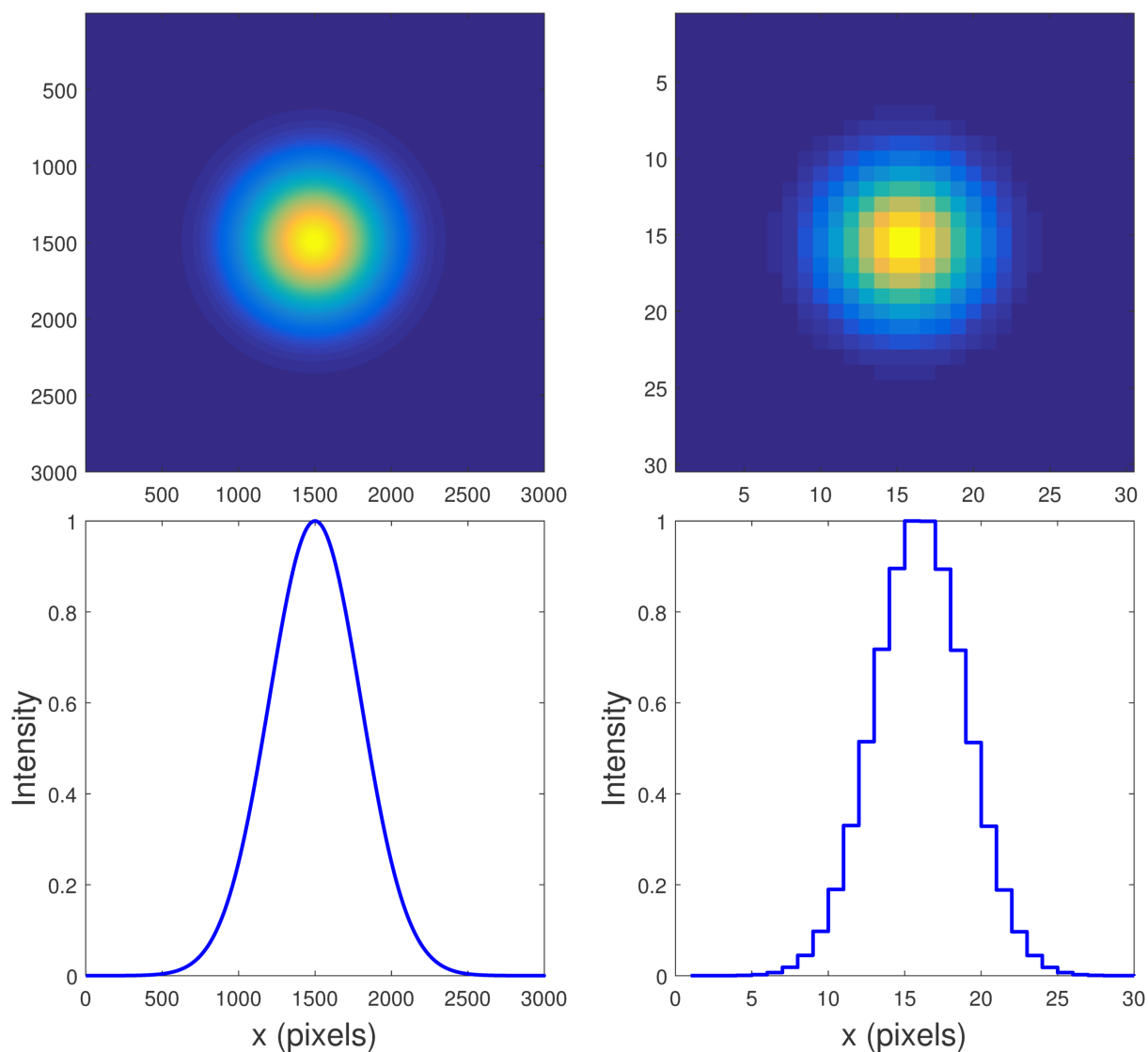


FIGURE 8.11: *Left:* The initial Gaussian PSFs are generated in high resolution to allow precise shifts; presumably, this is what the electric field distribution looks like before it is sampled by the sensor. *Right:* The continuous image is sampled by the sensor, according to the magnification / plate scale of the imaging system.

Adding Noise

Once the general shape is determined, each Gaussian is scaled by the desired intensity. Then, Poisson noise is added to the PSF, based on the resulting values in each pixel. Next, a normally distributed sky background is added to the image. At this point, other additive noise terms can be introduced, such as dark current noise and read noise. Lastly, the PSFs are padded with empty regions of sky background, to better simulate a sparse field.

8.2.1.2 Step 2. Modulating the PSF

At this point, the PSF corresponds to the total intensity image, as it would be measured by a conventional imaging sensor which is not sensitive to polarization. Next, I prescribe a fractional polarization, p_0 , and angle of linear polarization, ψ_0 , to this synthetic star. This is done by calculating the values S_k for each pixel, using equation 8.1, the properties of each pixel determined through characterization and the known parameters of the synthetic star. The resulting modulated PSFs can be quite complex, depending on the degree of polarization of the source. For highly polarized sources, the modulation is easily seen by eye (Figure 8.12); conversely, weakly polarized PSFs appear more-or-less unchanged.

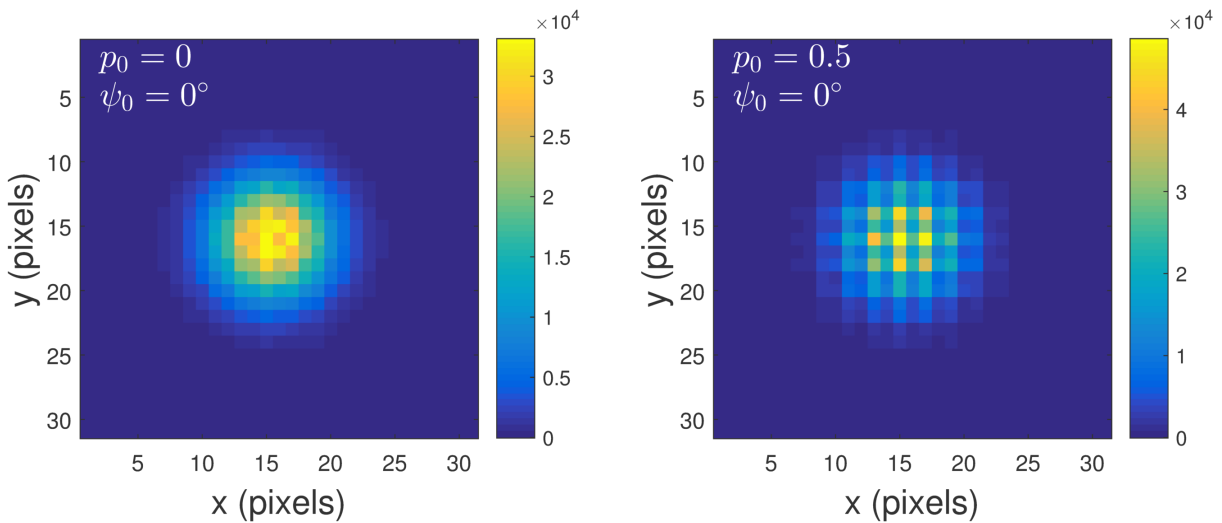


FIGURE 8.12: *Left:* The total intensity PSFs are modulated by the micropolarizer array based on the intrinsic properties of the source. Weakly polarized stars appear relatively unchanged. *Right:* Highly polarized stars show a strong modulation pattern. For example, this object is polarized with an angle of 0° , so the 0° pixels appear brighter than the rest.

At this point, these synthetic images represent the “raw” images one would acquire with a micropolarizer-based polarization sensor. These images can now be processed by data analysis software routines, to evaluate the ability of the system and the routines to accurately reconstruct the polarization properties of the source. In the next section, I use this synthetic data to analyse systematic sources of error, as well as the effects of sampling and shot noise SNR on the precision of the polarimetric analysis.

8.2.2 Effects of Sampling

Most astronomical imaging systems are designed with a special attention paid to the sampling in the focal plane. Astronomers normally interpret the Nyquist-Shannon sampling criterion to require a minimal number of two pixels across the full-width at half-maximum (FWHM) of the PSF. In general, astronomers oversample the PSF and make sure that the FWHM of the PSF spans more than two pixels. This oversampling appears to result in more stable photometry; a notable exception would be the Kepler photometer, which is severely undersampled ([Van Cleve and Caldwell, 2009](#)).

In the case of the micropolarizer array, the choice of sampling is even more critical and less obvious. Depending on the exact location of the PSF, some pixels might receive more or less flux due to the shape of the PSF, rather than the polarimetric content of the light. To investigate the effects of sampling in the presence of atmospheric seeing, I generated several sets of synthetic observations using a sampling from two to eight *superpixels* (2×2 pixel sets) across the FWHM.

For each set of observations, 500 images are generated and analyzed. The center of a star in each frame has a random offset from being perfectly centered (as in Figure 8.11), by some increment of 0.1 pixels, up to a maximum displacement of 2 pixels. These synthetic observations were performed for stars with varying degrees of polarization, $p = 0, 0.05,$ and 0.5 and $\psi = 0$; therefore, the signal should be completely in Stokes q and not in u . The simulations were performed using an ideal polarizer model (with perfect throughput, efficiency and orientation) and a non-ideal model, which uses the values determined for RITPIC during the characterization process.

In practice, the size of the PSF in the focal plane, the total flux and the peak intensity are related and they all affect the photometric and polarimetric precision. I attempt to separate these three effects by performing tests aimed at isolating the effects of sampling and photometric SNR.

8.2.2.1 Case 1. Constant Photometric SNR

In this case, I attempt to disentangle the effects of sampling on the polarimetric precision from those of photometric SNR. As I increase the sampling (and the size of the synthetic stars), I scale the peak intensity to keep the total number of photons (as would be measured by aperture photometry) constant. The resulting stars are shown in Figure 8.13).

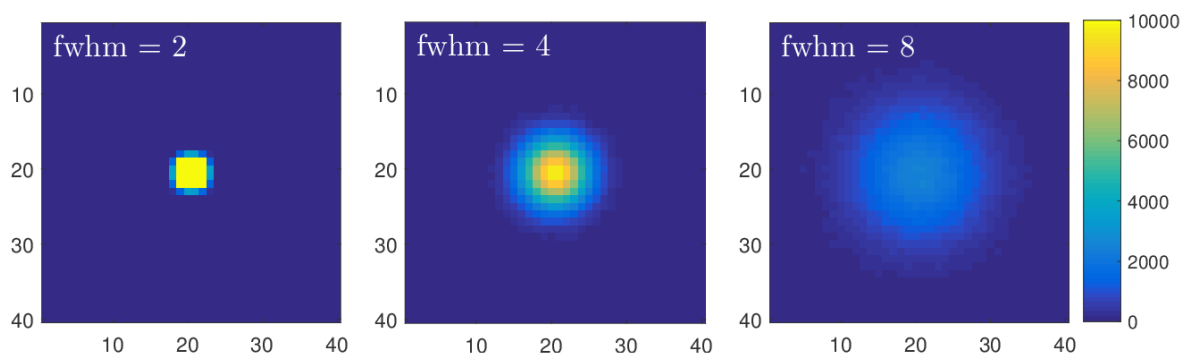


FIGURE 8.13: Synthetic stars generated to have 2, 4, and 8 superpixels across their full-width at half-maximum in the focal plane. Each star has the same total flux.

The estimation of Stokes u and u for this case is shown in Figure 8.14 and Figure 8.15, respectively. Each point corresponds to the mean value measured from a set of 500 synthetic images, while the error bars show the standard deviation. For the unpolarized source, the scatter of the Stokes q estimation decreases when the sampling is increased from 2 superpixels across the FWHM, to 3. Increasing the FWHM further does not seem to affect the uncertainty. When the fractional polarization increases to a mean level of $q = 0.05$ and $q = 0.5$, the scatter is again reduced by using 3 superpixels to sample the FWHM. The non-ideal polarizer appears to have a systematic bias, which depends on the sampling. This is due to calibration error during the demodulation process. I show how to correct this in the next section.

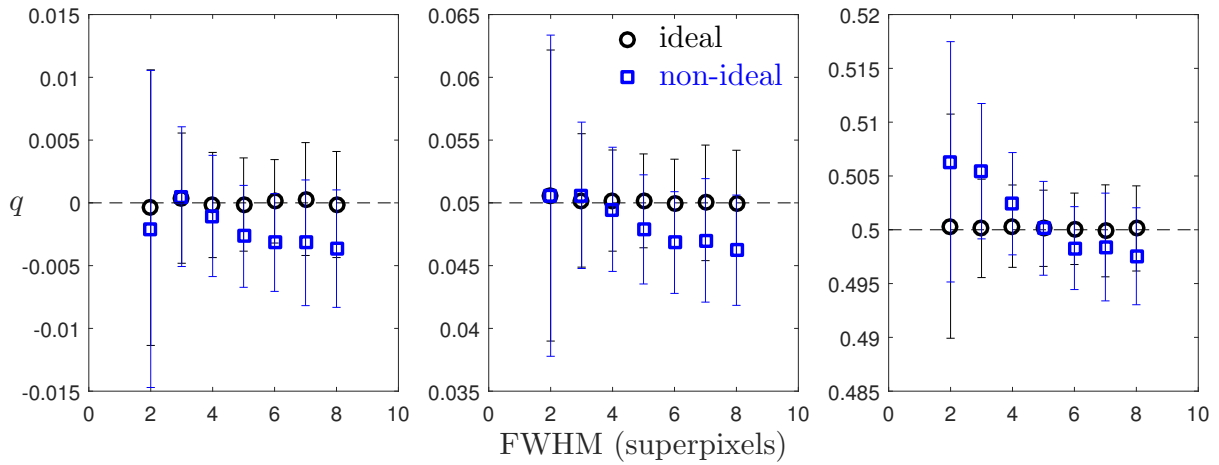


FIGURE 8.14: The estimation of q , for stars with intrinsic $q = 0, 0.05$, and 0.5 , using an ideal and non-ideal polarimeter. The total flux was held constant as the FWHM was increased (Figure 8.13). In each case, the scatter of the measurement is reduced by increasing the FWHM to 3 superpixels, with negligible gains seen with higher sampling.

The estimation of Stokes u shows trends similar to those seen for Stokes q . The measurement scatter is reduced by increasing the FWHM from 2 to 3, with only minimal gains seen at larger values. However, the systematic error seen in the non-ideal polarimeter's estimation appears to improve steadily with higher sampling. Although this looks like an improvement in accuracy, it may be caused by a decreasing per-pixel SNR. As noise begins to dominate, it becomes more difficult to measure a systematic difference between the fluxes measured by the 45° and 135° pixels. This results in the trend to zero polarization, except now zero happens to be the correct value.

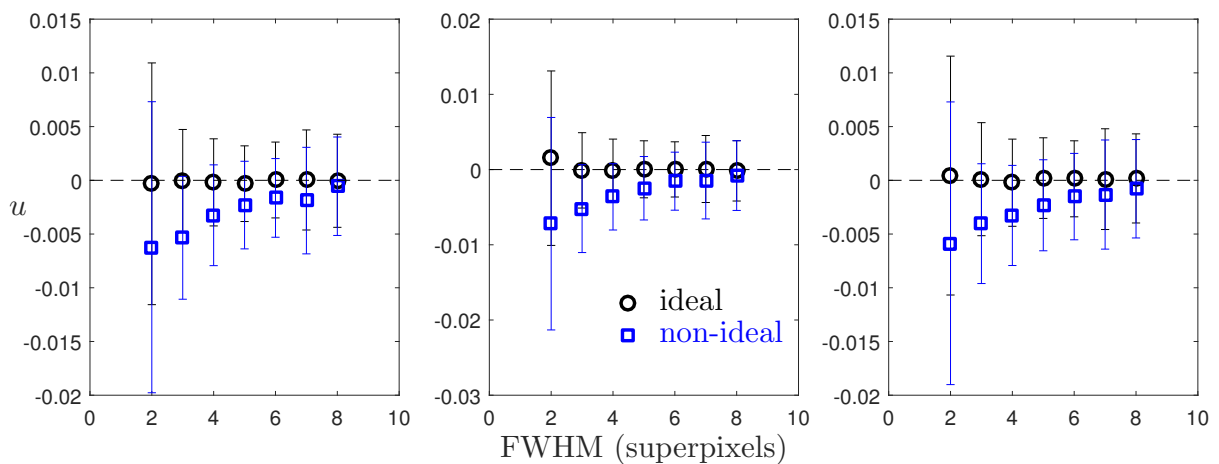


FIGURE 8.15: The estimation of u , for stars with intrinsic $u = 0$, using an ideal and non-ideal polarimeter. The total flux was held constant as the FWHM was increased (Figure 8.13). In each case, the scatter of the measurement is reduced by increasing the FWHM to 3 superpixels, with negligible gains seen with higher sampling.

8.2.2.2 Case 2. Constant Peak Intensity

Sometimes, it may be possible to increase the exposure time to maintain a constant peak intensity as the PSF grows larger. In practice, this might be a good idea to keep the measured signal in the linear regime of the sensor and to maintain the per-pixel SNR against the onslaught of sky noise and read noise. In this case, the total flux per exposure increases rapidly and the stellar profiles resemble those shown in Figure 8.16.

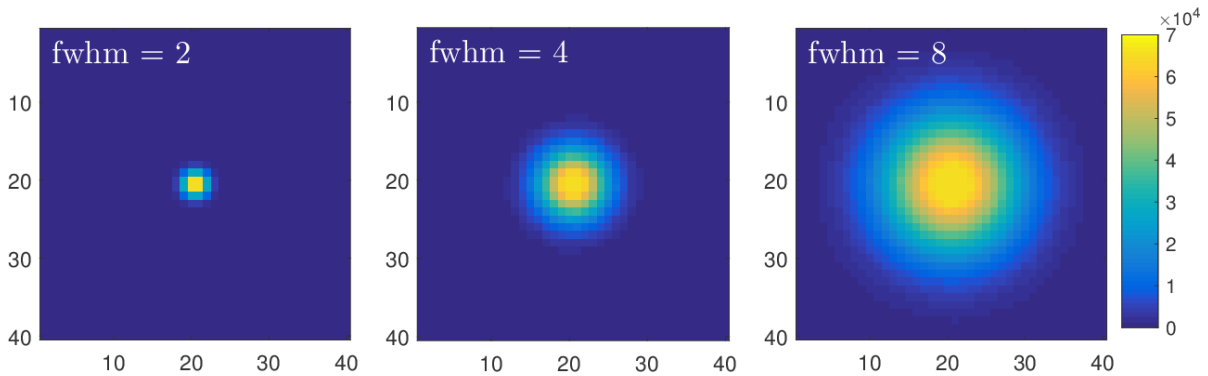


FIGURE 8.16: Synthetic stars generated to have 2, 4, and 8 superpixels across their full-width at half-maximum in the focal plane. Each star has the same peak intensity, but the total flux increases as the PSF grows larger.

The estimation of the Stokes q and u parameters is shown in Figure 8.17 and Figure 8.18, respectively. As the sampling (and total flux) increases, the scatter in the measurement of Stokes q decreases rapidly and levels off when the PSF is sampled with 5 superpixels across the FWHM. As the polarization of the star increases ($q = 0.05$ and $q = 0.5$), some systematic effects become apparent for the measurement made with the non-ideal polarimeter. Overall, the mean value of q decreases as the sampling increases. This was also seen for the previous case, where the flux was held constant. Looking more closely at the non-ideal curves, it appears that the slope changes around a sampling of 5 - 6 superpixels. For all three intrinsic values of q , the systematic error appears to level out at a value of $\Delta q \approx 0.003$.

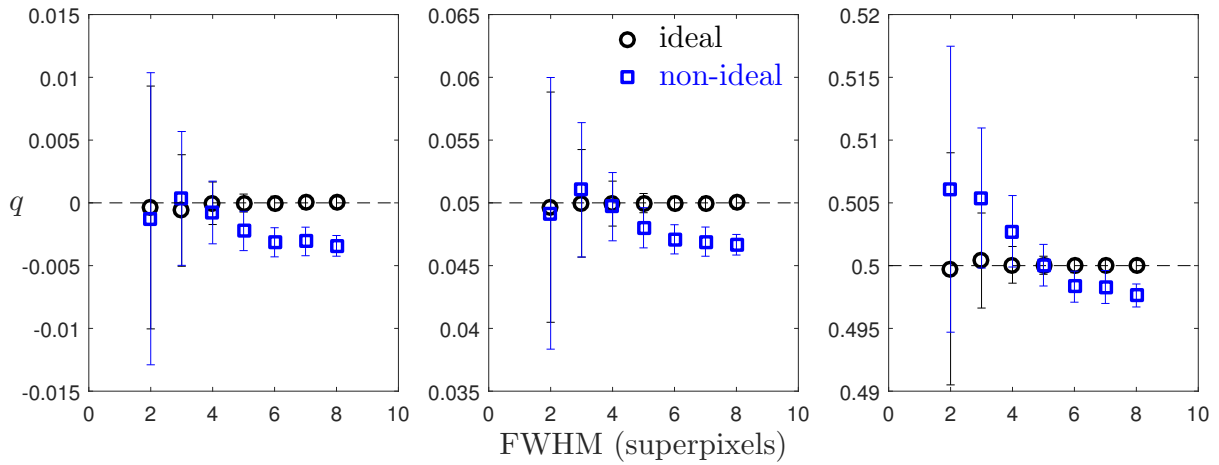


FIGURE 8.17: The estimation of q , for stars with intrinsic $q = 0, 0.05,$ and 0.5 , using an ideal and non-ideal polarimeter. The peak intensity at each sampling was held constant, allowing the total flux to increase (Figure 8.16). In each case, the scatter of the measurement is reduced by increasing the FWHM sampling to 5 superpixels, with negligible gains seen with higher sampling.

The measurement of Stokes u shows similar reduction of scatter, as the stars are sampled with more superpixels. As the sampling increases, the non-ideal polarimeter's accuracy improves and the estimation trends to zero. However, in this case, the per-pixel SNR is also increasing. This suggests that the improvement seen in the low SNR case (Figure 8.15) could be real.

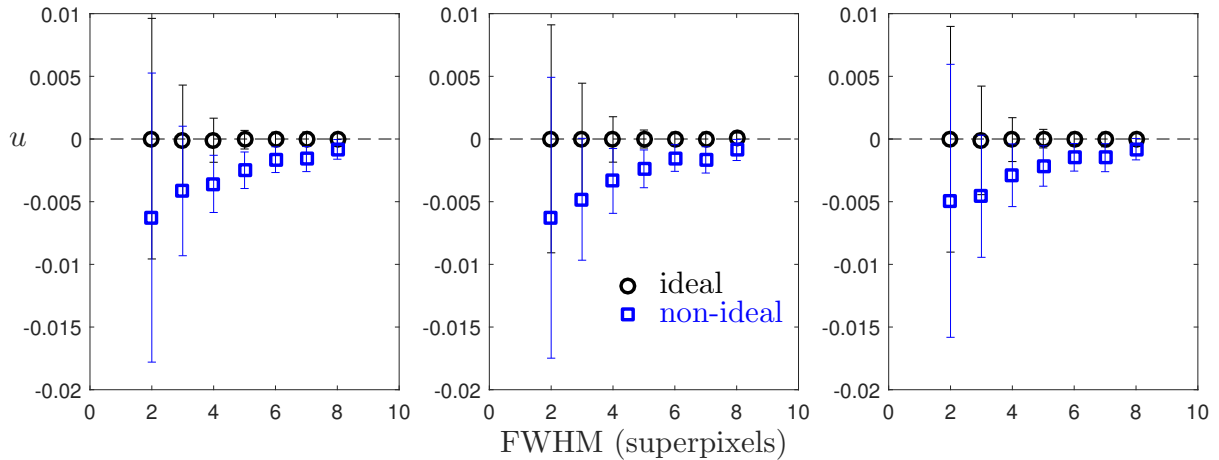


FIGURE 8.18: Synthetic stars generated to have 2, 4, and 8 superpixels across their full-width at half-maximum in the focal plane. Each star has the same peak intensity, but the total flux increases as the PSF grows larger.

8.2.2.3 Case 3. Constant Sampling, Varying Flux

Lastly, I look at the effect of photometric SNR, independent of the effects of sampling. This is done by keeping the size of the PSF constant at four superpixels across the FWHM and decreasing the peak value, thereby decreasing the photometric SNR. Some example intensity profiles are shown in Figure 8.19); note that the scaling was set to emphasize the low-signal regions and the saturated regions of the brighter stars have values higher than 1000 counts. The stars generated for this test had shot-noise SNR of 40, 75, 150, 375, 750, 1500, and 1850.

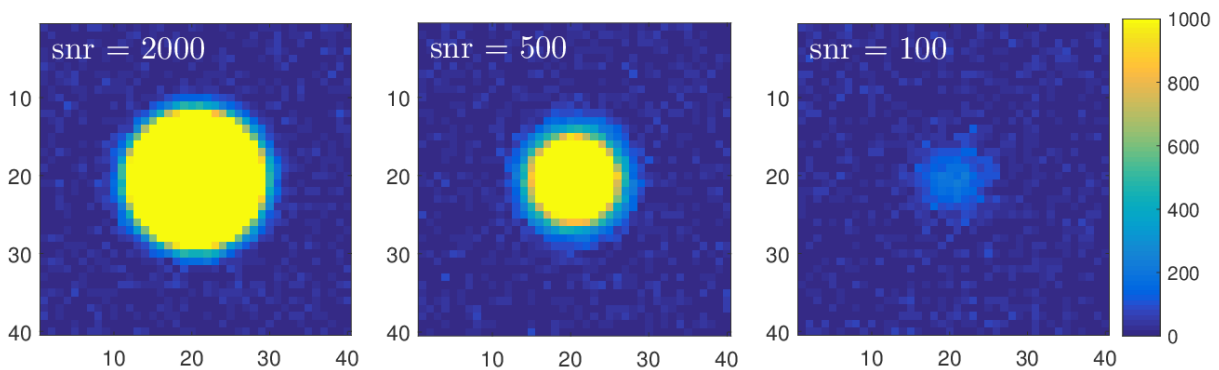


FIGURE 8.19: Synthetic stars generated to have 4 superpixels across their full-width at half-maximum in the focal plane. Each star has a different peak intensity and, as a result, photometric SNR. Note that the high SNR images appear saturated because the scaling was chosen to ease comparison with the faint case.

As might be expected, the shot-noise SNR has a dramatic effect on the precision of the polarimetry. The estimation of q is shown in Figure 8.20. When the total flux is low and the shot-noise SNR is $\lesssim 200$, the scatter about the true value of q is $\sim 2\%$. Raising the SNR to ~ 500 dramatically decreases the random scatter, with diminishing returns seen above SNR of ~ 750 .

The estimation of u , when the intrinsic $u = 0$, appears especially vulnerable to shot-noise (Figure 8.21). The scatter in the measurements does not decrease significantly until an SNR of ~ 750 is achieved. This is not surprising, because this estimate is an example of the notorious problem of subtracting two large quantities to determine a small quantity.

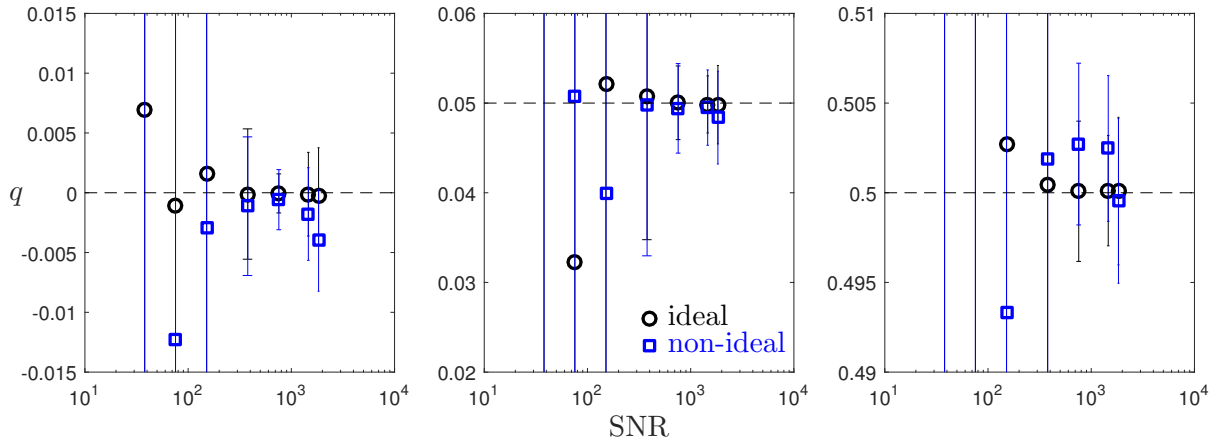


FIGURE 8.20: Synthetic stars generated to have 4 superpixels across FWHM. The peak intensity of each star was increased to increase the shot-noise SNR. The scatter about the true value decreases significantly for stars with $\text{SNR} \gtrsim 300$.

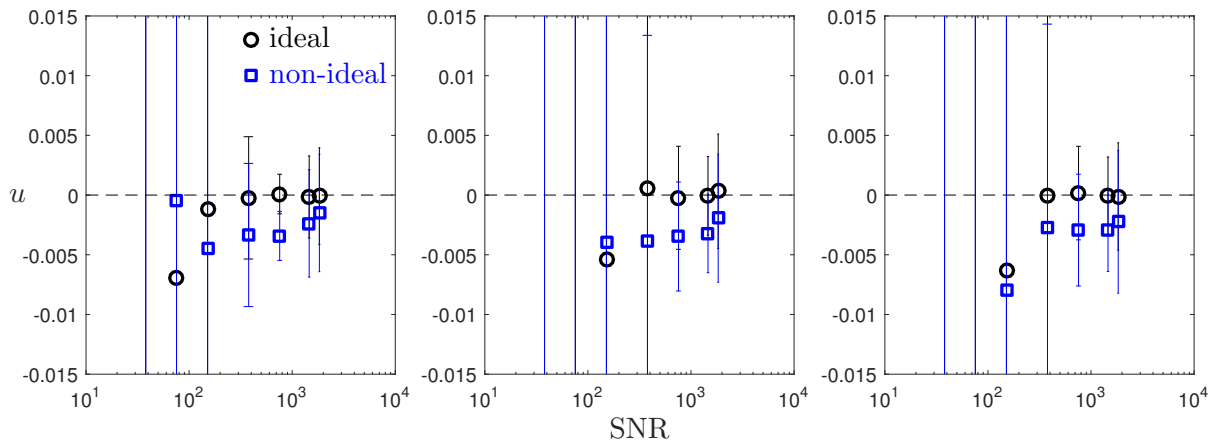


FIGURE 8.21: Synthetic stars generated to have 4 superpixels across their FWHM. The peak intensity of each star was increased to increase the shot-noise SNR. The scatter about the true value decreases significantly for stars with $\text{SNR} \gtrsim 750$.

8.2.3 Correcting the Systematic Drift

The estimations of q and u made with the non-ideal polarizer performed in this section shows a systematic drift as the sampling is increased and more pixels are used for the estimate. This is a systematic error that arises from the non-uniformity of pixel throughput. Because the intensity is measured in each sub-frame using the values of many pixels, the polarizer properties are specified as the average throughput, efficiency, and orientation of those pixels. However, polarimetric errors will arise if the differences between individual pixel throughputs are not accounted for using a flat fielding process. The effect becomes

stronger with higher sampling because more pixels are used in the measurement. Therefore, small systematic errors start to add up. The flat-field corrected estimates are shown in Figure 8.22 and Figure 8.23.

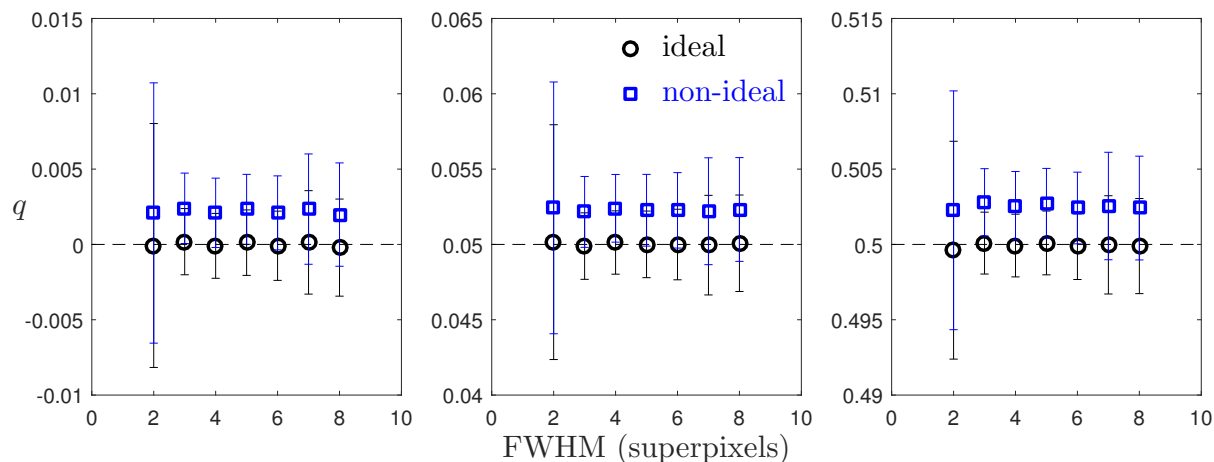


FIGURE 8.22: The estimation of q , for stars with intrinsic $q = 0, 0.05$, and 0.5 , using an ideal and non-ideal polarimeter. The total flux was held constant as the FWHM was increased (Figure 8.13).

Using the flat field correction has two effects on the Stokes q and u estimation. First, the systematic drift is removed and a constant offset remains. The offset is due to the imperfect characterization of the instrument. Second, as the number of pixels used to sample the star increases, the uncertainty first decreases, reaching a minimum value around $\text{FWHM} = 4$, and then begins to increase again. The uncertainty increases because as more and more pixels are used to measure the intensity, the variance due to the differences between pixels also increases, while the photon SNR is kept constant.

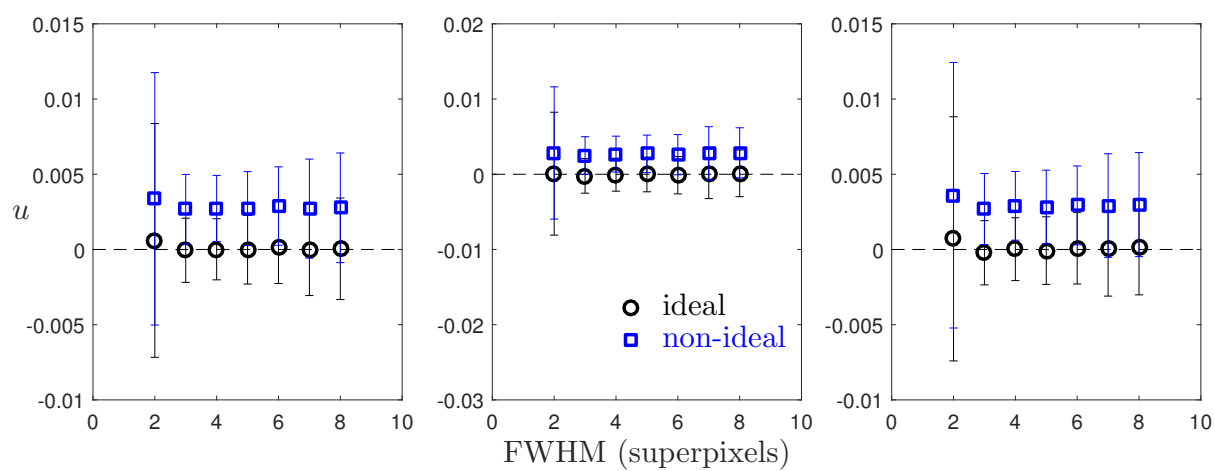


FIGURE 8.23: The estimation of u , for stars with intrinsic $u = 0$, using an ideal and non-ideal polarimeter. The total flux was held constant as the FWHM was increased (Figure 8.13).

Maintaining Constant Peak Intensity

If the exposure time is increased to maintain constant peak intensity as the sampling is increased, the scatter rapidly decreases (Figure 8.24 and Figure 8.25). The flat-field correction removes the systematic drift and does not appear to introduce random errors as the sampling increases, as in the case of constant flux.

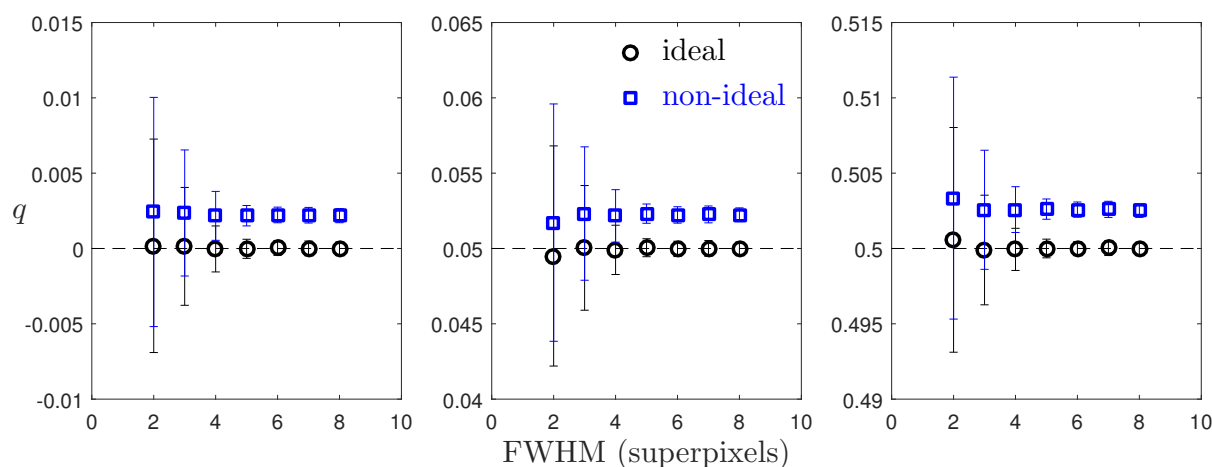


FIGURE 8.24: The estimation of q , for stars with intrinsic $q = 0, 0.05$, and 0.5 , using an ideal and non-ideal polarimeter. The peak intensity at each sampling was held constant, allowing the total flux to increase (Figure 8.16). In each case, the scatter of the measurement is reduced by increasing the FWHM sampling to 5 superpixels, with negligible gains seen with higher sampling.

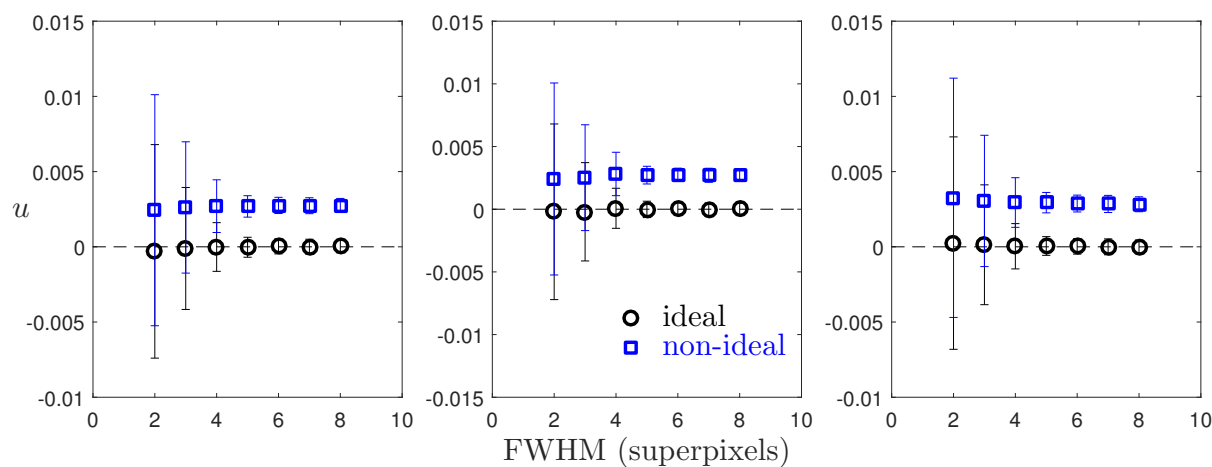


FIGURE 8.25: The estimation of u , for stars with intrinsic $u = 0$, and $q = 0, 0.05$, and 0.5 , using an ideal and non-ideal polarimeter. The peak intensity at each sampling was held constant, allowing the total flux to increase (Figure 8.16). In each case, the scatter of the measurement is reduced by increasing the FWHM sampling to 5 superpixels, with negligible gains seen with higher sampling.

Effects of Photometric SNR

Lastly, I revisit the case of constant FWHM and the effects of photometric SNR. The flat-field correction reduces the scatter of the q and u estimation and slightly improves the precision. Surprisingly, the scatter increases for simulations with the highest SNR. This is probably because the sampling of 4 superpixels is not sufficient for stars with the kind of extremely high peak intensity that's required to produce photometric SNRs of several thousand.

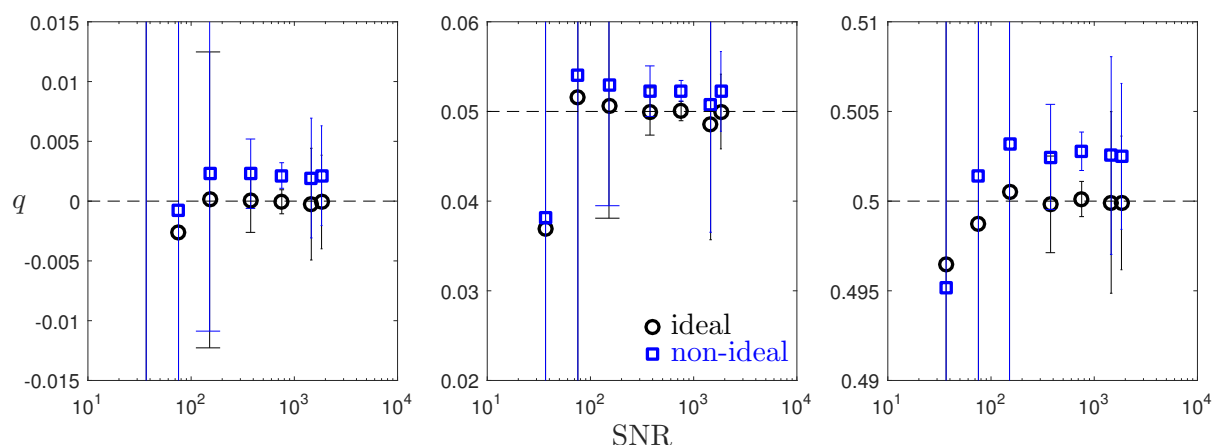


FIGURE 8.26: The estimation of q , for stars with intrinsic $q = 0, 0.05,$ and 0.5 , using an ideal and non-ideal polarimeter. The sampling was held constant at $\text{FWHM} = 4$ superpixels, and the SNR was varied, by increasing the peak intensity.

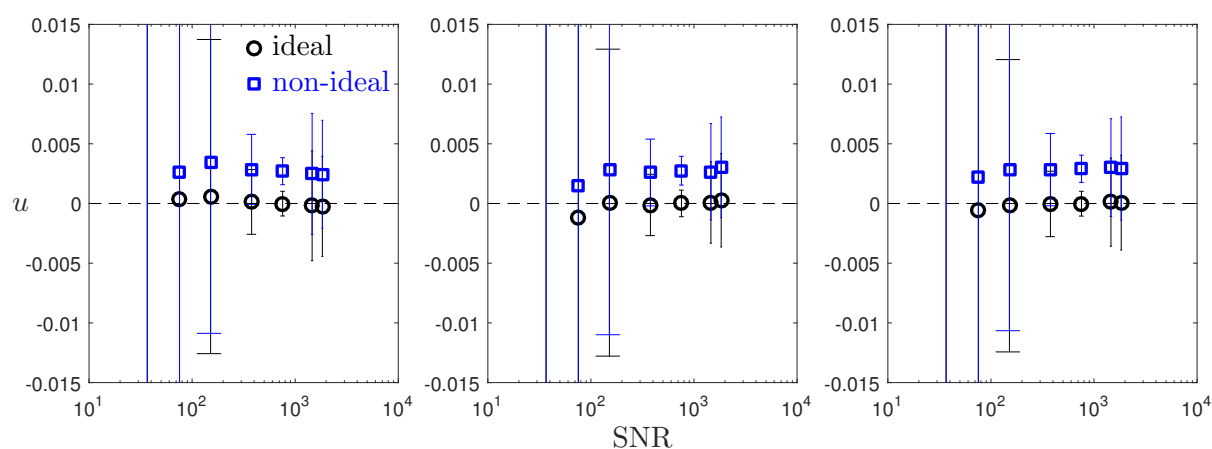


FIGURE 8.27: The estimation of u , for stars with intrinsic $u = 0,$ and $q = 0, 0.05,$ and 0.5 , using an ideal and non-ideal polarimeter. The sampling was held constant at $\text{FWHM} = 4$ superpixels, and the SNR was varied, by increasing the peak intensity.

8.2.4 Summary

In this section, I investigated the effects of sampling and photometric shot noise for unresolved sources on the accuracy (systematic errors) and precision (random scatter) of the estimation of the normalized Stokes parameters q and u . In each case, the traditional Nyquist approach to use 2 superpixels across the FWHM results in excessive scatter. The scatter can be reduced significantly by sampling with 4 or 5 superpixels. The scatter can be further reduced by maintaining a photometric SNR $\gtrsim 500$ in each exposure.

8.2.5 Effects of Sub-Pixel Displacement

In the previous section I looked at the effects of sampling as they might manifest themselves during observations. The stars in each set of 500 images were placed with random offsets from a position that was perfectly centered. This is useful to estimate the kind of scatter we can expect due to effects of sampling the steep intensity gradients that make up a typical PSF. Now, I wish to look at these effects in a more systematic way. Instead of randomly placing the stars in the focal plane, I translate the center of each star across 4 pixels, in steps of 0.1 pixels.

At each position, I make 50 measurements (including shot-noise and background noise) and calculate the mean and standard deviation of the Stokes parameters. The stellar PSF has a FWHM = 4 superpixels and a photometric SNR of ~ 700 . As before, the stars are polarized with a fractional polarization, $p = 0, 0.05, \text{ and } 0.5$ and angle $\psi = 0^\circ$; this creates intrinsic Stokes parameters $q = 0, 0.05, \text{ and } 0.5$ and $u = 0$ for all 3 cases.

Starting with the star perfectly centered on a point between 4 pixels, I translate the star along the grid direction, such that the center of the star is always between two rows of pixels. The results of the Stokes q estimation are shown in Figure 8.28. The perfect polarizer shows periodic systematic effect as each pixel receives slight more light than its neighbors. The largest effects occur when the peak of the star is in the center of a single pixel (rather than the center of a superpixel). The most significant deviations for the perfect polarizer (at this signal level and sampling) were $\sim 0.2\%$.

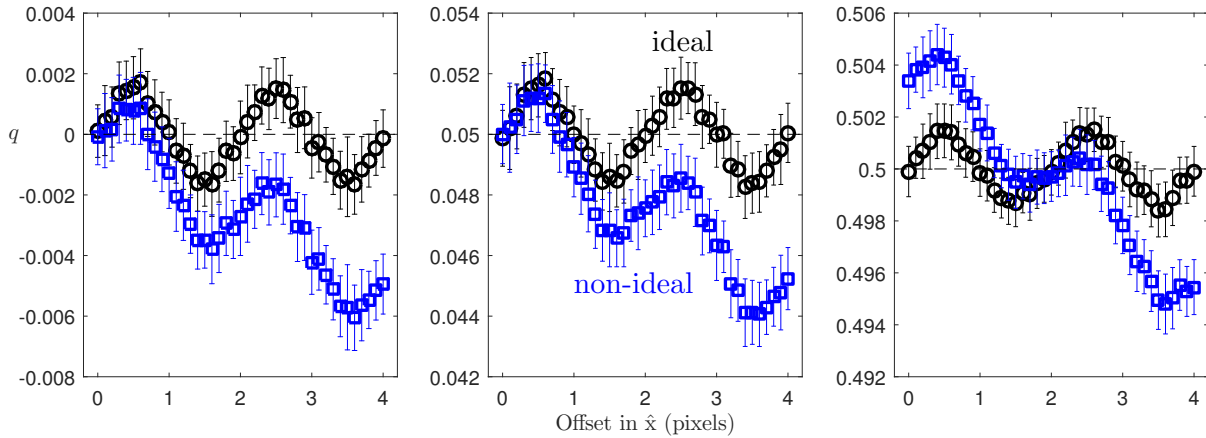


FIGURE 8.28: The Stokes q estimation depends systematically on the position of the PSF center. The ideal polarimeter shows a consistent error with a period of 2 pixels and amplitude of $\sim 0.2\%$; however, the non-ideal polarimeter shows an additional error, likely due to imperfect calibration.

The non-ideal polarizer also shows a systematic error with a period of 2 pixels and amplitude of $\sim 0.2\%$. However, this is superimposed on a larger deviation which appears to increase as the star is moved further away from the initial position. To determine what happens as the star continues moving across the array, I repeated this test over a distance of 10 pixels and a step size of 0.25 pixels. We see in Figure 8.29 that the non-ideal polarimeter suffers from systematic errors that depend on the PSF location on the array. The maximum amplitude of the error approaches 1% before the estimation begins to improve. This effect is likely due to the imperfect characterization of the polarimeter properties and errors introduced during the data analysis process. Specifically, the current process uses an average value for throughput, efficiency, and angle for pixels of the same orientation, rather than the values for specific pixels the star is on. Therefore, as the star drifts across different pixels, their properties may be different enough from the mean value to cause a significant error. The details of this process and alternative data analysis procedures are described in Chapter 9.

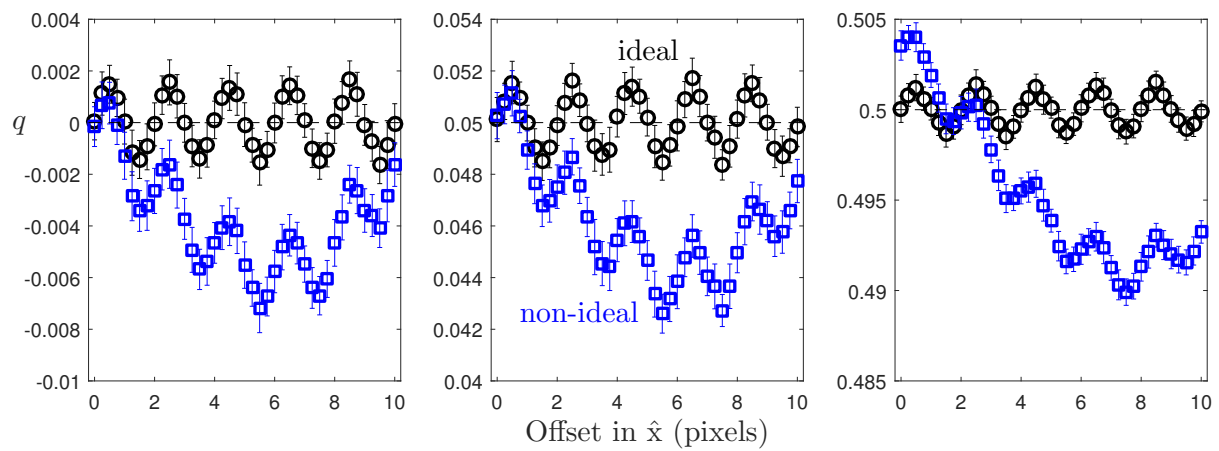


FIGURE 8.29: The non-ideal polarizer shows systematic errors that appear to be location-dependent. This is likely due to the way the device calibration is performed during data analysis (see Chapter 9).

The Stokes u estimation, as the star is translated across the array, is shown in Figure 8.30. The errors in the estimation are similar to those seen for the Stokes q . The ideal polarizer shows a maximum error of $\sim 0.2\%$, when the center of the star is aligned with the center of a single pixel. This error has a period of 2 pixels (or 1 superpixel). The non-ideal polarizer shows a systematic offset of $\sim 0.5\%$, on top of the periodic error. The amplitude of the systematic offset depends on the location in the focal plane. When the star was translated over 10 pixels (Figure 8.31), the systematic error is reduced to near-zero levels.

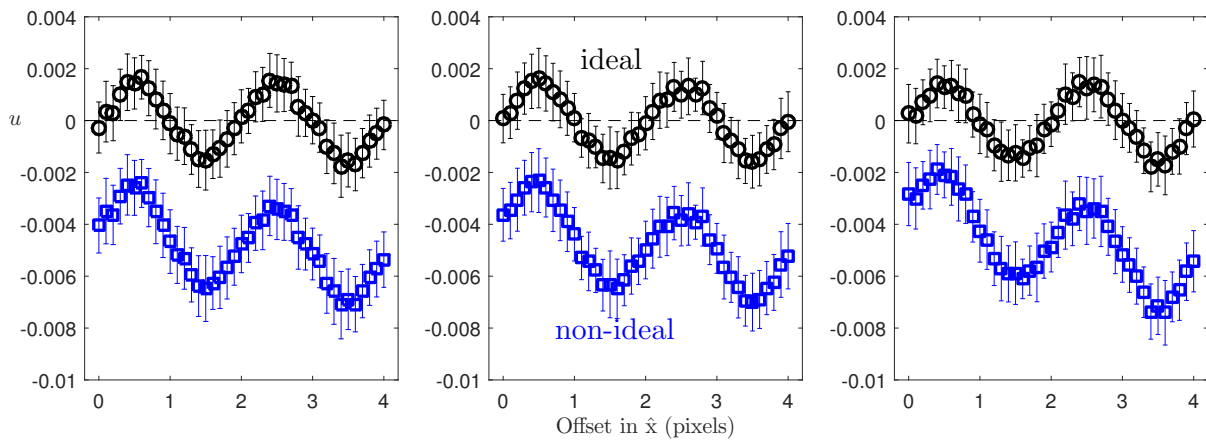


FIGURE 8.30: The Stokes u estimation depends systematically on the position of the PSF center. The ideal polarimeter shows a consistent error with a period of 2 pixels and amplitude of $\sim 0.2\%$; however, the non-ideal polarimeter shows an additional error, likely due to imperfect calibration.

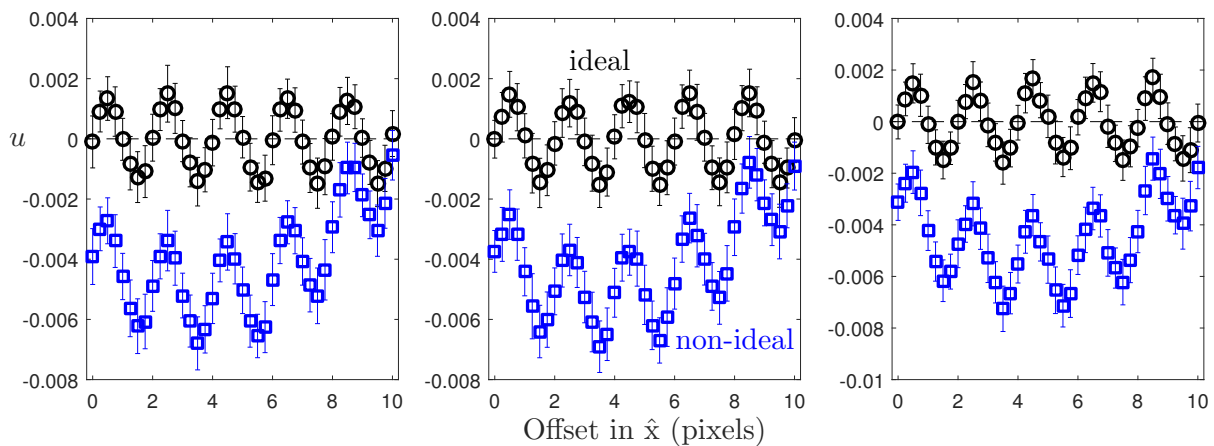


FIGURE 8.31: The non-ideal polarizer shows systematic errors that appear to be location-dependent. This can result from the way the device calibration is performed during data analysis (see Chapter 9).

8.2.6 Simulated Observations of Extended Objects

The basic process used to generate synthetic observations of point sources can be applied to simulations of extended objects. In this case, the input is an arbitrary 2D image. Somehow the effects of resolution, seeing and sampling must be accounted for. In other words, high spatial frequencies that aren't likely to appear in real data should be removed from the simulated images, to provide a better approximation of the observing process. I use simple Gaussian filtering, with the standard deviation given by the desired seeing FWHM. An example of the input object and the seeing-blurred object is shown in Figure 8.32.

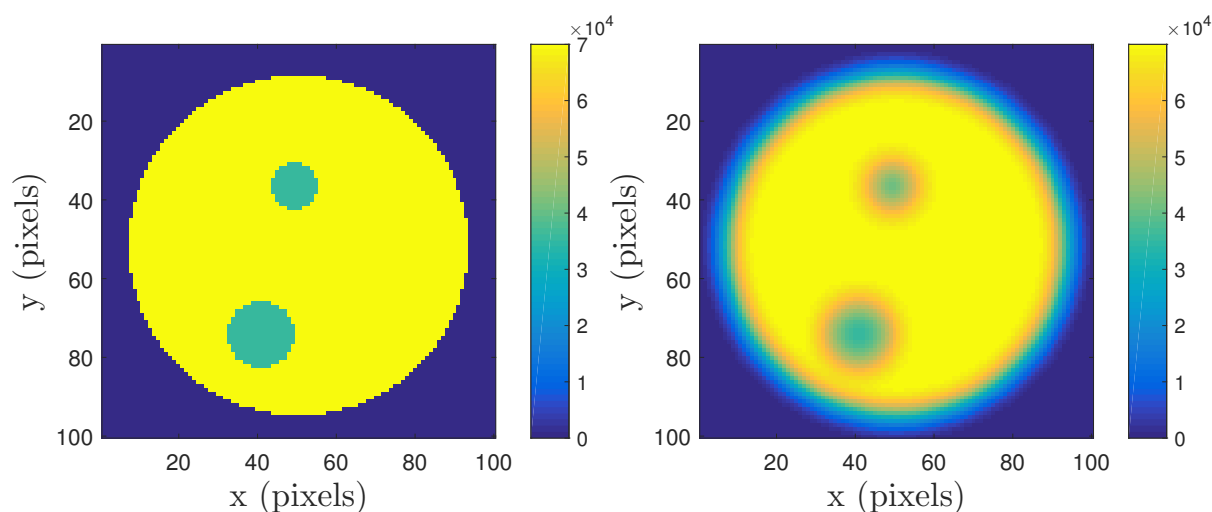


FIGURE 8.32: An example of a simulated object blurred by seeing effects. This plot show the raw intensity in counts.

Once the seeing-blurred intensity maps have been generated, the polarization properties for each pixel in the image must be specified. This can be done using two additional maps: one for the fractional polarization and one for the angle of polarization. This allows the generation of scenes with complex polarization properties, which are independent of the total intensity. As before, the measured properties of the polarimeter are used to produce the synthetic observations. For example, Figure 8.33 shows two scenes modulated by the properties determined for RITPIC; note that even though the original object had uniform intensity (other than the 2 darker circles), the non-uniform throughput of RITPIC's pixels is seen in the modulated images.

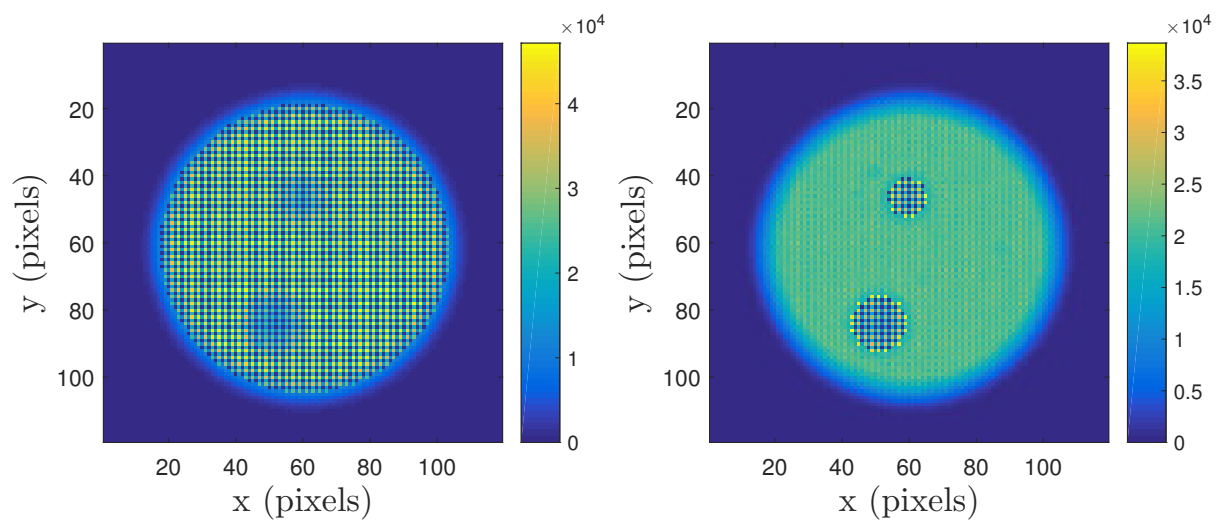


FIGURE 8.33: *Left:* A synthetic modulated image showing the raw intensity for an object has uniform polarization degree and angle. *Right:* Here, only the darker features show significant polarization, so the modulation pattern is only seen in these regions.

Chapter 9

Data Analysis Techniques

Polarimeters based on micropolarizer arrays (wiregrid or polymer) represent a new subset of the division of focal plane modulation strategy. As such, it offers new challenges which must be overcome in the design of the optical system and in the data reduction process. The most distinguishing feature of MPA-based polarimeters is the sampling of different parts of the scene by polarizers of different orientations. This means that each pixel's "instantaneous field of view" (Tyo et al. (2009)) is unique. In turn, the Stokes parameters cannot be estimated directly from the intensities measured by a set of four polarizers with orientations 0° , 45° , 90° and 135° , as described in equation 6.3, because each pixel might be sampling a portion of the scene that has an intrinsically higher intensity or different polarization properties. Furthermore, cross-talk present in the detector can introduce systematic errors during the data analysis stage (see Chapter 8). In this section I propose several ways to process the raw images acquired with MPA-based polarimeters and demonstrate some of the mechanisms that can lead to errors in the polarimetry.

9.1 Polarimetric Errors in Various Polarimeters

The Stokes parameters are calculated assuming that the intensity differences along different orientations are due solely to the modulation induced by the polarizing optics. In other words, the total intensity, the degree of polarization and angle of polarization do not change and the intensity variations are due to the polarized components of light. If this assumption is violated, polarimetric errors arise during data analysis. All polarimeter designs are inherently susceptible to this form of error. For example, division-of-time polarimeters are vulnerable to changes in the source on timescales shorter than the time it takes to cycle through all analyzer/waveplate positions to acquire data. Similarly, beam-splitting “snapshot” systems are insensitive to temporal fluctuations, but are vulnerable to misregistration errors between different channels. In other words, whatever the domain of modulation for a particular polarimeter (temporal, spatial, spectral, or a combination of two or more of these), the modulation is assumed to be solely due to the instrument.

Division-of-focal-plane polarimeters modulate the polarization state across the scene (which is imaged onto the focal plane), which means the intensity and polarimetric properties are assumed to be uniform across the “modulation element” of the array, which is a set of four (or more) pixels of differently oriented polarizers. Literally, it means that a division-of-focal plane polarimeter should be designed such that the scene imaged onto the polarization-sensitive array not have spatial frequencies higher than the sampling frequency of the superpixels of the array. Although this is an important design criterion, it is unlikely to ever be implemented in the most ideal fashion (an image consisting of “2D step functions”). As such, appropriate data-reduction techniques must be developed to minimize the effects of the instantaneous field of view differences.

This problem was identified by several groups, who used various techniques to combat the false polarization signals that it tends to cause ([Tyo et al. \(2009\)](#), [Gao and Gruev \(2011\)](#)). Although these approaches seem to offer improvements in the polarization analysis, it is difficult to estimate the effect on the accuracy and precision of the polarimetric estimation. To this end, I developed software tools to calibrate raw data acquired with micropolarizer-based division-of-focal-plane polarimeters. First, I will describe the image processing

tools developed for polarimetry of unresolved sources, followed by techniques for imaging polarimetry in the conventional sense.

9.2 Polarimetry of Unresolved Sources

Although micropolarizer-based polarimeters have inherent imaging capability, they may be used in applications where the source is unresolved. The obvious example is images of stars and other distant astronomical objects. Similarly, satellites of the Earth appear as unresolved objects from the ground. In the biomedical fields, the imaging of individual fluorophores (whether they are molecules or quantum dots) is a well established and important technique. If only one object is to be measured at a time and if extreme precision is required, a more conventional aperture-based polarimeter may be a more suitable instrument. Imaging polarimeters based on micropolarizer arrays are best suited for the measurement of many unresolved sources at once, with moderate accuracy ($\sim 0.5\%$).

9.2.1 Photometric Calibration

The first step in the data analysis process is the photometric calibration used for conventional photometry. The foundation of polarimetry is precise photometry.

Dark Current, Bias, and Gain

The dark current and bias must be subtracted using low-noise “super bias” and/or “super dark” frames. Next, the analog-to-digital units must be converted to electrons using the camera gain; RITPIC uses a gain of $0.597 \text{ e}^-/\text{ADU}$.

Sensor Non-uniformity

The individual throughput differences of micropolarizer pixels and the sensitivity variations of the detector pixels must be accounted for. Traditionally, this is done using flat field normalization. In the case of polarimetry, there are several ways to perform this correction, depending on the data analysis strategy. As such, the pixel non-uniformity correction is discussed below, as part of the demodulation process.

9.2.2 Demodulation Using Aperture Photometry

The most straightforward way to demodulate the measured intensities is using traditional aperture photometry. First, the full raw image must be divided into subframes, based on polarizer orientation (Figure 9.1). The total flux measured for the star in each subframe should be the result of the modulation by the micropolarizer pixels of the source, based on its intrinsic polarimetric properties. If the stellar PSF was sufficiently sampled, the flux in each subframe should be relatively stable to seeing variations and systematic effects associated with sub-pixel sampling (see Section 8.2.2 and 8.2.5). Therefore, the flux measured in each subframe can be used in equation 6.3 as the S_k terms, where $k = 0^\circ, 45^\circ, 90^\circ$ and 135° .

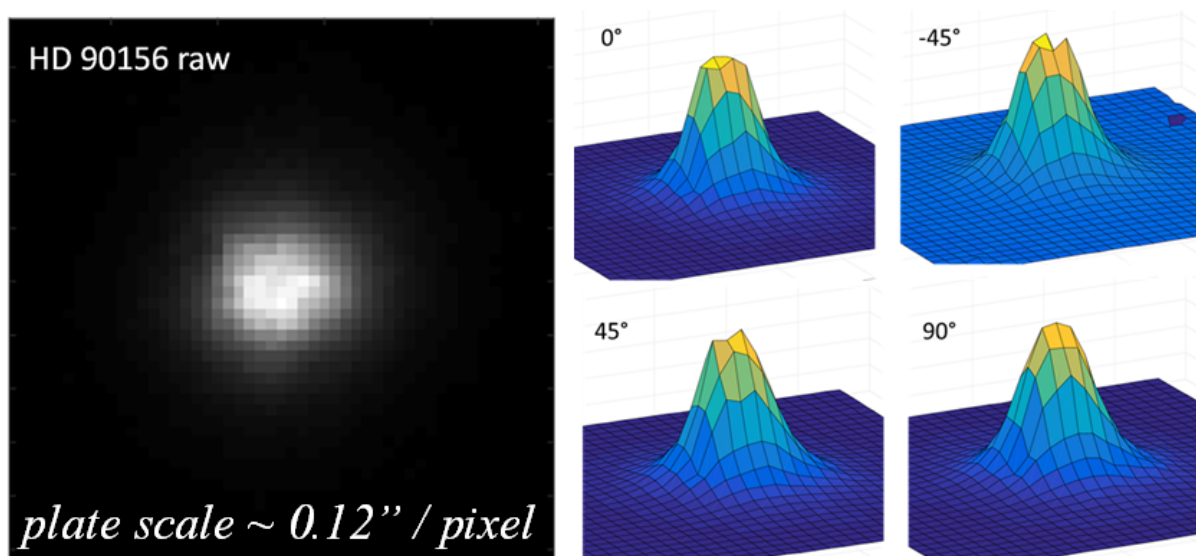


FIGURE 9.1: *Left:* A raw image of the unpolarized standard star HD 90156. *Right:* Once the full image is divided into subframes with pixels of the same orientation, the flux can be measured using conventional aperture photometry.

9.2.2.1 Pixel Non-Uniformity Correction With Flat Fields

The micropolarizer array used in RITPIC shows complex non-uniformity in the throughput, efficiency, and orientation of the pixels (see Chapter 8). The most significant differences are seen for the pixel throughput. The most rudimentary way to account for these differences is using flat fields. There are several approaches, but the most simple one uses unpolarized flat fields. It's difficult to acquire truly unpolarized flat fields or even

to determine the level of polarization in the flats. Traditional twilight sky flats acquired near zenith cannot be used for this purpose because the twilight sky is extremely polarized in that direction. Dome flats acquired using a reasonably non-specular screen and illumination parallel to the telescope’s optical axis can give decent results (Figure 9.2).

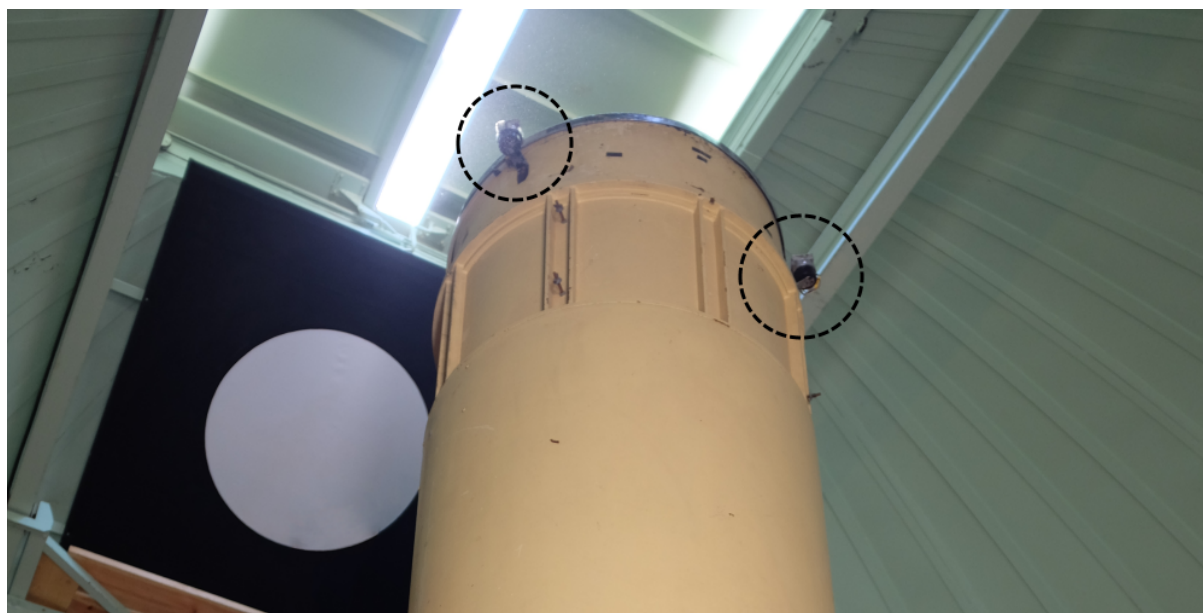


FIGURE 9.2: A non-specular screen can be used to acquire unpolarized “dome flats”, as long as the screen is illuminated along the telescope’s axis. For example, lamps arranged symmetrically around the aperture of the telescope do a decent job. Note that the dome slit was only open to take this photograph.

Normalizing the Flat

Once the individual flat frames have been acquired and combined into a “master flat”, it must be normalized. Conventional flats mostly correct for the small pixel-to-pixel differences due to intrinsic variations in pixel response, vignetting, or the presence of dust. However, micropolarizer pixels have large systematic throughput differences for pixels of different orientations, on top of variations for pixels of the same orientation. One way to account for this is to normalize the pixels by the mean or maximum value of all pixels, in one operation (Figure 9.3). Alternatively, the pixel-to-pixel differences for pixels of the same orientation can first be corrected individually, and then the mean offsets between the 0° pixels and 45° can be corrected. It’s not obvious which approach gives the best results or if the resulting improvement (if there is any) is significant in the face of other challenges associated with the aperture photometry method (see next section).

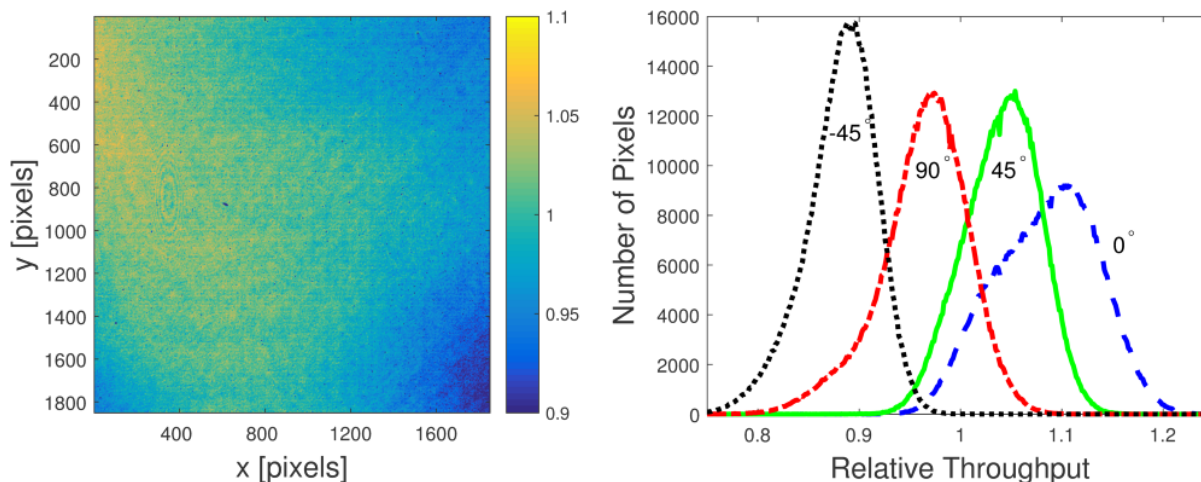


FIGURE 9.3: *Left:* An unpolarized flat field image of RITPIC, showing large scale and small scale throughput nonuniformity on the order of $\pm 5\%$; some dust is also visible. *Right:* A histogram of the relative pixel throughputs for each pixel orientation. Each pixel orientation has a systematically different throughput from the other orientations.

For example, the 0° pixels have lower throughput than 45° pixels.

9.2.2.2 Measure the Flux

After the photometric calibration is complete, the signal in each subframe must be measured, in units of electrons. As this is a fundamental measurement in astronomy, many techniques have been developed for this purpose. In this work I adopt traditional aperture photometry techniques. More advanced techniques, like PSF-fitting, may offer an improvement in photometric precision, however, this is a topic for future investigation.

The aperture size should be chosen to include as much flux as possible, without introducing unnecessary amounts of background. This can be estimated by calculating a traditional curve-of-growth for the enclosed flux as a function of aperture size, or by fitting a simple Gaussian to the stellar profile and using some multiple of the standard deviation. Next, the annulus used to estimate the sky background must be chosen with a large enough gap that no star light is included and a large enough width so that the background estimate is shot-noise limited. A typical configuration is shown in Figure 9.4.

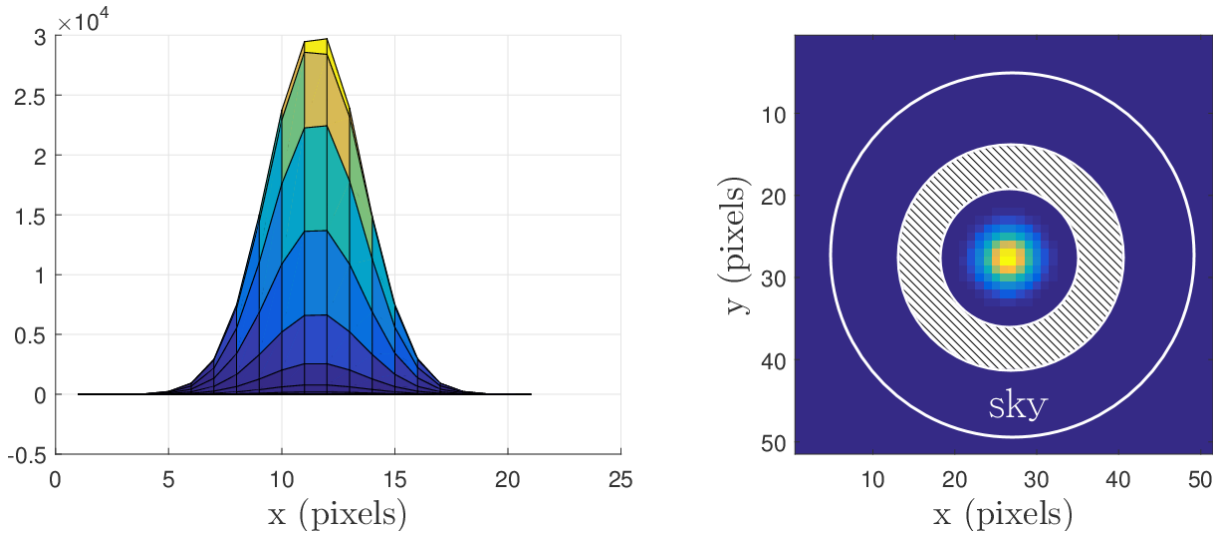


FIGURE 9.4: *Left:* A Stokes I image of synthetic star with 5 superpixels across the FWHM; because this isn't a raw image, each image pixel corresponds to a superpixel in the focal plane. *Right:* A schematic showing typical settings used for aperture photometry. The hashed region indicates the gap between the aperture around the star and the annulus used to estimate the sky background.

After the fluxes have been measured in the 4 subframes, the linear Stokes parameters can be calculated using the standard definitions,

$$I = \frac{1}{2} (S_0 + S_{45} + S_{90} + S_{135})$$

$$Q = S_0 - S_{90}$$

$$U = S_{45} - S_{135}$$

This approach does not take into account the polarizer efficiency or possible deviations from the nominal polarizer orientations. As a result, the accuracy and precision achievable with this method depend on the raw performance of the micropolarizer array. In other words, if the efficiency is high and if the orientations are very close to their nominal positions, this might produce results with sufficient precision. However, for devices that suffer from low efficiency and a high degree of non-uniformity (like RITPIC), a more robust calibration must be incorporated into the data analysis process.

9.2.2.3 Non-uniformity Correction Using the Full Characterization

The flat field calibration described in the previous section only attempts to account for the throughput differences between each pixel. To account for the imperfect polarizer efficiency and orientation, the demodulation procedure must incorporate the micropolarizer properties determined during a full characterization of the device (using a process similar to the one described in Chapter 8).

In this case, the “flat field” correction is performed as part of the demodulation process, using equation 6.3. Once again, there are two ways to perform the calibration. First, the systematic differences between pixels of different orientations (see Figure 9.3, Right) can be corrected using the average values of t_k , e_k , and ϕ_k as follows,

$$S_k = \frac{1}{2} \langle t_k \rangle I \left[1 + \langle \epsilon_k \rangle (\cos 2\langle \phi_k \rangle \cos 2\psi + \sin 2\langle \phi_k \rangle \sin 2\psi) \right], \quad (9.1)$$

where the angle brackets $\langle \rangle$ denote an average. This works well to correct the throughput differences between pixels of different orientation. However, this process does not take into the differences between pixels of the same orientation, and can lead to systematic errors when stars fall on pixels whose properties are sufficiently different than the mean. These errors were seen in Section 8.2.5, because there is a significant variance for pixel throughput, efficiency and orientation (Figure 9.5); in fact, the efficiency differences between differently oriented pixels are smaller than their own intrinsic variation (with 135° pixels being a clear outlier, see Figure 8.7).

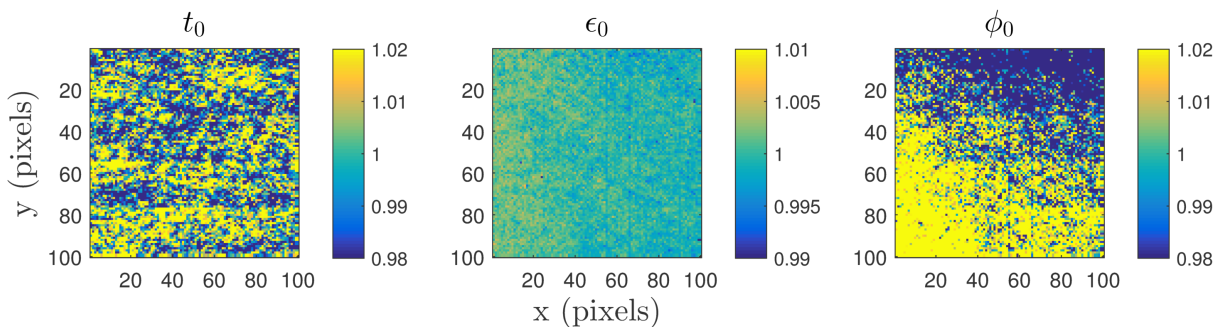


FIGURE 9.5: The mean-normalized properties of the 0° pixels, in a small region of the array; several percent deviations from the mean are common for t_k and ϕ_k .

The pixel-to-pixel variations of throughput in the same subframe can be calibrated by normalizing the pixel values by a flat field made using the mean-normalized maps of throughput, like the example in Figure 9.5, *Left*. This normalization allows one to use the mean value of the throughput in equation 9.1, without becoming vulnerable to the pixel-to-pixel variations. Using this normalization, the systematic errors seen as a star drifts across the array are greatly minimized. For example, Figure 9.6 and Figure 9.7 show how the estimation of Stokes q and u , respectively, changes as a star is translated across the array, in steps of 0.25 pixels. Although the estimation made with the non-ideal polarimeter is still systematically different than the true polarization (and the estimation made by the ideal polarimeter), the effects due to pixel-to-pixel differences have been removed.

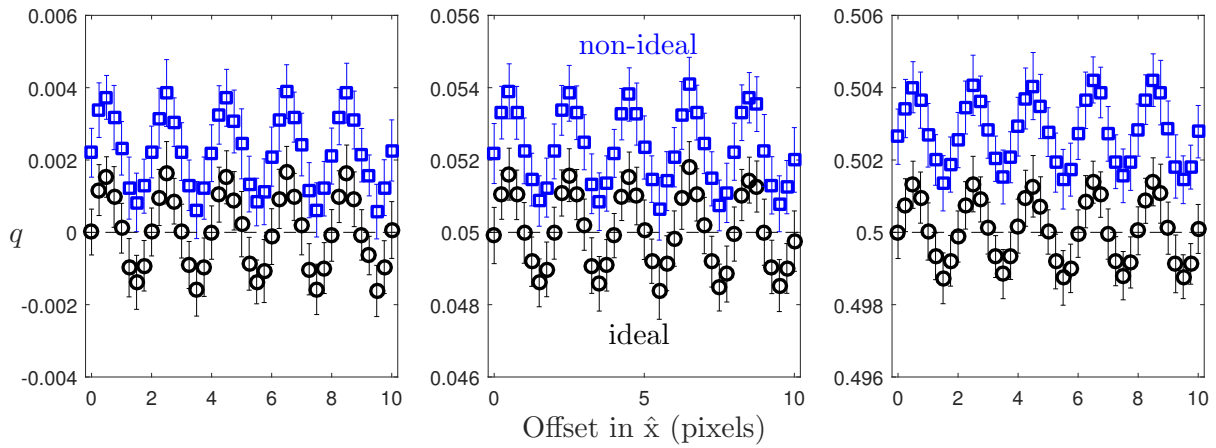


FIGURE 9.6: The estimation of Stokes q for stars with intrinsic polarization $q = 0, 0.05$ and 0.5 , made by ideal and non-ideal polarimeters, as a star is translated across the array.

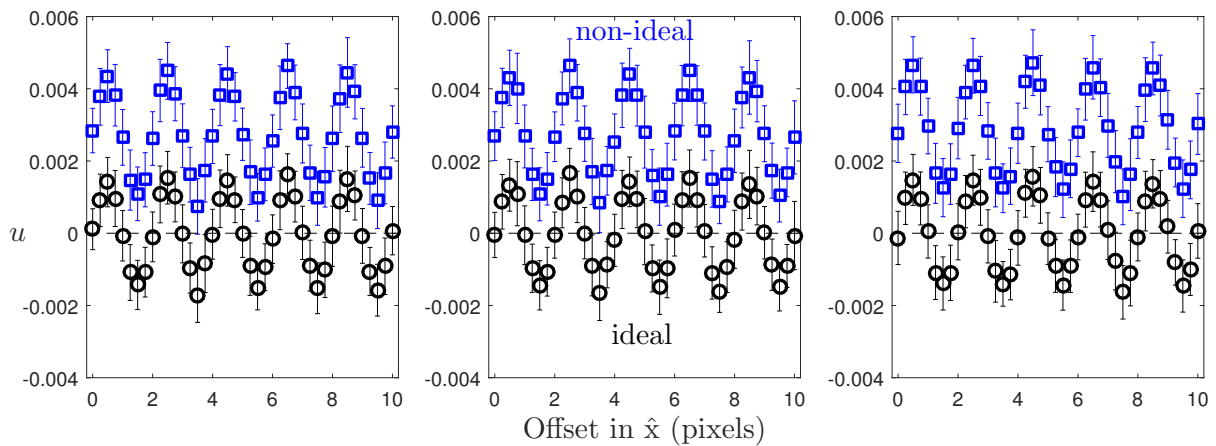


FIGURE 9.7: The estimation of Stokes u for stars with intrinsic polarization $u = 0$ and $q = 0, 0.05$, and 0.5 as a star is translated across the array.

9.2.3 Polarimetry of Spatially Resolved Sources

In the previous section, I showed how the “instantaneous field-of-view” problem can be circumvented when performing polarimetry of point sources using aperture photometry. In this section, I describe the process that can be used to perform true imaging polarimetry, using a per-pixel calibration, to determine the polarimetric properties for every pixel in an image.

Photometric Calibration

The dark signal subtraction and gain correction must be performed first. A flat field-type non-uniformity correction is performed on a per-pixel basis as part of the demodulation process.

9.2.3.1 Demodulation Using a Per-Pixel Calibration

As before, the first step in the demodulation process is separating the raw image into four subframes, based on pixel orientation (Figure 9.8). Next, each subframe must be flat-fielded to account for the pixel-to-pixel variations in throughput among pixels of the same orientation. This is done using mean-normalized throughput values, t_k , as determined during device characterization.

Because each pixel is physically offset from its neighbors in the superpixel, the object in the four subframes is also shifted by 1 pixel (or 0.5 superpixels). This is another way the instantaneous field-of-view problem manifests itself. To account for this, I choose one of the subframes to act as a reference frame and spatially register the remaining subframes. Depending on the exact micropolarizer configuration, the subframes must be moved ± 0.5 pixels in the \hat{x} and/or \hat{y} directions. To perform this sub-pixel shift, I first interpolate the images into a grid with finer sampling, shift an integer number of pixels, and downsample the image to the original size.

Once the images are registered, I demodulate the intensities using the linear least squares method, on a per-pixel basis. Practically this is done as a loop over all pixels in the subframes.

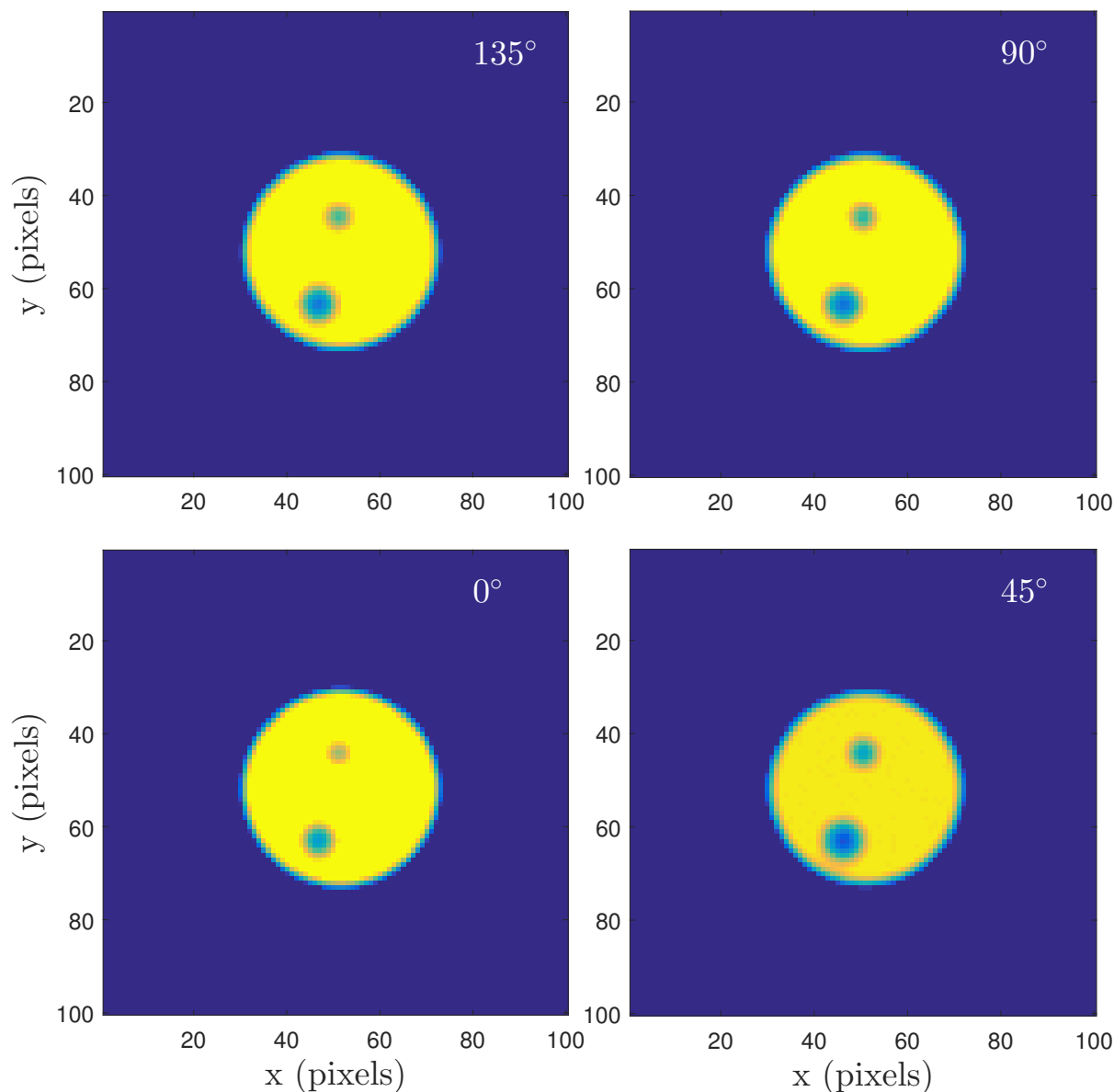


FIGURE 9.8: The subframes corresponding the four pixel orientations of a synthetically generated image. The two darker spots in the object are polarized, which is why they appear larger or smaller, depending on the subframe. The object is shifted ± 0.5 pixels in each frame, with respect to the other frames.

To better illustrate the kinds of systematic effects that appear due to improper calibration, the next few figures show the estimation of Stokes q and u and how it changes as the data analysis process is improved.

The original image has a mean shot noise SNR per pixel of ~ 150 . The two smaller circles are polarized with fractional polarization $p = 0.01$ and $\psi = 0^\circ$, resulting in $q = 0.01$ and $u = 0$. First, let's look at the resulting q and u maps without flat field correction or image registration (Figure 9.9).

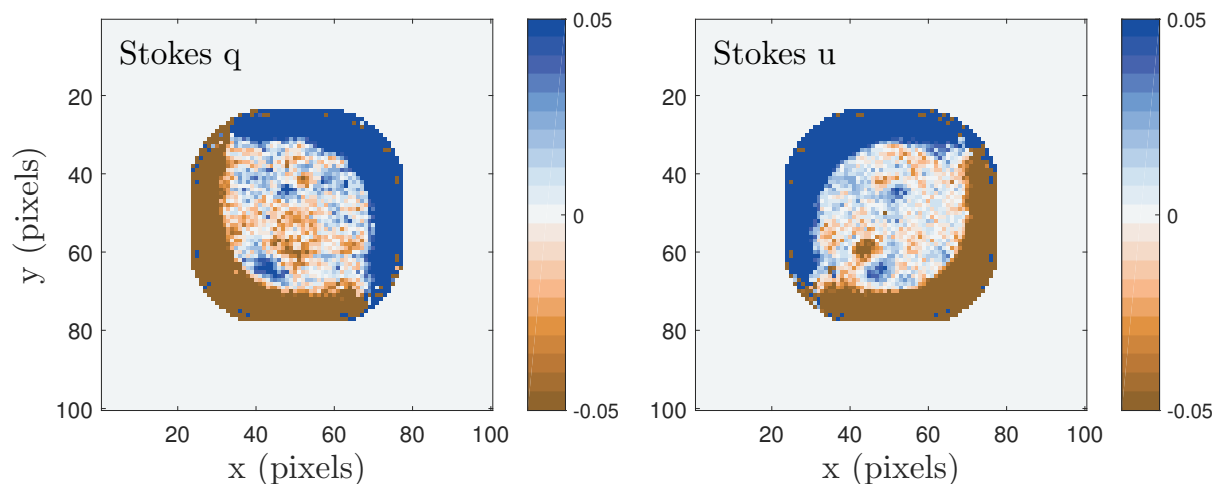


FIGURE 9.9: The estimation of Stokes q and u parameters for the object in Figure 9.8, without proper calibration. The two smaller spots have intrinsic values $q = 0.01$ and $u = 0$.

The Stokes q and u maps in Figure 9.9 show several characteristic errors associated with micropolarizer-based polarimeters. Most of the image has zero polarization, however the estimation shows regions of very high polarization near the edges of the object. In these areas, the steep gradients around the edges and lower photometric SNR are causing large systematic errors; the two smaller polarized spots show a bi-lobed structure in the polarization maps for the same reason. These large features are eliminated when the subframes are properly registered (Figure 9.10).

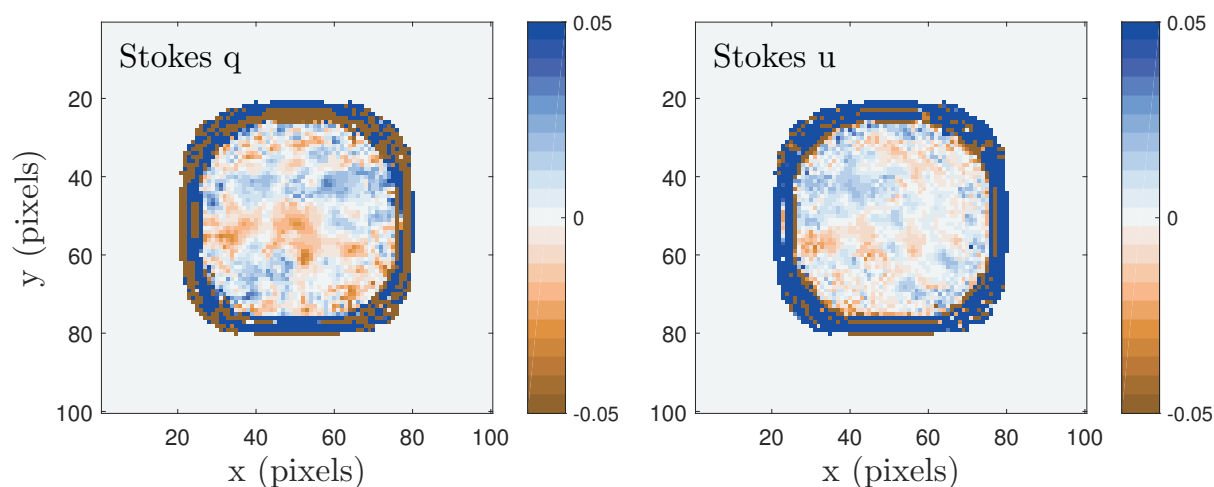


FIGURE 9.10: The estimation of Stokes q and u parameters for the object in Figure 9.8, with image registration but no flat field correction.

When the subframes are properly registered, the the bi-lobed asymmetric features disappear, but structure at $\sim 2\%$ level is seen across the face of the object. This is due to pixel-to-pixel variations in throughput that are not corrected. The next step is to correct the throughput variations using flat fields. The resulting polarization maps are shown in Figure 9.11. Performing the throughput correction removes the several-percent errors

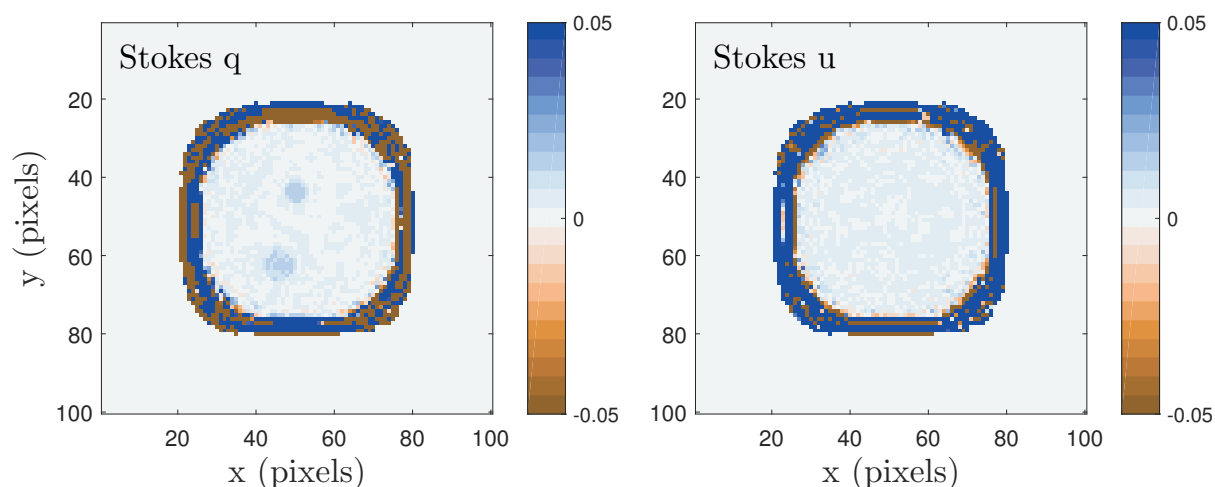


FIGURE 9.11: The estimation of Stokes q and u parameters for the object in Figure 9.8, with image registration and flat field correction.

seen across the face of the object, revealing the weakly polarized spots. The remaining artifacts around the edge of the object are due to low per-pixel SNR. Masking off pixels with SNR less than 30 removes most of the erroneous polarization (Figure 9.12).

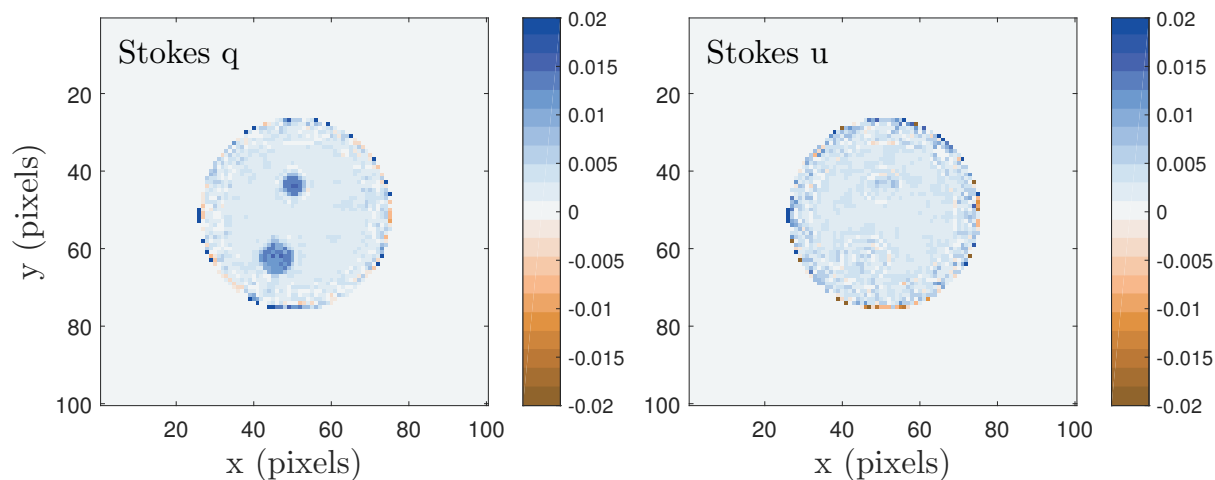


FIGURE 9.12: The estimation of Stokes q and u parameters for the object in Figure 9.8, with image registration and flat field correction.

Chapter 10

Initial On-Sky Evaluation

Two generations of prototypes fabricated have been deployed on telescopes for initial on-sky evaluation. The first generation prototype was deployed on a 0.5 m telescope at Kitt Peak National Observatory in 2014 and the 3rd generation prototype saw first light on the 0.9 m telescope at Cerro-Tololo Inter-american Observatory in 2016. In this section, I present some of the data acquired during these observing runs and evaluate the performance of these polarimeters.

10.1 Evaluation of the Gen 1 Prototype

In January 2014, we deployed the first prototype of the RIT Polarization Imaging Camera (RITPIC) on an astronomical telescope for on-sky evaluation. RITPIC and an FLI filter wheel were mounted at the Cassegrain focus of a 0.5 meter f/8.3 telescope at the Kitt Peak National Observatory in Tucson, Arizona. I obtained images of Jupiter and several polarized and unpolarized standard stars using the Bessel UBVRI filters. Unpolarized flats were obtained using a rough canvas screen illuminated by lamps mounted on the truss of the telescope. This resulted in a non-specular surface, with a very small scattering angle, which helps reduce contamination of the flats with polarized light. An example flat is shown in Figure [10.1](#).

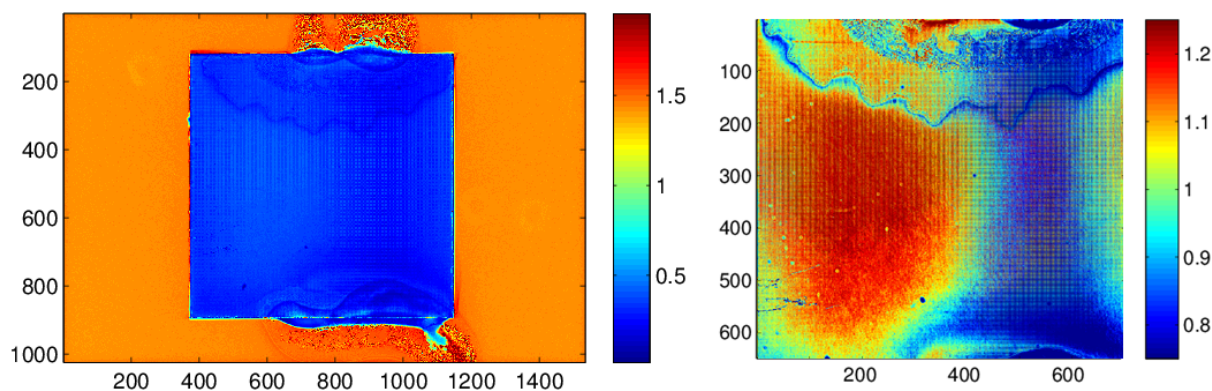


FIGURE 10.1: *Left*: A mean-normalized flat field image in the Bessel B filter, showing the full focal plane of RITPIC. The bright orange areas correspond to the uncovered regions of the sensor, while the darker blue section corresponds to the area covered by the micropolarizer. Uneven distribution of the adhesive is easily seen near the top and bottom edge of the micropolarizer. *Right*: Looking only at the polarization-sensitive region, we see how the transmission varies. Features like dust and scratches on the polarizer substrate are also apparent. Note: The high-frequency vertical and horizontal lines are not real; the flats have high-frequency features which easily cause aliasing when displayed.

10.1.1 Data Processing

Standard astronomical data calibration was performed on this data. The master dark (and bias) frames were subtracted from both image frames and flat field frames. The image data were normalized by the flat fields. The raw and calibrated data are shown in Figure 10.2. The polarimetry was performed using the registration technique described in Section 9.2.3.

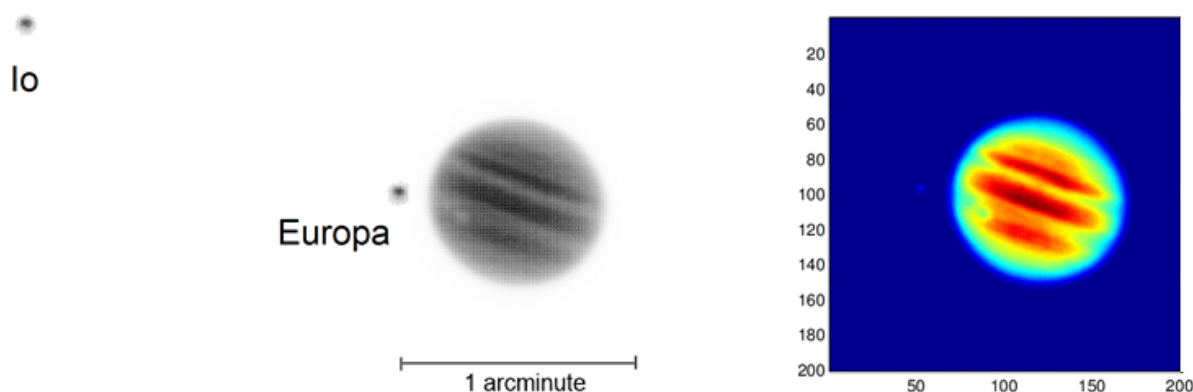


FIGURE 10.2: *Left*: A raw inverted intensity image of Jupiter and its two moons (Bessel B filter). Jupiter's disk shows the same aliasing effects seen in the flats, because the same structure is present in this not-yet flat-corrected image. *Right*: a flat-corrected image of Jupiter. The bright bands across the face of Jupiter appear red in this color map.

10.1.2 Polarimetric Analysis

Because RITPIC’s superpixels under-sampled this telescope’s PSF, our data shows spatial structure on the sub-superpixel scale. This creates strong false polarization signals, if unaccounted for. To remove the intrinsic intensity fluctuations we used the Stokes I images, calculated using the sum of all 4 subpixels in a super pixel, using the equation,

$$I = \frac{1}{2}(i_0 + i_{90} + i_{45} + i_{135})$$

The Stokes I map is obtained by 2×2 binning and rescaling the raw data. To normalize the data, it must be interpolated and “upscaled” to the original size. We use a bilinear interpolation to upscale the Stokes I map. Then, we normalize the data and perform the polarimetric analysis using Equations 2.5-2.7. The Stokes I, Q and U images are shown in Figure 10.3.

I estimate fractional polarization at the poles of Jupiter of $9\% \pm 2\%$, with a smaller polarization across the face of Jupiter of $\sim 1\%$ (which is consistent with zero given the 2% precision). Overall, these measurements agree with previous polarimetry of Jupiter (Gehrels et al., 1969; Coffeen and Gehrels, 1969; Schmid et al., 2011). However, direct comparisons to previous measurements are difficult, because Jupiter’s polarization changes at the several percent level with wavelength and time (see Figure 10.18).

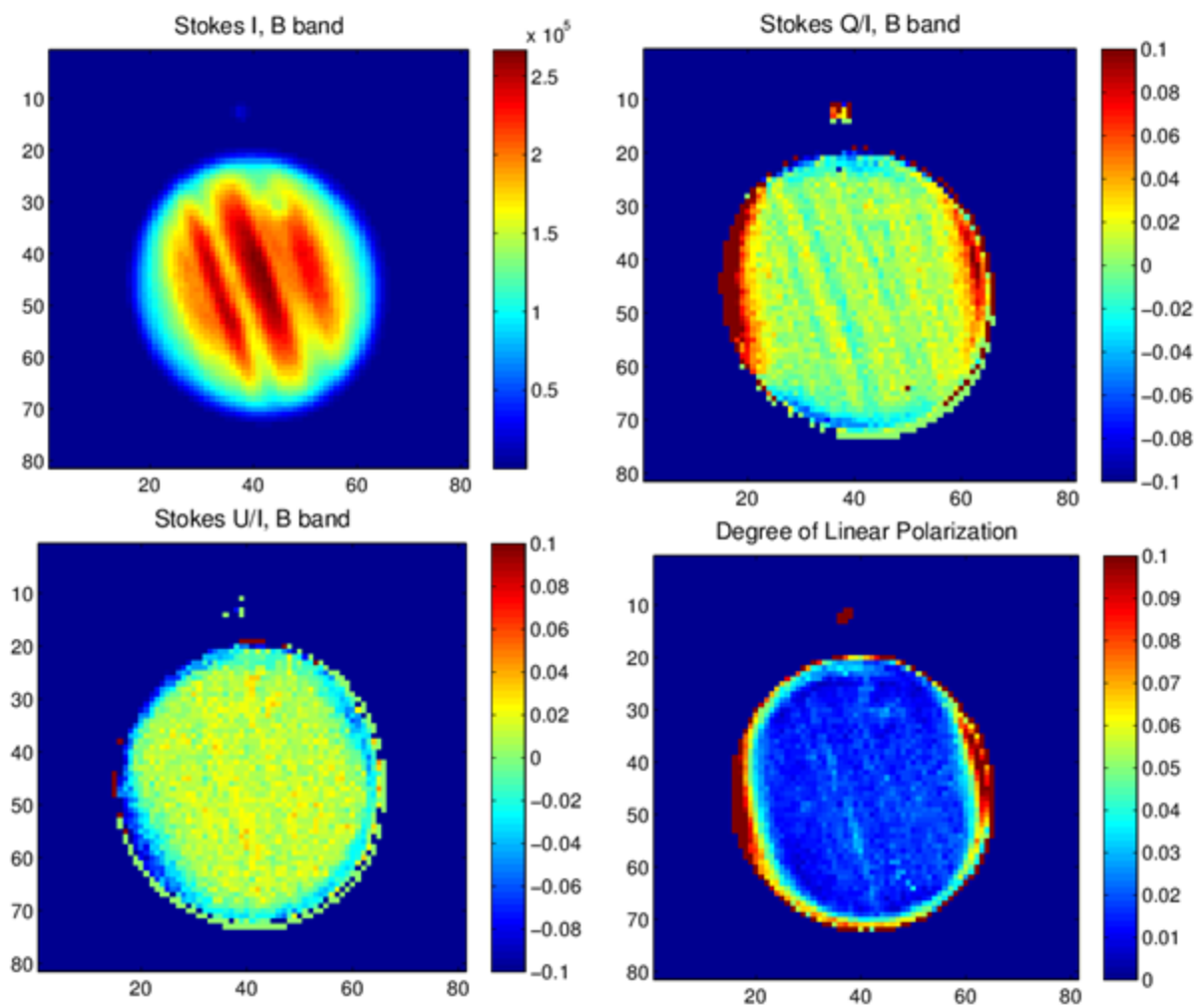


FIGURE 10.3: Polarization analysis of Jupiter data acquired with RITPIC. The polarization of the poles of Jupiter is immediately obvious. The face of Jupiter shows little polarization. Because the images are under-sampled, the polarimetric accuracy in these images is limited to ± 0.02 . Therefore, we find the poles to be polarized at the $9\% \pm 2\%$ level.

10.2 Evaluation of the Gen 4 Prototype

The current generation of the RIT Polarization Imaging Camera (RITPIC) was deployed on a Boller & Chivens 36" telescope at the Cerro Tololo Inter-American Observatory (CTIO) February 3 - 13, 2016. We had 9 clear nights and observed a wide range of objects: calibration stars, planetary nebulae, post-asymptotic giant branch stars, Solar System planets (Figure 10.12), protoplanetary nebulae (Figure 10.29), open clusters, globular clusters, quasars and the highly obscured supernova SN2016adj in Centaurus A. These objects were chosen to estimate the suitability of RITPIC for polarimetry of point sources and extended objects. Most of these objects have been observed by other polarimeters; however, some objects do not have polarimetric information and hold the potential for new discoveries.

The camera was mounted on the existing filter wheel, at the Cassegrain focus (Figure 10.4). Flat field illumination images were acquired using a screen in the dome (Figure 10.4, top left) and 3 lamps placed symmetrically around the telescope aperture.

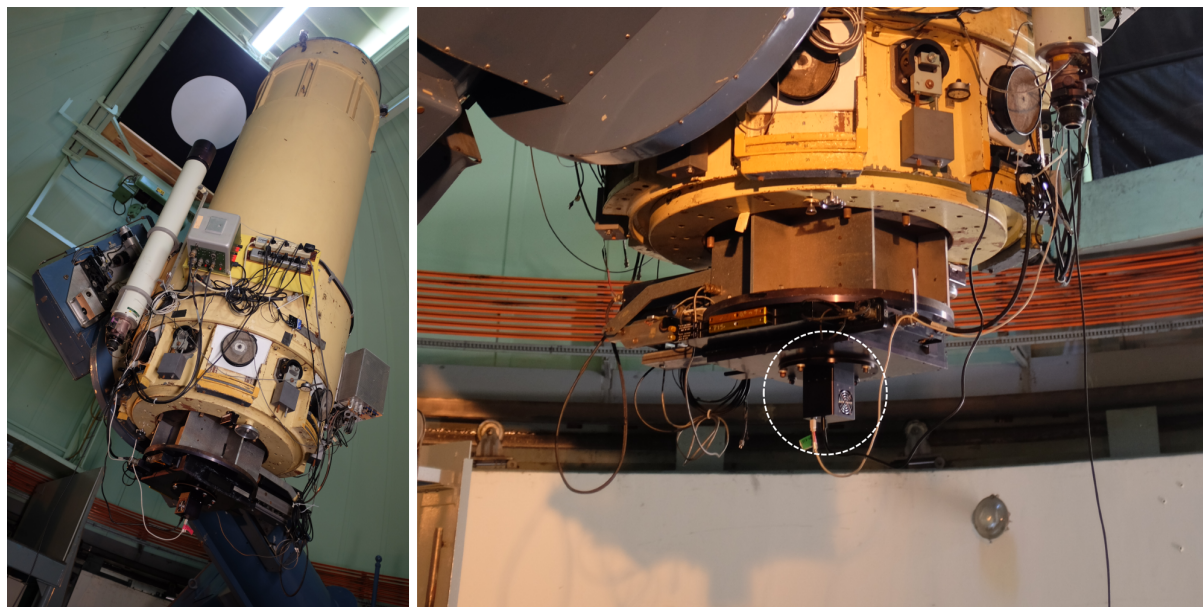


FIGURE 10.4: *Left:* RITPIC was mounted at the Cassegrain focus of the SMARTS 0.9 m telescope. The white spot in the upper left was used to acquire unpolarized dome flats. *Right:* RITPIC is a very compact imaging polarimeter.

The average seeing during the observing run ranged from 0.7 - 2 arcseconds measured by the full-width at half-maximum of the stellar PSF. The plate scale at the RITPIC focal

plane was $0.12''$ per pixel, or $0.24''$ per superpixel (which consists of 4 pixels oriented at 0° , 45° , 90° and 135°). When seeing was good, the PSF was close to critically sampled by the polarimeter's superpixels. An example raw image of the unpolarized standard star HD 90156 is shown in Figure 10.5.

10.2.1 Polarimetry of Point Sources

I observed several polarized and unpolarized standard stars to determine the accuracy and precision of RITPIC polarimetry of unresolved sources. First, I show the results obtained for HD 90156, an “unpolarized” star with a measured degree of linear polarization (DOLP) of 0.0001 (Heiles, 2000). HD 90156 is a variable star with a V magnitude of ~ 6.9 .

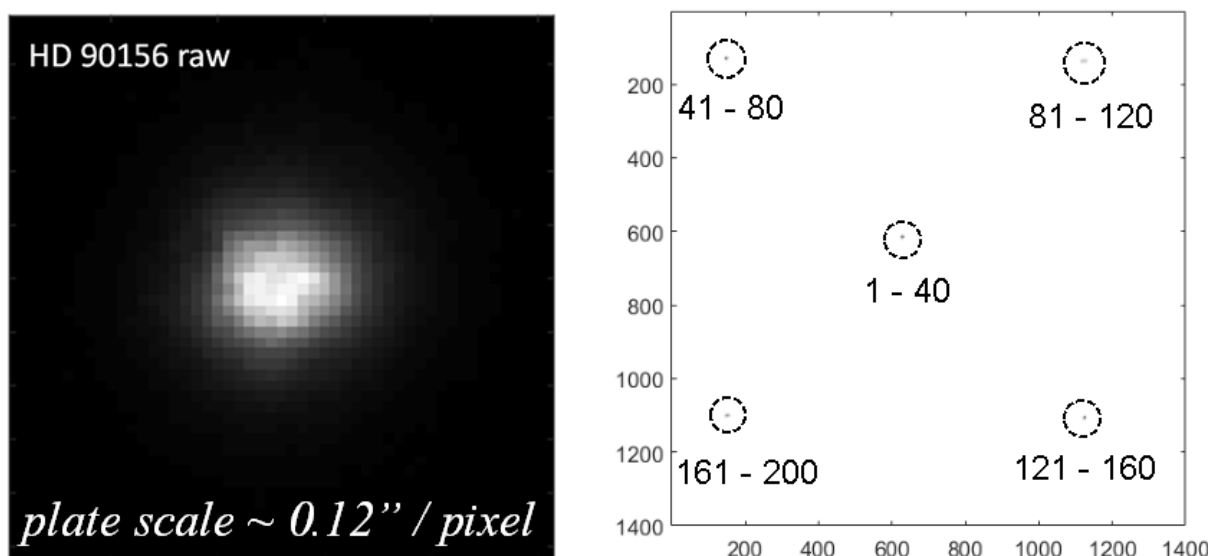


FIGURE 10.5: *Left:* The sampling in the RITPIC focal plane was $0.12''$ per pixel and $0.24''$ per superpixel. *Right:* HD 90156 was observed using 5 different locations on the array. The dashed circles are centered on the location of each star and the numbers indicate the frame numbers that correspond to each location.

10.2.1.1 HD 90156

The star HD 90156 was recently measured by Gil-Hutton and Benavidez (2003) to be very weakly polarized ($q = u = 0.00006 \pm 0.0001$). On February 8, 2016, I acquired 200

exposures of HD 90156, without any filter, in 5 regions on the array (40 exposures at each location). The five positions are shown as a collage in Figure 10.5.

The observations of HD 90156 were analyzed twice. First, I performed only a partial calibration, using unpolarized flats to account for pixel throughput nonuniformity. Then, I re-analyzed the data using a full calibration, which combines unpolarized flat fields obtained during the observing run and additional data acquired in the lab at RIT (see in Section 9.2). The additional characterization allowed me to account for the contrast and angular offsets of each pixel.

The estimation of Stokes q and u in each frame obtained using the partial calibration is shown in Figure 10.6. Overall, this method results in an estimated Stokes $q \approx 0.005 \pm 0.01$ and $u \approx 0 \pm 0.01$. Although the mean value of both measurements is consistent with zero, within 1 standard deviation, the systematic offset measured in q is likely due to improper calibration.

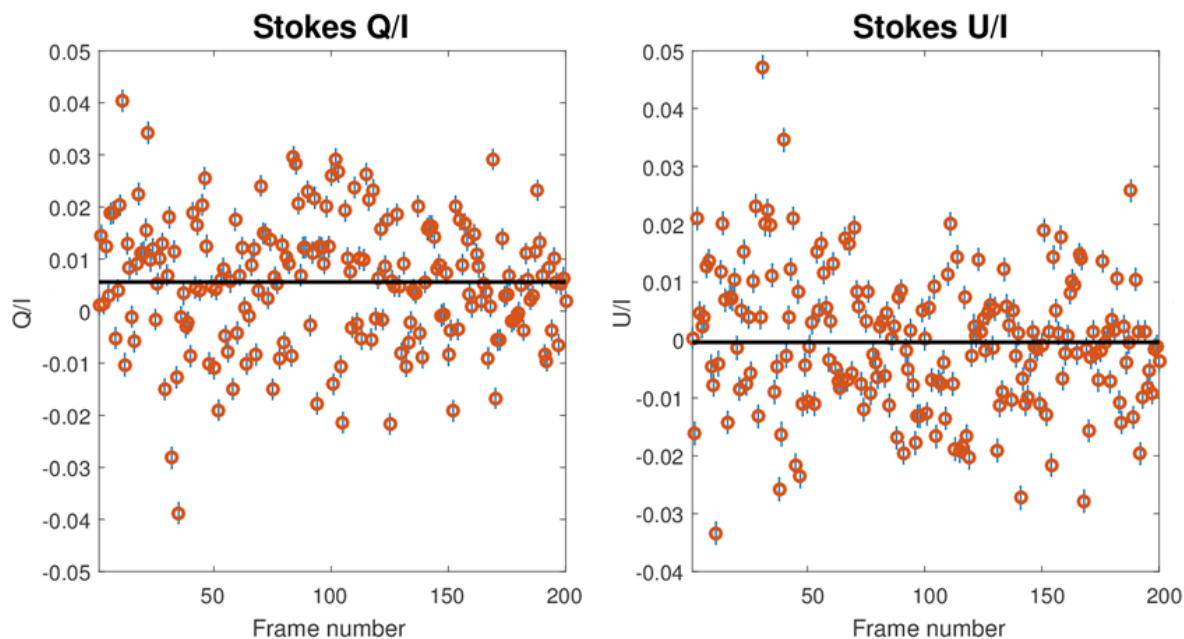


FIGURE 10.6: Estimation of the normalized Stokes parameters, q and u for each frame, using a flat field correction. The error bars on each measurement represent the photometric SNR.

The fractional polarization and angle of polarization corresponding to the measured Stokes parameters are shown in Figure 10.7. The bias of the DOLP estimator is clearly seen in the distribution of the individual measurements of DOLP (see Chapter 6). The

black lines show the DOLP and AOLP calculated using the mean values of q and u , whereas the points represent the DOLP and AOLP calculated in a each frame. The large scatter in the measurement of q and u results in large overestimation of DOLP. This highlights the need to perform all averaging steps before estimating the DOLP and AOLP. Note the large scatter in the estimation of the AOLP for this unpolarized star. This is expected, because the AOLP is not well defined for sources with very low polarization.

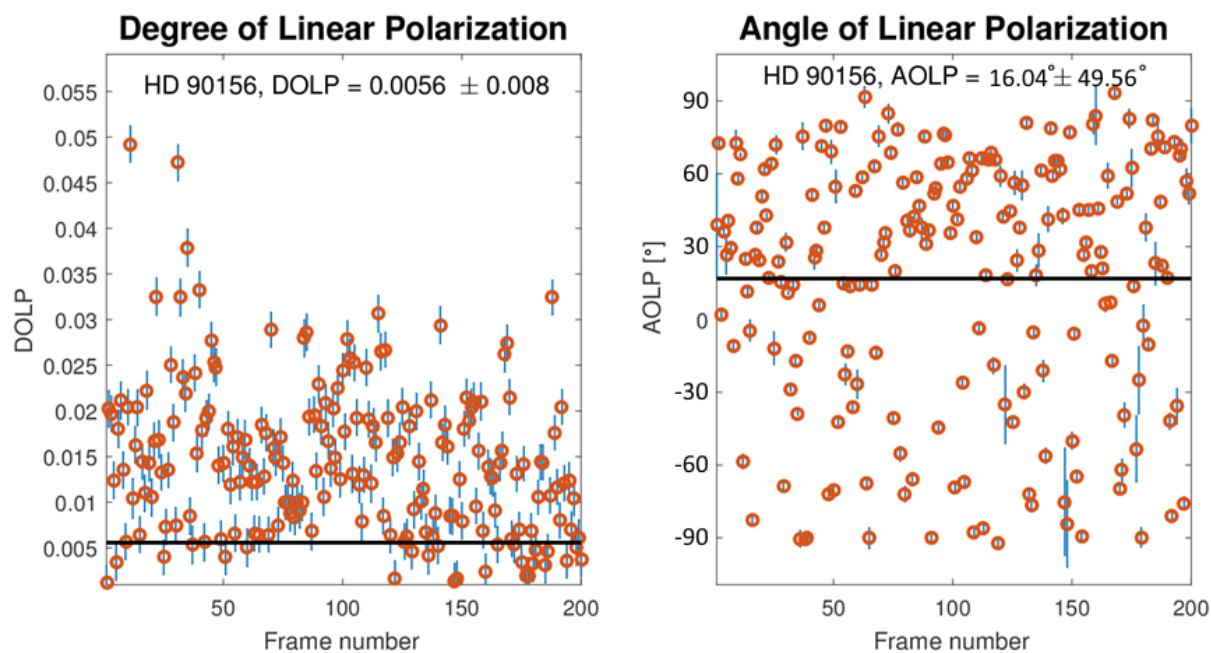


FIGURE 10.7: Estimation of the fractional polarization and angle of polarization for each frame, using only a flat field correction. The error bars on each measurement represent the photometric SNR.

Similar results were obtained when using a full calibration of the data, using a combination of flat fields and characterization data obtained in the lab. These results are shown in Figure 10.8. Although the mean values of q and u obtained using the two methods differ at the 0.002 level, the difference is still much smaller than the scatter in the data. The corresponding DOLP and AOLP estimates are shown in Figure 10.9.

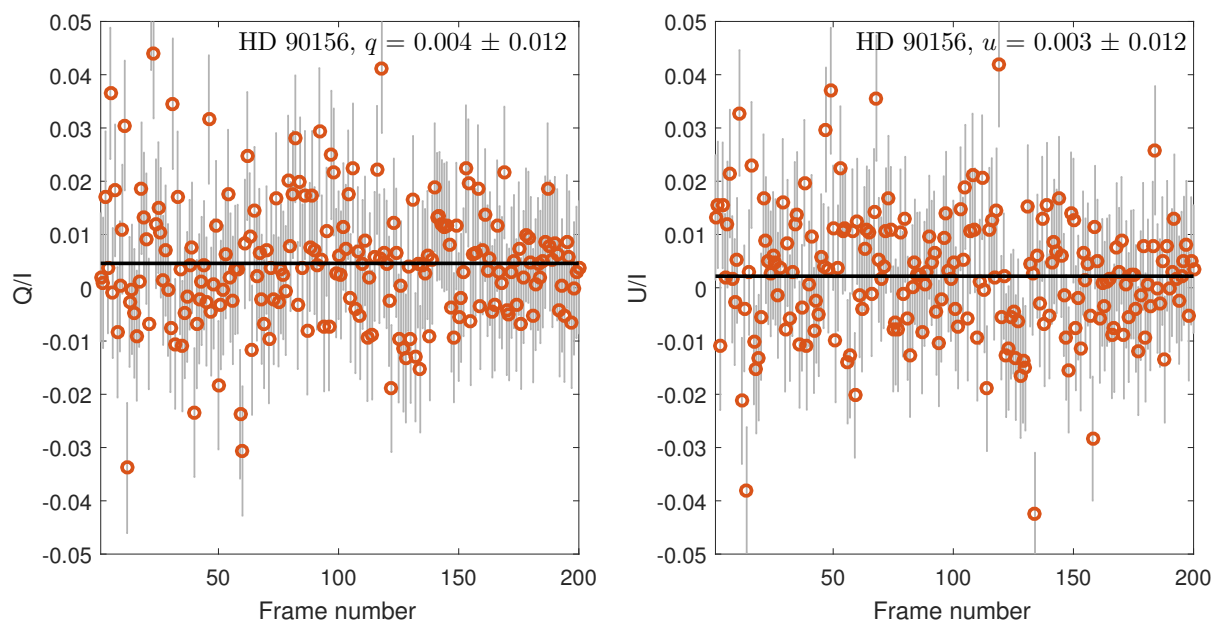


FIGURE 10.8: Estimation of the Stokes q and u parameters for each frame, using a combination of a flat field correction, as well as the efficiency and orientation data obtained in the lab.

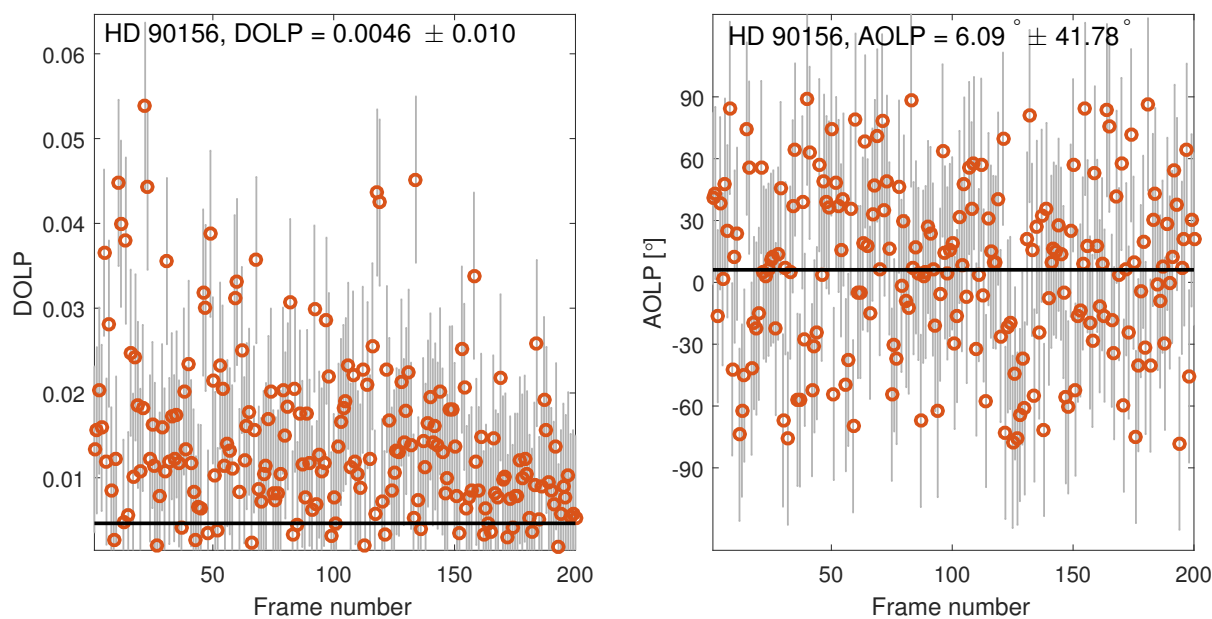


FIGURE 10.9: Polarimetry performed by RITPIC for the unpolarized star HD 90156 using the broadband response of the CCD.

10.2.1.2 HD 78344

Next, let’s look at the observations of HD 78344, acquired on February 14, 2016. This highly polarized star has been measured during the commissioning of the Gemini Planet Imager by Wiktorowicz et al. (2014) to have a fractional linear polarization of 0.0556 ± 0.00001 . First, let’s look at the estimation of Stokes q and u for a set of 20 exposures (5 seconds each) in the Bessel V band (Figure 10.10). This analysis was performed using the full calibration, accounting for differences in pixel throughput, contrast, and orientation. The estimation of q has a relatively high “polarimetric SNR” $q/\sigma_q \approx 9$, with a weaker polarization measured for Stokes u , with $u/\sigma_u \approx 3$.

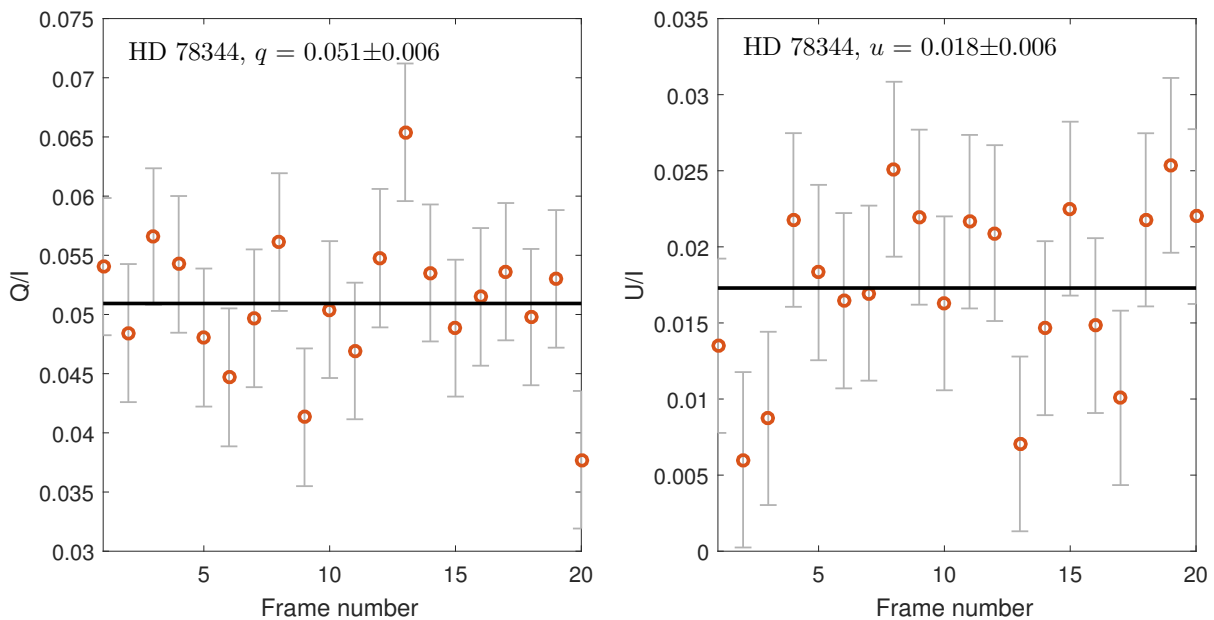


FIGURE 10.10: Normalized Stokes parameters q and u , measured by RITPIC for the polarized star HD 78344 in the V band. The error bars represent the scatter in the estimation (as 1 standard deviation).

The estimation of the degree and angle of linear polarization for HD 78344 is more straightforward than for HD 90156. The mean DOLP estimated using the mean of q and u is much closer to the center of the distribution of the individual DOLP measurements, because the bias of the estimator decreases as the polarimetric SNR increases. I estimate a mean DOLP = 0.0540 ± 0.006 and mean AOLP = 80.5 ± 3.4 degrees. These measurements agree with those made by GPI, within the measurement errors. A summary of the unpolarized and polarized standards is given in Table 10.1.

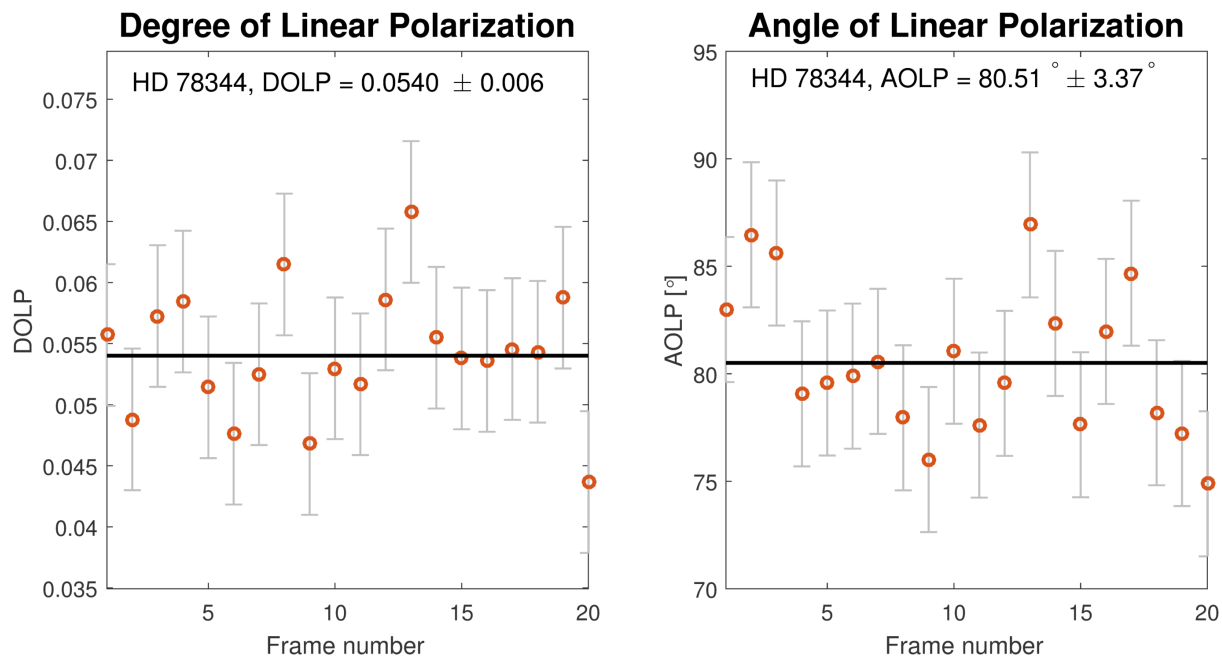


FIGURE 10.11: Polarimetry performed by RITPIC for the polarized star HD 78344 in the V band.

Target	DOLP ₀	DOLP _{RITPIC} (Mean ± S.D.)
HD 90156	0.0001 ¹	0.005 ± 0.01
HD 78344	0.0556 ²	0.054 ± 0.006

TABLE 10.1: Comparison of the polarimetric analysis of two standard stars performed by RITPIC to previous measurements (DOLP₀), made by 1. [Gil-Hutton and Benavidez \(2003\)](#) and 2. [Wiktorowicz et al. \(2014\)](#).

10.2.2 Polarimetry of Planets

I have acquired multi-band images of Venus, Jupiter and Saturn to determine the suitability of MPA-based polarimeters for applications with strong intensity gradients. Planets pose a significant challenge for these devices because they are extremely bright and their intensity drops off sharply near the limb. This is especially inconvenient because limb polarization is an interesting probe of planetary atmospheres.

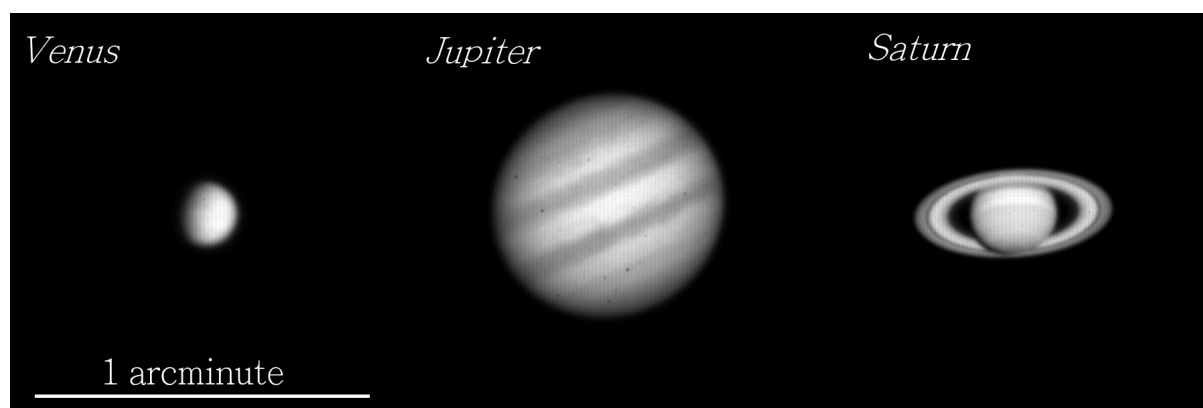


FIGURE 10.12: Raw images of Venus, Jupiter and Saturn acquired with Gen 4 RITPIC at the 36" telescope at CTIO.

10.2.2.1 Jupiter

Observations of Jupiter were made on February 8 and 11, 2016. The scattering angle, α , during these observations was $\sim 5.4^\circ$ and 5.2° , respectively. Images were obtained in the Bessel BVRI bands, using exposures 0.5 seconds - 2 seconds long.

Imaging polarimetry was performed on images of Jupiter in the R band, using approach the approach described in Section 9.2.3. The 20 individual Stokes q and u maps were combined using the median to generate the maps in Figure 10.13. For easier comparison to previous observations, I rotate the Stokes parameters to align them with respect to the scattering plane (Figure 10.14). The strong polarization at the poles of Jupiter is easily detected in both q and u . The maximum polarization measured for Stokes q is $\sim 8\%$, whereas the Stokes u map shows the “butterfly pattern” at the $\pm 4\%$ level. The East and West limbs in the equatorial regions show a slight negative polarization, which

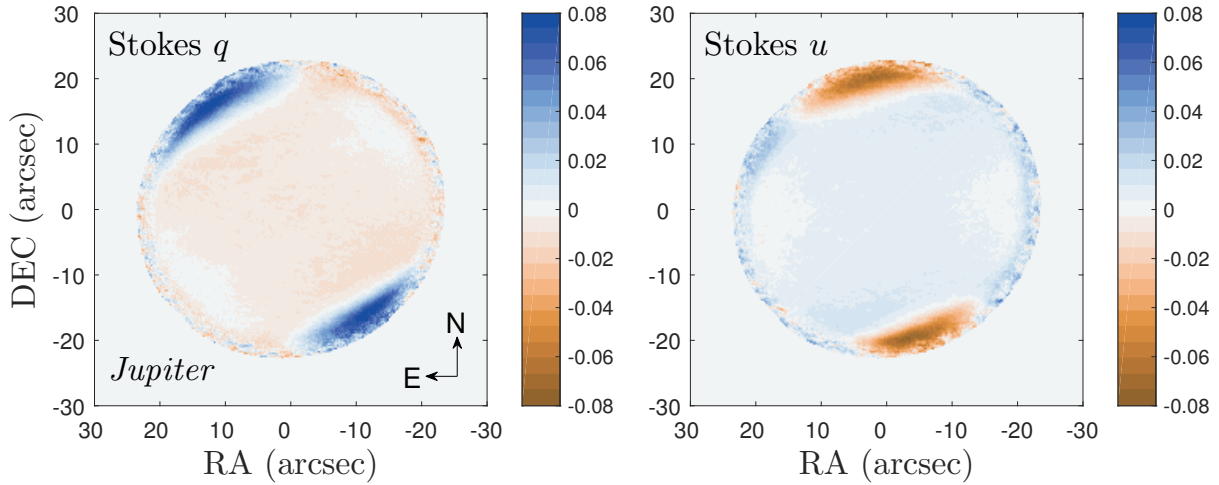


FIGURE 10.13: The Stokes q and u maps made using a median of 20 images of Jupiter in the Bessel R filter. The maximum polarization measured is $\sim q = 0.08$ and $u = -0.07$ in the instrumental reference frame.

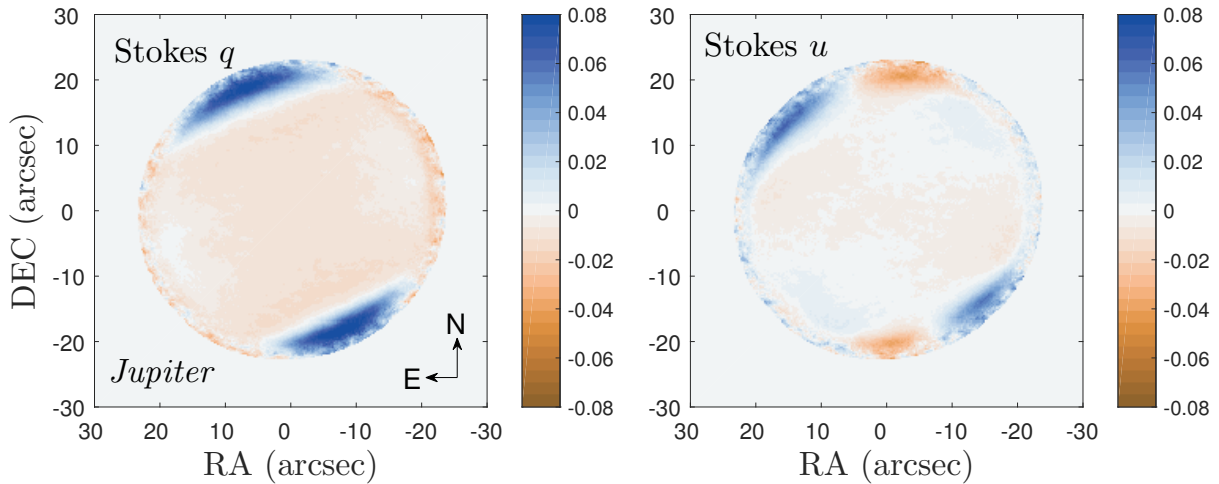


FIGURE 10.14: The Stokes q and u maps aligned with the scattering plane, to match observations of Schmid et al. (2011). The maximum polarization measured is $\sim q = 0.08$.

is also reported by Schmid et al. (2011), for observations made at phase angles of $\alpha \lesssim 6^\circ$; however, this signal appears to be near the limit of RITPIC's precision.

Uncertainty Analysis

The uncertainty in the Stokes q and u maps shown in Figure 10.13 can be estimated using the variance of the least squares estimator and formal error propagation for a linear parameter. The variance-covariance matrix associated with the Stokes vector is given by,

$$\text{Var}(\mathbf{b}) = \sigma^2(\mathbf{X}^T\mathbf{X})^{-1}, \quad (10.1)$$

where σ^2 is estimated using the sum of the difference between the measured intensities and the fitted model predictions,

$$\hat{\sigma}^2 = \sum_{n=1}^4 (y_i - \hat{y}_i)^2. \quad (10.2)$$

The diagonal elements of the variance-covariance matrix given by equation 10.1 are the estimates of the variance associated with the Stokes parameters, I, Q, and U. These variances are calculated in each frame. These variances are then used in the conventional propagation of error formula to determine the variance in the normalized Stokes parameters, $q = Q/I$ and $u = U/I$. These “error frames” are then combined using an average to produce an estimate of the uncertainty of the normalized Stokes parameters, q and u (Figure 10.15).

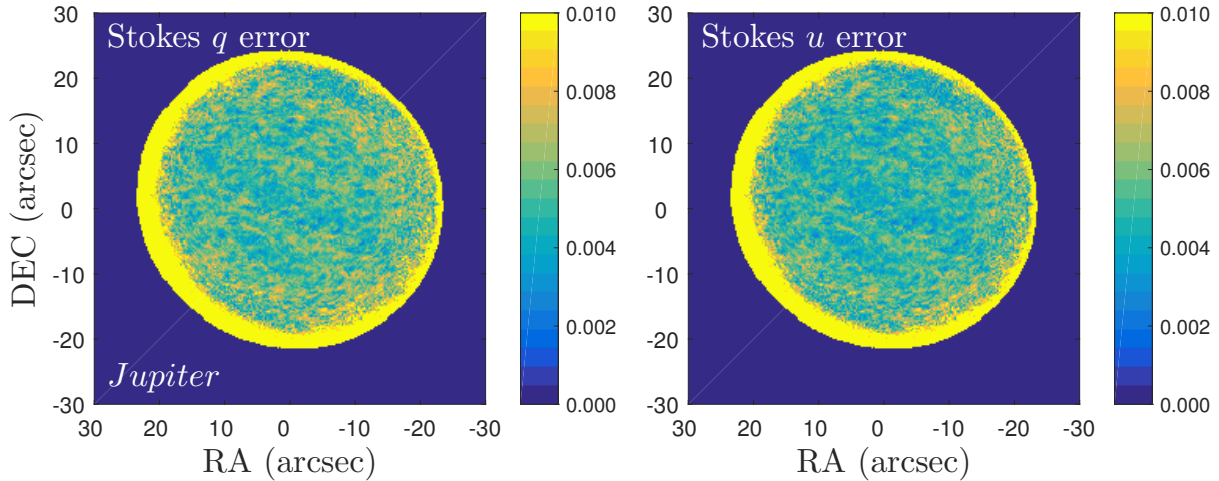


FIGURE 10.15: The uncertainty maps for the normalized Stokes parameters q and u , estimated using the variance-covariance of the linear least squares estimator and formal error propagation.

This is a conservative estimation of the uncertainty because it reflects the uncertainty in a single frame, whereas the maps shown in Figure 10.13 are averages of 20 frames. However, this method also assumes that the system matrix \mathbf{X} is known exactly. In reality, the polarizer properties are not known exactly and the system matrix has some

uncertainty, as well. A more robust treatment, like “total least squares” is required to properly assess the errors associated with an uncertain system matrix.

The error maps show that the estimation of the normalized Stokes parameters has an uncertainty of less than 1% across most of the disk of Jupiter, and increases towards the limbs. It’s not clear why the uncertainty is larger in the South. The increase in the uncertainty is likely due to several processes, the most significant of which are:

1. the flux sharply decreases at the limbs, and the photometric SNR drops
2. the steep drop in intensity near the limb exacerbates errors associated with the instantaneous field-of-view that are discussed in [Chapter 9](#)

Degree and Angle of Linear Polarization

The Stokes parameter maps in Figure 10.13 can be used to generate a map of the total fractional polarization, using the degree of linear polarization (DOLP) estimator (Figure 10.16). The polarization at the poles is clearly seen in this map, as are the regions of low polarization near the East and West limbs. This figure shows a few things worth nothing. First, this method of quantifying the fractional polarization is biased at low signal levels, as discussed in Section 6.5.3.

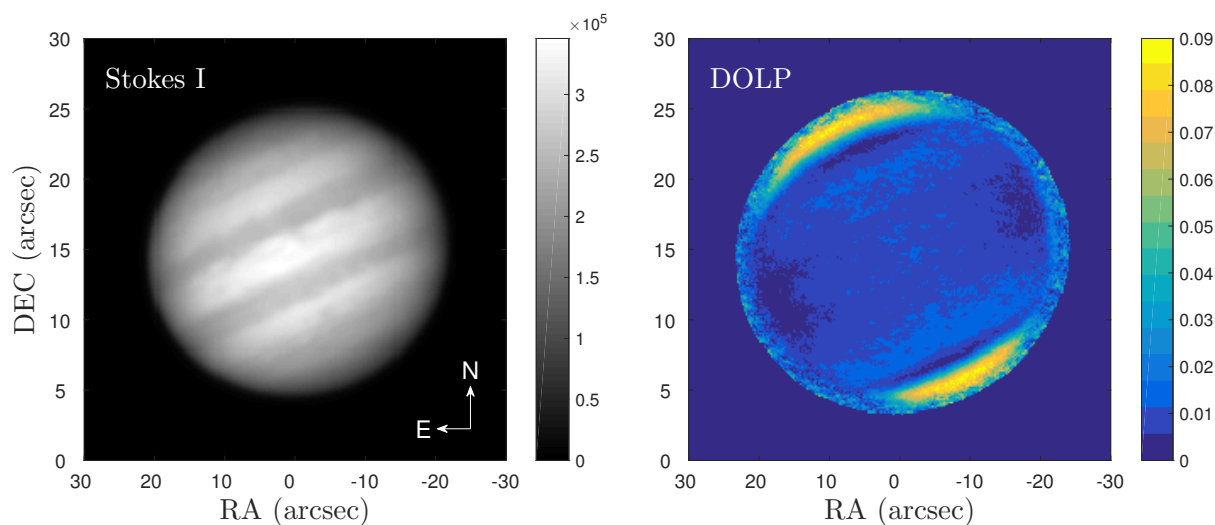


FIGURE 10.16: *Left:* The Stokes I “intensity” map of Jupiter in the Bessel R filter. *Right:* The fractional polarization of Jupiter, estimated using the degree of linear polarization. The polarization at the poles is $\sim 8\%$, and it rapidly and smoothly decreases towards the equator.

Second, the polarization maps use a threshold that makes Jupiter appear slightly larger than in the Stokes I map. The threshold is set based on the signal level in the Stokes I map, such that all pixels with values less than $\sim 1,500$ electrons are suppressed. The scaling in the Stokes I map renders these pixels such that they are almost indistinguishable from the background. However, they are much more easily seen in the polarization maps, making Jupiter appear larger by several arcseconds. The signal in these regions fluctuates significantly due to low flux and seeing effects, which can be seen in the maps of estimated errors for the Stokes q and u maps (Figure 10.15). The angle of linear polarization varies across the face of Jupiter and shows strong radial polarization near the poles (Figure 10.17).

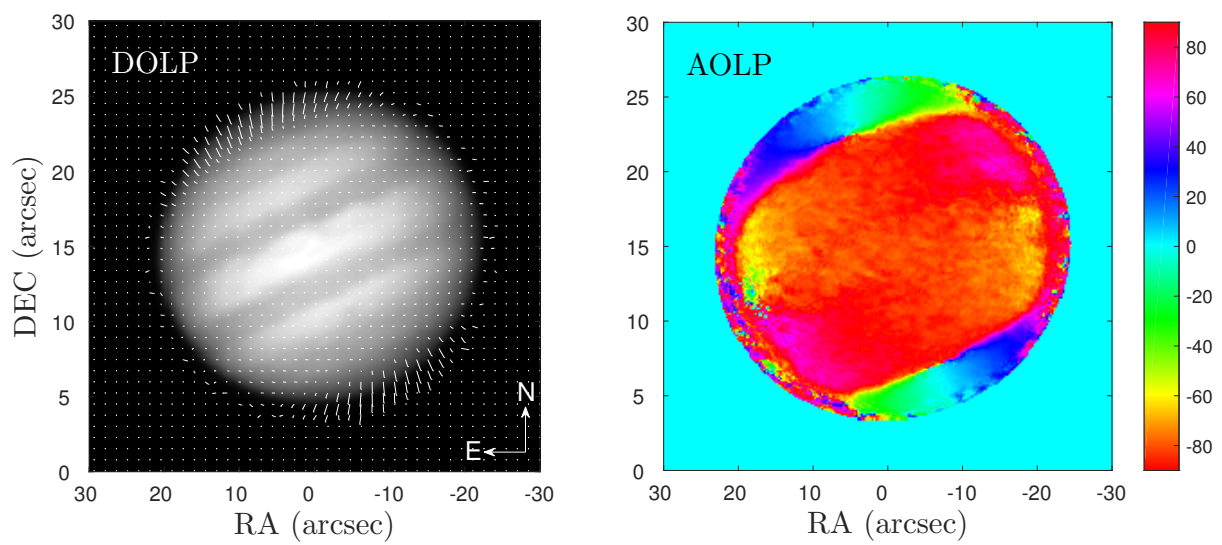


FIGURE 10.17: *Left:* Degree and angle of polarization shown with a vector plot. *Right:* Angle of polarization across the face of Jupiter shown as a colormap.

Comparison with Previous Observations

Comparison with previous observations is challenging. Although Jupiter's polarization was discovered nearly 100 years ago (Lyot, 1929), spatially-resolved polarimetry of Jupiter is scarce. Furthermore, the polarization of Jupiter has a strong dependence on wavelength and it varies with time (due to a changing phase angle and dynamics in the atmosphere). For example, Gehrels et al. (1969) show that the polarization near the poles and the limb has a strong dependence on wavelength, which changes dramatically between observations made in 1960 and 1963 (Figure 10.18). Moreover, the North-South asymmetry is minimal at ~ 500 nm in 1960 ($\alpha = -10.6^\circ$), but maximal in 1963 ($\alpha = -8.9^\circ$).

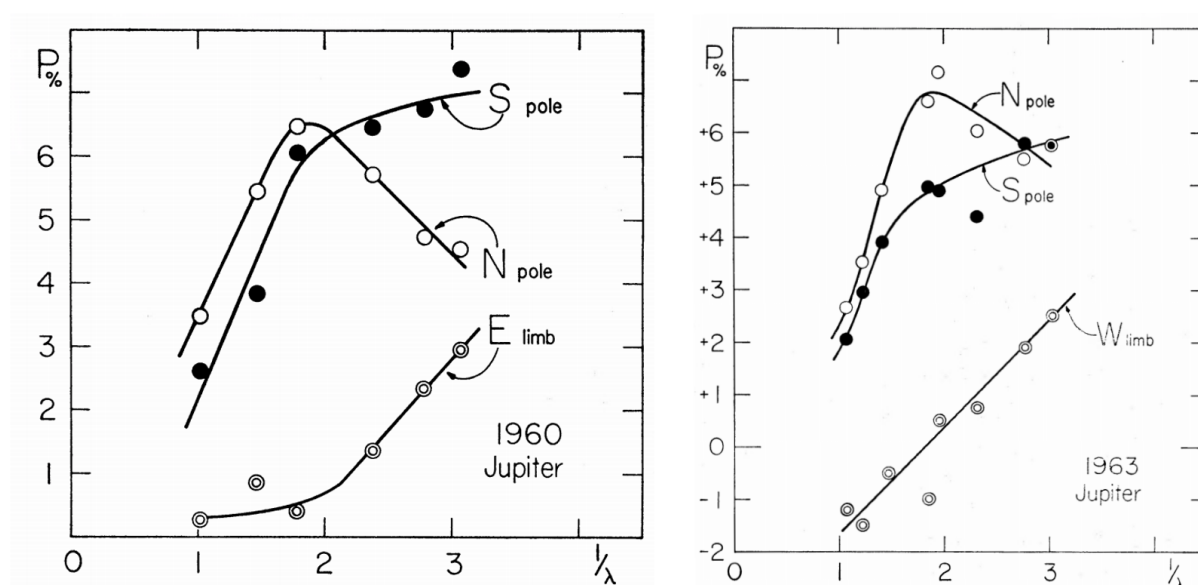


FIGURE 10.18: *Left:* Polarization at the poles and limbs of Jupiter, as a function of reciprocal wavelength, measured by Gehrels et al. (1969) in April 1960, with scattering angle $\alpha = -10.6^\circ$. Note that the asymmetry between the North and South pole polarization is minimal at ~ 500 nm. *Right:* The same measurements repeated in November and December 1963, with scattering angle $\alpha = 8.9^\circ$ and $\alpha = 9.8^\circ$, respectively. Note that the largest discrepancy is now at ~ 500 nm. ©AAS. Reproduced with permission.

With these issues in mind, I compare my observations to those made by Schmid et al. (2011) using the Zurich Imaging Polarimeter in March 2003. ZIMPOL is a very accurate imaging polarimeter; however, Schmid et al. (2011) mention that the fold mirrors on the McMath-Pierce telescope introduced systematic polarization errors which were not fully calibrated. The RITPIC and ZIMPOL observations were made at somewhat similar scattering angles but in different wavelength bands. Nevertheless, the observations made

with ZIMPOL appear to be the most recent and with sufficient precision to evaluate RITPIC's performance.

Overall, the results agree with the imaging polarimetry performed by [Schmid et al. \(2011\)](#) in 2003, within $\sim 1\%$. The Stokes q and u maps obtained with ZIMPOL at the McMath-Pierce Solar Telescope at Kitt Peak National Observatory are shown in [Figure 10.19](#). These maps were made using images acquired in March 2003, using a filter centered at 730 nm. North is up and East is left; note that Jupiter's tilt was different by $\sim 25^\circ$ degrees in March 2003, compared to February 2016, when the RITPIC observations were made.

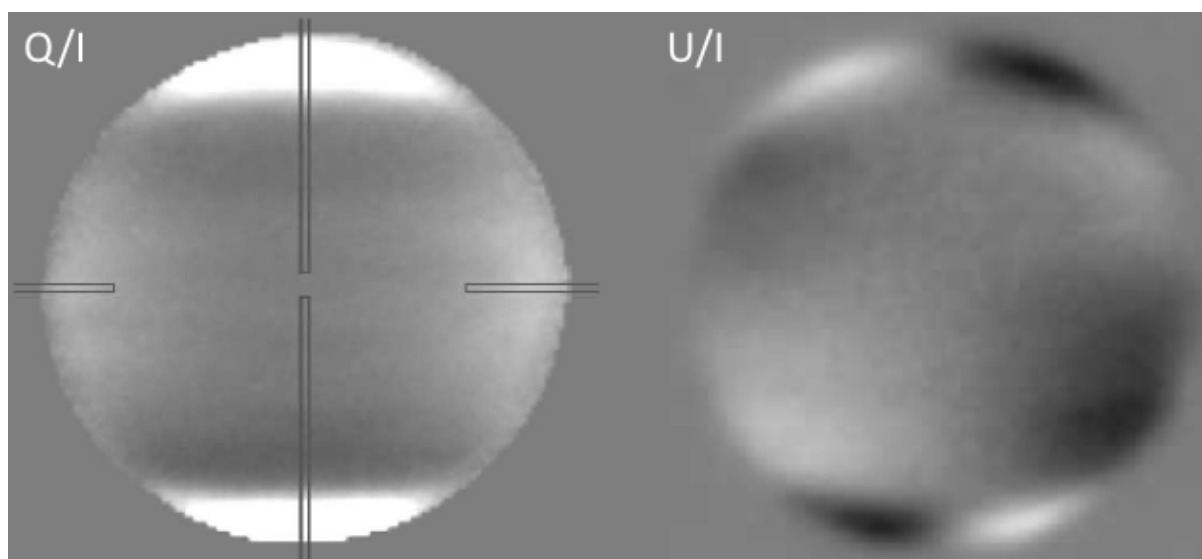


FIGURE 10.19: The Stokes q and u maps made by [Schmid et al. \(2011\)](#) during the testing of the Zurich Imaging Polarimeter. The scale is set between 1% (white) and -1% (black). The lines in the Q/I image show the slit positions for spectropolarimetry performed with the EFOSC2 instrument on the ESO 3.6m telescope. Reprinted from [Schmid et al. \(2011\)](#), Copyright (2011), with permission from Elsevier.

Limb-to-limb Profiles

To take a closer look at the profile of the polarization near the poles and across the disk, I calculated the average polarization in a narrow (~ 5 arcsec wide) rectangular region that runs roughly North-South, through the center of Jupiter (Figure 10.20). The intensity profiles obtained with RITPIC roughly agree with those obtained by ZIMPOL. Note, the intensity profile measured by ZIMPOL has been scaled here, so the maximum value matches the maximum signal measured by RITPIC.

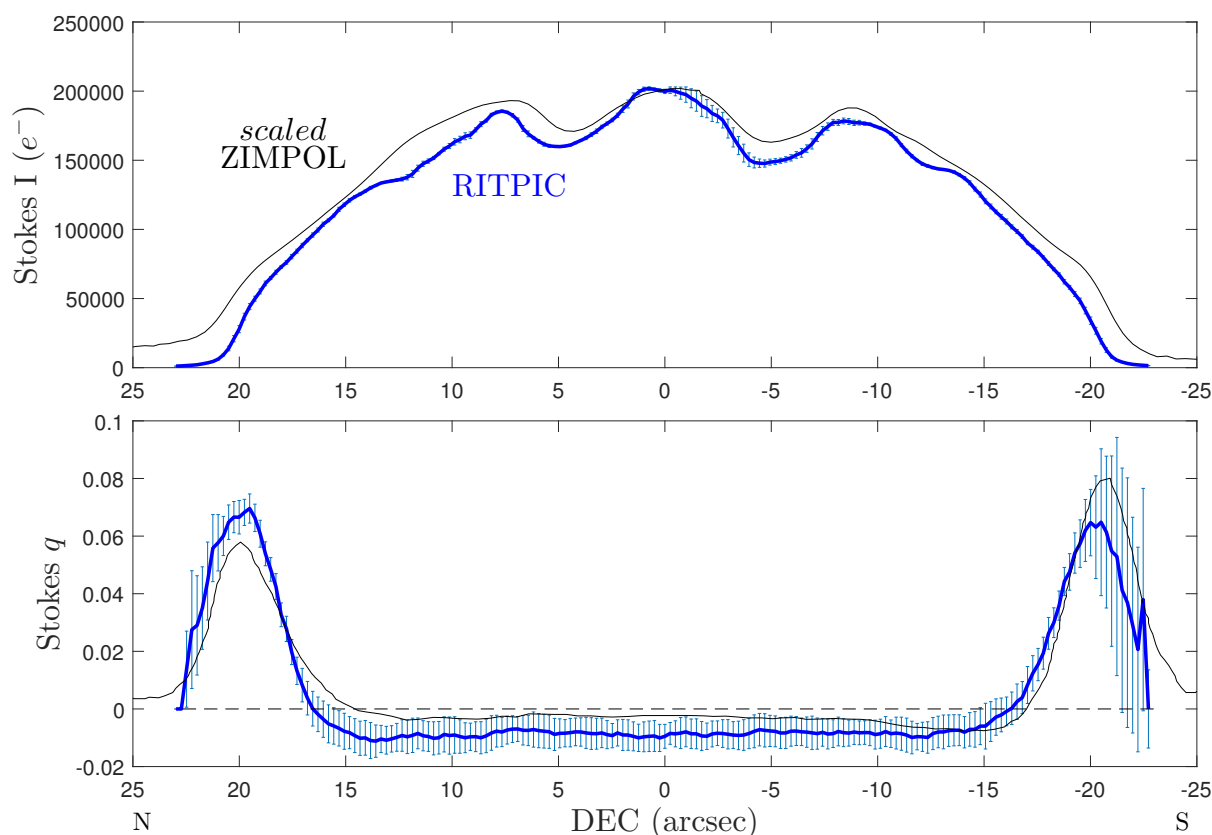


FIGURE 10.20: A comparison of the North-South profile of the intensity and normalized Stokes parameter q for observations made with RITPIC (blue line) and ZIMPOL (black line). The ZIMPOL intensity profile was scaled to have the same peak value as the RITPIC profile.

The North-South profiles of the normalized Stokes q parameter obtained with RITPIC and ZIMPOL agree at $\sim 1\%$ level; however, some differences are evident. Most notably, the polarization at the North and South pole, as measured by RITPIC, is much more symmetric than the ZIMPOL measurement. Overall, the RITPIC measurements in the equatorial regions are systematically more negative than the ZIMPOL values. Several factors could account for the disagreement:

1. the observational passbands were different, with Bessel R (~ 640 nm central wavelength and 150 nm FWHM used for RITPIC observations and a 20 nm wide filter at 730 nm used for ZIMPOL).
2. The scattering angle was different, $\alpha_{\text{RITPIC}} \approx 5.4^\circ$ vs $\alpha_{\text{ZIMPOL}} \approx 6.9^\circ$
3. the observations were taken 13 years and 1 month apart
4. (probably) different longitudes were observed

The East-West intensity and polarization profile made by averaging an ~ 16 arcsecond wide band along Jupiter's equator is shown in Figure 10.21. The intensity profile shows similar agreement between ZIMPOL and RITPIC results as for the North-South profile. The Stokes q profile measured by RITPIC is very different from the ZIMPOL result. It's not obvious which of the factors listed above could cause this type of discrepancy.

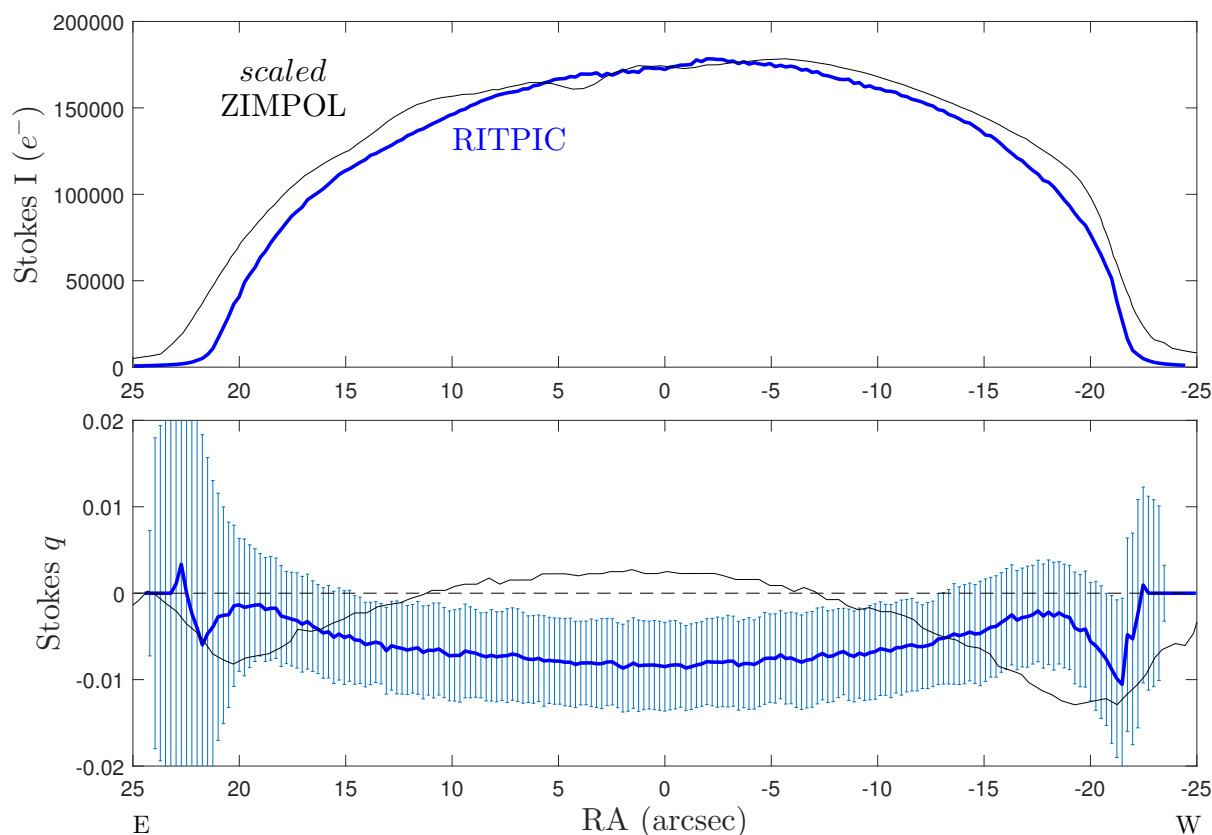


FIGURE 10.21: A comparison of the East-West profile of the intensity and normalized Stokes parameter q for observations made with RITPIC (blue line) and ZIMPOL (black line). The ZIMPOL intensity profile was scaled to have the same peak value as the RITPIC profile.

10.2.2.2 Saturn

As part of the commissioning run of RITPIC, I observed Saturn on the night of February 8, 2016. Images of Saturn were acquired in the Bessel BVR bands, using 1 and 2 second exposures. The phase angle, α was $\sim 5.1^\circ$. The maps of the normalized Stokes parameters, q and u are shown in Figure 10.22.

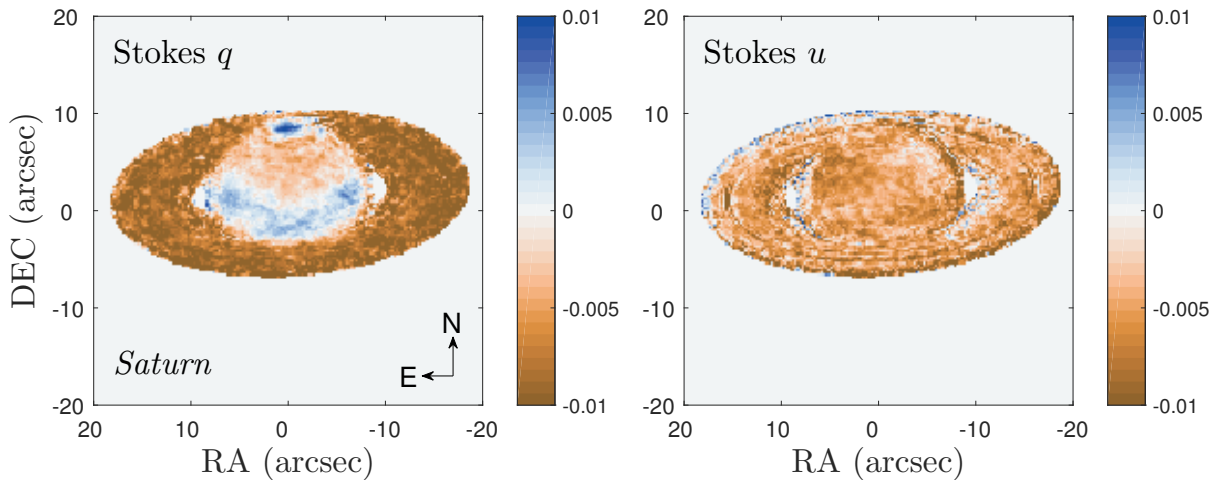


FIGURE 10.22: Polarization of Saturn and its ring system in Stokes q and u . Although the overall polarization is low, some large scale features are clearly seen, such as the polarization of the rings, the northern and southern hemisphere and the south pole.

Saturn is weakly polarized, however, some features are clearly visible. The disk of Saturn is polarized at $\sim q = 0.005$ level in the north and ~ -0.005 in the south. The south pole of Saturn shows strong polarization at a level of $\sim q = 0.02$. The rings appear to have a more-or-less uniform polarization in Stokes q of $\sim q = -0.01$. Both the disk and rings of Saturn show very low levels of polarization in Stokes u , with a faint feature near the equator. Schmid et al. (2011) report mostly weak Stokes u polarization of ~ -0.003 , which is consistent with my results. A polarization of $\sim 0.3\%$ appears to be close to the sensitivity limit of the current calibration and data analysis procedure.

The angle of linear polarization polarization of Saturn shows strong, large scale patterns. The rings appear polarized at roughly -45° with respect to the East-West direction. In regions of higher polarization on the disk of Saturn, the polarization angle is roughly $+45^\circ$ on the East side and 90° in the West. There appears to be a faint feature in the AOLP map that corresponds to the bright band near Saturn's equator. Both this band and the south pole show an angle of $\sim +45^\circ$.

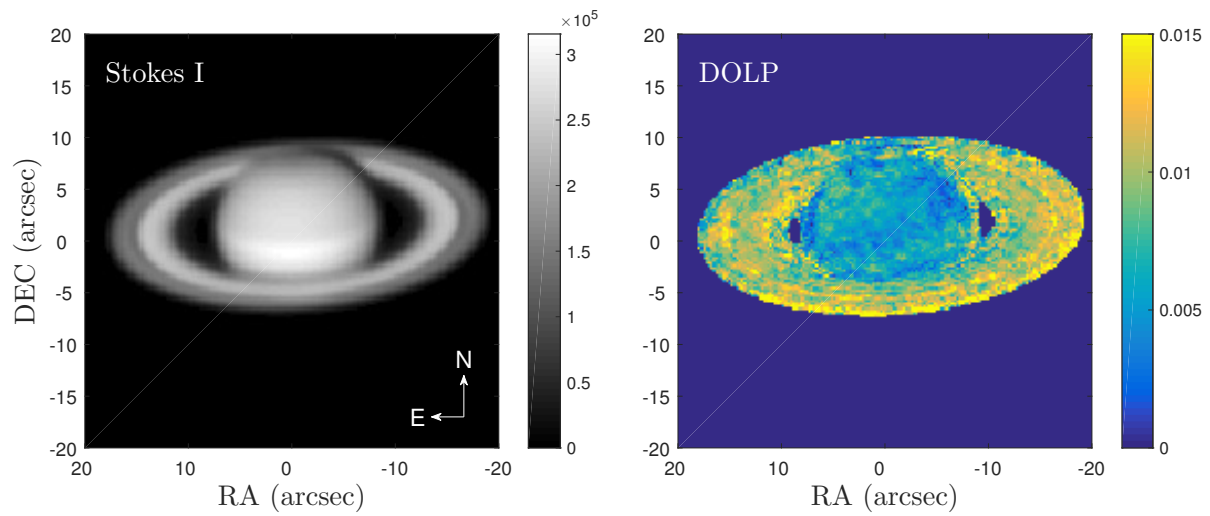


FIGURE 10.23: *Left:* A Stokes I “intensity” map of Saturn in the Bessel R band. *Right:* The fractional polarization of Saturn closely matches the Stokes q maps, because there is very little signal in u .

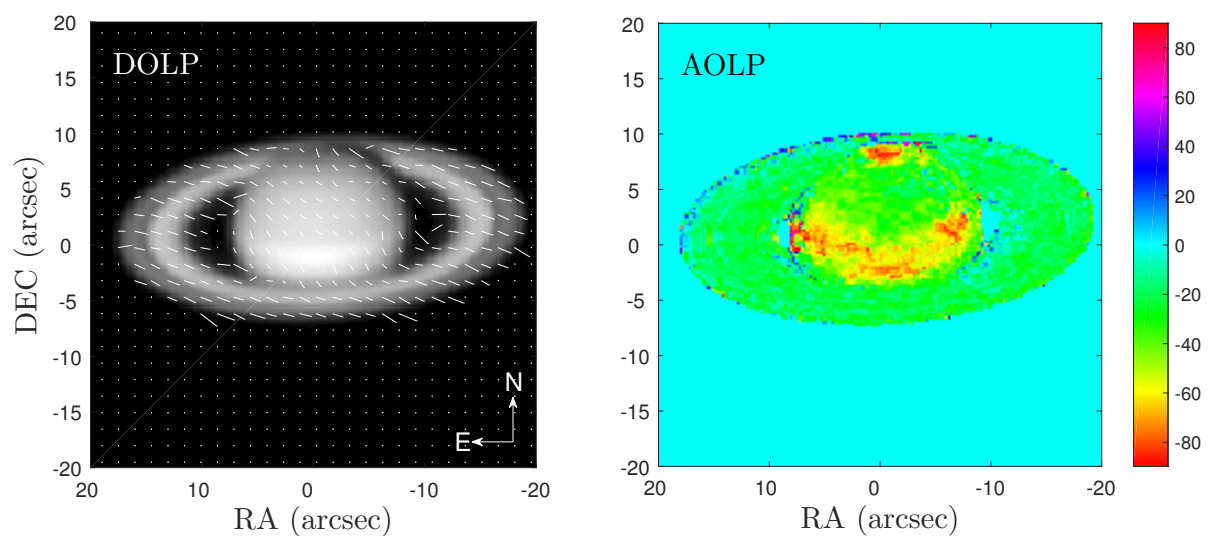


FIGURE 10.24: The angle of linear polarization shows a complex, large scale pattern across the rings and disk of Saturn.

10.2.2.3 Venus

I observed Venus on February 8, 2016 in the Bessel BVRI bands. The scattering angle, α , was $\sim 41^\circ$. Polarimetry of Venus in the R band shows strong polarization, with a maximum polarization of $\sim -4\%$ in Stokes q (Figure 10.25). The high polarization along the edge of the disk is probably not real and instead an artifact of the sharply decreasing flux near the limb. These effects can be seen in the polarimetry of Jupiter and Saturn. However, it's not clear to me why the artifacts are so much stronger for Venus.

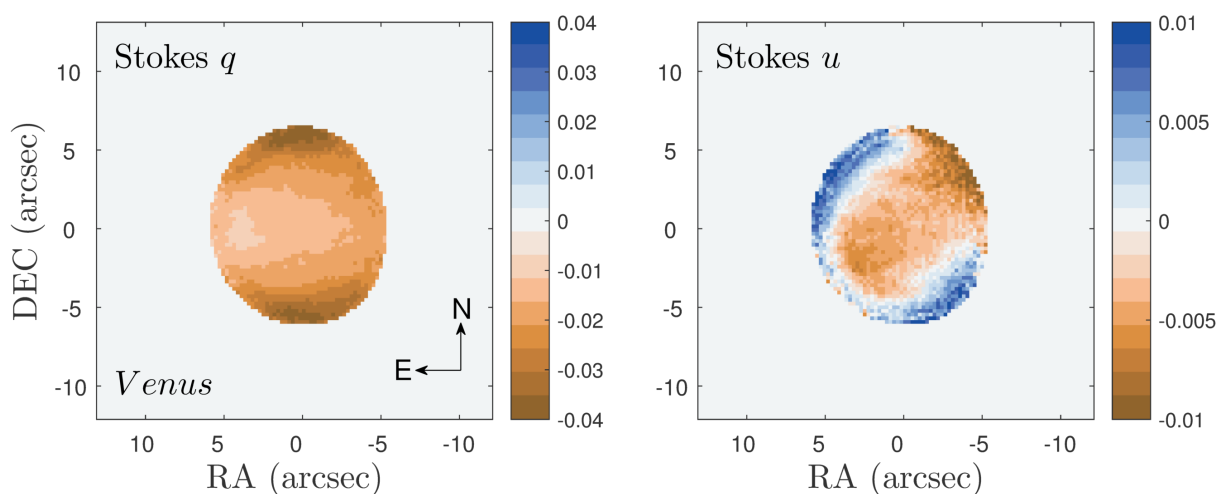


FIGURE 10.25: Polarization of Venus in Stokes q and u . The strongest polarization is seen in Stokes q , with a maximum near the poles and a minimum in the direction of the Sun.

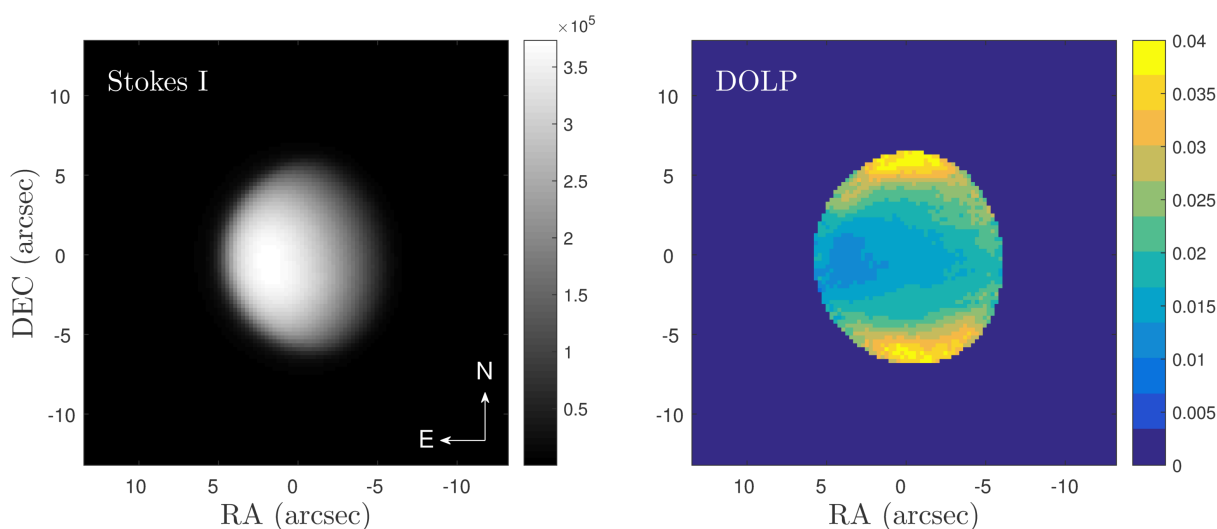


FIGURE 10.26: *Left:* A Stokes I “intensity” map of Venus in the Bessel R band. *Right:* The fractional polarization of Venus, estimated using the degree of linear polarization. The polarization at the poles is $\sim 4\%$ and $\sim 1\%$ at the lower latitudes.

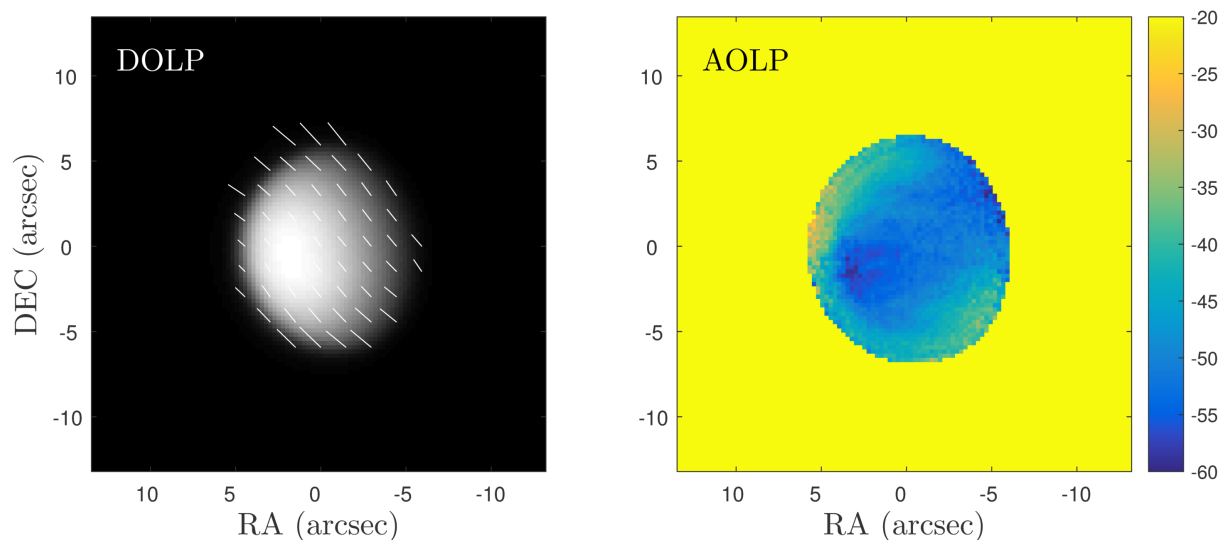


FIGURE 10.27: The polarization is oriented at $\sim -45^\circ$ with respect to the East-West direction across the entire disk of Venus.

I will close the section on polarimetry of Solar System planets by comparing the polarization of Venus to the previous measurements and the models of Hansen and Hovenier (1974). Measurements made by Coffeen and Gehrels in 1969 at similar phase angles and wavelengths, and the models of atmospheric composition are shown in Figure 10.28. The degree of polarization measured for Venus with RITPIC integrated over the entire disk is $q = -2.01\%$, which is slightly less than, but roughly in line with measurements of Coffeen in Gehrels. The value measured by RITPIC is also $\sim 0.3\%$ less than the disk-integrated polarization predicted by the model of Hansen and Hovenier (1974) for 655 nm light. It's not clear how much different the model prediction would be for light integrated over the R band. The polarization at the equator measured by RITPIC is $\sim -1.2\%$, which is also $\sim 0.3\%$ less than the value predicted by the equatorial model. This may indicate that RITPIC has a systematic error of $\sim 0.3\%$ in Stokes q , or the difference may be explained by the mismatch of the model parameters and the wide passband used for observations.

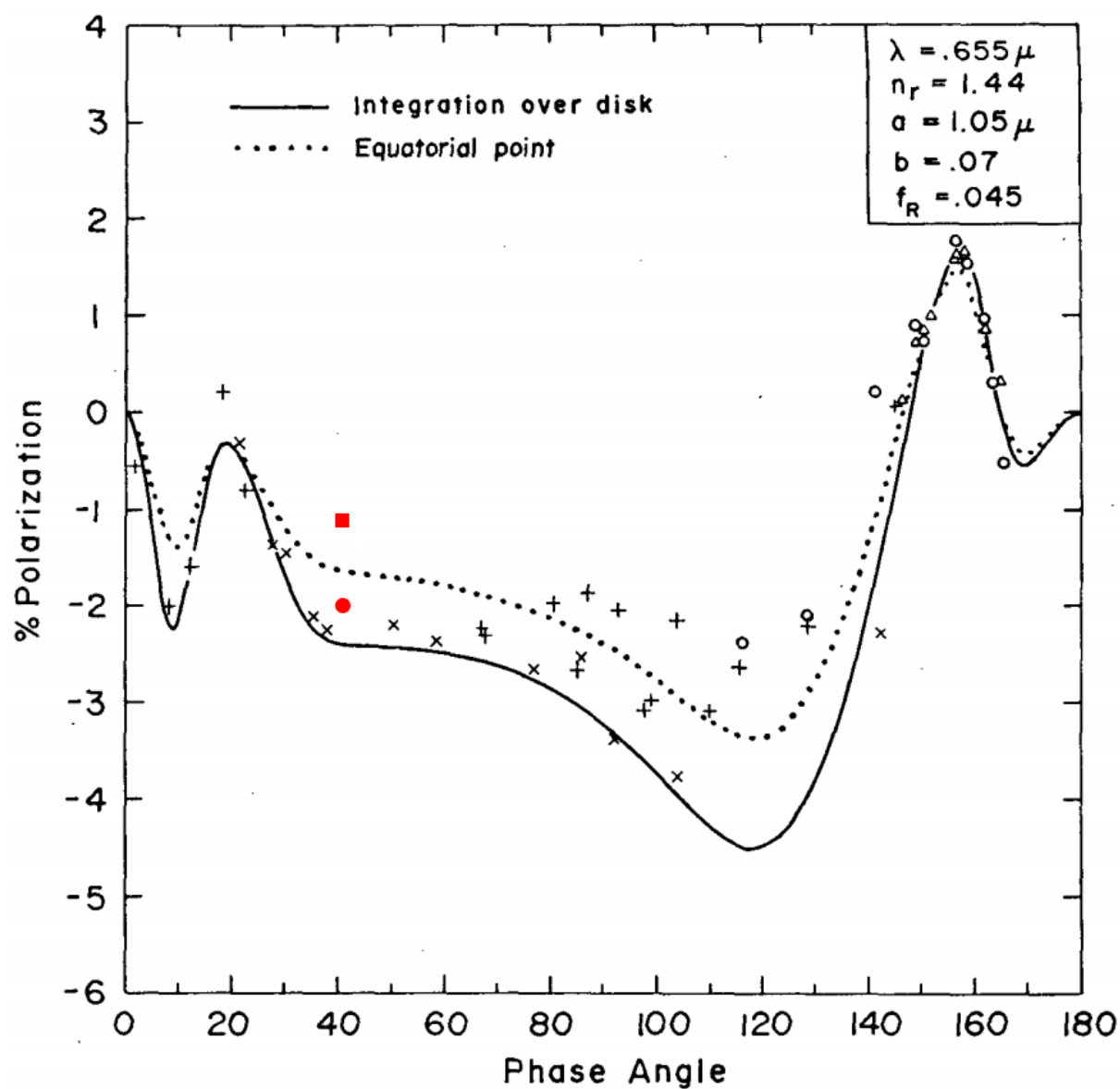


FIGURE 10.28: Previous polarimetric observations of Venus and the models of Hansen and Hovenier (1974) for the Venereal atmosphere. The red circle shows the integrated polarization in Stokes q measured by RITPIC in the Bessel R band and the square shows the polarization at the equatorial point. This figure is adopted from Fig. 12 of Hansen and Hovenier (1974) ©American Meteorological Society. Used with permission.

10.2.3 Observations of Nebulae

The final class of objects observed during the first on-sky deployment of RITPIC were a number of reflection and planetary nebulae. These objects are very challenging to observe due to their low surface brightness. On the other hand, nebulae rarely show the kind of steep intensity gradients that are seen in images of stars or solar system planets.

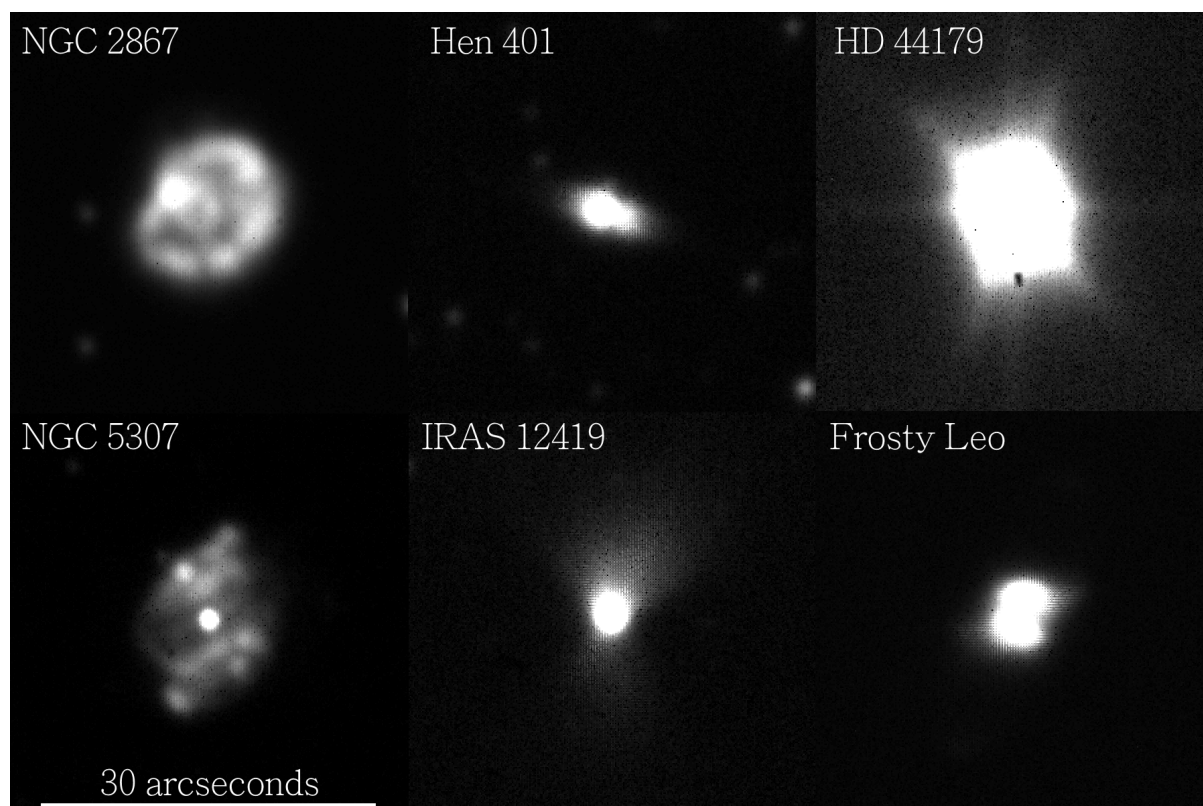


FIGURE 10.29: Raw images of some planetary (and protoplanetary nebulae) acquired with Gen 4 RITPIC at the 36" telescope at CTIO. The scale is the same in all images.

The images of nebulae were processed using the procedure described in Section 9.2.3. First, the individual subframes were registered to account for the 1 pixel offset. Next, the subframes for all exposures were co-added. Finally, the polarimetry was performed on a pixel-by-pixel basis. In this section, I present some initial observations of polarized nebulae and compare with previous polarimetry of these objects.

10.2.3.1 Hen 401

Henize 3-401 (IRAS 10178-5958) is a bipolar proto-planetary nebula, surrounding a Be post-AGB star. *HST* imaging shows Hen 401 to be $\sim 20 \times 5$ arcseconds. I acquired 5300 second exposures in the R filter of Hen 401 on February 6th, 2016. The normalized Stokes parameter maps for Hen 401 are shown in Figure 10.30. The nebula shows very strong polarization in both q and u , reaching a maximum of $\sim 50\%$ in the lobes. The region near the central star is very weakly polarized. The degree of linear polarization map for Hen 401 is shown in Figure 10.31.

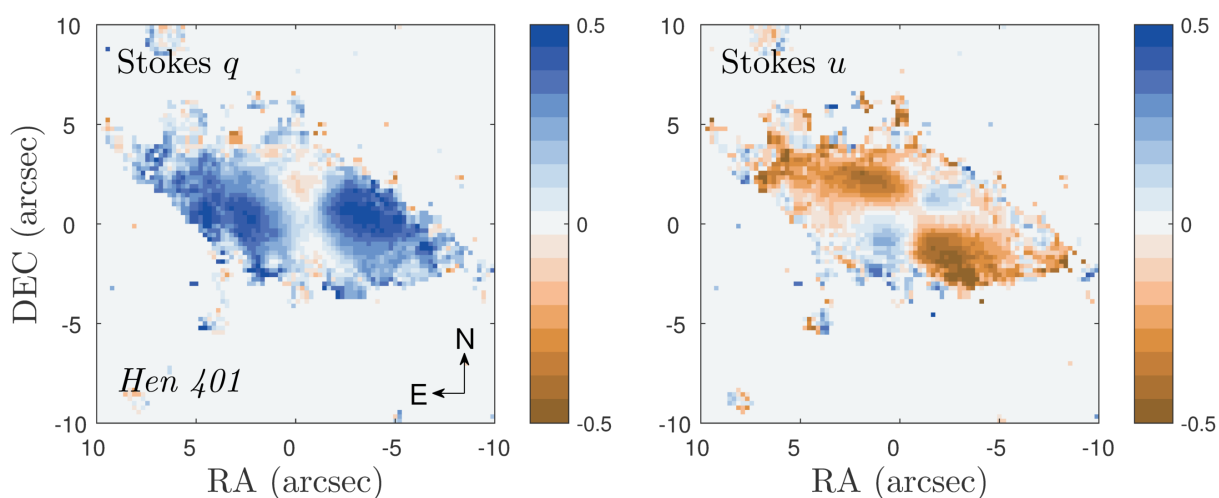


FIGURE 10.30: Normalized Stokes parameters q and u calculated for Hen 401 using 5300 second exposures in the R filter.

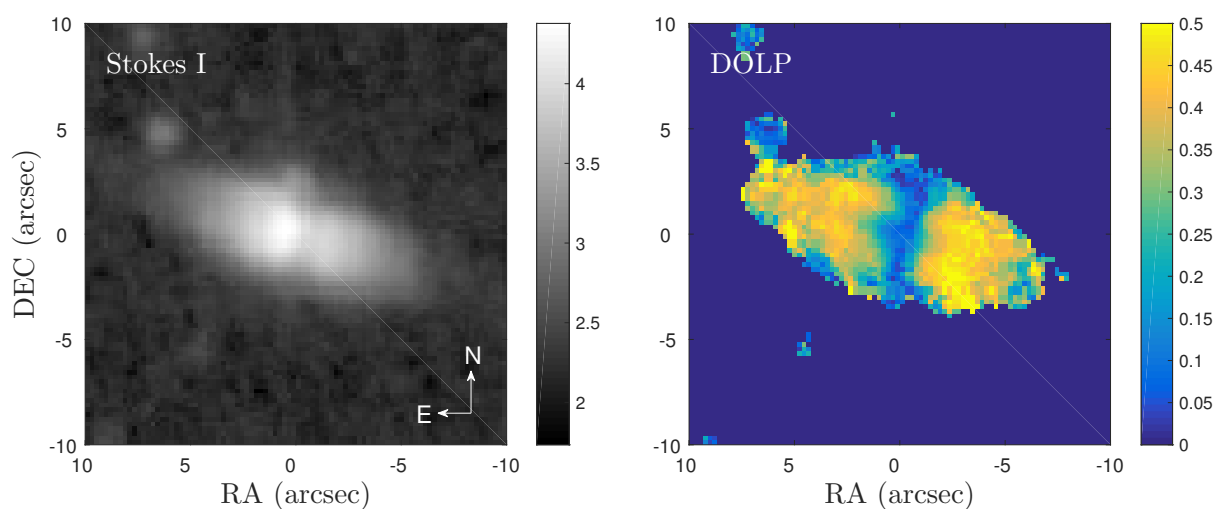


FIGURE 10.31: The R band Stokes I image and the degree of linear polarization map for Hen 401.

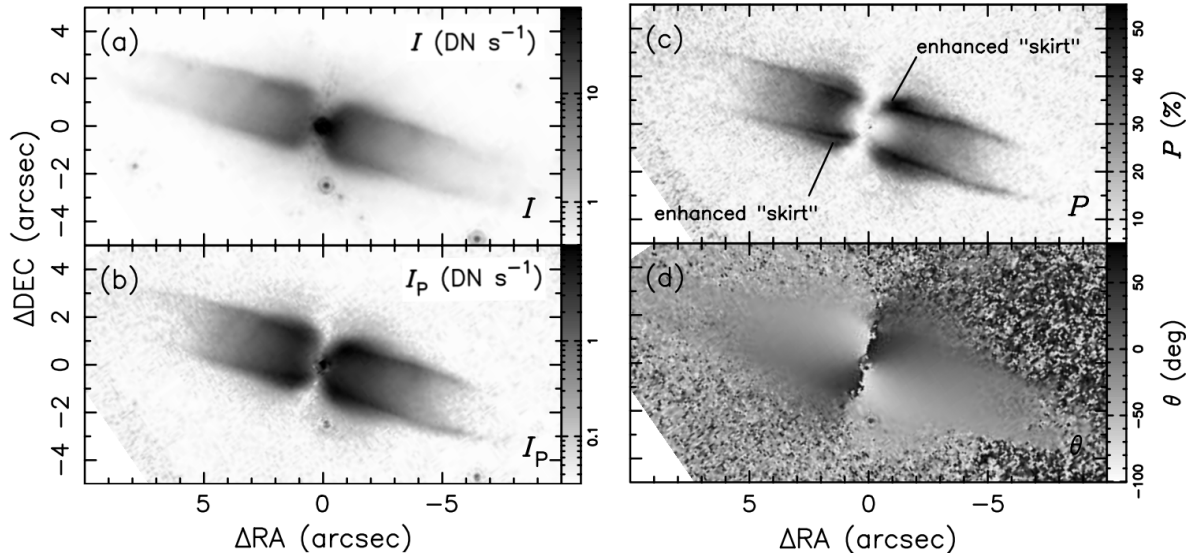


FIGURE 10.32: *Left:* *HST* imaging of Hen 401 from Ueta et al. (2007) showing the total (a) and polarized (b) flux. *Right:* Maps of the degree (c) and angle (d) of linear polarization. ©AAS. Reproduced with permission.

The peak polarization in the lobes and the low polarization “trench” near the center agree with previous *HST* polarimetry performed by Ueta et al. (2007) (Figure 10.32). Furthermore, RITPIC observations correctly reconstruct the structure in the angle of linear polarization (Figure 10.33). The sharp transition near the central region is clearly resolved in RITPIC images, even with seeing-limited data.

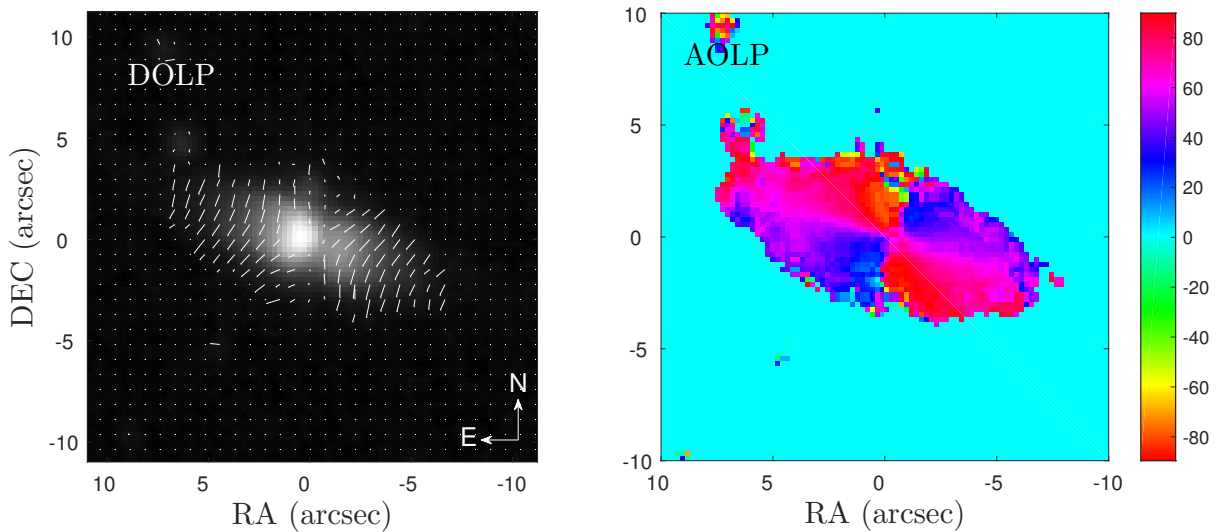


FIGURE 10.33: *Left:* The DOLP and AOLP of Hen 401 overlaid on the intensity image. *Right:* a detailed map of the angle of linear polarization shows good agreement with *HST* polarimetry.

10.2.3.2 Hen 404

Henize 3-404 (IRAS 10197-5750) is a proto-planetary nebula, also known as Roberts 22. I observed Hen 404 with RITPIC using 9 300 second exposures without any filter. This nebula is very compact and roughly rectangular, with approximate dimensions of $\sim 12 \times 10$ arcseconds. The Stokes q and u maps for Hen 404 are shown in Figure 10.34. The peak polarization measured is $\sim 35\%$ in both q and u .

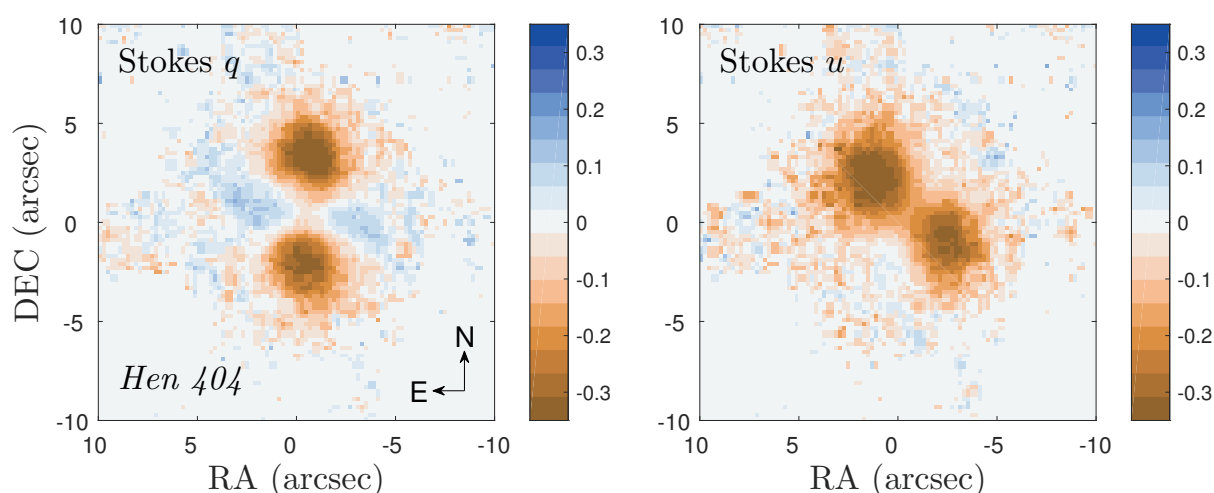


FIGURE 10.34: Normalized Stokes parameters q and u calculated for Hen 404 using 9 300 second exposures, without any filters.

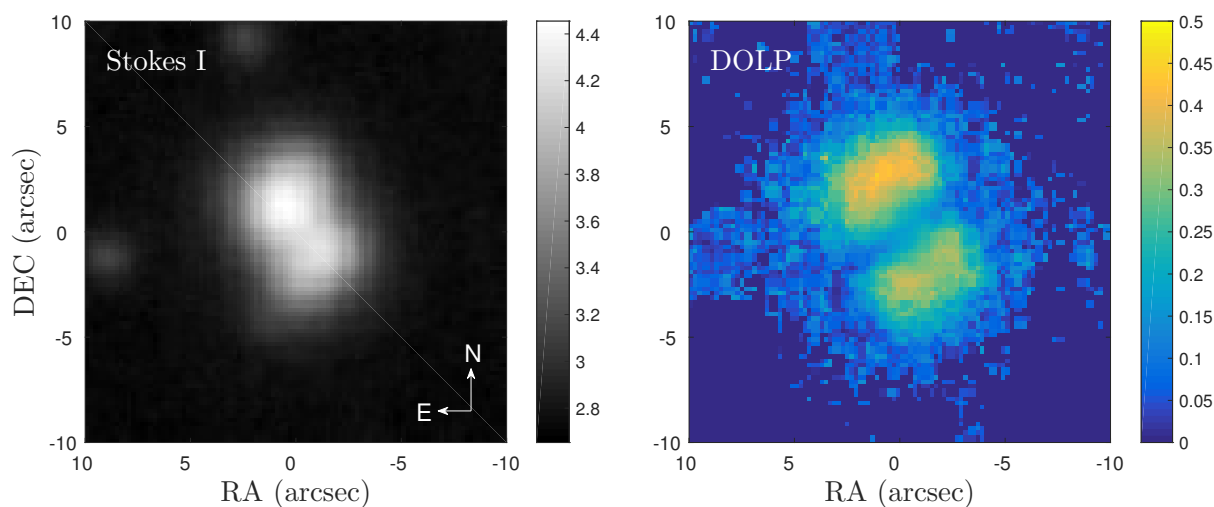


FIGURE 10.35: The Stokes I intensity and the degree of linear polarization for Hen 404 measured by RITPIC.

The degree of linear polarization and the Stokes I intensity map are shown in Figure 10.35. Compared with *HST* polarimetry of Ueta et al. (2007), the images acquired with RITPIC show a significant loss of detail due to atmospheric blurring. Because

the polarization structure of Hen 404 shows very localized regions of high polarization, the peak polarization measured by Ueta et al. (2007) is higher than that measured by RITPIC. However, the structure in the angle of linear polarization is still resolved in the RITPIC polarimetry.

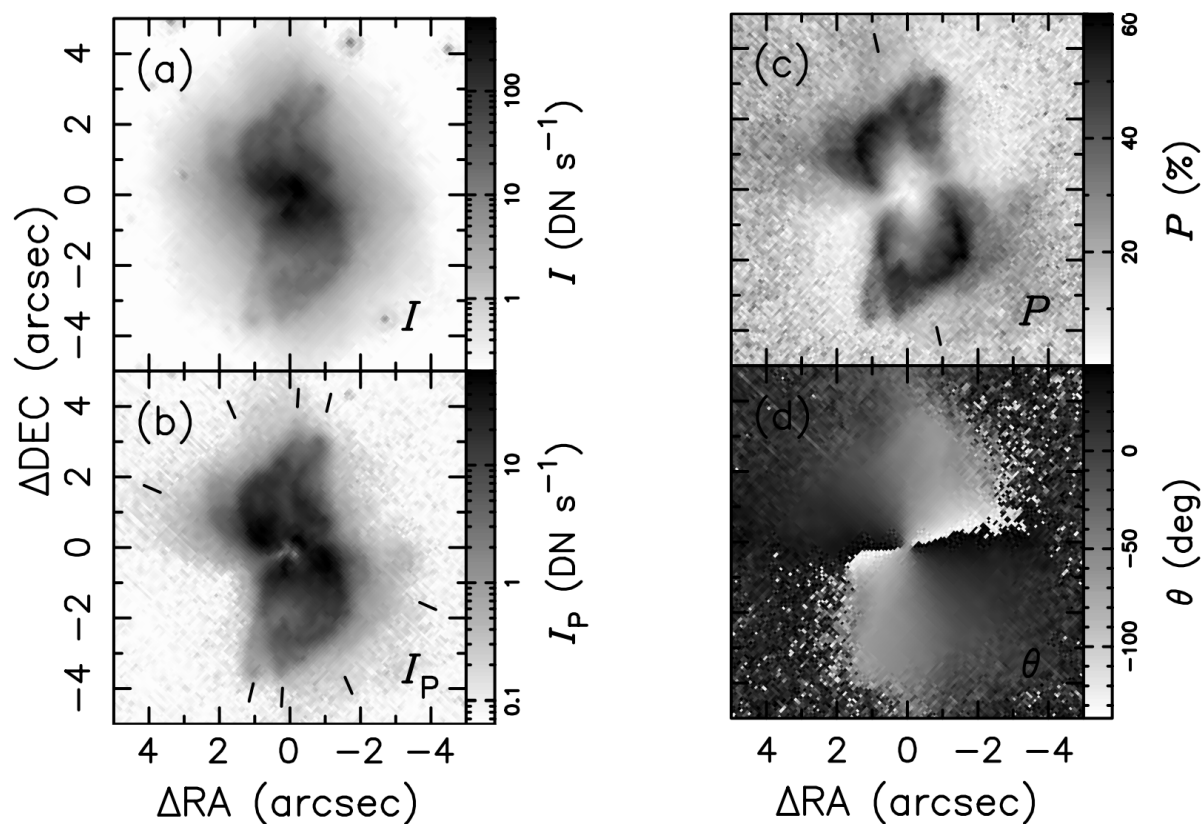


FIGURE 10.36: *Left:* *HST* imaging of Hen 404 from Ueta et al. (2007) showing the total (a) and polarized (b) flux. *Right:* Maps of the degree (c) and angle (d) of linear polarization. ©AAS. Reproduced with permission.

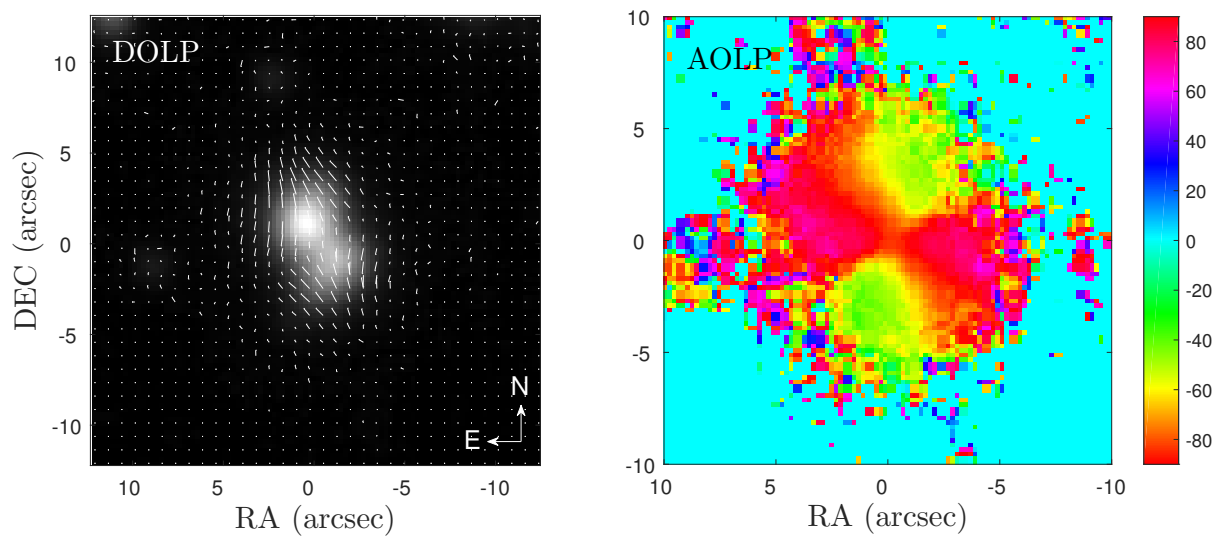


FIGURE 10.37: *Left:* The DOLP and AOLP of Hen 404 overlaid on the intensity image. *Right:* a detailed map of the angle of linear polarization shows good agreement with *HST* polarimetry. ©AAS. Reproduced with permission.

10.2.3.3 Frosty Leo

Frosty Leo (IRAS 09371) is a well known, highly polarized, proto-planetary nebula. I observed Frosty Leo on February 8, 2016, using 10 120-second exposures without using any filters. The Stokes q and u maps are shown in Figure 10.38). Some polarization artifacts can be seen in the background of these images, where the signal-to-noise ratio is very low. The Stokes I and degree of linear polarization maps are shown in Figure 10.39. The peak polarization observed with RITPIC is $\sim 50\%$ for this system, which agrees with previous measurements (Scarrott and Scarrott, 1994).

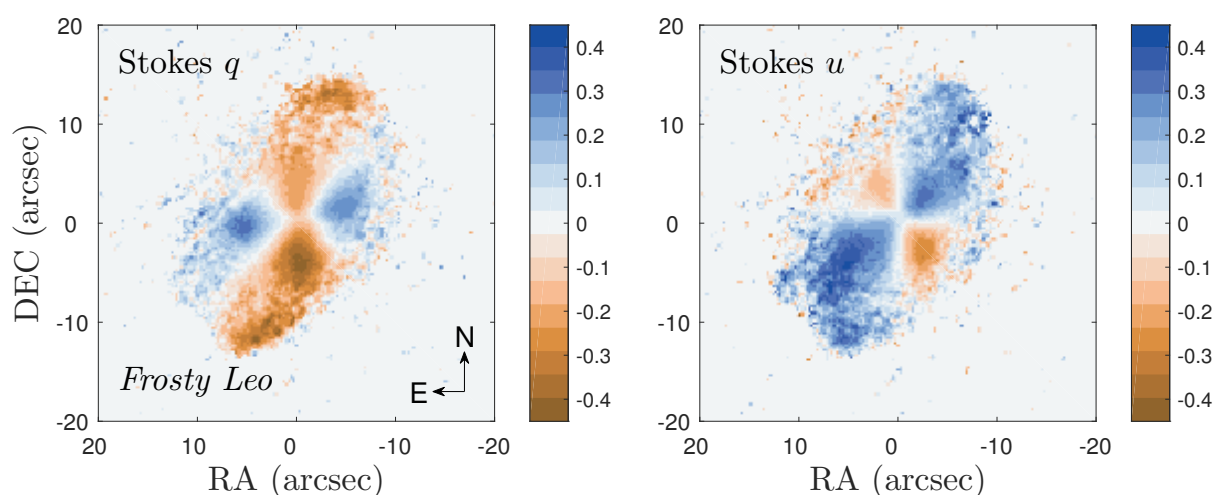


FIGURE 10.38: The Stokes q and u polarization for Frosty Leo. Peak polarization is $\sim 40\%$ and -45% , respectively.

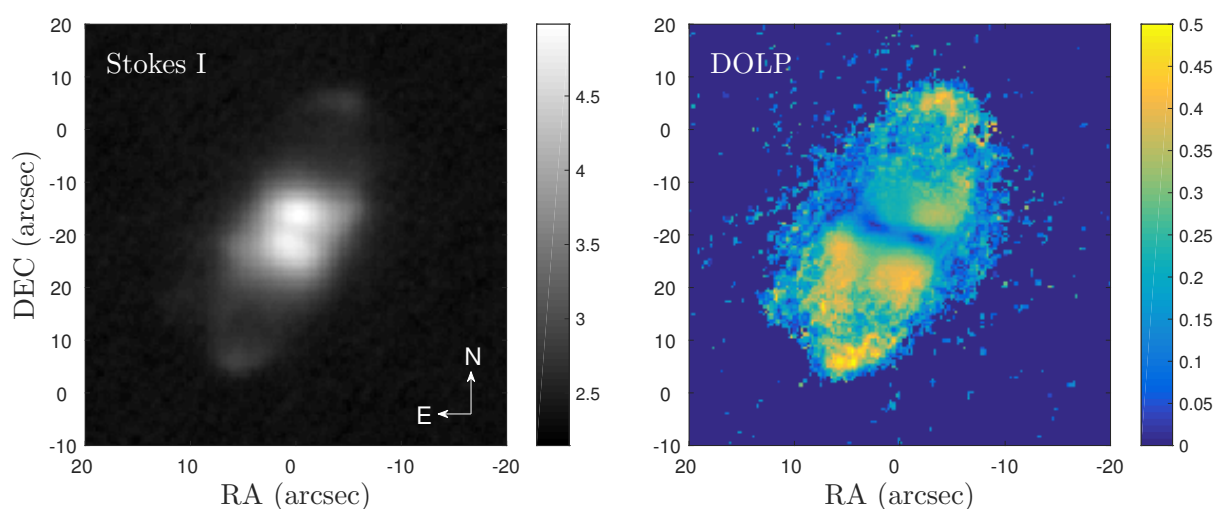


FIGURE 10.39: *Left:* The Stokes I intensity shown on a log scale. *Right:* The maximum fractional polarization peaks at $\sim 50\%$ in the ansae.

The angle of linear polarization maps are shown in Figure 10.40. The outflows driven by the central star show a complex and coherent structure, which is traced with high resolution by the angle of linear polarization.

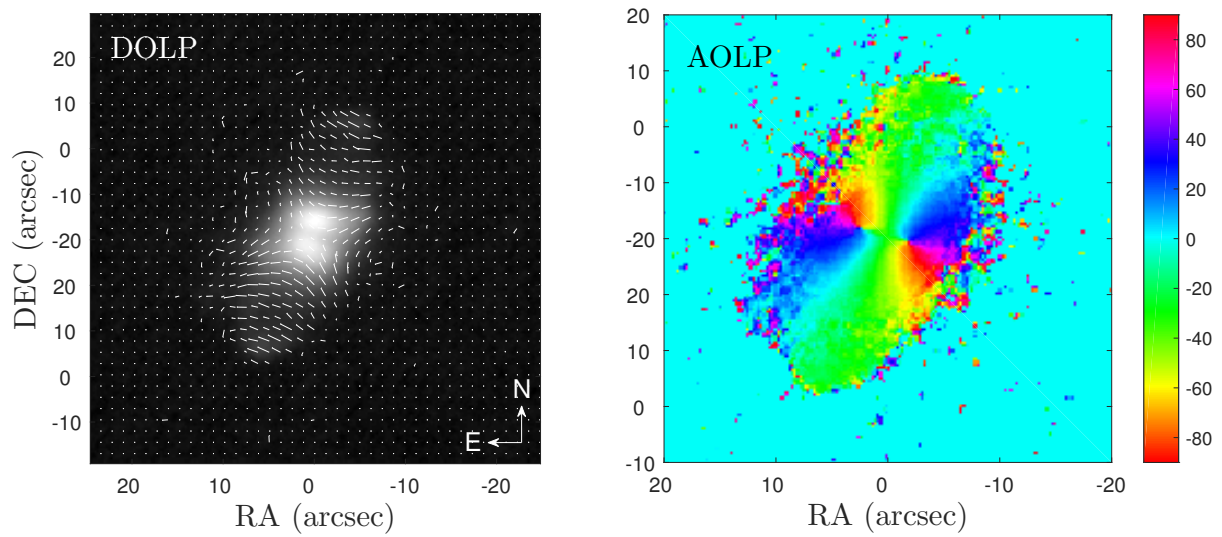


FIGURE 10.40:

Left: The degree and angle of polarization of Frosty Leo, indicated by the length and orientation of the marks. *Right:* The angle of linear polarization shown as a colormap.

Chapter 11

Conclusion

The work described in this dissertation was performed with the goal of establishing the suitability of micropolarizer-based polarization sensors for astronomical polarimetry. To that end, I investigated the design of MPA-based detectors, developed device characterization and data calibration techniques, and performed on-sky evaluations by observing a variety of astronomical sources. In this chapter, I summarize the key findings of this work and discuss applications that are most suited for these versatile devices.

11.1 Design and Performance of MPA-based Sensors

The current generation of polarization sensors, fabricated by aligning a micropolarizer array with an off-the-shelf imaging sensor, show a throughput of $\sim 35\%$ (for unpolarized light) and an average broadband contrast of $\sim 35:1$. The performance is roughly constant across the visible range (with a decrease in contrast to $\sim 20:1$ in the 300 nm - 400 nm range). The throughput appears to be limited by the nonuniform fill-factor of the micropolarizer arrays, caused by opaque gaps around each micropolarizer. The contrast ratio is limited by several cross-talk mechanisms (see Figure 11.1). Of these, the three most significant ones are:

- Diffraction of light by micropolarizers, which causes light transmitted by one micropolarizer to end up in a detector pixel designated for a neighboring polarizer (see

Section 5.2). The fraction of light collected by a single detector pixel that can be attributed to this mechanism depends on the pixel size, distance from the micropolarizer array, and the wavelength of light. In the visible range, with $9\ \mu\text{m}$ pixels, at a distance of several microns, the contrast is $\sim 200:1$ (Figure 5.9 and Figure 5.10).

- Reflections within the glass substrate (Figure 11.1, Path 1), as well as between the micropolarizer array and the detector surface (Figure 11.1, Path 2) are the second important cross-talk mechanism. We have not yet developed models to study this mechanism; however, it is easy to imagine that even a 2% reflection from the detector surface, to the polarizer and back can put a lot of light into a pixel which should have measured nothing, based on the orientation of its own micropolarizer.
- The third channel for cross-talk is related to geometric optics. If the micropolarizer array is too far above the detector surface, its effective area (as seen by a detector pixel) is reduced, if it is illuminated by converging light rays. This means light rays passing from a single polarizer can end up in a detector pixel designated for another polarizer (Figure 11.1, Path 3). This effect becomes stronger for faster (smaller $f/\#$) beams.

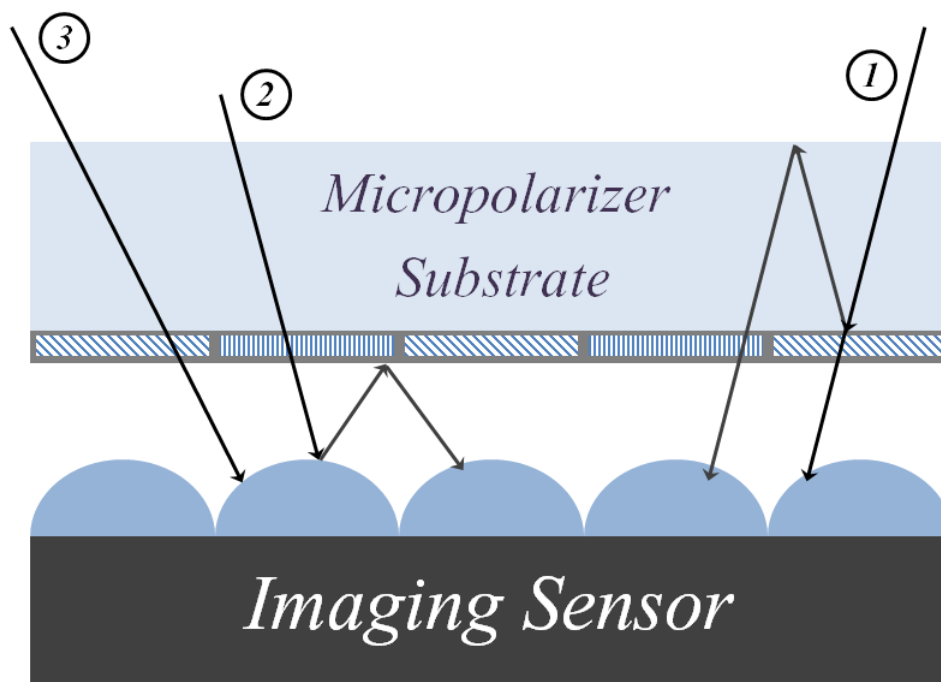


FIGURE 11.1: Several mechanisms for cross-talk exist in micropolarized-based sensors that use off-the-shelf devices.

The last two mechanisms conspire to reduce the contrast of micropolarizer-based sensors from the theoretical limit of $\sim 200:1$, to the much lower values seen in detectors like RIT-PIC. It isn't clear that the contrast can be significantly improved by refining the process of attaching micropolarizer arrays to off-the-shelf sensors. However, better performance may be achieved by integrating the micropolarizer into the sensor, as part of the sensor fabrication process.

11.2 Polarimetry with MPA-based Sensors

The throughput and contrast of micropolarizer-based sensors are important performance parameters, however, they do not limit the ultimate accuracy or precision of measurements made with these polarimeters. **The measurement uncertainty is limited by the accuracy of the device characterization, the measurement strategy, and photometric shot noise.** Higher average throughput and contrast only help by allowing a certain photometric SNR to be reached with fewer incident photons. In this section, I will discuss some practical considerations important to polarimetry with these sensors.

11.2.1 Device Nonuniformity and Characterization

Compared to conventional CCDs (or even sCMOS sensors), MPA-based detectors exhibit significant nonuniformity. The throughput of pixels with two polarizer orientations can differ by as much as 20%, and even pixels with the same orientation can vary by $\sim 10\%$, with respect to their mean (Figure 8.5). The contrast and orientations of micropolarizer pixels also vary at a level of several percent (Figure 8.7 and Figure 8.9).

The differences in throughput, contrast, and orientation limit the polarimetric precision of these devices. Because polarimetric information is inferred by comparing intensity differences measured by different pixels, any intrinsic variability between those pixels will manifest in polarimetric error. This is in contrast to beam-exchange polarimeters, where the same pixel is used to sample the intensity along several orientations, which results in a truly relative measurement. Therefore, the intrinsic differences between pixels must

be precisely determined during the characterization process and accounted for during the demodulation process.

Device nonuniformity results in both systematic and quasi-random errors. Differences between pixels of *different orientations*, will give rise to systematic errors. For example, almost all 0° pixels show higher throughput than 45° pixels (Figure 8.5). Therefore, comparing intensities measured by a 0° pixel and a 45° pixel without correcting for this difference will, almost certainly, result in a systematically biased measurement of polarization. Differences between pixels of the *same orientation* will result in quasi-random errors. Generally, this type of nonuniformity increases the uncertainty of the photometry, which re-emerges as increased scatter in the polarimetric estimation.

11.2.1.1 Performing the Characterization

The parameters that describe the polarimeter (pixel throughput, contrast/efficiency, and orientation) can be determined by illuminating the system with light whose polarization state is known *a priori*. The equations that describe the response of each pixel (Equation 6.3) have 3 unknowns, and can be solved directly using 3 different input states (or more, using linear least-squares). If the input state is not precisely known, for example if there is some uncertainty in the angle of polarization of the incident light, the characterization can still be performed by fitting a model of each pixel's response (Equation 8.1) to polarized light over a wide range of angles. I adopted the latter approach to characterize RITPIC (see Section 8.1).

The data acquired during the on-sky evaluation of RITPIC was calibrated using a two-step characterization process. First, I acquired unpolarized¹ dome flats to characterize the non-uniformity of the telescope+polarimeter system, using a variety of spectral filters. These flats were used in the usual way, to account for throughput differences across the focal plane and pixel-to-pixel throughput variations (for example, due to dust on various surfaces). The second stage of characterization involved measurements in the lab with a

¹The exact level of polarization in the flats wasn't independently measured; however, the configuration of the acquisition setup (see left panel of Figure 10.4) was designed to minimize polarization from reflection.)

rotating polarizer (Figure 8.1), to fully determine the relative throughput, contrast ratio, and orientation of every pixel in the RITPIC focal plane.

Ideally, the full response of the entire system (telescope and polarimeter) would be determined in one step. This could be done by introducing a rotating polarizer before the telescope aperture or before the polarimeter, which is easier in practice. By illuminating the system using minimally polarized flats, the polarimetric response of the entire system could be estimated, using measurements made at multiple polarizer orientations. Due to time constraints, this wasn't done for RITPIC's first on-sky deployment; however, it is the subject of future work.

11.2.1.2 Determining the Quality of Device Characterization

There is no straightforward way to quantify the quality of the device characterization, with measurements or with models. However, there are some useful methods to estimate the quality of the characterization/calibration process. First, one can compare the scatter in the raw intensities and Stokes parameters, to the variance expected from shot noise alone. If the photometric error is shot noise-dominated, one can assume that the uncertainty due to poor characterization is negligible. Conversely, if the photometry is not shot noise-limited, the extra uncertainty is likely due to poor characterization. For example, the total flux estimation of the unpolarized standard star HD 90156 has a scatter of $\sim 1\%$, from frame to frame (Figure 11.2).

Once the scatter in the measurements is understood, any instrumental bias can be investigated by observing polarimetric standards. Stars that have been measured to be very weakly polarized are excellent targets for estimating the “noise floor” or “sensitivity” of the instrument. However, the polarimeter should also be evaluated using polarization standards that are as close to the science target as possible in terms of overall brightness and degree of polarization.

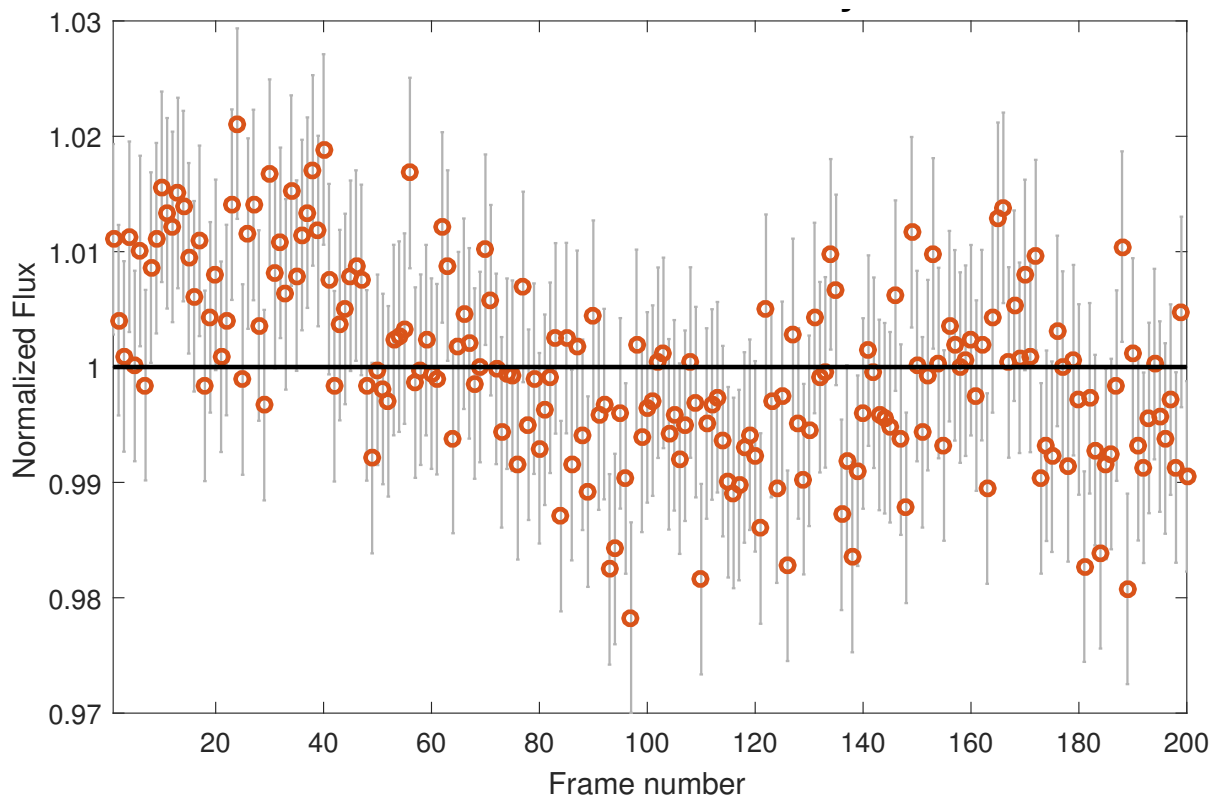


FIGURE 11.2: The photometry of HD 90156 shows a standard deviation of $\sim 1\%$ about the mean. This scatter is due to shot noise and errors associated with device nonuniformity.

11.2.2 Developing an Observing Strategy

An exquisite characterization of the telescope+polarimeter system does not, by itself, guarantee a high level of measurement precision. Even a perfectly uniform division-of-focal plane polarimeter is susceptible to errors associated with the “instantaneous field-of-view” of each pixel (see Section 8.2.2 and Section 9.1). The magnitude of the errors is related to the sampling of the telescope PSF by the polarimeter’s superpixels. Using simulated observations, I found that a sampling rate of 4 - 5 superpixels across a stellar FWHM is ideal. Sampling with fewer superpixels leads to an increased scatter in the photometry, because stars do not uniformly illuminate the pixels. Increasing the magnification beyond this point leads to other practical challenges, like decreasing the flux per pixel and the field of view of the instrument.

The polarimetry of unresolved sources and extended objects requires slightly different considerations. Stars are the most susceptible to sampling errors, because they represent

the steepest intensity gradients across the focal plane. However, stellar polarimetry can make use of techniques like aperture photometry, which can efficiently add the flux from many pixels and increase the measurement SNR. Proper sampling is especially important for bright sources and exposures shorter than ~ 1 s, where speckle patterns begin to emerge. Conversely, extended objects in astronomy often vary quite smoothly, which helps mitigate the instantaneous FOV artifacts. The downside is that observations of extended objects are often limited by the per-pixel photometric SNR and there is no easy way to “add up flux”, the way we can for stars.

11.2.3 Notes on Data Analysis

There is some flexibility in processing the data acquired with micropolarizer-based polarimeters. Although the raw data is modulated and sampled in a non-trivial way, sub-frames created using pixels of the same orientation can be treated much like conventional imaging data; they can be spatially registered, co-added, and even processed with spatial filters. Quantities like the raw pixel intensities and the Stokes parameters are normally distributed and are largely insensitive to the order of operations. For example, determining the Stokes parameters from an average of several intensity frames gives similar results to averaging several estimations of the Stokes parameters. Also, these quantities are linear and can be described using formal propagation of uncertainty. For these reasons, it’s advisable to work with (normalized) Stokes parameters as much as possible and avoid biased estimators like the degree and angle of linear polarization. If the DOLP and AOLP are needed (for example, to compare with other measurements), they should be constructed using the averaged Stokes parameters, to reduce the effects of noise as much as possible.

11.3 Performance of RITPIC and Future Outlook

The performance of a polarimeter is challenging to specify, because it also depends on the source properties. The scatter in the estimation of the Stokes parameters derived from

multiple measurements of the same source made with RITPIC (using $\sim 60\%$ of the pixel well depth) is $\sim 0.5\%$. This means RITPIC cannot easily determine the polarization of sources with fractional polarization less than $\sim 0.5\%$. However, for sources with a higher intrinsic polarization (when $p/\sigma_p \gtrsim 2$), many measurements can be averaged to result in an accuracy of $\sim 0.3\%$. For example, RITPIC's measurement of the polarization of HD 78344 agrees with previous measurements at the 0.2% level (see Table 10.1). Similarly, imaging polarimetry of Jupiter and Saturn shows structure at $\sim 0.3\%$ level. Saturn is an especially good test case, because it has regions of very low polarization, where structure at this level can be discerned (see Figure 10.22).

11.3.1 Expected Performance of Similar Devices

The data acquired with RITPIC during its commissioning run was not optimally calibrated (see Section 11.2.1.1). The quality of the polarimetry attainable with devices like RITPIC is ultimately limited by the quality of the photometric calibration, which relies on accurate characterization of the device parameters like throughput, contrast, and pixel orientation. As such, the photometric precision of RITPIC is limited by the same challenges that plague CCD-based differential photometry. As a general rule, the precision of differential photometry is limited to the level of a few millimagnitudes (Everett and Howell, 2001). Therefore, I expect that micropolarizer-based sensors can be calibrated to result in a polarimetric sensitivity of $0.1\% - 0.2\%$, which corresponds to a photometric precision of 1 mmag and 2 mmag, respectively.

11.4 Promising Science Cases

Micropolarizer-based polarimeters are extremely versatile detectors and are suited for a wide range of observations. Any object (extended or unresolved) that is sufficiently bright (for shot noise-limited observations), with an intrinsic polarization $\gtrsim 0.5\%$ can be measured with these sensors in a relatively straightforward way; a more rigorous characterization should allow observation of objects with polarization as small as $\sim 0.2\%$.

The inherent stability, compactness, and ease of use (as compared to conventional polarimeters) afforded by micropolarizer-based sensors makes them especially suited for deployment on smaller ground-based telescopes, as well as space-based and airborne platforms. In this section, I will outline several examples of targets that can be observed by micropolarizer-based sensors.

Solar System Planets

The surfaces and atmospheres of planets in the Solar System show changes on scales that range from hours to years and polarization fractions that are easily accessible to instruments like RITPIC. High cadence, long term polarimetry of the inner planets and the gas giants may reveal interesting insights into the seasonal and daily aspects of their atmospheres.

Comets

Polarimetry is a key tool in the study of comets. Over the course of their orbit, comets allow measurements at a wide range of phase angles, which helps constrain the microscopic geometry of the scattering particles in the coma. Because these sensors are inexpensive, they can be used to develop a world-wide network of observers to provide continuous monitoring of comets as they enter and leave the inner Solar System. The stability of these polarimeters makes it relatively straightforward to compare measurements made with different telescopes.

Proto-planetary Nebulae

Stars in the post-asymptotic giant branch stage of their evolution often show strong polarization and rapid variability. These objects are often accompanied by nebulae that also show complex and prominent polarization structure. Polarimeters like RITPIC on 1 m class telescopes provide an excellent platform for long-baseline monitoring of these objects.

11.5 A General Purpose Polarimeter

From Lyot's polariscope, to state-of-the-art polarimeters like the Gemini Planet Imager and SPHERE-ZIMPOL, astronomical polarimeters have been built for very specific measurements by diligent scientists. Many of these instruments were capable of extreme precision and all of them required highly skilled and dedicated scientists for operation. The idiosyncrasies of these instruments and the infrastructure needed to support them hindered the spread of polarimetric techniques and instrumentation into fields beyond astronomy. The polarimetric expertise developed by astronomers remained largely unknown to the outside world.

Micropolarizer-based polarization sensors represent the first "general purpose" polarimeter. Although these devices are not the most precise polarimeters that have been built, they are the first that can be taken off a telescope and immediately used with a microscope, or any other imaging system. The calibration and data analysis techniques developed for these devices can be easily used to study the Earth's surface, fluorophores on a microscope slide, or the structure of human skin. This flexibility may end up being the most useful property of these devices.

Appendix A

Dissemination of Results

The work described in this dissertation forms the basis of three upcoming publications that will be submitted to refereed journals:

1. **Dmitry Vorobiev**, Zoran Ninkov and Ray West, “High resolution 2D and 3D modeling of wire grid polarizers and micropolarizer arrays”, To be submitted to *Optical Engineering*.
2. **Dmitry Vorobiev**, Zoran Ninkov and Ray West, “Astronomical Polarimetry with the RIT Polarization Imaging Camera I. Characterization, Calibration, and Data Analysis Techniques”, To be submitted to *Publications of the Astronomical Society of the Pacific*.
3. **Dmitry Vorobiev** & Zoran Ninkov, “Astronomical Polarimetry with the RIT Polarization Imaging Camera II. Polarimetry of Point Sources, Nebulae and Solar System Planets”, To be submitted to *Publications of the Astronomical Society of the Pacific*.

While working on this project, I also contributed significantly to the development and space-qualification of digital micromirror devices (DMDs) for use in novel multi-object spectrometers. This work is described in two refereed publications:

1. Anton Travinsky, **Dmitry Vorobiev**, Zoran Ninkov, Alan Raisanen, Manuel Quijada, Stephen Smee, Jonathan Pellish, Timothy Schwartz, Massimo Robberto, Sara Heap, Devin Conley, Carlos Benavides, Nicholas Garcia, Zach Bredl, Sebastian Yllanes, "Evaluation of Digital Micromirror Devices for use in space-based Multi-Object Spectrometer application," *Journal of Astronomical Telescopes, Instruments, and Systems*, Submitted.
2. Anton Travinsky, **Dmitry Vorobiev**, Zoran Ninkov, Alan D. Raisanen, Jonny Pellish, Massimo Robberto, and Sara Heap, "Effects of heavy ion radiation on digital micromirror device performance," *Optical Engineering*, **55** (9), 094107 (Sep 29, 2016). doi:10.1117/1.OE.55.9.094107

Conference Presentations and Proceedings

Much of the work described in this proposal has been presented at various conferences and published in the conference proceedings:

- **Dmitry Vorobiev**, Zoran Ninkov, Neal Brock, Ray West, "On-sky performance evaluation and calibration of a polarization-sensitive focal plane array," *Proc. SPIE*. 9912, Advances in Optical and Mechanical Technologies for Telescopes and Instrumentation II, 99125X. (July 22, 2016) doi: 10.1117/12.2233333
- **Dmitry Vorobiev** and Zoran Ninkov, "Design, fabrication and characterization of a polarization-sensitive focal plane array," *Proc. SPIE*, 9403, Image Sensors and Imaging Systems 2015: Sensors, Color and Spectroscopy, 9403-9 (February 08, 2015).
- **Dmitry Vorobiev** and Zoran Ninkov, "Compact polarimeters based on polarization-sensitive focal plane arrays," *Proc. SPIE*, 9143, Space Telescopes and Instrumentation 2014: Optical, Infrared, and Millimeter Wave, 91435F. (August 02, 2014).
- **Dmitry Vorobiev**, Michael Gartley and Zoran Ninkov, "Polarization in a snap: imaging polarimetry with microgrid polarizer arrays," *Proc. SPIE*. 9099, Polarization: Measurement, Analysis, and Remote Sensing XI, 909904. (May 21, 2014).

Conference proceedings related to the DMD MOS:

- **Dmitry Vorobiev**, Anton Travinsky, Alan D. Raisanen, Zoran Ninkov, Timothy A. Schwartz, Massimo Robberto, Sara Heap, “Shock and vibration testing of digital micromirror devices (DMDs) for space-based applications,” *Proc. SPIE*. 9912, Advances in Optical and Mechanical Technologies for Telescopes and Instrumentation II, 99125M. (July 22, 2016) doi: 10.1117/12.2233591
- **Dmitry Vorobiev**, Anton Travinsky, Manuel A. Quijada, Zoran Ninkov, Alan D. Raisanen, Massimo Robberto, Sara Heap, “Measurements of the reflectance, contrast ratio, and scattering properties of digital micromirror devices (DMDs),” *Proc. SPIE*. 9912, Advances in Optical and Mechanical Technologies for Telescopes and Instrumentation II, 99125U. (July 22, 2016) doi: 10.1117/12.2233638
- Anton Travinsky, **Dmitry Vorobiev**, Alan D. Raisanen, Jonathan Pellish, Zoran Ninkov, Massimo Robberto, Sara Heap “The effects of heavy ion radiation on digital micromirror device performance,” *Proc. SPIE*. 9761, Emerging Digital Micromirror Device Based Systems and Applications VIII, 976108. (March 15, 2016) doi: 10.1117/12.2213634
- Manuel A. Quijada, Anton Travinsky, **Dmitry Vorobiev**, Zoran Ninkov, Alan Raisanen, Massimo Robberto, Sara Heap, “Optical evaluation of digital micromirror devices (DMDs) with UV-grade fused silica, sapphire, and magnesium fluoride windows and long-term reflectance of bare devices,” *Proc. SPIE*. 9912, Advances in Optical and Mechanical Technologies for Telescopes and Instrumentation II, 99125V. (July 22, 2016) doi: 10.1117/12.2233341

Bibliography

- Adams, W. S. and Dunham, T., Jr. Absorption Bands in the Infra-Red Spectrum of Venus. *Publications of the Astronomical Society of the Pacific*, 44:243–245, August 1932. doi: 10.1086/124235.
- Alfvén, H. Cosmic radiation as an intra-galactic phenomenon. *Arkiv för matematik, astronomi och fysik*, 25(29), 1937.
- Ambirajan, A. and Look, D. C., Jr. Optimum angles for a polarimeter: part ii. *Optical Engineering*, 34(6):1656–1658, 1995. doi: 10.1117/12.202098. URL <http://dx.doi.org/10.1117/12.202098>.
- Antonucci, R. R. J. and Miller, J. S. Spectropolarimetry and the nature of NGC 1068. *The Astrophysical Journal*, 297:621, 1985. ISSN 0004-637X. doi: 10.1086/163559.
- Baade, W. The polarization of the Crab nebula on plates taken with the 200-inch telescope. *Bull. Astron. Inst. Netherlands*, 12:312, May 1956a.
- Baade, W. Polarization in the Jet of Messier 87. *ApJ*, 123:550–551, May 1956b. doi: 10.1086/146194.
- Bohren, C. F. and Huffman, D. R. *Absorption and scattering of light by small particles*. New York: Wiley, 1983, 1983.
- Brock, N., Kimbrough, B. T., and Millerd, J. E. A pixelated micropolarizer-based camera for instantaneous interferometric measurements. *Proc. SPIE*, 8160:81600W–81600W–9, 2011. doi: 10.1117/12.896608. URL <http://dx.doi.org/10.1117/12.896608>.
- Coffeen, D. L. and Gehrels, T. Wavelength Dependence of Polarization. XV. Observations of Venus. *AJ*, 74:433, April 1969. doi: 10.1086/110822.

- Dave, J. V. Scattering of visible light by large water spheres. *Appl. Opt.*, 8(1):155–164, Jan 1969. doi: 10.1364/AO.8.000155. URL <http://ao.osa.org/abstract.cfm?URI=ao-8-1-155>.
- Davis, L., Jr. and Greenstein, J. L. The Polarization of Starlight by Aligned Dust Grains. *ApJ*, 114:206, September 1951. doi: 10.1086/145464.
- Dollfus, A. and Coffeen, D. L. Polarization of Venus I Disk Observations. *A&A*, 8:251, October 1970.
- Donati, J.-F., Semel, M., Rees, D. E., Taylor, K., and Robinson, R. D. Detection of a magnetic region on HR 1099. *A&A*, 232:L1–L4, June 1990.
- Everett, M. E. and Howell, S. B. A technique for ultrahigh-precision ccd photometry. *PASP*, 113(789):1428, 2001. URL <http://stacks.iop.org/1538-3873/113/i=789/a=1428>.
- Gao, S. and Gruev, V. Bilinear and bicubic interpolation methods for division of focal plane polarimeters. *Opt. Express*, 19(27):26161–26173, Dec 2011. doi: 10.1364/OE.19.026161. URL <http://www.opticsexpress.org/abstract.cfm?URI=oe-19-27-26161>.
- Gehrels, T., Herman, B. M., and Owen, T. Wavelength Dependence of Polarization. XIV. Atmosphere of Jupiter. *AJ*, 74:190, March 1969. doi: 10.1086/110790.
- George, M. C., Bergquist, J., Petrova, R., Wang, B., and Gardner, E. Infrared wire grid polarizers: metrology and modeling. *Proc. SPIE*, 8873:887302–887302–16, 2013. doi: 10.1117/12.2024752. URL <http://dx.doi.org/10.1117/12.2024752>.
- Gil-Hutton, R. and Benavidez, P. Southern stars that can be used as unpolarized standards. *Monthly Notices of the Royal Astronomical Society*, 345(1):97, 2003. doi: 10.1046/j.1365-8711.2003.06957.x. URL [+http://dx.doi.org/10.1046/j.1365-8711.2003.06957.x](http://dx.doi.org/10.1046/j.1365-8711.2003.06957.x).
- Hall, J. S. Observations of the polarized light from stars. *Science*, 109:166–167, February 1949.

- Hansen, J. E. Multiple Scattering of Polarized Light in Planetary Atmospheres. Part I. The Doubling Method. *Journal of Atmospheric Sciences*, 28:120–125, January 1971. doi: 10.1175/1520-0469(1971)028<0120:MSOPLI>2.0.CO;2.
- Hansen, J. E. and Hovenier, J. W. The doubling method applied to multiple scattering of polarized light. *J. Quant. Spec. Radiat. Transf.*, 11:809–812, 1971. doi: 10.1016/0022-4073(71)90057-4.
- Hansen, J. E. and Hovenier, J. W. Interpretation of the polarization of Venus. *Journal of Atmospheric Sciences*, 31:1137–1160, May 1974. doi: 10.1175/1520-0469(1974)031<1137:IOTPOV>2.0.CO;2.
- Hansen, J. E. and Travis, L. D. Light scattering in planetary atmospheres. *Space Science Reviews*, 16(4):527–610, 1974. ISSN 1572-9672. doi: 10.1007/BF00168069. URL <http://dx.doi.org/10.1007/BF00168069>.
- Hecht, E. *Optics*. Pearson education. Addison-Wesley, 2002. ISBN 9780321188786. URL <https://books.google.com/books?id=T3ofAQAAMAAJ>.
- Heiles, C. 9286 stars: An agglomeration of stellar polarization catalogs. *The Astronomical Journal*, 119(2):923, 2000. URL <http://stacks.iop.org/1538-3881/119/i=2/a=923>.
- Hiltner, W. A. On the Presence of Polarization in the Continuous Radiation of Stars. II. *ApJ*, 109:471, May 1949. doi: 10.1086/145151.
- Hiltner, W. A. Polarization of the Crab Nebula. *ApJ*, 125:300, March 1957. doi: 10.1086/146308.
- Hines, D. C., Schmidt, G. D., and Schneider, G. Analysis of Polarized Light with NICMOS. *PASP*, 112:983–995, July 2000. doi: 10.1086/316594.
- Hsu, W.-L., Myhre, G., Balakrishnan, K., Brock, N., Ibn-Elhaj, M., and Pau, S. Full-stokes imaging polarimeter using an array of elliptical polarizer. *Opt. Express*, 22(3):3063–3074, Feb 2014. doi: 10.1364/OE.22.003063. URL <http://www.opticsexpress.org/abstract.cfm?URI=oe-22-3-3063>.

- Jourlin, Y., Guttman, M., Lacour, F., Laukkanen, J., Yadel, K., Celle, F., Veillas, C., Kämpfe, T., Matthis, B., and Parriaux, O. Wide band, wide angular width wire-grid polarizer using galvanic growth technology. *Proc. SPIE*, 9130:913008–913008–8, 2014. doi: 10.1117/12.2051429. URL <http://dx.doi.org/10.1117/12.2051429>.
- Kervella, P., Bond, H. E., Cracraft, M., Szabados, L., Breielfelder, J., Mérand, A., Sparks, W. B., Gallenne, A., Bersier, D., Fouqué, P., and Anderson, R. I. The long-period Galactic Cepheid RS Puppis. III. A geometric distance from HST polarimetric imaging of its light echoes. *A&A*, 572:A7, December 2014. doi: 10.1051/0004-6361/201424395.
- King, O. G., Blinov, D., Ramaprakash, A. N., Myserlis, I., Angelakis, E., Baloković, M., Feiler, R., Fuhrmann, L., Hovatta, T., Khodade, P., Kougentakis, A., Kylafis, N., Kus, A., Modi, D., Paleologou, E., Panopoulou, G., Papadakis, I., Papamastorakis, I., Paterakis, G., Pavlidou, V., Pazderska, B., Pazderski, E., Pearson, T. J., Rajarshi, C., Readhead, A. C. S., Reig, P., Steiakaki, A., Tassis, K., and Zensus, J. A. The RoboPol pipeline and control system. *MNRAS*, 442:1706–1717, August 2014. doi: 10.1093/mnras/stu176.
- Lehmuskero, A., Kuittinen, M., and Vahimaa, P. Refractive index and extinction coefficient dependence of thin al and ir films on deposition technique and thickness. *Optics Express*, 15(17):10744–10752, Aug 2007. doi: 10.1364/OE.15.010744. URL <http://www.opticsexpress.org/abstract.cfm?URI=oe-15-17-10744>.
- Lin, M. Y., Tsai, T. H., Hsiao, L. J., Tu, W. C., Wu, S. H., Wang, L. A., Lee, S. C., and Lin, H. Y. Design and fabrication of nano-structure for three-dimensional display application. *IEEE Photonics Technology Letters*, 28(8):884–886, April 2016. ISSN 1041-1135. doi: 10.1109/LPT.2016.2516338.
- Lyot, B. Recherches sur la polarisation de la lumiere des planetes et de quelques substances terrestres. *Annales de l'Observatoire de Paris*, 8(1), 1929.
- Macintosh, B., Graham, J., Palmer, D., Doyon, R., Gavel, D., Larkin, J., Oppenheimer, B., Saddlemyer, L., Wallace, J. K., Bauman, B., Evans, J., Erikson, D., Morzinski, K., Phillion, D., Poyneer, L., Sivaramakrishnan, A., Soummer, R., Thibault, S., and Veran, J.-P. The Gemini Planet Imager. In *Society of Photo-Optical Instrumentation*

- Engineers (SPIE) Conference Series*, volume 6272 of Proc. SPIE, page 62720L, June 2006. doi: 10.1117/12.672430.
- McPeak, K. M., Jayanti, S. V., Kress, S. J. P., Meyer, S., Iotti, S., Rossinelli, A., and Norris, D. J. Plasmonic films can easily be better rules and recipes. *ACS Photonics*, 2(3):326–333, 2015. doi: 10.1021/ph5004237. URL <http://dx.doi.org/10.1021/ph5004237>. PMID: 25950012.
- Mélen, G., Rosenfeld, W., and Weinfurter, H. Impact of the slit geometry on the performance of wire-grid polarisers. *Opt. Express*, 23(25):32171–32178, Dec 2015. doi: 10.1364/OE.23.032171. URL <http://www.opticsexpress.org/abstract.cfm?URI=oe-23-25-32171>.
- Myhre, G., Hsu, W.-L., Peinado, A., LaCasse, C., Brock, N., Chipman, R. A., and Pau, S. Liquid crystal polymer full-stokes division of focal plane polarimeter. *Opt. Express*, 20(25):27393–27409, Dec 2012. doi: 10.1364/OE.20.027393. URL <http://www.opticsexpress.org/abstract.cfm?URI=oe-20-25-27393>.
- Nordin, G. P., Meier, J. T., Deguzman, P. C., and Jones, M. W. Micropolarizer array for infrared imaging polarimetry. *Journal of the Optical Society of America A*, 16(5):1168, 1999. ISSN 1084-7529. doi: 10.1364/JOSAA.16.001168.
- Oort, J. H. and Walraven, T. Polarization and composition of the Crab nebula. *Bull. Astron. Inst. Netherlands*, 12:285, May 1956.
- Palik, E. D. *Handbook of optical constants of solids*, volume 3. Academic press, 1998.
- Peltzer, J. J., Bachman, K. A., Rose, J. W., Flammer, P. D., Furtak, T. E., Collins, R. T., and Hollingsworth, R. E. Plasmonic micropolarizers for full stokes vector imaging. *Proc. SPIE*, 8364:83640O–83640O–12, 2012. doi: 10.1117/12.919324. URL <http://dx.doi.org/10.1117/12.919324>.
- Perlman, E. S., Biretta, J. A., Zhou, F., Sparks, W. B., and Macchetto, F. D. Optical and radio polarimetry of the m87 jet at 02 resolution. *The Astronomical Journal*, 117(5):2185, 1999. URL <http://stacks.iop.org/1538-3881/117/i=5/a=2185>.

- Pye, D. *Polarised Light in Science & Nature*. Institute of Physics Publishing, 2001. ISBN 0750306734.
- Raisanen, A. D., Presnar, M. D., Ninkov, Z., Fourspring, K., Meng, L., and Kerekes, J. P. Simulation of practical single-pixel wire-grid polarizers for superpixel stokes vector imaging arrays. *Optical Engineering*, 51(1):016201–1–016201–6, 2012. doi: 10.1117/1.OE.51.1.016201. URL <http://dx.doi.org/10.1117/1.OE.51.1.016201>.
- Reifenstein, E. C., Brundage, W. D., and Staelin, D. H. Crab nebula pulsar npo527. *Phys. Rev. Lett.*, 22:311–311, Feb 1969. doi: 10.1103/PhysRevLett.22.311. URL <https://link.aps.org/doi/10.1103/PhysRevLett.22.311>.
- Rodenhuis, M., Canovas, H., Jeffers, S. V., de Juan Ovelar, M., Min, M., Homs, L., and Keller, C. U. The extreme polarimeter: design, performance, first results and upgrades. volume 8446, pages 84469I–84469I–18, 2012. doi: 10.1117/12.927203. URL <http://dx.doi.org/10.1117/12.927203>.
- Roelfsema, R., Schmid, H. M., Pragt, J., Gisler, D., Waters, R., Bazzon, A., Baruffolo, A., Beuzit, J.-L., Boccaletti, A., Charton, J., Cumani, C., Dohlen, K., Downing, M., Elswijk, E., Feldt, M., Groothuis, C., de Haan, M., Hanenburg, H., Hubin, N., Joos, F., Kasper, M., Keller, C., Kragt, J., Lizon, J.-L., Mouillet, D., Pavlov, A., Rigal, F., Rochat, S., Salasnich, B., Steiner, P., Thalmann, C., Venema, L., and Wildi, F. The zimpol high-contrast imaging polarimeter for sphere: design, manufacturing, and testing. volume 7735, pages 77354B–77354B–17, 2010. doi: 10.1117/12.857045. URL <http://dx.doi.org/10.1117/12.857045>.
- Rybicki, G. B. and Lightman, A. P. *Radiative processes in astrophysics*. New York, Wiley-Interscience, 1979. 393 p., 1979.
- Ryu, H., Yoon, S. J., and Kim, D. Influence of surface roughness on the polarimetric characteristics of a wire-grid grating polarizer. *Appl. Opt.*, 47(30):5715–5721, Oct 2008. doi: 10.1364/AO.47.005715. URL <http://ao.osa.org/abstract.cfm?URI=ao-47-30-5715>.
- Sabatke, D. S., Descour, M. R., Dereniak, E. L., Sweatt, W. C., Kemme, S. A., and Phipps, G. S. Optimization of retardance for a complete stokes polarimeter. *Opt.*

- Lett.*, 25(11):802–804, Jun 2000. doi: 10.1364/OL.25.000802. URL <http://ol.osa.org/abstract.cfm?URI=ol-25-11-802>.
- Scarrott, S. M. and Scarrott, R. M. J. Bvri imaging polarimetry of the frosty leo nebula. *Monthly Notices of the Royal Astronomical Society*, 268:615, June 1994. doi: 10.1093/mnras/268.3.615.
- Scarrott, S. M., Warren-Smith, R. F., Pallister, W. S., Axon, D. J., and Bingham, R. G. Electronographic polarimetry - The Durham polarimeter. *MNRAS*, 204:1163–1177, September 1983. doi: 10.1093/mnras/204.4.1163.
- Schmid, H., Joos, F., Buenzli, E., and Gisler, D. Long slit spectropolarimetry of jupiter and saturn. *Icarus*, 212(2):701 – 713, 2011. ISSN 0019-1035. doi: <http://dx.doi.org/10.1016/j.icarus.2011.01.016>.
- Semel, M., Donati, J.-F., and Rees, D. E. Zeeman-Doppler imaging of active stars. 3: Instrumental and technical considerations. *A&A*, 278:231–237, October 1993.
- Serkowski, K. Statistical Analysis of the Polarization and Reddening of the Double Cluster in Perseus. *Acta Astron.*, 8:135, 1958.
- Serkowski, K., Mathewson, D. S., and Ford, V. L. Wavelength dependence of interstellar polarization and ratio of total to selective extinction. *ApJ*, 196:261–290, February 1975. doi: 10.1086/153410.
- Shiles, E., Sasaki, T., Inokuti, M., and Smith, D. Y. Self-consistency and sum-rule tests in the kramers-kronig analysis of optical data: Applications to aluminum. *Phys. Rev. B*, 22:1612–1628, Aug 1980. doi: 10.1103/PhysRevB.22.1612. URL <http://link.aps.org/doi/10.1103/PhysRevB.22.1612>.
- Shiltsev, V. The 1761 discovery of Venus’ atmosphere: Lomonosov and others. *Journal of Astronomical History and Heritage*, 17:85–112, March 2014.
- Simmons, J. F. L. and Stewart, B. G. Point and interval estimation of the true unbiased degree of linear polarization in the presence of low signal-to-noise ratios. *A&A*, 142: 100–106, January 1985.

- Snik, F., Craven-Jones, J., Escuti, M., Fineschi, S., Harrington, D., De Martino, A., Mawet, D., Riedi, J., and Tyo, J. S. An overview of polarimetric sensing techniques and technology with applications to different research fields. *Proc. of SPIE*, 9099: 90990B, 2014. ISSN 1996756X. doi: 10.1117/12.2053245. URL <http://proceedings.spiedigitallibrary.org/proceeding.aspx?doi=10.1117/12.2053245>.
- Sparks, W. B. and Axon, D. J. Panoramic Polarimetry Data Analysis. *PASP*, 111: 1298–1315, October 1999. doi: 10.1086/316434.
- Tyo, J. S. Design of optimal polarimeters: maximization of signal-to-noise ratio and minimization of systematic error. *Appl. Opt.*, 41(4):619–630, Feb 2002. doi: 10.1364/AO.41.000619. URL <http://ao.osa.org/abstract.cfm?URI=ao-41-4-619>.
- Tyo, J. S., Goldstein, D. L., Chenault, D. B., and Shaw, J. A. Review of passive imaging polarimetry for remote sensing applications. *Applied Optics*, 45(22):5453–5469, 2006. ISSN 0003-6935. doi: 10.1364/AO.45.005453.
- Tyo, J. S., LaCasse, C. F., and Ratliff, B. M. Total elimination of sampling errors in polarization imagery obtained with integrated microgrid polarimeters. *Opt. Lett.*, 34(20):3187–3189, Oct 2009. doi: 10.1364/OL.34.003187. URL <http://ol.osa.org/abstract.cfm?URI=ol-34-20-3187>.
- Ueta, T., Murakawa, K., and Meixner, M. Hubble space telescope nicmos imaging polarimetry of proto-planetary nebulae. ii. macromorphology of the dust shell structure via polarized light. *The Astronomical Journal*, 133:1345–1360, April 2007. doi: 10.1086/511265.
- Van Cleve, J. and Caldwell, D. *Kepler Instrument Handbook*. NASA Ames Research Center, ksci-19033-001 edition, 2009.
- Vorobiev, D. and Ninkov, Z. Compact polarimeters based on polarization-sensitive focal plane arrays. *Proc. SPIE*, 9143:91435F–91435F–9, 2014. doi: 10.1117/12.2059201. URL <http://dx.doi.org/10.1117/12.2059201>.
- Wardle, J. F. C. and Kronberg, P. P. The linear polarization of quasi-stellar radio sources at 3.71 and 11.1 centimeters. *ApJ*, 194:249–255, December 1974. doi: 10.1086/153240.

- Wiktorowicz, S. J., Millar-Blanchaer, M., Perrin, M. D., Graham, J. R., Fitzgerald, M. P., Maire, J., Ingraham, P., Savransky, D., Macintosh, B. A., Thomas, S. J., Chilcote, J. K., Draper, Z. H., Song, I., Cardwell, A., Goodsell, S. J., Hartung, M., Hibon, P., Rantakyrö, F., and Sadakuni, N. Gemini planet imager observational calibrations vii: on-sky polarimetric performance of the gemini planet imager. *Proc. SPIE*, 9147: 914783–914783–11, 2014. doi: 10.1117/12.2056616. URL <http://dx.doi.org/10.1117/12.2056616>.
- Wiscombe, W. J. Improved mie scattering algorithms. *Appl. Opt.*, 19(9):1505–1509, May 1980. doi: 10.1364/AO.19.001505. URL <http://ao.osa.org/abstract.cfm?URI=ao-19-9-1505>.
- Zhao, X., Bermak, A., Boussaid, F., and Chigrinov, V. G. Liquid-crystal micropolarimeter array for full stokes polarization imaging in visible spectrum. *Opt. Express*, 18(17):17776–17787, Aug 2010. doi: 10.1364/OE.18.017776. URL <http://www.opticsexpress.org/abstract.cfm?URI=oe-18-17-17776>.